Università degli Studi di Padova

Dipartimento di INGEGNERIA CIVILE EDILE E AMBIENTALE

SCUOLA DI DOTTORATO DI RICERCA IN

SCIENZA DELL'INGEGNERIA CIVILE EDILE E AMBIENTALE

XXVIII CICLO

CALIBRATION STRATEGIES OF A DEPTH-INTEGRATED NUMERICAL MODEL FOR THE PROPAGATION OF FLOW-LIKE LANDSLIDES

Direttore della Scuola: ***Ch.mo Prof. Stefano Lanzoni***

Supervisore: ***Ch.mo Prof. Simonetta Cola***

Controrelatore: ***Ch.mo Prof. Marina Pirulli***

Dottorando: **Lorenzo Brezzi**

Padova, Luglio 2016

Università degli Studi di Padova

Dipartimento di INGEGNERIA CIVILE EDILE E AMBIENTALE

SCUOLA DI DOTTORATO DI RICERCA IN

SCIENZA DELL'INGEGNERIA CIVILE EDILE E AMBIENTALE

XXVIII CICLO

CALIBRATION STRATEGIES OF A DEPTH-INTEGRATED NUMERICAL MODEL FOR THE PROPAGATION OF FLOW-LIKE LANDSLIDES

Direttore della Scuola: ***Ch.mo Prof. Stefano Lanzoni***

Supervisore: ***Ch.mo Prof. Simonetta Cola***

Controrelatore: ***Ch.mo Prof. Marina Pirulli***

Dottorando: **Lorenzo Brezzi**

Padova, Luglio 2016

To mommy, daddy and Gordon,
Lovely supports in every situation.

To Noah,

Love child of two special persons:

You are welcome.

You only live once,
but if you do it right,
once is enough.
Mae West

Live as if you were to die tomorrow.
Learn as if you were to live forever.
Gandhi

INDEX

ABSTRACT (IN ENGLISH)

Nowadays, the numerical models are important allies for the study of physical and natural phenomena. They become progressively more complicated because various differential equations are included to consider the different processes involved in a singular phenomenon. The number of parameters used to adapt the numerical results to the real measurements increase consequently.

Among the huge quantity of natural phenomena studied, the landslides are definitely important and, among them, the flow-slides are a type, which actually have an increasing occurrence frequency because of the climate change. When the velocity of the flowing material is high, this type of natural hazard becomes even more worrying. The risk and the damage, which may result, are significant, especially when the landslide is located in close proximity to residential areas. The catastrophic effects range from the destruction of buildings and infrastructures, to the most tragic loss of human lives.

Three processes of a flow-slide could be individuated: the trigger mechanism, the propagation and the final deposit. Topic of this thesis is the study of the last two phases that occur after the mass collapse has already happened. The propagation and the deposit phases will be here analyzed using a model which integrates the Saint Venant's equations developed for the flow of an equivalent homogeneous material according to the shallow water hypothesis. The model is applied before to the simulation of several laboratory experiments and, then, for reproducing a debris flow really occurred in 2010 in Italy.

The calibration phase is the basic operation for using a numerical model. The parameters considered have to be smartly defined to reproduce the phenomenon with a satisfactory likelihood. When the parameters have a physical meaning, it is necessary to check if they allow the model to produce reliable results, even when the model necessarily introduces strong approximations. Sometimes, anyway, the parameters to include in the calculation have just a mathematical significance. In this case, it is even more important to calibrate the model paying attention to all the complexities of the phenomenon, because if the calibration strategy does not take into account the various aspects of the case study, the parameters obtained by the back-analysis may be senseless.

This thesis wants to show the complexity that may characterize the calibration procedure. Once the numerical model has been adopted and its possibilities and limitations have been evaluated, the analysis of different cases will help to evidence the difficulties that the back-analysis can present. To this aim, in this work, three main case studies are presented: the spreading of a column of cohesive material on a horizontal plane, numerous flume tests performed using three-phases mixtures and, finally, a real debris flow occurred in 2010 along the Rotolon stream, in North-Western sector of Veneto region (Italy). It is important to underline that all the laboratory tests are performed on purpose to apply the back-analysis, paying therefore particular attention to the data acquisition conditions.

For all the case studies, many calibration procedures are applied in order to individuate the most suitable to reduce the uncertainty in the determination of the fitting parameters.

ABSTRACT (IN ITALIAN)

Oggigiorno, i modelli numerici ricoprono un ruolo di fondamentale importanza per lo studio di fenomeni fisici e naturali. Essi diventano via via sempre più complessi grazie all'aumento del numero di equazioni differenziali implementate in ciascun modello al fine di tener conto dei differenti aspetti che caratterizzano il fenomeno oggetto studio. Conseguentemente cresce anche il numero dei parametri da valutare per adattare i risultati ottenuti dal modello numerico alle misure reali.

Tra tutti i fenomeni naturali che si possono considerare, i frane sono indiscutibilmente molto importanti. Tra i diversi tipi di frane, le colate sono una tipologia che si presenta sempre con maggior frequenza a causa dei cambiamenti climatici in atto e con effetti molto dannosi. Quando, poi, la velocità raggiunta in questi fenomeni diventa elevata, aumenta il loro potere distruttivo. I rischi e i danni che ne possono nascere non sono trascurabili, in modo particolare quando le colate avviene in prossimità di aree residenziali. Gli effetti catastrofici che ne possono scaturire spaziano dalla distruzione di edifici e infrastrutture, fino ad arrivare alla ancor più tragica perdita di vite umane.

Quando si studia un movimento di colata, tre processi devono essere presi in considerazione: il meccanismo di innesco, la fase di propagazione ed infine il deposito. Questa tesi riguarda principalmente lo studio degli ultimi due processi che si verificano, cioè, quando il materiale ha già iniziato il suo movimento. Le fasi di propagazione e di arresto sono qui analizzate utilizzando un modello numerico sviluppato integrando le equazioni di Saint Venant per il flusso di un materiale monofase omogeneo in acque basse. Il modello è stato applicato sia per la simulazione di esperimenti di laboratorio sia per riprodurre un debris flow avvenuto nel nord Italia nel 2010.

Quando si utilizza un modello numerico, la fase di calibrazione rappresenta un'operazione essenziale affinché si possano ottenere buoni risultati. I parametri utilizzati dal codice devono essere attentamente definiti in modo che il modello possa riprodurre il fenomeno fisico con elevata accuratezza. Quando i parametri hanno un significato fisico, risulta necessario controllare se il loro utilizzo, considerando le approssimazioni che il modello inevitabilmente comporta, permette di produrre risultati affidabili.

A volte, tuttavia, i parametri che devono essere inseriti nel modello prescindono dalla natura fisica del caso in esame, ed hanno solamente un significato in termini matematici. Quando questo avviene, risulta ancor più importante calibrare il modello, cercando di cogliere l'intera complessità del fenomeno. Se la strategia di calibrazione non tiene conto dei vari aspetti che caratterizzano il caso di studio, infatti, i parametri ottenuti tramite back-analysis potrebbe non aver alcun senso.

Questa tesi si pone l'obiettivo di sottolineare la complessità che può contraddistinguere il processo di calibrazione. Dopo aver deciso quale modello numerico utilizzare ed averne comprese possibilità e limitazioni, lo studio di casi di studio differenti permette di evidenziare le criticità e le problematiche che la back-analysis può presentare. A tale scopo, in questo lavoro vengono considerati principalmente tre casi di studio. Il primo riguarda il collasso di una colonna di materiale coesivo su di un piano orizzontale. Successivamente la procedura è applicata ad un gruppo di prove in canaletta condotte con diverse miscele di argilla e sabbia. Infine, viene analizzata la colata detritica avvenuta nel 2010 lungo il torrente Rotolon, situato in nella parte nord-occidentale del Veneto. È importante sottolineare che tutti i test di laboratorio sono stati eseguiti appositamente

per la successiva applicazione della back-analysis, prestando quindi particolare attenzione alle modalità di acquisizione dei dati.

Per tutti e tre i casi, è stata ricercata ed applicata una strategia di calibrazione per ridurre l'incertezza nell'identificazione dei parametri ottimali.

1 INTRODUCTION

Natural hazards are aggressive events, capable of producing damage to the physical and social space where they take place not only at the moment of their occurrence, but on a long-term basis due to their associated consequences. When these consequences have a major impact on society and/or infrastructure, they become natural disasters. Specifically, they are considered within a geological and hydro-meteorological conception, where earthquakes, volcanoes, floods, landslides, storms, droughts and tsunamis are the main types. These hazards are strongly related to geomorphology since they are important ingredients of the Earth's surface dynamics. Natural hazards take place in a certain place and during a specific time, but their occurrence is not instantaneous. Time is always involved in the development of such phenomena.

The debris flows are manifestations with paroxysmal impulsive sediment transport along the secondary hydrographic network. This kind of phenomena affects the geomorphological evolution of the valley in a rather pronounced, as the main responsible for the accumulation processes on alluvial fans and placing sediment in hydrographic auctions of higher order. In many cases, the most dangerous risk is related to the terminal basin areas, corresponding to the alluvial fans.

When these areas are used for habitation, production and sales, the dangerousness of the flows gives rise to a high degree of risk. In fact, they have devastating effects because of the rapidity of movement and force of impact related to significant transport of stone materials.

The recent expansion of road infrastructure and urban centers, which took place after the II World War in the mountain areas mainly for tourist purposes, has often prepended criteria of economic convenience to those of security. The soils in alluvial fans, in fact, were among the hardest hit by the indiscriminate employment centers and other infrastructure, with a significant increase in exposure to danger. The protection from the danger of debris flows, or more generally from flooding and floods, has become almost a requirement priority in the interventions placing the protection of various types of infrastructures. The progressive involvement in this issue by research groups and institutions responsible for land management has allowed preparing systematic studies in order to deepen knowledge on the subject. It is particularly difficult to have the correct identification of the source areas, to interpret the triggering mechanisms and to define the boundaries of areas potentially involved. Due to the high concentration of facilities in the fan zones, it is increasingly felt the need to define the areas potentially affected by a debris flow and to plan interventions and countermeasures for the defense of the villages and the safety of roads crossing these areas.

The study of debris flows is very difficult due to the strongly time unpredictability of the phenomenon, its short duration and its high destructive force that make difficult and dangerous to carry out systematic observations and to obtain field surveys. In recent decades, many studies have focused on this phenomenon, in order to understand the behavior and to try to derive the laws that may help in the prediction of these events. In fact, if the initial parameters related to the movement of the water-sediment mixture are known, as for example the speed, the flow rate, the depth of the flow, the coefficient of resistance to motion, etc., the extension of the deposit downstream can be rather easily calculated. However, it is almost impossible to detect directly in the field these

parameters when the debris flow is taking place, except in the experimental basins that have adequate equipment such as video cameras and ultrasonic level sensors.

To study these phenomena, there are different approaches: on one hand, it is investigated the trigger mechanism that starts a flow, taking into account the rainfall information and the characteristics of the area (Wieczorek, 1987; Zhou et al., 2015; Tang et al., 2012). On the other hand, many numerical models have been developed to reproduce the propagation and deposit phases of these flows (Savage & Hutter, 1989; O'brien et al., 1993; Hungr, 1995; Iverson & Denlinger, 2001; Mangeney-Castelnau et al., 2003; Pirulli, 2005; Pitman & Le, 2005; Pudasaini et al., 2005; Pastor et al., 2008; Armanini et al., 2009) (Hungr & McDougall, 2009; Pudasaini, 2012; Rosatti & Begnudelli, 2013). The final aim in this contest is to calibrate the model they are using, depending on the type of material and of the main geomorphological features of the site in order to be able to reproduce numerically the flow. A good comprehension of this, make it possible to fill a database that can give you the possibility to predict a new case.

Real rapid landslides are commonly difficultly predictable. For this reason, few information about the physical and rheological characteristics of the material are available. It is therefore rare to collect kinematic measurements of the flow and to have precise data about the erosion and deposition areas.

To overcame these difficulties, various researchers have used different physical in reduced-scale models in order to simulate the deposition mechanisms of debris flows (Mainali & Rajaratnam, 1994; Egashira et al., 2001; Cochard & Ancey, 2009; Canelli et al., 2012; Haas et al., 2015). Variables such as speed, particle size distribution, the impacting forces and the density of the solid-liquid mixture, which are extremely difficult to estimate in the field, can be easily measured by means of a small-scale model.

Even large-scale models, such as the artificial canal in concrete (95m long and 2m wide) built by the US Geological Survey (Major, 1997; Iverson et al., 2010), or the straight concrete flume (45 m long and 0.7 m wide) constructed in China (Zhou et al., 2015), have been developed and used to simulate the behavior of debris flows, focusing the transport mechanism and energy dissipation.

Both types of model, small-scale and big-scale ones, allow the researchers to analyze the shape of the debris flow deposits, being able to measure the width, length and thickness, in order to understand the relationships that exist among these values and the rheological parameters. The latter are the basis of zoning of danger to mitigate and prevent the risk arising from such events.

The physical and mathematical modeling of this phenomenon has only recently been systematically addressed. The first sufficiently comprehensive analyzes have appeared in the late '70s (Takahashi, 1978). In recent years, the rapid development of information technology and the continuous increase in computing power have made possible the creation of numerical computer models to simulate complex phenomena such as landslides and debris flows.

The numerical models are used to simulate the phase of deceleration and stopping of debris flows, and then to understand the rheological scheme able to describe the different types of movements investigated in the field or in the laboratory. It is important to verify the reliability of mathematical models to understand the goodness of the results that are obtained from the

simulation and especially to identify the more suitable type of software for the particular case you intend to play.

This research deals with the study and modeling of the process of propagation of debris flows by focusing on specific stages of slowing down and stopping, and the definition of rheological law attached to them. The main goal of this thesis is to underline the dependency of the most reliable parameters on the calibration strategy used.

Starting with a simple laboratory case, in this paper, it will be analyzed the strengths and weaknesses of the numerical results you can obtain with the increase of the complication of the study case. The simple axial-symmetrical spreading of a cohesive material column is initially considered. Subsequently, a slightly more complicated case, consisting in several flume tests, is analyzed. The final application of the back-analysis to a real debris flow required a data assimilation procedure to reduce the uncertainty of the rheological parameters choice.

The GeoFlow-SPH code (Pastor et al., 2008) is the tool used to follow the described goals. It is a depth-integrated model that solves the shallow water equations to simulate flow-like landslides. Various rheological laws can be included in the calculation.

In the case studies considered, it is decided to apply the viscoplastic model proposed by Bingham (1919) to analyze cohesive mixtures composed by kaolin and water. The frictional model of Voellmy (1955) is instead used when the material has a granular content or when the flow is mainly composed by debris.

2 LANDSLIDES CLASSIFICATION

2.1 INTRODUCTION

The system of landslide classification devised by the late D.J. Varnes has become the most widely used system in the English language (Varnes, 1954; 1978; Cruden & Vernes, 1996). Many authors aim to introduce modifications to the Varnes classification to reflect recent advances in understanding of landslide phenomena and the materials and mechanisms involved.

The type of material is one of the most important factors influencing the behavior of landslides. However, the threefold material division proposed by Varnes (1978), including "rock, debris, and earth," is compatible neither with geological terminology of materials distinguished by origin, nor with geotechnical classifications based on mechanical properties (Morgenstern, 1992).

I was therefore necessary to modernize this cataloguing. In that sense, Hungr et al. (2014) composed an interesting update of the Varnes classification of landslide types. From his overview, many helpful information in the identification of the various family of landslides are available.

A landslide is a physical system that develops in time through several stages. As reviewed by Skempton and Hutchinson (1969), the history of a mass movement comprises pre-failure deformations, failure itself and post-failure displacements. Many landslides exhibit a number of movement episodes, separated by long or short periods of relative quiescence. Failure is the single most significant movement episode in the known or anticipated history of a landslide, which usually involves the first formation of a fully developed rupture surface as a displacement or strain discontinuity.

The degree of strength loss during failure determines the post-failure velocity of the landslide. The failure stage may involve a kinematic change from sliding to flow or fall, which is also relevant to post-failure behavior and destructiveness of the landslide.

The number of classes proposed by Hungr is reasonably small and this make the system simple and easy to use. The system is respectful of previous usage and adopts established terms to the greatest extent possible, to enhance "backward compatibility" with older literature. Hungr proposed a classification sufficiently flexible to allow application both in cases where only meager preliminary data exist, as well as those where data are detailed and abundant.

One of the most interesting aspects of the review proposed by Hungr is that contains class names supported by concise, but comprehensive formal definitions. The principles of the classification he wanted to introduce would remain valid, repeatable, and refutable, regardless of the actual words that are used in forming the class name.

2.2 BRIEF HISTORY

Some of the earliest landslide classification systems originated in the Alpine countries. Baltzer (1875) in Switzerland seems to have been the first to distinguish between the various basic modes of motion: fall, slide, and flow. This division persists to the present time, supplemented by toppling and spreading (Figure 2.2.1).

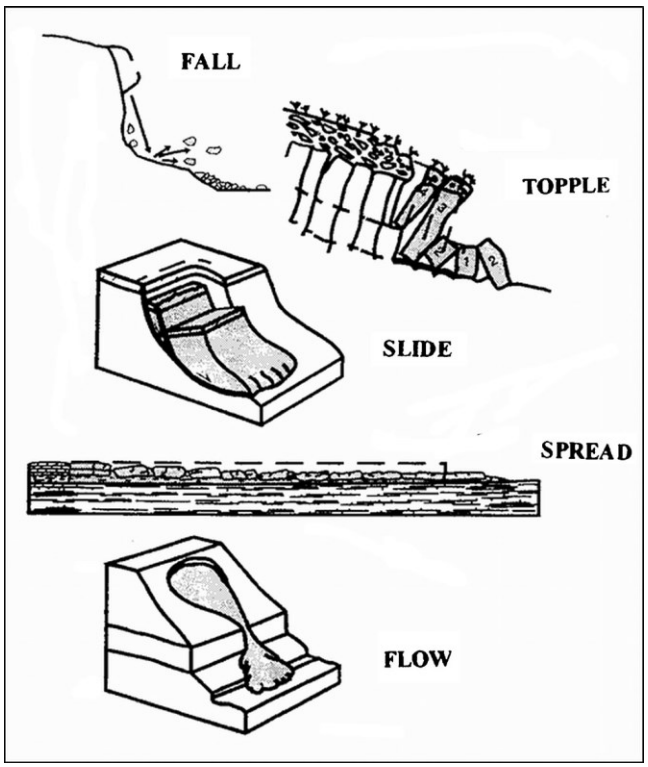

Figure 2.2.1 Types of movement defined by Baltzer (1875), Cruden and Varnes (1996).

Debris flows represent a particularly important hazard in mountainous terrain and have attracted special attention from early days. In the USA, Sharpe (1938) introduced a tri-dimensional classification system recognizing type of movement, material and movement velocity. He also coined (presumably) the important terms debris flow (channeled), debris avalanche (open-slope), and earth flow.

The term "earth flow" was reinforced and thoroughly described in the work of Keefer and Johnson (1983) and is used in North America as a synonym for the British "mudslide" (Hutchinson, 1988). Sharpe's framework was expanded by Varnes (1954; 1978) in his influential articles prepared for the Transportation Research Board of the National Research Council in Washington. Cruden and Varnes, to concentrate on the type and rate of movement, modified this in 1996.

Movement type	*Rock*	*Debris*	*Earth*
Fall	*1. Rock fall*	*2. Debris fall*	*3. Earth fall*
Rotational sliding	*4. Rock topple*	*5. Debris topple*	*6. Earth topple*
Translational sliding	*7. Rock slump*	*8. Debris slump*	*9. Earth slump*
Lateral spreading	*10. Block slide*	*11. Debris slide*	*12. Earth slide*
Flow	*13. Rock spread*		*14. Earth spread*
	15. Rock creep	*16. Talus flow*	*17. Dry sand flow*
		18. Debris flow	*19. Wet sand flow*
		20. Debris avalanche	*21. Quick clay flow*
		22. Solifluction	*23. Earth flow*
		24. Soil creep	*25. Rapid earth flow*
			26. Loess flow
Complex	*27. Rock slide-debris avalanche*	*28. Cambering, valley bulging*	*29. Earth slump-earth flow*

Table 2.2.1 A summary of Varnes' 1978 classification system.

Another important aspect that characterize a landslide can be found in the study of the velocities of the movement. For this reason, a velocity scale, later updated by International Geotechnical

Society's UNESCO Working Party on World Landslide Inventory (WP/WLI) (1995) and Cruden and Varnes (1996) completes the classification (Table 2.2.2).

Velocity class	*Description*	*Velocity (mm/s)*	*Typical velocity*
7	*Extremely rapid*	*5×10^{3}*	*5 m/s*
6	*Very rapid*	*5×10^{1}*	*3 m/min*
5	*Rapid*	*5×10^{-1}*	*1.8 m/h*
4	*Moderate*	*5×10^{-3}*	*13 m/month*
3	*Slow*	*5×10^{-5}*	*1.6 m/year*
2	*Very slow*	*5×10^{-7}*	*16 mm/year*
1	*Extremely slow*		

Table 2.2.2 Landslides velocity scale (WP/WLI 1995 and Cruden and Varnes 1996)

2.3 MATERIAL TERMINOLOGY

To clearly describe a landslide, it is necessary to consider the material involved. The material composition play a fundamental role in the determination of the mechanical behavior of the phenomenon. The proposed list of material types, compiled by means of a simplification of existing soil and rock description systems, is summarized in Table 2.3.1.

Material name	*Character descriptors*	*Simplified description for the purpose classification*	*Corresponding unified soil classes*	*Laboratory indices (if available)*
Rock	*Strong*	*Strong—broken with a hammer*		*UCS>25 MPa*
	Weak	*Weak—peeled with a knife*		*2<UCS<25 MPa*
Clay	*Stiff*	*Plastic, can be molded into standard thread when moist, has dry strength*	*GC, SC, CL, MH, CH, OL, and OH*	*Ip> 0.05*
	Soft			
	Sensitive			
Mud	*Liquid*	*Plastic, unsorted remolded, and close to Liquid Limit*	*CL, CH, and CM*	*Ip>0.05 and Il>0.5*
Silt, sand, gravel and boulders	*Dry*	*Non-plastic (or very low plasticity), granular, sorted. Silt particles cannot be seen by eye*	*ML*	*Ip<0.05*
	Saturated		*SW, SP, and SM*	
	Partly saturated		*GW, GP, and GM*	
Debris	*Dry*	*Low plasticity, unsorted and mixed*	*SW-GW*	*Ip<0.05*
	Saturated		*SM-GM*	
	Partly saturated		*CL, CH and CM*	
Peat		*Organic*		
Ice		*Glacier*		

Table 2.3.1 Landslide-forming material types

These types: “rock,” “clay,” “mud,” “silt,” “sand,” “gravel,” “boulders,” “debris,” “peat,” and “ice” replace the former threefold material classes used by Varnes (1978). Characteristics listed in the second column of the table can be used as supplementary terms. For example, “sensitive” clay will lose strength on remolding, while “partially saturated” silt may lose apparent cohesion on wetting.

Of course, many soils are transitional between textural classes. It is suggested that transitional terms be simplified to the component that is the most significant in terms of physical behavior. For example, a clayey silt should be called silt if it has very low plasticity, or clay if it is plastic.

Where the landslide source contains alternating zones of various materials (e.g., sand and clay), the material that plays the dominant role in the failure or propagation mechanisms should be used, even at the cost of a certain subjectivity. Where a dominant component cannot be identified, it is possible to use two terms, e.g., “rock and ice avalanche.”

The words “debris” and “mud” do not have clear equivalents in geotechnical terminology, but have acquired status in geology and landslide science and have therefore been retained (Bates & Jackson, 1984). These are materials that have been mixed from various components by geomorphic processes such as weathering (residual soil), mass wasting (colluvium), glacier transport (till or ice contact deposits), explosive volcanism (granular pyroclastic deposits), or human activity (e.g., fill or mine spoil).

Practically, debris is a mixture of sand, gravel, cobbles and boulders, often with varying proportions of silt and clay. Mud is a similar unsorted material, but with a sufficient silt and clay content to produce plasticity (cohesiveness) and with high moisture content. Both may contain a proportion of organic matter (Swanston, 1974) and may be gap-graded (“diamictons”).

An important aspect of debris or mud involved in landslides is that their water content may have been modified by mixing with surface water during motion and could thus be significantly different from the water content of the source material. It may also vary during motion. Spatial gradational sorting of such materials due to the development of inverse grading or coarse surge fronts is common and may have an important bearing on the flow behavior.

Hungr et al. (2001) proposed that the term “mud” should be used for remoulded mixed clayey soils whose matrix (sand and finer) is significantly plastic (Plasticity Index>5 %) and whose Liquidity Index during motion is greater than 0.5 (i.e., they are in or close to a liquid state). To convert insensitive stiff or dry cohesive soil at a landslide source into mud, rapid mixing with surface water and increase in porosity is required. Such a mechanism is not often available in nature and this limits the origins of mud to certain specific geological scenarios. For example, many of the mudflows described by Bull (1964) from the desert regions of southwestern USA, contain smectitic clays likely to exhibit dispersive behavior. The word “mud” should not be used to describe remoulded or liquefied clays or silts, which are well sorted and liquefy at their original water content, often without significant mixing with water or other materials.

The word “earth” does not have established status in either geological or geotechnical material description schemes and its use invites confusion with the conventional meaning of earth as construction material or agricultural soil (Bates & Jackson, 1984). However, it is required as part of the established term “earth flow.” In this context, it means a cohesive, plastic, clayey soil, often

mixed and remoulded, whose Liquidity Index is below 0.5. Many earthflows contain fragments of material in different stages of remolding and may carry granular clasts.

2.4 DEFINITIONS OF LANDSLIDE TYPES

Considering the publications by Varnes (1978), Hutchinson (1988), Hungr (2001) and other authors, a general classification of the landslide types can be explicated. First of all, some macro-families can be identified: we can recognize falls and topples of different types of material; slides in rock, with different evolutions; slides in soil; spreading of rock or sand/silt or clay; flow-like landslides, which can be dry or wet and include different kind of materials; slope deformation. According to this classification, Table 2.4.1 can be filled. The various types of landslide included in this list will be described above.

Type of movement	Rock	Soil
Fall	*1. Rock/ice fall*	*2. Boulder/debris/silt fall*
Topple	*3. Rock block topple*	*5. Gravel/sand/silt topple*
	4. Rock flexural topple	
Slide	*6. Rock rotational slide*	*11. Clay/sild rotational slide*
	7. Rock planar slide	*12. Clay/silt planar slide*
	8. Rock wedge slide	*13. Gravel/sand/debris slide*
	9. Rock compound slide	*14. Clay/silt compound slide*
	10. Rock irregular slide	
Spread	*15. Rock slope spread*	*16. Sand/silt liquefaction spread*
		17. Sensitive clay spread
Flow	*18. Rock/ice avalanche*	*19. Sand/silt/debris dry flow*
		20. Sand/silt/debris flow-slide
		21. Sensitive clay flow-slide
		22. Debris flow
		23. Mud flow
		24. Debris flood
		25. Debris avalanche
		26. Earthflow
		27. Peat flow
Slope deformation	*28. Mountain slope deformation*	*30. Soil slope deformation*
	29. Rock slope deformation	*31. Soil creep*
		32. Solifluction

Table 2.4.1 Summary of the proposed new version of the Varnes classification system

2.4.1 Falls and topples

Hungr et al. included in this group the *rock/ice fall* and they described this phenomenon as a detachment, fall, rolling and bouncing of rock or ice fragments. It can occur singly or in clusters, in any case the dynamic interaction between the most mobile moving fragments is still present. Even if fragments can break during impacts, it can be said that fragment deformation is unimportant. Normally, this kind of event includes limited quantity of volume.

They speak about *boulder/debris/silt fall* referring to detachment, fall, rolling and bouncing of soil fragments such as large clasts in soil deposits, or block of cohesive soil. Practically, the mechanism of collapse is similar to the previous case. The main difference consist in the fact that the impacts may be strongly reduced by the weakness of the moving particles.

A third family of landslides includes the forward rotation and overturning of rock columns or plates, separated by steeply dipping joints. In this kind of movement, called *rock block topple*, the rock is relatively massive and rotation occurs on well-defined basal discontinuities. The variation of velocities can be very high: the movement may begin slowly, but the last stage of failure can be extremely rapid.

The bending and forward rotation of a rock mass characterized by very closely spaced, steeply dipping joints of schistose partings, striking perpendicular to the fall line of the slope is identified as *rock flexural topple*. The rock is relatively weak and fissile. There are no well-defined basal joints, so that rotation of the strata must be facilitated by bending. The movement is generally slow and tends to self-stabilize. However, secondary rotational sliding may develop in the hinge zone of the topple. Occurs at large scale.

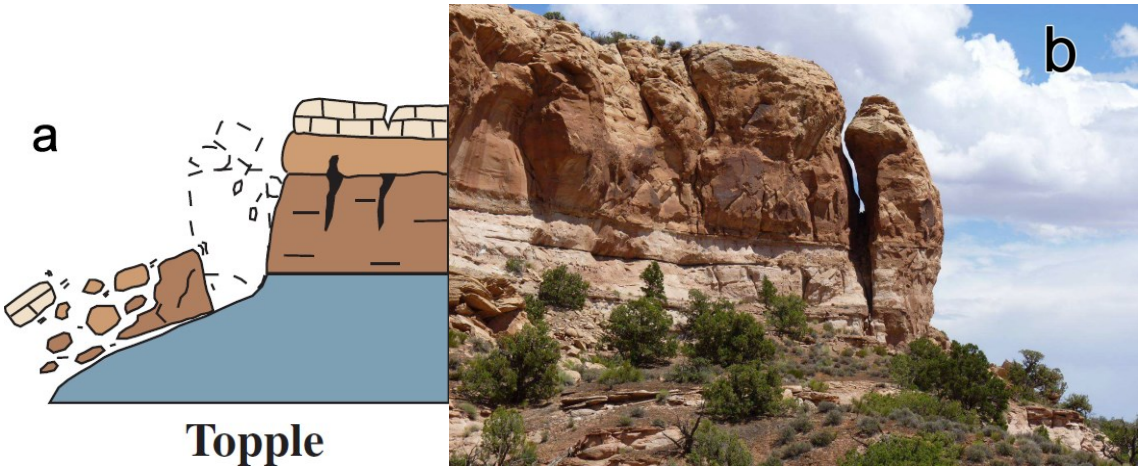

Figure 2.4.1 Scheme (a) and example (b) of a topple.

2.4.2 Slides in rock

This group obviously concerns mass of rock that moves according to different mechanism of collapse.

When a mass of weak rock on a cylindrical or other rotational rupture surface slides, we can speak about *rock rotational slide*. A prominent main scarp, a characteristic back-tilted bench at the head and limited internal deformation, characterizes the morphology.

Contrarily, when the movement happens on a planar rupture surface and includes a mass of rock, it is called *rock planar slide*. Commonly, the sliding causes little or no internal deformation. Usually, this kind of event is extremely rapid.

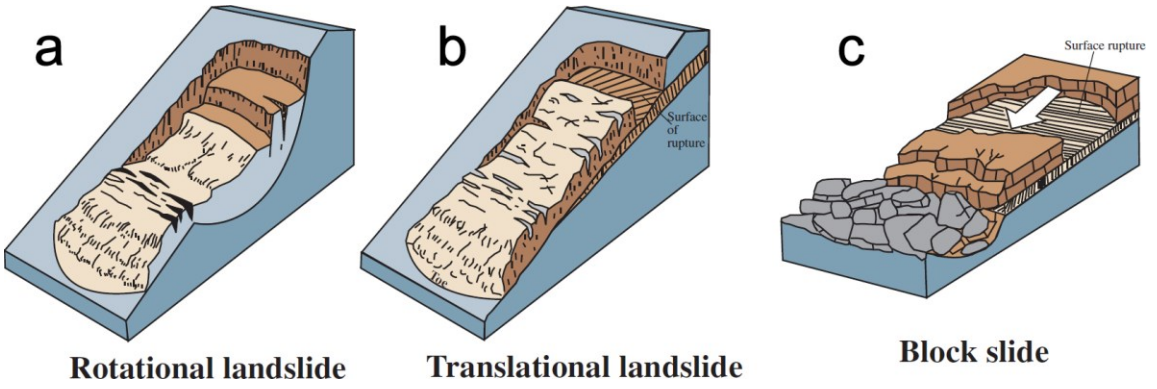

Figure 2.4.2 Schemes of slides.

The *rock wedge slide* is the sliding of a mass of rock on a rupture surface formed of two planes with a downslope-oriented intersection. The phenomenon is extremely rapid and there is not any internal deformation.

The sliding of a mass of rock on a rupture surface consisting of several planes, or a surface of uneven curvature, so that motion is kinematically possible only if accompanied by significant internal distortion of the moving mass is defined as *rock compound slide*. It can be slow or rapid.

Finally, when the rock collapse happen on an irregular rupture surface we can speak about *rock irregular slide*. Occurs commonly in strong rocks with non-systematic structure, so the rupture is casual. For this reason, the failure mechanism is complex and often difficult to describe. Often it is very sudden and extremely rapid.

2.4.3 Slides in soil

A classification similar to the one made for rock-slides, can be repeated with soil. We can distinguish a *clay silt rotational slide* from a *clay/silt planar slide* depending on the type of rupture surface. The first normally pass from slow to rapid, while the second may be slow or rapid.

When gravel, sand or debris compose the soil, the landslide becomes a *gravel/sand/debris slide*. The granular material slides on a shallow, planar surface parallel with the ground. Many debris slides become flow-like after moving a short distance and transform into extremely rapid debris avalanches.

The *clay/silt compound slide* consists in the sliding of a mass of soil on a rupture surface consisting of several planes, or a surface of uneven curvature, so that motion is kinematically possible only if accompanied by significant internal distortion of the moving mass. The basal segment of the rupture surface often follows a weak horizon in the soil stratigraphy.

2.4.4 Spreading

The near-horizontal stretching of a mass of coherent blocks of rock resulting of intensive deformation of an underlying weak material is defined as *rock slope spread*. Usually, this event causes limited and slow total displacement.

When the lateral spreading of a series of soil blocks floating on a layer of saturated (loose) granular soil, liquefied by earthquake shaking or spontaneous liquefaction happens in an extremely rapid way, the *sand/silt liquefaction spread* takes place.

If the rapid lateral spreading is caused by the floating of a series of coherent clay blocks on a layer of remoulded sensitive clay, we can speak about *sensitive clay spread*.

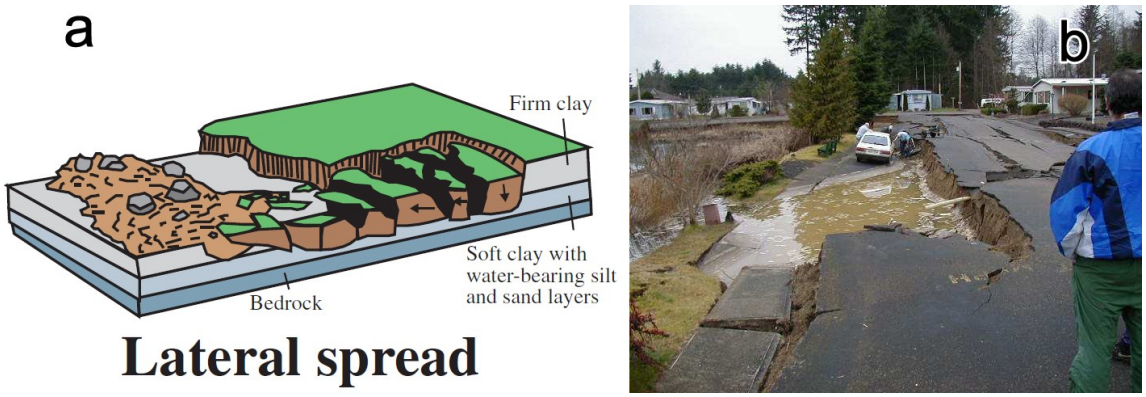

Figure 2.4.3 Scheme (a) and example (b) of a lateral spread.

2.4.5 Flow-like landslides

The flow-like landslides can be subdivided in various groups, depending on the moved material, on the velocity of the flow and on the saturation of the soil. The material is commonly inconsistent and the flow evolves depending on the basal topography of the site.

The *rock/ice avalanches* are extremely rapid, massive flow-like motion of fragment rock, starting from a rock fall or a large rockslide (Figure 2.4.4b).

When the debris are dry or at least not liquefied, we can identify a *dry sand/silt/gravel/debris flow*. Practically, the flow can be rapid or slow, and there is not excess pore-pressure (Figure 2.4.4a).

The *sand/silt/debris flow-slides* are very or extremely rapid flow of sorted or unsorted saturated granular material on moderate slopes, involving excess pore-pressure or liquefaction of material originating from the landslide source. The material may range from loose sand to loose debris (fill or mine waste), loess and silt. Usually originates as a multiple retrogressive failure. May occur sub-aerially, or under water.

If the material involved in an extremely rapid flow is mainly composed by liquefied sensitive clay, *the sensitive clay flow-slides* take place.

Generally, a *debris flow* is a very or extremely rapid surging flow of saturated debris in a steep channel. Commonly, it is characterized by a strong entrainment of material and water from the flow path.

The classification continues identifying the *mudflow* as very or extremely rapid surging of flow of saturated plastic soil in a steep channel. Even in this case, the entrainment of material and water from the flow path is still common.

Figure 2.4.4 a) Dry sand flow on the lee slope of a sand dune, Namib Desert (Hungr et al., 2014)
b) The 1999 rock avalanche deposited on a glacier surface, Mt. Munday, British Columbia, Canada (Hungr et al., 2014).

When there a rapid flow of water, heavily charged with debris takes place, we can identify a *debris flood*. The event is strongly dominated by the liquid matrix.

Continuing speaking about debris, the *debris avalanche* is a very or extremely rapid shallow flow of partially or fully saturated debris on a steep slope. The main difference compared to the debris flow is the fact that it takes place without confinement in an established channel.

The *earthflow* is rapid or slower, intermittent flow-like movement of plastic, clayey soil, facilitated by a combination of sliding along multiple discrete shear surfaces, and internal shear strains.

Finally, the *peat flows* are rapid flows of liquefied peat, caused by an undrained failure.

2.4.6 Slope deformation

Slow velocities of deformation characterize the last group of landslides. Five types of landslide are included in this last family.

We can identify the *mountain slope deformation* as large-scale gravitational deformation of steep, high mountain slopes, manifested by scarps, benches, cracks, trenches and bulges, but lacking a fully defined rupture surface. Extremely slow or unmeasurable movement rates.

Deep-seated slow to extremely slow deformation of valley or hill slopes are called *rock slope deformation*. The movement is very slow. If the event includes cohesive soil, instead of rock, we can speak of *soil slope deformation*.

The *soil creep* is an extremely slow movement of surficial soil layers on a slope, typically less than 1 m deep, because of climate-driven cyclical volume changes (wetting and drying, frost heave).

We can conclude the classification description proposed by Hungr et al. (2014) defining the *solifluction* as a very slow but intensive shallow soil creep involving the active layer in Alpine or polar permafrost.

3 RHEOLOGY OF THE DEBRIS FLOWS

3.1 INTRODUCTION

Rheology is an interdisciplinary science that involves different fields, including engineering, computer science, thermodynamics, advanced materials design, physics, chemistry, biology and health sciences, among others. Consequently, at present it is the result of several and important researchers' efforts and contributions belonging to various branches of knowledge.

The debris flows represent one of the manifold problems of this discipline because of its analysis. The Bingham, Herschel and Bulkley, Bagnold are some examples of models used to describe their behaviors. In the last five decades, they have made significant strides in the drafting of a due theoretical framework of the phenomenon, in which the rheological laws and parameters constitute a fundamental part. In this regard, the choice of this law and the determination of the material properties are essential for the analysis or prediction of the movement in the debris flows, since the results of the mathematical models largely depend on the rheological model employed to estimate the shear stress in the bottom and the integrated stresses in depth.

As described in the previous paragraph, water, clay, silt, sand, gravel, pebbles and boulders in general, commonly compose the materials that flow down during landslides and earth-flows. A first approximation can subdivide the solid particles into two main groups, based on the interaction that they have with water. It is possible to define the fine particles (<40μm), that give rise to colloidal interactions and can be subject to Brownian motions. On the other hand, the granular particles that are characterized principally by frictional and collisional interactions. The first group describes mudflows and, in general, any movement of a cohesive material. The second group conversely contains fluxes of granular material like the debris flows.

3.2 RHEOLOGICAL MODELS AS PART OF THE RAPID LANDSLIDES ANALYSIS

The debris flows are a mixture of water and air with sediments in high concentration - rocks, gravel, clay and organic materials that quickly move under their own weight in the canyons in high mountain areas.

These phenomena often start with a slope landslide, induced by different causes including heavy rains, growth of the interstitial pressures, seismic movements, volcano eruptions etc. Until this moment, the solid mass of soil undergoes changes in its state and starts turning into a liquid state, whose volume and mobility are increased by two factors: the incorporation of water from rain and runoff and the dragging of other materials found on the way.

Considering the characteristics described in the previous paragraph, at first they attempted studying these phenomena by the mechanics of the traditional fluids, but these flows with high concentrations of solid matter, because of its non-Newtonian behavior, are not well represented by the methods that are generally employed in liquids such as water.

In this regard, they have been several proposals to address its analysis, but all postulate a unique rheological relationship between the shear stress and the strain rate (Iverson, 1997).

Johnson (1965), Yano and Daido (1965) are the first, though independently, to consider the debris flows as a continuum with intrinsic shear stress and viscosity and to employ the Bingham viscoplastic model (Bingham & Green, 1919). Since then, this model has been one of the most used in the evaluation of the natural rapid landslides with fine particle-size, such as mudflows. It considers low strain rates, and, in that sense, its representation has a reasonable degree of approximation (Major & Pierson, 1992; Huang & Garcia, 1998; Chen & Lee, 2002).

Dzui and Boger (1983), Coussot and Piau (1994) suggested to employ a more complex and comprehensive model as the Bulkley one, considering that suitably reproduce the behavior of fine granular material mixtures, in a broader level both of particle-size and strain rates. Afterwards, this model has been used by Coussot and Piau (1995), Coussot et al. (1998), Huang and García (1998), Parson et al. (2001), Imran et al. (2001), Schatzmann et al. (2003; 2009), Coussot et al. (2003), Ancey (2007), among many others.

Based on field observations and experimentation with materials resulting from real debris flows, Johnson (1970) suggested the Coulomb-viscous model consisting of a modification of the Bingham, in which the term “shear stress” is developed as the sum of Coulomb cohesion and friction components.

On the other hand, Bagnold (1954) was the first to evaluate the effects of the interaction between particles, in the analysis of the debris flows behavior. Assuming the hypothesis of the dilatant fluid of the Bagnold experimental work, Takahashi (1978) elaborated his own constitutive equation that considers the dispersive stress induced by the collision between particles. In later works, Takahashi have made changes to improve the quality of prediction. This model is the most popular in Japan.

The model of the frictional fluid is one of the most simple and effective, especially when you are working with the structure of the combined solid-fluid behavior. Voellmy (1955) developed his model for the snow avalanches. Just some years later Körner used this model for rock avalanches (1976).

The models of O’Brien and Julien (1985) and Chen (Chen, 1988) are more complex and seek the generalization of their use in any case.

All these models consider the mass as a continuum that, when it moves, depletes energy and each of them has its own application limitations, depending on which the following mechanisms are taken into consideration: viscosity, turbulence, friction for contact and collision between particles. In this regard, the qualitative classification of Jen and Shen (1997) is useful for flow regimens that may arise in the debris flows.

Rheology leads to find out the better way to describe the behavior of a flow. It connects the material properties to its microstructure, to its liquid and solid phases and finally to its physical parameters.

During the propagation phase, the earth-flows are continuously deforming. Consequently, it is necessary to use the fluids mechanics to study such as these phenomena. The behavior of the material displays, however, a viscosity that is greater than the water resistance. It has to be taken into account all the properties of the mass that is moving during these circumstances.

The configuration of a fluid changes when some deformations occur. The elements that compose this fluid change their position, exchanging momentum. To make that these movements take place at a microscopic scale, it is necessary that an external force deforms the fluid at a macroscopic one. The resistance that the material opposes to the motion is known as viscosity. Practically, when an external stress tries to rapidly deform a fluid, the internal frictional forces delay the distortion, causing in that way a steady state in which a constant external stress involves a constant strain rate. The ratio between stress and strain rate is called viscosity.

Therefore, if you have a good knowledge of the microstructural interactions within a given material, it is reasonable to identify a link between the physical properties of the material and its mechanical behavior. That is why it is important to know if the particles included in the material are fine or granular. Accordingly, it is possible to assess the type of interactions that are established between the various grains (collisions, Van der Waals attractions, hydrodynamic interactions, etc.) and consequently to study how the distribution and the change of these bonds affect the resistance of the fluid.

It is therefore quite clear how the viscosity changes from one fluid to another: the microstructure and consequently the inter-particle interactions change from material to material. Additionally, the resistance to motion in a fluid is not always characterized by a single parameter, and it can be represented not only by the viscosity, but also by a critical stress (yield stress): the fluid remains at rest below a critical stress, after which it moves. Thus, overall, the resistance of a material depends both on the viscosity, both on the intensity of the shear stress to which it is subjected.

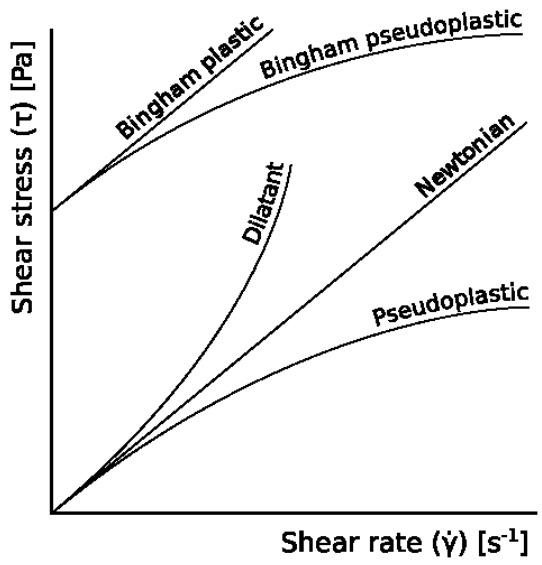

Figure 3.2.1 Behavior of different fluids in a $\dot{\gamma} - \tau$ reference system.

Figure 3.2.1 provides a representation of some typical behaviors of fluids, in the form of t-$\dot{\gamma}$ graphic. The viscosity is given by the slope of these curves ($m = d\tau/d\dot{\gamma}$). A straight line passing through the origin represents a Newtonian fluid. In fact, to a null stress corresponds a zero speed value. A second type of fluids has a constant viscosity, but they needs a minimum stress to start to scroll. These are the so-called Bingham fluid, represented in Figure 3.2.1 by a straight line which intercepts the y-axis at the value τ_c, said sliding threshold. Figure 3.2.1 also shows typical curves of pseudo-plastic fluids, the viscosity of which decreases with the increase of the intensity of the effort, and those dilatant, whose viscosity increases conversely. A final class of behavior shown is that of pseudo-plastic fluids with a threshold slider which are represented by a slope descending curve which intercepts the y-axis in correspondence of a value τ_c.

The concept of non-Newtonian fluid introduces some ambiguity with respect to the most basic classifications used to define the state of the bodies. The distinction between solid and liquid is no longer so clear if it is true that the same body can manifest predominantly solid or liquid depending on the state of stress to which it is subjected. The question can be considered from another point of view. Reiner introduced in 1964 a dimensionless quantity called Deborah number:

$$De = \frac{\tau}{T} \qquad \textit{Equation 3-1}$$

defined as the ratio between a characteristic time τ of the material and a characteristic observation time *T*, stating that with high Deborah numbers you have a solid-like behavior, while with low Deborah ones you can observe a liquid type. Therefore, a material can performance as a solid because it has a very high characteristic time, or because the process used to investigate the properties is very quick. Conversely, a material manifests ability to flow if its characteristic time is low, or if the observation time is quite high. The molten polymer, for example, have stretching times rather long, in the order of 1-100 s, and very often, problems of practical interest, can be studied as elastic bodies. Many materials have characteristic times in the order of 1s and then appear, in our common experience, as viscoelastic.

Below, these flow regimens and the main rheological models used in each of them to describe, with different degrees of approximation, the fluidized soils are classified and explained.

3.2.1 The frictional regime

In these flows, the mass movement aims to be rather slow in order that the particles are kept in almost permanent contact and the moment exchange is mainly due to the friction mechanism. The flows in this regimen have properties of a plastic material; there is not correspondence between the stresses and the strain rate employed, but the relationship between normal and shear stresses can be considered a constant. It is also called friction regimen, plastic regimen or quasi-static regimen.

The analysis considers that the starting-point of the plastic flows of the granular solids is the balance limit condition in the Coulomb law (shear condition largely depends on the pressure), even though it does not suit any information about kinematics of the material movement.

In this regime, the most common models are the pure frictional and the Voellmy.

3.2.1.1 Pure frictional model

It is one of the simplest models. It is based on the mechanical fluidization of the material can be explained by the premise that to elevated strain rates the Coulomb friction law is simplified due to the change in the type of contact between particles and the cohesion doesn't intervene.

The expression is the famous Coulomb law, dismissing the cohesion term:

$$\tau = \sigma_n \tan\phi \qquad \textit{Equation 3-2}$$

Pore strains are taken into account replacing the total normal stress with the effective one.

$$\tau = \sigma_n' \tan\phi = (\rho - \rho_w) g h \cos\theta \tan\phi \qquad \textit{Equation 3-3}$$

where σ_n is the normal stress, θ is the inclination of the ground, ϕ is the angle of the interior friction, and ρ e ρ_w are of the mixture and the water densities respectively.

Hungr and Morgenstern (1984) realized a series of tests in laboratory, which proved that the internal friction angle of the granular materials is independent of the strain rate and the normal stresses.

In this model, the shear stress in the fluid bottom is independent of the velocity - it only depends on the effective normal stress. Generally, it is expected that the shear stresses are concentrated in a tight zone at the basis of the flow, where the material is finer, it may be saturated and with low pore pressures.

3.2.1.2 Voellmy model

Voellmy (1955) developed it to model snow avalanches and its use in rock avalanches was introduced by Körner (1976). It consists of two parameters: the coefficient of friction and a term of turbulence that depends on the square of the rate and the density of the debris flow. Voellmy included this second term to take into consideration all flow resistance factors that depend on the rate. In the rock avalanches, these may derive from changes in the undrained pore pressures, due to the dilatancy in a thin layer at the basis of the flow.

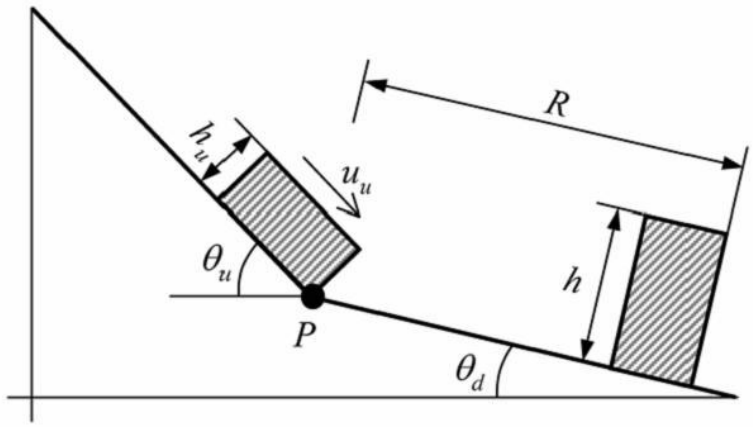

Figure 3.2.2 Simplified scheme of Voellmy rheological model.

The hypothesis of Voellmy model is to assume that the motion of an avalanche in the sliding area has characteristics similar to those of the free surface stationary hydraulic currents. The avalanche is therefore assimilated, limited to the sliding region, to an incompressible fluid in steady flow conditions. In this model, the actual geometry of the slope is greatly simplified, through two sections having a constant slope, which is representative of the scroll area, respectively, and the stop zone (Figure 3.2.2).

In the sliding zone, the model assumes that the avalanche, after a short "transitional" initial accelerative, reaches a steady-state motion condition characterized by a limit speed. It should be noted that among the various assumptions of the model, it is also to consider the short transients and thus to admit that the avalanche is able to reach a steady-state conditions of motion after traveling short distances. In these particular conditions, the balance of momentum results in a condition of equilibrium between the acting forces and, with reference to a column of unit area of fluid, can be written as:

$$F_S = \rho g h_u \ sin\,\theta = F_R \qquad \text{Equation 3-4}$$

where F_S is the component of the weight of the column in a direction parallel to the slope, h_u is the sliding height of the avalanche, ρ is the density of the avalanche, θ is the average slope of the scroll area and F_R represents all the resisting basal forces.

To describe F_R, Voellmy adopted the correct Chezy formula with the addition of a resistive component of Coulomb type, which is independent from the velocity, but then linked only to the normal component to the external load. The overall strength per unit area at the bottom is therefore expressed by the following relationship:

$$F_R = \frac{\rho g}{\xi} v_u^2 + \mu \rho g h_u \ cos\,\theta \qquad \text{Equation 3-5}$$

This is valid for slope flows, replacing the coefficient of Chezy with the turbulent coefficient ξ and indicating with μ the Coulomb friction coefficient, equal to $\tan\phi'$. The two parameters are dependent on the properties of the snow, on the roughness of the track and finally on the starting volume. According to the Equation 3-5, the friction slope is given by:

$$\tau = \mu\, cos\,\theta + \frac{v_u^2}{\xi\ h_u} \qquad \text{Equation 3-6}$$

In Voellmy model, described in the Equation 3-6, the coefficient of kinematic friction μ and that of turbulent coefficient ξ are the parameters to be defined.

A critical point of the calibration procedure is the definition of a range for these two parameters, according to the type of flow you want to reproduce. Sosio et al. (2008) summarizes the results obtained by many authors (Ayotte & Hungr, 2000; Chen & Lee, 2003; Crosta et al., 2006) and consequently Table 3.2.1 can be filled.

	Voellmy rheology	
	Frictional coefficient angle μ	*Turbulent coefficient ξ*
	[-]	*[ms^{-2}]*
Rock avalanches	*0.10-0.25*	*450-1000*
Debris avalanches	*0.07-0.10*	*200-250*
Rockslide-debris avalanches	*0.05-0.20*	*200-400*
Ice-rock avalanches	*0.03-0.10*	*1000*
Debris flows	*0.05-0.20*	*200-500*
Volcanic-rock avalanches	*0.05-0.10*	*100-140*

Table 3.2.1 Typical ranges of values for the rheological parameters adopted in the literature for Voellmy rheology.

From the analysis of this table, it is visible that passing from a rock avalanches to a viscous mudflows muddy viscose, the minimum value of the kinetic coefficient of friction is increased

according to an exponential or parabolic function, while the maximum value of the turbulent friction coefficient decreases almost linearly. This trend is in accordance with the physical phenomena that characterize the types of flow.

Ayotte and Hungr (2000) proposed an empirical criterion to determine the value of the turbulence coefficient:

- With real phenomena of debris flow, confined, highly saturated and with very high slopes, the turbulence coefficient is generally very low, i.e. less than $400\ m/s^2$. This is because the turbulence coefficient is an inverse parameter: an increase of its value results in a decrease of the turbulent effects and in an increase of the sliding speed, determine greater mobility storage.
- On the contrary, an unstable flow, with lower saturation and confinement, will have a very high turbulence coefficient, indicatively greater than $700 - 800\ m/s^2$.
- A mixture with intermediate saturation requires the use of intermediate values of the turbulence coefficient, indicatively between 400 and $700\ m/s^2$.

In some cases modeled (Ayotte & Hungr, 2000), working with natural debris flows at small-medium scale, it has been noted how, with increasing mobilized volumes, the turbulence coefficient remains constant while the friction angle decreases. Such "anomalous" behavior is due, primarily, to the type of material.

3.2.2 The collisional regime

In this regime, there is a wide separation between solid particles, the strain is quick, the duration of the contacts is short and the momentum is mainly transferred by collisions. It is also called dynamic regimen or granular-inertial regimen.

Dilatant fluid models like Takahashi and Bagnold analyse this regimen.

3.2.2.1 Dilatant fluid model

In a dilatant fluid, the viscosity raises in accordance with the increment of strain rate, therefore the mobility decreases since the shear stresses overcome the flow resistance. Dilatancy can be explained by understanding that at low strain rates, the solid particles of various shapes and sizes can keep an arrangement, having contact with each other; the liquid fraction occupies the interstitial spaces and lubricates the movement between them and this makes the viscosity is low. By increasing of strain rates, the structure changes, the separation of the particles get bigger and there is not enough liquid to lubricate the friction against each other, so that the viscosity increases. The high strain rates cause frequent collisions between particles. These clashes produce dispersive pressures and stresses favouring in the material a certain tendency to expansion, therefore granular masses subjected to shear stresses are classified dilatant. This dispersion mechanism further provides an additional suspension source to the particles.

Bagnold and Takahashi models fall under the models based on the conceptualization of the dilatant fluid.

3.2.2.1.1 Bagnold model

Bagnold tested several granular dispersions in the rheometer built by him-self. Since the behavior observed in his experiments, he proposes a theoretical model that to have the merit of being the first to clearly explain the physics of the phenomenon. The theory starts by saying that the clash between particles generates an increase in the liquid pressures in radial direction, which he named "dispersive stresses or pressures" and that are proportional to the shear stresses. He equates three regimens: macro-viscous, transitional and granular-inertial, whose limit is made by a non-dimensional parameter, known nowadays as Bagnold number, B_a, in which inertial and viscous stresses are related.

- Macro-viscous regime: $B_a < 40$
- Transitional regime: $40 \leq B_a \leq 450$
- Granular-inertial regime: $B_a > 450$

This parameter is calculated by the equation presented below:

$$B_a = \frac{\lambda^{1/2} \rho c^2 (dv/dz)}{\mu} \qquad \textit{Equation 3-7}$$

where

$$\lambda = \frac{1}{(C_0/C)^{1/3} - 1} \qquad \textit{Equation 3-8}$$

and c particles diameter, λ linear concentration of Bagnold, C volume concentration of the solid fraction (always less than $0.9C_0$), C_0 maximum possible concentration (in spherical particles and in granular materials), dv/dz the strain rate, μ the interstitial fluid viscosity and ρ the soil particles density.

Bagnold developed expressions to estimate the stresses in the extreme regimes.

In the macro-viscous regime, the strain rates are small and viscous effects dominate the behavior. Normal and shear stresses are linear functions of the strain rate:

$$\tau = a_v \lambda^{3/2} \mu \frac{dv}{dz} sin\, \alpha_i \qquad \sigma_n = \frac{\tau}{tan\, \alpha_i} = a_v \lambda^{3/2} \mu \frac{dv}{dz} cos\, \alpha_i \qquad \textit{Equation 3-9}$$

In the granular-inertial regime, the strain rate is large and the collisions between particles are the determining factors. Normal and shear stresses are proportional to the square of the strain rate:

$$\tau = a_i \rho \lambda^2 c^2 \left(\frac{dv}{dz}\right)^2 sin\, \alpha_i \qquad \sigma_{nd} = \frac{\tau}{tan\, \alpha_i} = a_i \rho \lambda^2 c^2 \left(\frac{dv}{dz}\right)^2 cos\, \alpha_i \qquad \textit{Equation 3-10}$$

In the above expressions, τ represent the shear stresses, σ_{nd} the dispersive stresses, a_i is an experimental constant and α_i is the dynamic friction angle that depends on the collision conditions.

Bagnold suggested the following values experimentally determined:

- Macro-viscous regime $a_v = 3.75$, $\tan \alpha_i = 0.75$ and $\alpha_i \cong 37°$

- Granular-inertial regime $a_i = 0.042$, $\tan \alpha_i = 0.32$ and $\alpha_i \cong 17°$ when $\lambda < 14$. However, a_i quickly increases from this value to 0.24 when λ goes from 14 to 17.

3.2.2.1.2 Takahashi model

It is based on the concept of dispersive stresses developed by Bagnold, described in the previous paragraph, in whose formulation he changed the parameter a_i. This model was proposed by Takahashi (1978) and is the model most used in Japan to represent debris flows of coarse granular material. He realizes several experiments with natural materials in a variable pitch channel and from the results obtained, he proposes to take values between 0.35 and 0.50, instead of 0.42 given by Bagnold, for granular-inertial regime.

$$\tau = a_i \rho \lambda^2 c^2 \left(\frac{dv}{dz}\right)^2 sin\, \alpha_i \qquad \sigma_{nd} = \frac{\tau}{tan\, \alpha_i} = a_i \rho \lambda^2 c^2 \left(\frac{dv}{dz}\right)^2 cos\, \alpha_i \qquad \text{Equation 3-11}$$

$$0.35 \leq a_i \leq 0.50$$

Takahashi (1991) suggests incorporating a new equation to the model to estimate $\tan \alpha_i$, in order to overcome the above simplification considering a uniform particles distribution with depth. The new expression is now function of the concentration and is acceptable for concentrations above 30% ($C > 0.3$):

$$tan\, \alpha_i = \left(\frac{C_0}{C}\right)^{1/3} tan\, \phi \qquad \text{Equation 3-12}$$

with ϕ internal friction angle of the granular material.

3.2.3 The collisional-frictional regime

It is an intermediate regime between the collisional and the frictional, where both effects affect mixture behavior. McTigue's (1982) constitutive relation falls in those for such granular materials flows.

3.2.3.1 McTigue model

The equation proposed by McTigue consists of two parts: one frictional and one collisional. Considering the motion of granular materials flowing down an inclined plane, the model can expressed as:

$$\tau = c_c\, cos\, \phi + \eta_1 (C^2 - C_0^2)\, sin\, \phi + \eta_2 (C_{max}^2 - C^2) \left(\frac{dv}{dt}\right)^2 \qquad \text{Equation 3-13}$$

where c_c is the cohesion, ϕ is the angle of friction, η_1 and η_2 are empirical coefficients, C_0 and C_{max} are the minimum and maximum concentrations in volume respectively.

The sum of the first two terms on the right side of the Equation 3-13 represents the shear stress τ_y, which must be reached to make the flow starts. A more general expression for this regimen is:

$$\tau = \tau_y + \alpha \left(\frac{dv}{dt}\right)^2 \qquad \text{Equation 3-14}$$

3.2.4 Macro-viscous regime

It's a very dilute mixture of particles suspended in a Newtonian fluid. The concentration of solid particles is usually less than 9% but it is sufficient to increase the viscous dissipation. However, the relationship of stresses and strains still maintain similarity with Newtonian fluids.

3.2.4.1 Newtonian fluid model

Mixtures of fluid and sediment can be treated as a Newtonian fluid by the following expression:

$$\tau = \mu_m \frac{dv}{dz} \qquad \textit{Equation 3-15}$$

Where μ_m is the effective viscosity depending not only on the properties of the fluid and temperature, but also on the sediments concentration.

Several authors have suggested expressions to determine the effective viscosity. Einstein (1956) evaluated theoretically viscous dissipation increase produced by spheres suspended in a Newtonian fluid as:

$$\mu_m = \mu_f(1 + 2.5C) \qquad \textit{Equation 3-16}$$

where μ_f is the fluid viscosity and C is the suspension concentration.

Einstein's equation and its extensions have been supported only in very dilute suspensions of spherical particles, which does not affect the interaction between them. Therefore, its application to debris flows is very uncertain, and in these cases, sediment concentrations are important and the effect of these interactions is significant.

Assuming that Einstein's equation is valid for an infinitesimal increase in the concentration of particles, Krone (1986) reached:

$$\mu_m = \mu_f \, exp(2.5C) \qquad \textit{Equation 3-17}$$

Bagnold (1954), basing on his experiments at low spheres concentration in neutral lift, proposed the following expression for macro-viscous flow regime:

$$\mu_m = 2.25\lambda^{3/2}\mu_f \qquad \textit{Equation 3-18}$$

3.2.5 Viscoplastic regime

Viscoplastic conceptualization is based on the fact that sediment concentration increases the viscosity and contributes to the shear strength of the flow. In debris flows, this property is provided by fine-grained matrix that favours cohesion and coarse particles, which derive from internal friction.

3.2.5.1 Viscoplastic fluid models

The mixture is considered as a continuum in which the interaction between the fluid and the particles is not analysed. The movement begins when a stress, that exceeds the shear stress, is applied and viscous effects dominate its behavior. Practically, the viscosity reduces the ability of suspended particles to settle, allows limiting the shear deformations and controls the strain rate of the flow.

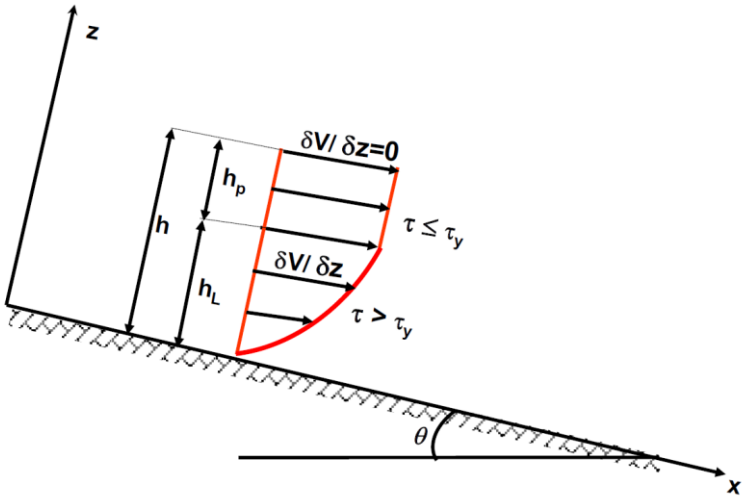

Figure 3.2.3 Schematization of rates profile in a viscoplastic model.

The Figure 3.2.3 shows the typical distribution of strain rates for viscoplastic models in a simple shear flow. Two distinct layers can be distinguished: the viscous, where the deformation take place with contact with the ground, where $\tau > \tau_y$ and the rates profile is parabolic; and the upper layer that changes into a constant flow when $\tau \leq \tau_y$, since rate gradient is null.

Bingham, Herschel and Bulkley and Coulomb-viscous are viscoplastic models.

3.2.5.1.1 Bingham model

It was introduced by Bingham and Green in 1919. The flow starts once the shear stresses exceed the threshold represented by the shear stress, then the movement is governed by a linear relationship between shear stresses and strain rates, whose constant of proportionality is Bingham viscoplastic parameter. The rheological law is as follows:

$$\tau = \tau_y + \mu \frac{\partial v}{\partial z} \qquad \textit{Equation 3-19}$$

where τ and τ_y are the shear stress and the shear yield stress respectively, $\partial v/\partial z$ is the velocity gradient and μ is the Bingham's viscosity.

According to experimental data, parameters τ_y and μ are linked with the sediments concentration and granulometric distribution.

3.2.5.1.2 Herschel and Bulkley model

It was suggested by Herschel and Bulkley (1926) and establishes that non-Newtonian fluids, after exceeding the shear stress, the stress-strain relationship is non linear and is governed by the following expression:

$$\tau = \tau_y + \kappa \frac{\partial v^n}{\partial z} \qquad \textit{Equation 3-20}$$

with κ consistency coefficient and n index connected with the flow behavior, normally lower than 1.

κ and n are empirical parameters. For natural mud suspensions n is approximates equal to $1/3$ (Chen & Lee, 2002). It is defined as a general law, since other models are obtained as special cases

employing its formulation: when $n = 1$, it is Bingham model; if $\tau_y = 0$ and $n > 1$, it is the dilatant model and if $\tau_y = 0$ and $0 < n < 1$, it is the pseudo-plastic model.

Coussot and Piau (1994) consider that the application of this rheological law is advantageous because it suitably allows represent mudflows under a wide range of particle-sizes and strain rates.

3.2.5.1.3 Coulomb-viscous model

Basing on field observations and experimental data of real debris flows, Johnson (1970) suggests a model known as Coulomb-viscous, in which the total dynamic resistance is a combination of shear resistance, frictional resistance and viscous resistance. Therefore, he modified the Bingham model and discerned the resistance to shear into two components, one of friction and another cohesive.

$$\tau = \left(\tau_{xy} + \sigma_{ny}\, tan\, \phi\right) + \eta \frac{\partial v}{\partial z} \qquad \textit{Equation 3-21}$$

where τ_{xy} is the cohesive component of shear stress, σ_{ny} is the normal shear stress and ϕ is the internal friction angle.

Although the constitutive equation of Mohr-Coulomb limit state represents a condition of structural failure, applicable to solid bodies such as soil and rock, Johnson interpreted this criterion of resistance as the beginning of a plastic flow. He therefore associated these important unalterable deformations to state change of the material, which goes from solid to liquid.

In general, the values of the rheological parameters - cohesive shear stress τ_{xy}, normal stresses σ_{ny}, internal friction angle ϕ and apparent dynamic viscosity η - changes with properties of the mixture, as solids concentration, amount and type of clay, particles shape and granulometric distribution (Chen & Lee, 2002).

3.2.6 Viscoplastic-collisional regime

Coarse debris flows are a fluid mixture with sediments, having a wide particle-size with a substantial amount of coarse particles, but also including intermediate and fine sizes. The momentum exchange is affected both by the interaction between particles and fluid viscosity. O'Brien and Julien' (1985) quadratic models and generalized viscoplastic models (Chen, 1988; Chen & Ling, 1996) analyse this behavior in debris flows.

3.2.6.1 Quadratic model

O'Brien and Julien (1985) investigated the motion nature in flows with large sediments content, called hyper-concentrated, including mudflows and debris flows. Basing on the principles of fluid mechanics and considering the mixture as a continuum, to contain the wide range of concentrations O'Brien and Julien postulate a general model in which each term represents a well-defined physical property. The mathematical expression is:

$$\tau = \tau_y + \mu\left(\frac{dv}{dz}\right) + \zeta\left(\frac{dv}{dz}\right)^2 \qquad \textit{Equation 3-22}$$

with τ_y shear stress, which does not depends on the strain rate, $\mu\left(\frac{dv}{dz}\right)$ viscous stress of the fluid, interacting with solid particles and exterior elements, $\zeta\left(\frac{dv}{dz}\right)^2$ expresses turbulence effects, caused

by fluid interaction with particles and exterior elements, just like dispersive effects due to interaction between particles, such as collisions, friction, and dispersive stresses. The inertial stress coefficient ζ overlaps the turbulent and dispersive stresses, as both are proportional to the square of the shear rate.

The expression for its calculation is presented below:

$$\zeta = \rho_m l_m^2 + a_1 \rho \lambda^2 c^2 \qquad \textit{Equation 3-23}$$

where ρ_m and l_m are the density and the length of the mixture respectively; a_1 is an empirical constant that relates to Bagnold-defined one in inertial regime, $a_1 = a_i \sin \alpha_i \cong 0.01$; ρ, λ and c are the solid density, linear concentration and particles diameter, already defined in Bagnold model.

The length mixture l_m is a function of the distance until the boundary and the Von Karman constant, κ. In integrated flows in depth, it can be $\kappa = 0.4$ and the distance to the boundary as the flow depth, whereby

$$l_m = \kappa h = 0.4h \qquad \textit{Equation 3-24}$$

The quadratic model considers the main processes of energy dissipation during movement, which are a function of the shear stress - first term -, viscous stresses - second term -, and of the turbulent and dispersive stresses - third term.

All of these processes largely depend on the concentration and quantity of soil and on the type of fines present in the mixture. In this regard, it is important to point out O'Brien and Julian (1988) experimental work, where they connect expressions relating the viscosity and shear stress with the sediments volume concentration and the proportion of cohesive fines. Julien and Lan (1991) modify the Equation 3-22 to present it in non-dimensional form and define the conditions of applicability of the model. The non-dimensional quadratic law is as follows:

$$\tau^* = 1 + (1 + T_D^*) a_1 D_v^* \qquad \textit{Equation 3-25}$$

in which τ^* is the non-dimensional parameter for the mobilized shear stresses, T_D^* relates turbulent and dispersive stresses; D_v^* relates dispersive and viscous stresses and a_1 is the empirical constant proposed by Bagnold. The equations for these non-dimensional parameters are given below.

The non-dimensional relation for the mobilized shear stress is:

$$\tau^* = \frac{\tau - \tau_y}{\mu \dfrac{dv}{dz}} \qquad \textit{Equation 3-26}$$

The turbulent-dispersive shear parameter is:

$$T_D^* = \frac{\rho_m l_m^2}{a_1 \rho \lambda^2 c_s^2} \qquad \textit{Equation 3-27}$$

The dispersive-viscous shear parameter:

$$D_v^* = \frac{\rho \lambda^2 c_s^2}{\mu} \frac{dv}{dz}$$ *Equation 3-28*

where ρ and c_s are the density and diameter of particles respectively.

The model applicability is given by D_v^*:

- $D_v^* < 30$, the flow can be approximated by Bingham model, i.e. the first two terms of Equation 3-22
- $30 < D_v^* < 400$, it is recommended to use the complete quadratic model
- $D_v^* > 400$, Bagnold model is suitable, i.e. the third term in Equation 3-22

3.2.6.2 Generalized viscoplastic model

It was introduced by Chen (Chen, 1988), it is based on considering two parts: one independent and another dependent of strain rate; as well as two very important rheological properties such as the effect of the normal stresses and the criterion of shear stress. Although conventional practice is to use a single equation in which shear stresses and strain rates are related, now two are used, since not consider pressure as a constant, a single expression cannot describe the effect of normal stresses. The formulation is as follows:

$$\tau = c_c \cos\phi + p \sin\phi + \mu_1 \left(\frac{dv}{dz}\right)^{n_1} = \tau_y + \mu_1 \left(\frac{dv}{dz}\right)^{n_1}$$ *Equation 3-29*

$$\sigma = -p + \frac{1}{3}\mu_2 \left(\frac{dv}{dz}\right)^{n_2}$$ *Equation 3-30*

where c_c is the cohesion, ϕ is the internal friction angle of the material, p the pressure, μ_1 the consistency index, μ_2 the transverse consistency index and n_1 and n_2 indices of flow behavior.

Chen and Ling (1996) lightly modify the expressions to evaluate the indexes μ_1 and μ_2 presented by Chen (1988) and whereby they are:

$$\mu_1 = a_1 \rho^{n_1 - 1} c^{2(n_{1-1})} \mu_f^{2-n_1} \mu_m$$ *Equation 3-31*

$$\mu_2 = -a_2 \rho^{n_2 - 1} c^{2(n_{2-1})} \mu_f^{2-n_2} \mu_m$$ *Equation 3-32*

where a_1 and a_2 are numerical constants depending on material properties, that along with n_1, n_2 are evaluated from experimental data. ρ and c are the density and solid particles diameter respectively and μ_f the viscosity of interstitial fluid. Regarding μ_m, it is the effective viscosity parameter suggested by Krieger and Dougherty (1959) depending on the concentration C and it is evaluated from:

$$\mu_m = (1 - KC)^{B/K}$$ *Equation 3-33*

With $K = \frac{1}{C_0}$, C_0 is the maximum possible concentration of solid particles in suspension and B is the intrinsic viscosity that can be equal to 3, when device walls of experiment are smooth, or 4.5 if they are coarse, in any case it is a value close to Equation 3-8 suggested by Einstein (1956).

3.3 EROSION LAWS

During the propagation phase of landslides or debris flows, it is often observed erosion of the base or incorporation of material from the sliding surface. These accretion processes of the mobilized volume, for which the material lying below the moving mass is incorporated in the system, can give rise to considerable increases in volume in dependence on the type of slope and its saturation conditions. In some cases, part of the material may also abandon the flow for deposit in the form of embankments or isolated languages. These changes in the mass, which is affected by the motion, influence its behavior and define the extent of the area affected.

During the propagation of this kind of flows, the initial involved volume erodes the bottom, incorporating more and more material inside the unstable mass. The increase of the volume can reach a final value, even, of a couple of orders of magnitude greater than the initial. The mechanisms that regulate the increase of the volumes are due to destabilization and erosion of the mass of the sliding layer crumbling. When movement is confined, this can be due to instability of the banks.

The trigger of the erosion mechanisms, such as the mobilization phase, is due to the disequilibrium between the forces acting on the sliding layer and its internal resistance. This can take place for the formation of wave fronts that increases the drag forces acting at the base of the crumbling body, intensifying the phenomenon. Furthermore, a rapid increase in load, when there is not a drainage, or the liquefaction of the sliding layer cause loss of strength and consequent erosion (Hungr et al., 2005).

The increase of the mobilized masses, due to the incorporation of material from the bottom or from the sides, can affect the mobility of the landslide (Pirulli & Pastor, 2012; Iverson, 2012). This happens because this phenomenon, by acting on the layer that defines the contours motion taking out some material, in reality modifies the basal characteristics. It is clear that the bed material, on which the landslide or debris flow moves, is crucial for the volumes that can be mobilized from detachment, and as regards the mobility of such volumes and the damage that the landslide may then cause.

Rapid changes of the stress conditions to which is subjected the soil, such as those induced by the passage of a current on a bed of granular debris, cause the mobilization of the latter, which can be incorporated in the body flowing. The mobilization of material from the layer, on which flows the landslide, is similar to the transport to the river bottom (McDougall & Hungr, 2005).

The collapse of a layer of material can in fact be caused by friction at the bottom due to the passage of granular current or to isolated interactions of the grains (from impact excavation) and generation of considerable interstitial pressures for rapid loading in undrained conditions, with the possibility of liquefaction. Dynamical and turbulent effects can play an important role in the mobilization of the upper layer of material from the basal soil, especially if we consider diluted flows.

Starting from the classical mass and momentum balance equations for a defined volume in the debris flow space, Chen et al. (2006) look for a link between the basal characteristics of the erodible soil and the flows above. The analysis is performed under the assumption that the density of the erodible bed in motion and that of the flow are equal. The authors assume that the mass flow for a

given volume of control is proportional to the area A_{eff} affected by erosion and to the flow velocity v

$$Q = \int_{A_{eff}} E\rho v q \, dA \qquad \text{Equation 3-34}$$

where E is the is the so-called yield rate, positive for entrainment and negative for deposition, and ρ is the flow density.

The original definition by Hungr et al. (1984) is in essence $Q = E\rho v$, considering that E is interpreted as the volume of material eroded per unit length of the path, having the dimension *[m³/m]*. It needs to be integrated over (or normalized with) the instantaneous total volume of mass if it is assigned to each discretized mass element in a dynamic analysis. In the present modification, however, E is dimensionless and is defined as follows: E units of volume of material are to be eroded via a unit contact area as the debris travels a unit length of its path. The static increase of debris depth at the instant of erosion will compensate the decrease of basal elevation while the contact area and the free surface remain unchanged.

For the mass-change landslide cases considered in the present study, E is typically taken at an $O(10^3)$. Although the deposit volume can reach a couple of times the initial volume, the bed topography change is still minor, because the eroded material is collected from the entire footprint area. Attributed to the heterogeneous soil properties and the complex slope topography, an overall/equivalent yield rate can be determined only with an accurate analysis of known events. However, for preliminary estimates in geotechnical practice, we propose the following simple guideline.

$$E \cong \alpha \frac{V_{erod}}{A_{eff} d_{center}} \qquad \text{Equation 3-35}$$

where V_{erod} is the total eroded volume, A_{eff} is the total erosion-affected area, d_{centre} is the travel distance of the center of mass and α is a correction coefficient that has to be calibrated.

The Egashira empirical approach (2001) to the problem of the stability of the bottom provides for the definition of a slope of equilibrium, defined for the single granulometric class, assuming that the bed erodible and mass flowing have the same particle size characteristics. In this way, for the identification of a formula for estimating the rate of erosion, it is required that the slope of the bottom, if erodible, evolves in order to satisfy the equality with the "equilibrium slope". The relation proposed by Egashira is:

$$E = c^* v \tan(\beta - \beta_e) \qquad \text{Equation 3-36}$$

where v is the average velocity of the flow, β is the bed slope, β_e is the equilibrium bed slope corresponding to sediment concentration of the debris flow body and c^* is the concentration by volume of bed sediment. This equilibrium bed slope can be defined as

$$\beta_e = \tan^{-1}\left\{\frac{(\rho_s - \rho_w)\, c}{(\rho_s - \rho_w)\, c + \rho_w} \tan \phi_s\right\} \qquad \text{Equation 3-37}$$

in which ρ_s is the density of the sediment particles, ρ_w is the water density, c is the sediment concentration of debris flow by volume and ϕ_s is the internal friction angle of the sediment.

Takahashi et al. (1986) proposed a formula for erosion rate and another for deposition rate, separately:

$$E_{eros} = \alpha \frac{c_e - c}{c^* - c_e} \frac{h}{d} v \qquad \text{Equation 3-38}$$

$$E_{dep} = \beta (c_e - c) \frac{h}{d} v \qquad \text{Equation 3-39}$$

in which α and β ar the experimental coefficients, c_e is the equilibrium sediment concentration of debris flow by volume corresponding to bed slope β, h is the flow depth and d is the grain size of debris flow.

To estimate the erosion at the bottom, McDougall & Hungr (2005), based on a model developed by the latter in 1995 (Hungr, 1995), propose to correlate the eroded depth from the bed with the height of the wave front of debris and the length L on which the flow develops. In the model, the authors, as a result of numerous observations, make the increase of the erosion rate dependent on the increases of the depth of the flowing mass. In this way, they obtain a distribution of incorporated material proportional to the depth and an exponential growth of landslide volumes with the displacement in the downstream direction. The law proposed by Hungr is

$$E_s = \frac{ln(V_0/V_{final})}{L} \qquad \text{Equation 3-40}$$

where V_0 and V_{final} are the initial and final volumes of the mass flowing respectively and L is the distance covered by the material. The total erosion depends on the erosion rate so defined, on the flow depth and on the velocity on the motion.

$$e_r = E_s \times h \times v \qquad \text{Equation 3-41}$$

Although this relation is purely empirical, however, it has physical significance in wanting to correlate changes in stress conditions due to the depth of the wave front of debris, to destabilization of the bottom material. The wide use of this formulation is justified by the extreme simplicity with which it presents, which allows its use as a starting point for more complex models and the relative ease to the extent of the quantities involved (Pirulli & Pastor, 2012; Iverson, 2012).

The problem of estimating volumes incorporated is tackled by Medina et al. (2008), considering the shear stress conditions at the bottom. The definition of the resistant strain is carried out with two approaches, to better understand what are the mechanisms that cause the incorporation of material to the bottom. A first approach, static, simply considers the static equilibrium between the frictional forces exerted by the flow and the resistance executed by the material on the basal soil. A second, dynamic, approach takes account of the fact that the material on the bottom, because there is incorporation, must exchange momentum with the flow, and once incorporated, causes a variation of the characteristics of the motion. In fact, by changing the composition, the regime of interstitial pressures consequently changes. In any case, once the balance between the applied

shear stress and the resistant is not assured, the calculation of the thickness h of the eroded soil comes to depend on the excess of the bottom shear stress as follows:

$$h = \frac{\tau_b - \tau_r}{\rho g(\cos\beta \tan\phi - \sin\beta)} \qquad \text{Equation 3-42}$$

where τ_b and τ_r are the applied and the resistant shear stress respectively, ρ is the soil density, equal to the one of the flow, β is the angle defined by the horizontal plane and the velocity direction, and ϕ is the internal friction angle of the soil.

Iverson developed a simplified analytical model with three layers (Figure 3.3.1), of which the upper in motion, the lower retainer and the intermediate animated by a speed comparable with that of the upper layer (Iverson, 2012). The formulation considers the incorporation rate to the bottom as a function of the shear forces exerted by the two layers in motion on their common interface.

$$E = \frac{\tau_{1,bot} - \tau_{2,top}}{\rho[v_{1,bot} - v_{2,top}]} \qquad \text{Equation 3-43}$$

The numerator of this equation can be interpreted as an excess of boundary shear stress, which expresses the difference between the basal shear traction exerted by the flow $\tau_{1,bot}$ and the boundary shear resistance exerted by the bed $\tau_{2,top}$. On the other hand, the denominator indicates that E decreases as the basal slip velocity $v_{1,bot}$ increases, knowing that $v_{2,top}$ is the upper velocity of the flow. The numerator of Equation 3-43 implies that deposition rather than entrainment occurs if $\tau_{1,bot} < \tau_{2,top}$ provided that $v_{1,bot} > v_{2,top}$. The denominator of the same equation indicates that $E \to \infty$ if $\tau_{1,\mathrm{bot}} > \tau_{2,top}$ and $v_{1,bot} = v_{2,top}$, consistent with the view that layers 1 and 2 behave as a single layer if there is no velocity contrast at the flow-bed interface.

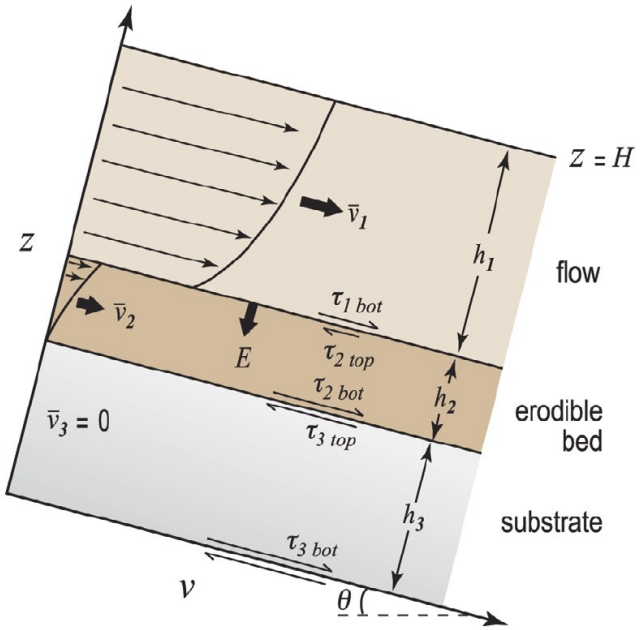

Figure 3.3.1 Schematic illustration of velocity profiles v(z), depth-averaged velocities, boundary shear tractions and thicknesses in a three-layer model of flow interaction with an erodible bed and strong substrate.

In the case of laboratory tests, that interface is unfortunately not easily detectable and this fact makes therefore complicated the direct application of this formulation. To make the model more accessible it is opportune to consider a characteristic velocity, at least for the subaerial surface flow. Thanks to investigations on the velocities field in the flowing layer (Johnson et al., 2012), it is possible to express the rate

of incorporation in dependence on an observed velocity v_1^* as follows

$$E = \frac{\tau_{1,bot} - \tau_{2,top}}{\rho\left[(1 - s_1)v_1^* - v_{2,top}\right]} \qquad \text{Equation 3-44}$$

where s_1 is a fitting parameter that ranges from $s_1 = 0$, if there is no simple shear, to $s_1 = 1$, if there is no basal slip. In Equation 3-44, the basal slip velocity v_1 is supposed equal to $(1 - s_1)v_1^*$. The relationship between $v_{1,bot}$ and v_1^* depends on the flow velocity profile, $v_1(z)$, but for flows of opaque geological debris, direct measurements of $v_1(z)$ are really problematic and perhaps impossible. Distinctions between alternative velocity profiles that involve various combinations of homogeneous simple shear and basal slip have been made on the basis of particle tracking studies, however (Johnson et al., 2012).

If you want to refer to the interstitial pressures regime, the shear stresses can be expressed as a function of the effective stress with Coulomb's law, and then, with some steps, as a function of the pore pressure. The rate of incorporation is then:

$$E = \frac{\rho g h_1(\mu_1 - \mu_2)\cos\beta + \mu_2 p_{2,top} - \mu_1 p_{1,bot}}{(1 - s_1)\rho v_1^*} \qquad \text{Equation 3-45}$$

where μ_1 and μ_2 are the Coulomb friction coefficients for layers 1 and 2, respectively, and $p_{1,bot}$ and $p_{1,top}$ are boundary pore fluid pressures for layers 1 and 2, and β is the slope angle. This equation indicates that $E > 0$ requires a contrast in Coulomb friction coefficients $(\mu_1 > \mu_2)$, a contrast in pore fluid pressures $\left(p_{2,top} > p_{1,bot}\right)$, or some combination of the two.

If the top of the bed sediment becomes completely liquefied by high pore pressures (i.e., $p_{2,top} = \rho g h_1 \cos\beta$) and the value $s_1 = 1/2$ is adopted to describe the flow velocity profile, then Equation 3-45 reduces to

$$E = \frac{2\mu_1 g h_1 \cos\beta\,(1 - \lambda_1)}{v_1^*} \qquad \text{Equation 3-46}$$

where $\lambda_1 = p_{1,bot}/\rho g h_1 \cos\beta$ is a pore pressure ratio that indicates the degree of liquefaction, $0 \le \lambda_1 \le 1$.

Larsen et al. (2010) connect the eroded volumes in flow-like landslides to a simple law proposed by Simonett (1967). This simple formulation correlates the volume V_e eroded from the slope only to the area A on which propagates the casting phenomenon via two coefficients b_0 and b_1, to be calibrated on site via statistical analysis, according to the following equation:

$$V_e = b_0 A^{b_1} \qquad \text{Equation 3-47}$$

where the coefficient b_1 would take into account the geo-mechanical characteristics of the soil, assuming values ranging from 1.5 for bedrock to 1.1 for inconsistent soil with high organic component.

4 DEPTH INTEGRATED SPH MODEL

4.1 INTRODUCTION

The simulation model here presented has been implemented by Professor Manuel Pastor and his team. In a first phase, the analysis was approached through an Eulerian scheme, whose equations were discretized with finite elements (*GEOFLOW*). Since 2005, they have been working on the implementation of a numerical technique without mesh, known as SPH, to solve the system of equations consisting of mathematical and rheological models. Both allow to estimate the basic features of interest with satisfactory accuracy, the difference between the two is the computational efficiency. In fact, the SPH takes a significant advantage over the *GEOFLOW*.

In general, the simulation method for flow-like landslides has three main components:

- A mathematical model
- A rheological model
- A numerical model

The *mathematical model* has been developed by Professor Manuel Pastor and his co-workers. It is a depth-integrated, coupled, nonlinear formulation, initially raised to *GEOFLOW* in an Eulerian frame, where the fundamental principles of mass and momentum conservations are based in the continuum mechanics. This formulation was subsequently converted to a pseudo-Lagrangian one, because the SPH requires this scheme of calculation.

The *rheological model* provides additional mathematical expressions to the previous system, which relate stresses and strain rates. Various models are included in the code, such as Bingham and Voellmy ones.

With the *numerical model*, the integration in space and time of the system of first order hyperbolic differential equations is performed. This system combines the mathematical and the rheological models.

In a depth-integrated model, the balance equations are integrated along the vertical axis. This integration has been performed basing on the simplified method of the shallow water hydrodynamic, in which the shear stresses in the depth direction are neglected and some hypothesis are required:

- The flow depth is small with respect to its length and width
- The depth variation is small and gradual along the length and width of the slide (there is a strong vertical uniformity)
- The pressure has a linear distribution on the vertical axis, zero at the surface and maximum at the bottom

This procedure leads to remove a dimension in the balance equations. However, it is possible to simulate the motion on the surface of a three-dimensional body.

The model is therefore two-dimensional, but the results are displayed in three dimensions, i.e., you can follow the movement of the sliding mass through the 3D terrain topography.

The mathematical model is coupled is sense that considers the mixing theory to describes the coupling between the solid soil and pore fluid. It is applied to both the initiation and the propagation phases of rapid flow-like landslides.

4.2 MATHEMATICAL MODEL

4.2.1 Introduction

The continuous material analyzed is generally composed of several phases. Soils and rocks are heterogeneous materials, composed by solid particles surrounded by space that can be filled by air, water or other fluids. Therefore, they are multiphase materials characterized by the interactions existing between the different components.

It is necessary to use a numerical model able to represent the behavior of rapid flows, particularly the debris flows or the rock/debris avalanches, in which the permeability is high and the relative velocities between the phases may reach important values.

The classical approach of numerical analysis is based on displacement formulations where the main variables are the stress and the displacement.

4.2.2 Equations of the model

The starting point of this numerical model is the $v - p_w$ Zienkiewicz-Biot model that can be summarized in two points:

i) The balance of mass, combined with the balance of linear momentum of the pore fluid, which in the case of saturated soils reads

$$-div(k_w\ grad\ p_w) + div\ v_s + \frac{1}{Q}\frac{D^{(s)}p_w}{Dt} = 0 \qquad \textit{Equation 4-1}$$

where k_w is the permeability coefficient, v_s is the velocity of soil skeleton, $\mathrm{D}^{(s)}$ refers to a material derivative following the soil particles and the equivalent volumetric stiffness Q is given in terms of soil porosity n and volumetric stiffnesses of pore water $K_w$and soil grains K_s as

$$\frac{1}{Q} = \frac{n}{K_w} + \frac{1-n}{K_s} \qquad \textit{Equation 4-2}$$

ii) The balance of linear momentum for the mixture soil skeleton-pore fluid is given by

$$\rho\frac{D^{(s)}v_s}{D_t} = \rho b + div\ \sigma \qquad \textit{Equation 4-3}$$

where ρ is the density of the mixture, b the body forces and σ the Cauchy stress tensor.

The model is completed by suitable rheological and kinematical relations relating (i) the stress tensor to the rate of deformation tensor d and (ii) the rate of deformation tensor to the velocity field v_s.

From here, the propagation–consolidation model can derive, assuming that the velocity and the pressure fields can be split into two components as

$$v = v_0 + v_1 \qquad \text{Equation 4-4}$$

$$p_w = p_{w0} + p_{w1} \qquad \text{Equation 4-5}$$

where the sub-indexes 0 and 1 refer, respectively, to the propagation and consolidation components.

Iverson and Denlinger et al. (2001) and Pastor et al. (2004) have used this approach. The equations of the propagation–consolidation model are

$$\rho \frac{Dv_0}{Dt} = \rho b + div\ \sigma \qquad \text{Equation 4-6}$$

with

$$div\ v_0 = 0 \qquad \text{Equation 4-7}$$

$$\frac{Dp_w}{Dt} = \frac{\partial}{\partial x_3}\left(c_v \frac{\partial p_w}{\partial x_3}\right) \qquad \text{Equation 4-8}$$

where $c_v$is the coefficient of consolidation. In what follows, we will drop the sub-indexes '0' in the velocity field and '1' in the pressures.

Often the average depths of phenomena such as debris flows, mudflows and landslides in general are small in comparison with their length or width. When this happens, an important simplification is possible. The 3D propagation-consolidation model can be simplified by integrating its equations along the vertical axis. A combination of accuracy and simplicity characterized the resulting 2D depth-integrated model, which can provides important information such as velocity of propagation, time to reach a particular place, depth of the flow at a certain location, etc. Various authors have used this approach to model flow-like landslides (Savage & Hutter, 1991; Laigle & Coussot, 1997).

With this simplification, the number of unknown variables is reduced. Therefore, it does not require special techniques to describe the location of the free surface of the flowing mass.

The equations of the depth-averaged model are obtained by integrating along x_3 the balance of mass and momentum equations and taking into account the Leibniz's rule:

$$\int_a^b \frac{\partial}{\partial s} F(r,s)dr = \frac{\partial}{\partial s}\int_a^b F(r,s)dr - F(b,s)\frac{\partial b}{\partial s} + F(a,s)\frac{\partial a}{\partial s} \qquad \text{Equation 4-9}$$

Figure 4.2.1 shows the reference system and the notation used in the calculations. The vertical integration is not performed in a material volume, so it is difficult to obtain directly a Lagrangian form of the depth-integrated equations. Sometimes, it has been found convenient to refer to an equivalent 2D continuum having the depth-integrated velocities as the velocities of their material points. Anyway, it has to be noticed that the moving points have no exact connection with material particles, so this cannot be considered as a Lagrangian formulation. It can be defined either "quasi-Lagrangian" or arbitrary Lagrangian-Eulerian formulation.

Indeed, a moving point in the depth-integrated model represents a column of material extending from the bottom to the free surface. The column travels with the depth-averaged velocity, and

therefore, fluid particles travelling faster will enter it whereas fluid particles with a smaller velocity will be left behind.

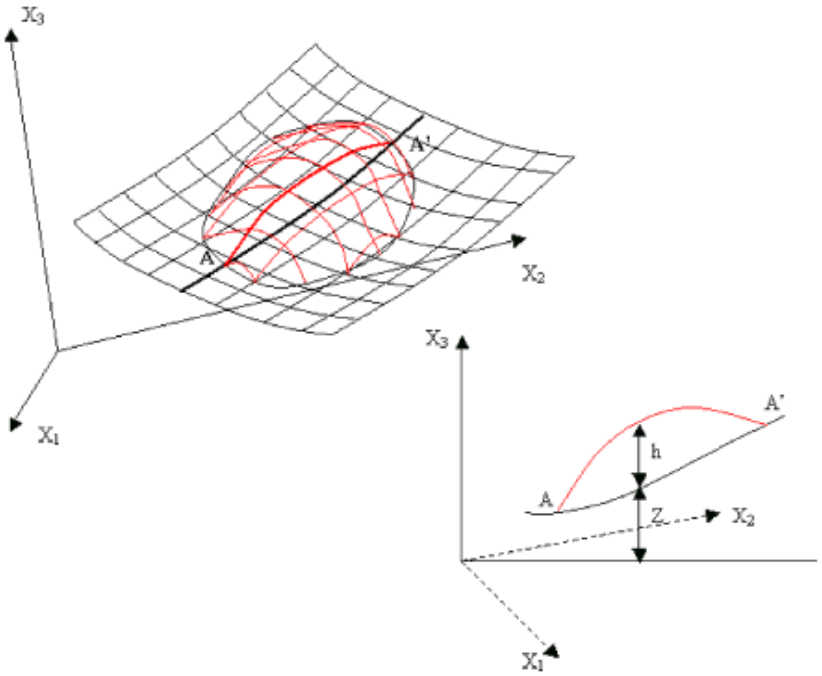

Figure 4.2.1 Reference system and the notations used in the analysis.

The derivative of a quasi-Lagrangian of the depth-integrated equations start from the introduction of a "quasi-material formulation" defined as

$$\frac{\bar{d}}{dt} = \frac{\partial}{\partial t} + \bar{v}_j \frac{\partial}{\partial x_j} \qquad \textit{Equation 4-10}$$

from where we can obtain the "quasi-Lagrangian" form of the balance of mass, depth-integrated equation:

$$\frac{\bar{d}h}{dt} + h\frac{\partial \bar{v}_j}{\partial x_j} = 0 \qquad \textit{Equation 4-11}$$

The balance of momentum equation is

$$h\frac{\bar{d}}{dt}\bar{v}_i - \frac{\partial}{\partial x_i}\left(\frac{1}{2}b_3 h^2\right) = \frac{1}{\rho}\frac{\partial}{\partial x_j}\left(h\bar{\sigma}_{ij}^*\right) + b_i h + \frac{1}{\rho}|N^B|t_i^B \qquad \textit{Equation 4-12}$$

considering the following relation

$$\sigma_{ij} = -\bar{p}\delta_{ij} + \sigma_{ij}^* \qquad \textit{Equation 4-13}$$

with

$$\bar{p} = \frac{1}{2}\rho b_3 h \qquad \bar{\sigma}_{ij}^* = \bar{\sigma}_{ij} + \bar{p}\delta_{ij} \qquad \textit{Equation 4-14}$$

The tensile stress component is considered as positive. The term t_i^B is the i-th component of a normal stress acting on a basal surface, and $|N^B|$ is

$$|N^B| = \left(\frac{\partial Z^2}{\partial x_1} + \frac{\partial Z^2}{\partial x_2} + 1\right)^{1/2} \qquad \text{Equation 4-15}$$

where Z is the height of the basal surface.

Finally, the vertical consolidation equation can be integrated in depth, arriving after some passages to

$$\frac{\bar{d}}{dt}(\bar{p}_w h) = c_v \frac{\partial p_w}{\partial x_3}\Big|_Z^{Z+h} \qquad \text{Equation 4-16}$$

The pore pressure can be approximated as

$$p_w(x_1,\, x_2,\, x_3, t) = \sum_{k=1}^{Np_w} P_k(x_1,\, x_2, t) N_k(x_3) \qquad \text{Equation 4-17}$$

in which shape functions have been used along x_3 fulfilling the boundary conditions. It can be assumed that the pore pressure at the surface is zero and the influx at the basal surface in zero. The shape functions can be consequently chosen as

$$N_k(x_3) = cos\frac{(2k-1)}{2h}\pi\,(x_3 - Z)\ , \qquad k = 1, N\,p_w \qquad \text{Equation 4-18}$$

The first term is given by

$$N_1(x_3) = cos\frac{\pi}{2h}(x_3 - Z) \qquad \text{Equation 4-19}$$

If the analysis is limited to a single Fourier component, the pore pressure becomes

$$p_w(x_1,\, x_2,\, x_3, t) = P_1(x_1,\, x_2, t)\, cos\frac{\pi}{2h}(x_3 - Z) \qquad \text{Equation 4-20}$$

from where we obtain

$$\frac{\bar{d}P_1}{dt} = \frac{\pi^2}{4h^2} c_v P_1 \qquad \text{Equation 4-21}$$

Which is the quasi-Lagrangian form of the vertically integrated 1D consolidation equation.

The results obtained above depend on the rheological model chosen, from which the basal friction and the depth-integrated stress tensor $\bar{\sigma}_{ij}^*$ are directly given.

4.2.3 Evaluation of the erosion rate

The model equations may include the erosion rate. In this work, the evaluation on this term is done using the formulation proposed by Hungr (1995). This law is based on an empirical parameter that represents the thickness of material entrained per unit flow depth per unit length, whose dimension is L^{-1} and is calculated using the Equation 3-40.

4.3 NUMERICAL MODEL

4.3.1 Introduction

M. A. Biot has proposed the first mathematical model that describes the coupling of solid, water and gas for materials with linear elastic behavior. The formulation proposed by Biot describes the interaction of the solid part with the interstitial fluid for an elastic material using as variables: the soil skeleton displacements (*u*) and the relative displacements of the interstitial fluid in relation to the solid skeleton (*w*).

The Biot theory was later expanded thanks to the work done University of Swansea (Zienkiewicz, 1982; Zienkiewicz & Shiomi, 1984) to consider the nonlinear large deformation and behavior of saturated porous materials. Among the numerical formulas, proposed by different authors, for the resolution of Biot equations, the one by Zienckiewicz Bettess (1982) which uses as the independent variables of the system of equations of the soil skeleton displacements (u) and the interstitial water pressure (pw), is very reliable.

This type of formulation of a two-phase material can be used to solve a large number of issues regarding the geomaterial. It is obtainable a further improvement to the u-pw formulation for the resolution of problems regarding partially saturated materials assuming that the air or gas pressure within the domain is not negligible. To correctly represent the behavior of the terrain, it is necessary then treat it as a three-phase medium where we take into account the variations in pressure air. The interstitial fluid pressure (liquid or gas) has a key role in behavior of the soil structure, could cause breakage of the material.

Three balance equations, which will be formulated in the following paragraphs, are the base of this model. In addition to these, an adequate constitutive or rheological model, which can define the link between stress and strain through kinematic relations of movement and speed, is also included.

The propagation of a landslide has no analytic solution and therefore it must resort to numerical methods to obtain an approximate solution. There are some models in which the information is structured in "mesh" that are able to solve this problem, such as the finite element method and/or the finite difference. Although these models have gone through a period of great development from the 80s onwards, they still have difficulties in the free surface problems or large deformations. The last decade has thus appeared a group of numerical methods, which do not associating information to a mesh, were generally named as "without mesh methods", to which also the Smoothed Particle Hydrodynamics, or SPH, belongs.

The SPH method is based on the discretization of a set of nodes through approximations of integral type of a function and of its derivatives.

4.3.2 Approximations of integral of functions

The SPH method is developed in two stages:

1. It approximates a given function ϕ (x) and its derivatives through integral approximations characterized by a Kernel type core;

2. It introduces a set of nodes or "particles" that used to build numerical approximations based on numerical integration whose integration points are just the nodes themselves, without therefore resort to the mesh or elements.

The concept of associating the node to that of one of the continuous medium particle presents on one hand the advantage that the method is more intuitive and easy to interpret but, on the other hand, does lose perspective and generality.

We can consider the scalar function ϕ (x), with $x \in \Omega \subset \mathrm{R}$, where Ω is the function dominium

$$\Phi(x) = \int_{\Omega} \Phi(x')\, \delta(x' - x)\; dx' \qquad \textit{Equation 4-22}$$

where $\delta(x)$ is the generalized Dirac delta function, traditionally defined as

$$\delta(x) = \begin{cases} \infty & x = 0 \\ 0 & |x| > 0 \end{cases} \qquad \textit{Equation 4-23}$$

with the following condition

$$\int_{\Omega} \delta(x)\; dx = 1 \qquad \textit{Equation 4-24}$$

The Dirac delta, in the theory of distribution, is defined starting with a sequence of functions $W_k\ (x, h)$, such as for example

$$W_k(h, k) = \frac{1}{\sqrt{2\pi h}} exp\left(-\frac{x^2}{h}\right) \qquad \textit{Equation 4-25}$$

It is possible to demonstrate that

$$\lim_{h \to 0} \int_{\Omega} W_k(x' - x, k)\, \phi(x')\; dx' = \int_{\Omega} \Phi(x')\, \delta(x' - x)\; dx' = \Phi(x) \qquad \textit{Equation 4-26}$$

The function $W_k\ (x, h)$ depends on the width $h \to 0$ and on the integer number k, where h is the smoothing length defining the influence area of the Kernel W. It is possible to plot some approximations of the Dirac delta through a series of functions for different values of its parameters, which are integral representations of vector or scalar function $\Phi(\mathrm{x})$ with the function $W(x)$.

The previous expressions can be immediately generalized to 2 or 3 dimensions, considering a scalar or vector $\Phi(\mathrm{x})$ of $x \in \Omega \subset R^{dim}$, with Ω open and bounded domain.

These results are the starting point for the SPH approximations, where regular distributions are used to approximate the value of the function. The classical notation used for the SPH method is:

$$\langle \Phi(x) \rangle = \int_{\Omega} \Phi(x')\, \delta(x' - x)\; dx' \qquad \textit{Equation 4-27}$$

4.3.3 Kernel functions: some basic characteristics and examples

The smoothing kernel functions determine the dimension of the area of influence of particles, or support domain of particles. The SPH accuracy of the approximation depends on the characteristics of the Kernel $W(x,h)$. Various kernel functions have been used in SPH methods. A special class of functions is the ones with radial symmetry, which depend only on $r = |x' - x|$, and if we define $\xi = \frac{|x'-x|}{h} = \frac{r}{h}$ it is possible to have

$$W(x' - x) = W(\xi) \qquad \textit{Equation 4-28}$$

Generally speaking, the functions $W(x,h)$ used as functions for the SPH, have to satisfy the following conditions:

- The smoothing kernel function should verify the Dirac delta function condition as the smoothing length approaches to zero

$$\lim_{h\to 0} W(x' - x, h) = \delta(x - x') \qquad \textit{Equation 4-29}$$

- The smoothing kernel function must be normalized over its support domain

$$\int_{\Omega} W(x' - x, k)\, dx' = 1 \qquad \textit{Equation 4-30}$$

- The smoothing kernel function should be positive for any points at x' within the support domain of a particle at point x

$$W(x - x') \geq 0 \qquad \textit{Equation 4-31}$$

- The smoothing kernel function should be a monotonically decreasing function of $\xi = \frac{|x'-x|}{h}$ which means that the kernel should monotonically decrease with the increase of the distance away from the particle
- The smoothing kernel function should be a symmetric function of $(x - x')$.

The variable ξ is useful because it allows expressing $W(x - x', h)$ as $W(\xi)$. Any function, which satisfies the properties presented above, can be used as kernel for the SPH approximations. It is possible to mention three smoothing kernel functions proposed in the literature: the Gaussian kernel, the cubic spline kernel and the quantic kernel.

In 1977 Gingold and Monaghan (1977) proposed the following Gaussian kernel to simulate the non-spherical stars:

$$W(\xi, h) = \frac{C}{h^{ndimn}} \begin{cases} e^{-\xi^2} & \forall \xi \leq 3 \\ 0 & Otherwise \end{cases} \qquad \textit{Equation 4-32}$$

Where ndimn is the dimension of the space and C is $1/\pi^{0.5}$, $1/\pi$ and $1/\pi^{3/2}$ in one, two and three-dimensional space respectively. Approximatively 8 years later, Monaghan and Lattanzio (1985) proposed the cubic spline function known as the B-spline function:

$$W(\xi,h)=\frac{C}{h^{ndimn}}\begin{cases}\left(1-\frac{3}{2}\xi^2+\frac{3}{4}\xi^3\right) & 0\le\xi\le 1\\ \frac{1}{4}(2-\xi)^3 & 1\le\xi\le 2\\ 0 & \xi\ge 2\end{cases}$$ *Equation 4-33*

Where C is $2/3$, $10/7\pi$ and $1/\pi$ is one, two and three-dimensional space respectively.

The most used function in the current SPH literature is the cubic spline kernel because it is similar to a Gaussian function whereas it has a narrow compact support. Morris introduced higher order quantic spline that is closer to the Gaussian and more stable. This kernel has a larger compact support than that of the cubic spline kernel and therefore its use increases the computational cost

$$W(\xi,h)=\frac{C}{h^{ndimn}}\begin{cases}(3-\xi)^5-6(2-\xi)^5+15(1-\xi)^5 & 0\le\xi\le 1\\ (3-\xi)^5-6(2-\xi)^5 & 1\le\xi\le 2\\ (3-\xi)^5 & 2\le\xi\le 3\\ 0 & \xi\ge 3\end{cases}$$ *Equation 4-34*

Where C is 120, $7/478\pi\ and\ 3/359\ \pi$ is one, two and three-dimensional space respectively.

Generally speaking, the more a kernel function is similar to a Gaussian one, the better results you can obtain- Nevertheless higher order is the kernel function, larger will be its compact domain and therefore will be the computational time.

4.3.4 Integral approximations of derivatives

It is possible to write the integral representation of the derivatives in SPH as:

$$\langle\phi'(x)\rangle=\int_{\Omega}\phi'(x')\,W(x'-x,k)\,dx'$$ *Equation 4-35*

In this formulation, it is necessary to notice that h decreases and the function W(x,h) approximates the Dirac delta. Consequently, this formulation can approximates the derivative value. If this equation is integrated, taking to account that the function W(x,h) has a local support, it is possible to obtain:

$$\langle\phi'(x)\rangle=-\int_{\Omega}\phi(x')\,W(x'-x,k)\,dx'$$ *Equation 4-36*

4.3.5 Discrete approximation of functions

The integral approximation of functions and derivatives written above are valid at a continuum level. If the information is stored in a discrete manner, for instance in a series of nodes, it is necessary to construct discrete approximations. The SPH method introduces the concept of "particles", to which information concerning fields variables and their derivatives is linked. These particles are nodes, in the same way that those found in the finite elements or the finite differences. All the operations are consequently to be referred to nodes. Therefore, we will introduce the set of particles $\{x_K\}$ with K=1…N. Obviously, the level of the approximation will depend on the spacing and the location of these nodes.

It was shown that

$$\langle \phi'(x) \rangle = \int_{\Omega} \phi'(x')\, W(x' - x, k)\, dx' \qquad \textit{Equation 4-37}$$

Where dx' represent the infinitesimal volume at the location of particle J and can be replaced by the finite volume ΔV_J of the particle J, which is related to the mass m_J and the density ρ_J of the particle by

$$m_J = \Delta V_J\, \rho_J \qquad \textit{Equation 4-38}$$

As the information concerning the function is only available at a set of particles $\{x_K\}$ with K=1…N, the integral could be evaluated using a numerical integration formula of type:

$$\langle \phi(x_I) \rangle_p = \sum_{J=1}^{N} \frac{m_J}{\rho_J} \phi(x_J) W(x_I - x_J)\, \Delta V_J \qquad \textit{Equation 4-39}$$

Where "p" denotes the particle approximation. For simplifying, we will introduce

$$\phi_I = \langle \phi(x_I) \rangle_p \qquad \textit{Equation 4-40}$$

In this formulation, ϕ_I is the particle approximation of the function ϕ at the location of the particle I, while $\phi(x_I)$ is the value of the function ϕ at the location of the particle I, so they are basically different.

Introducing equation $m_J = \Delta V_J\, \rho_J$ in the discrete approximation written above, the particle approximation of the function can be written as

$$\phi_I = \sum_{J=1}^{N} \frac{m_J}{\rho_J} \phi(x_J)\, W(x_I - x_J, h) \qquad \textit{Equation 4-41}$$

As the smoothing kernel function, W, has a compact support in such way that $W(x_I - x_J, h) = 0$ when $|x_I - x_J| \geq \kappa h$, the summation written above extends to the N_p nodes which are in the support domain of the particle I

Therefore, it is possible to obtain

$$\phi_I = \sum_{J=1}^{N_p} \frac{m_J}{\rho_J} \phi(x_J)\, W_{IJ} \qquad \textit{Equation 4-42}$$

Where $W_{IJ} = W(x_I - x_J, h)$. Due to the symmetric property of the smoothing kernel function, it is interesting note that

$$W_{IJ} = W(x_I - x_J, h) = W(x_J - x_I, h) = W_{JI} \qquad \textit{Equation 4-43}$$

Using a similar procedure for the spatial derivative of the function, it is possible to write:

$$\langle grad\phi_I(x_I) \rangle_p = -\sum_{J=1}^{N_p} \frac{m_J}{\rho_J} \phi(x_J)\, gradW(x_I - x_J, h) \qquad \textit{Equation 4-44}$$

Where $\mathrm{gradW}(\mathrm{x_I} - \mathrm{x_J}, \mathrm{h})$ is taken with respect to the particle J.

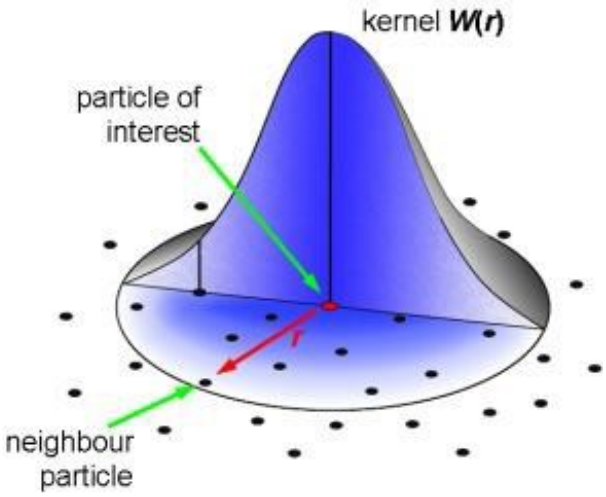

Figure 4.3.1 Kernel function representation.

4.3.6 Discretization of integrated equations in depth

Many landslides have averages depth that are small compared to their length or width. It is so possible to simplify 3D models of the consolidation integrating the equations along the vertical axis. The in depth-integrated 2D model provides excellent results on the propagation velocity, flow depth, etc.

The discretization of the SPH process for the integrated in-depth model considers the interstitial water dissipation during the propagation phase.

The equations system that solves this problem is:

$$\frac{\partial}{\partial t}\begin{bmatrix} h \\ h\bar{v}_1 \\ h\bar{v}_2 \\ hP_{w1} \end{bmatrix} + \frac{\partial}{\partial x_1}\begin{bmatrix} h\bar{v}_1 \\ h\bar{v}_1^2 \\ h\bar{v}_2\bar{v}_1 \\ hP_{w1}\bar{v}_1 \end{bmatrix} + \frac{\partial}{\partial x_2}\begin{bmatrix} h\bar{v}_2 \\ h\bar{v}_1\bar{v}_2 \\ h\bar{v}_2^2 \\ hP_{w1}\bar{v}_2 \end{bmatrix} = \begin{bmatrix} 0 \\ b_1 h \\ b_2 h \\ 0 \end{bmatrix} + \frac{1}{\rho}\left[\frac{\partial}{\partial x_1}\begin{pmatrix} 0 \\ h\bar{\sigma}_{11} \\ h\bar{\sigma}_{12} \\ 0 \end{pmatrix} + \frac{\partial}{\partial x_2}\begin{pmatrix} 0 \\ h\bar{\sigma}_{12} \\ h\bar{\sigma}_{22} \\ 0 \end{pmatrix} + \begin{pmatrix} 0 \\ t_1^A + t_1^B \\ t_2^A + t_2^B \\ 0 \end{pmatrix}\right] + \begin{bmatrix} 0 \\ 0 \\ 0 \\ c_v P_{w1} \frac{\pi^2}{4h} \end{bmatrix}$$

Equation 4-45

The system of equations is of hyperbolic type of the first order; these equations are very frequent in physical and engineering problems, but they present many difficulties for the existence of convective terms that produce instability and requiring the use of special discretization methods for obtaining a correct solution.

It is necessary to introduce a set of particles $\{x_K\}$ with K=1…N and the following variables:

- h_I: height of material at the I node;
- $\bar{v}_I$: integrated velocity along the vertical;
- t_B^I: basal tension;
- σ_I: integrated tension along the vertical;
- $P_{w1,I}$: interstitial pressure at the base.

If we define that each node has an area Ω_I, we can introduce:

- A fictitious mass that is moving with the I node: $m_I = \Omega_I h_I$
- $\bar{p}_I$: tension integrated in depth equal to $\bar{p}_I = \frac{1}{2}\rho b_3 h_I^2$.

The SPH approximation of the mass balance equation integrated in depth is:

$$\langle \frac{dh}{dt} + h\frac{\partial \bar{v}_J}{\partial x_J} \rangle = 0 \qquad \textit{Equation 4-46}$$

And if we write it for the I node, it becomes

$$\frac{\bar{d}}{dt}\langle h_I \rangle + h_I \langle \frac{\partial \bar{v}_J}{\partial x_J} \rangle = 0 \qquad j = 1,2 \qquad \textit{Equation 4-47}$$

With the divergence term that is

$$div(v_I) = -\sum_J \Omega_J v_J gradW_{IJ} = -\sum_J \frac{m_J}{h_J} v_J gradW_{IJ} \qquad \textit{Equation 4-48}$$

While the height can be obtained from the node position with the following expression:

$$\langle h_I \rangle = \langle h(h_I) \rangle = \sum_J h_J \Omega_J W_{IJ} = \sum_J m_J W_{IJ} \qquad \textit{Equation 4-49}$$

And it can also be normalized thus improving the approximation close to the boundary nodes:

$$h_I = \frac{\sum_J m_J W_{IJ}}{\sum_J \left(\frac{m_J}{h_J}\right) W_{IJ}} \qquad \textit{Equation 4-50}$$

The discretized formulation of the balance of linear momentum is:

$$\langle \frac{\partial}{\partial t}(h\bar{v}_I) + \frac{\partial}{\partial x_J}(h\bar{v}_I\bar{v}_J) = \frac{1}{\rho}\left[\frac{\partial}{\partial x_J}(h\sigma_{IJ}) + b_I h + t_I^A + t_I^B\right] \rangle \qquad \textit{Equation 4-51}$$

Which, in the SPH model is used with the simplified formulation $\left(\frac{\partial}{\partial x_J}(h\bar{v}_I\bar{v}_J) = 0\right)$ and with the decomposition $\sigma_{IJ} = -\bar{p}\delta_{IJ} + \sigma^*_{IJ}$, knowing that $\bar{p} = \frac{1}{2}\rho b_3 h_I^2$ and $\sigma^*_{IJ} = \bar{p}\delta_{IJ} + \bar{\sigma}_{IJ}$ and becomes:

$$\frac{\bar{d}}{dt}\bar{v}_I = -\sum_J \Omega_J p_J gradW_{IJ} + \sum_J \Omega_J \sigma_J gradW_{IJ} + b + \frac{1}{h_I} t_I^B \qquad \textit{Equation 4-52}$$

Finally, the discretized formulation for the dissipation of the water pressure is:

$$\langle \frac{\partial (P_{w1} h)}{\partial t} + \frac{\partial (P_{w1}\bar{v}_I h)}{\partial x_I} = c_v P_{w1}\frac{\pi^2}{4h} \rangle \qquad \textit{Equation 4-53}$$

Which is used with the simplified formulation:

$$\frac{\bar{d}}{dt}P_{w1,I} = -\frac{\pi^2 c_v}{4h_I}P_{w1,I} \qquad \textit{Equation 4-54}$$

4.4 USE OF THE NUMERICAL MODEL

4.4.1 Introduction

The numerical model used allows you to define the parameters you want to use in four different files. Basically, these files contain the information about the topography of the system, the geometry of the source mass and the boundary conditions.

You need to select the type of analysis you are simulating that is directly connected with the case study you are considering. These files also include all the rheological parameters depending on the law you decide to implement, the erosional parameters and the type of output variables you want to export. Finally, the integration time step and the total analysis time are explicated.

In this program, a depth-integrated model that reproduces a rapid flow-like landslide can be used depending on the type of phenomenon you are considering. Totally, the code can reproduce:

- Debris flows
- Mudflows
- Sliding flows
- Dry granular material flows

Depending on the case you want to reproduce, the model allows you to choose the type of problem to solve:

- SW ⟾ Debris flows, mudflows and sliding flows, based on the shallow water hypothesis
- NS ⟾ Navier Stokes equations
- DF ⟾ Dry flows

The SW equations are applicable to landslides that behave like flows, in which one dimension – the depth – is much smaller than the other two sizes – length and width.

In all the case studies presented in this work, the shallow water hypothesis are used to solve the first order hyperbolic differential equations. All the rapid landslides considered, in fact, follow the preview assumptions.

4.4.2 Input files

4.4.2.1 Topography file

This file is used to define the basal topography of the problem. Various cases are present in the model, to simplify the definition of the geometrical dimensions of the problem. The variable *ictop* is used to define the type of mesh.

4.4.2.1.1 Tridimensional topographic mesh, *ictop=0*

In this case, the file contains the coordinates X, Y, Z of all the mesh nodes and the program just read these information. You have to define that you are using *ictop=0*, the number of node in X direction and the number in Y direction.

```
ictop
0
npoigx     npoigy
 101         101
Coordinate X      Coordinate Y      Coordinate Z
 1672006.72        5062875.00          548.00
 1672011.72        5062875.00          546.00
 1672016.72        5062875.00          546.00
 …                 …                   …
 …                 …                   …
 1669656.72        5065390.00          1224.00
```

Figure 4.4.1 Topographical input file for ictop=0.

4.4.2.1.2 Topography with constant elevation, *ictop=1*

This index is used to define a horizontal mesh, so the Z value is the same for all the nodes of the mesh. The file includes the maximum and minimum values of X and Y limiting the study area, explicates the numbers of nodes you want to create between the maximum and the minimum values of X and Y. Finally, the constant value of Z has to be indicated. The model read the file, calculates the coordinates of all the mesh points and assigns the constant value of Z to all these points.

```
ictop
1
Xmin   Xmax   Ymin   Ymax
150.0  450.0  100.0  120.0
npoigx     npoigy
 300         20
Z constant
15.0
```

Figure 4.4.2 Topographical input file for ictop=1.

4.4.2.1.3 Topography for connecting a slope to an horizontal plane, *ictop=2*

```
ictop
2
Xmin   Xmax   Ymin   Ymax
 0.0    450.0   0.0   100.0
npoigx     npoigy
 100         20
 T1        R       Theta       T3
100.0   50.0      20        150.0
```

Figure 4.4.3 Topographical input file for ictop=2.

When the soil is composed by a constant slope that finish connecting to a horizontal plane (Z=0), assuming a cylindrical transition between the two zones, you can use *ictop=2*. The limits of X and Y coordinates have to be written and the number of points in which subdivide the topography has to

be indicated for both the directions. Finally, the user has to define the values of some geometrical variables, as shown in Figure 4.4.4. Practically, the zones T1 and T3, the slope angle θ and the transition radius between T1 and T3 are defined.

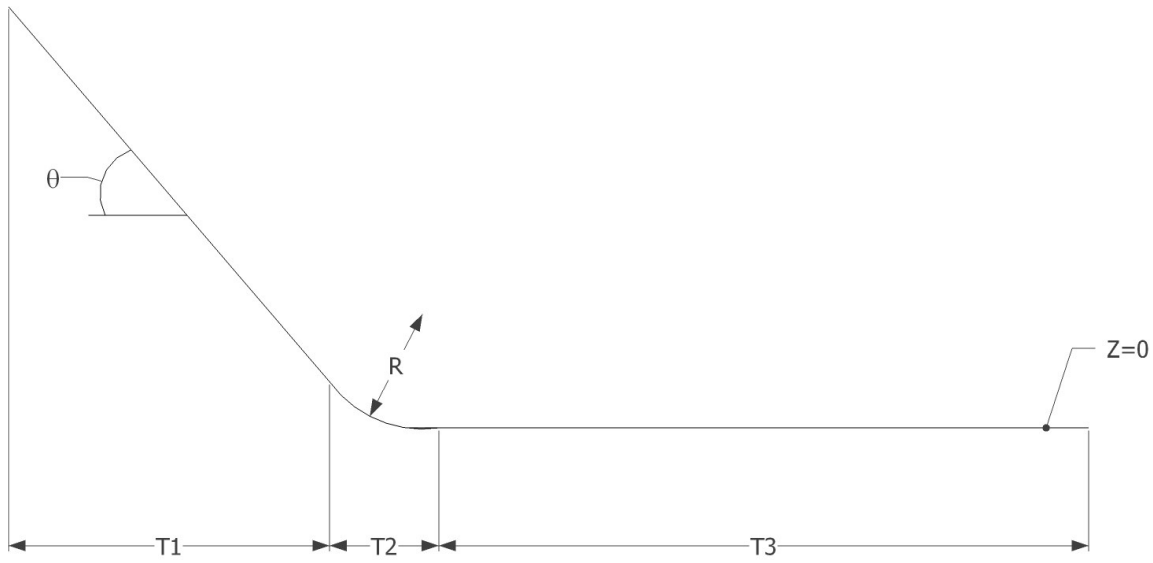

Figure 4.4.4 Geometrical scheme for ictop=2.

4.4.2.1.4 Topography with two different angles of slope, *ictop=3*

If the soil has two sections of different slope whose elevation can be obtained by a linear law depending on X coordinate, the *ictop* index can be put equal to *3*. In addition to the values of X maximum and minimum, Y maximum and minimum and to the number of nodes to discretize the topography, some other geometrical values have to be defined (Figure 4.4.6). All the values are expressed in meters and the reference system is local.

```
ictop
3
Xmin   Xmax   Ymin   Ymax
 0.0    800.0  -10.0   10.0
npoigx     npoigy
 20           2
 x0       d0       x1       d1       x2       d2
-0.001  10.0     300.0    70.0     800.0    120.0
```

Figure 4.4.5 Topographical input file for ictop=3.

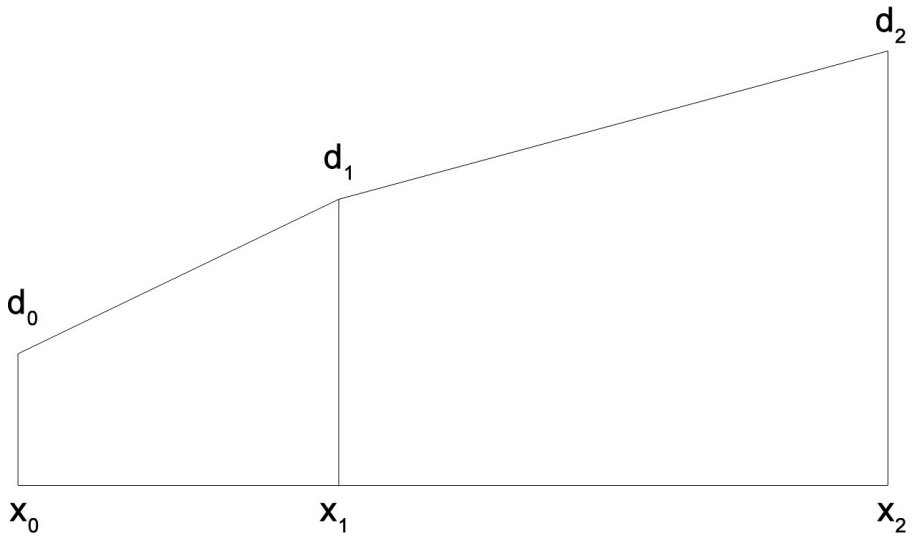

Figure 4.4.6 Geometrical scheme for ictop=3.

4.4.2.1.5 Topography with two different angles of slope, *ictop=4*

This index is used when the elevation of the topography can be expressed with a linear law depending on x values, in a similar way to the previews case. In this circumstance, the number of sections is higher: in fact, six segments have to be defined.

4.4.2.1.6 Conical topography, *ictop=5*

When the topography can be approximated to a conical shape, the input files has to include the X and Y limits, the number of nodes you want to consider. Finally, you have to explicate the radius and the elevation of the basal circle and of the top circle of the topography.

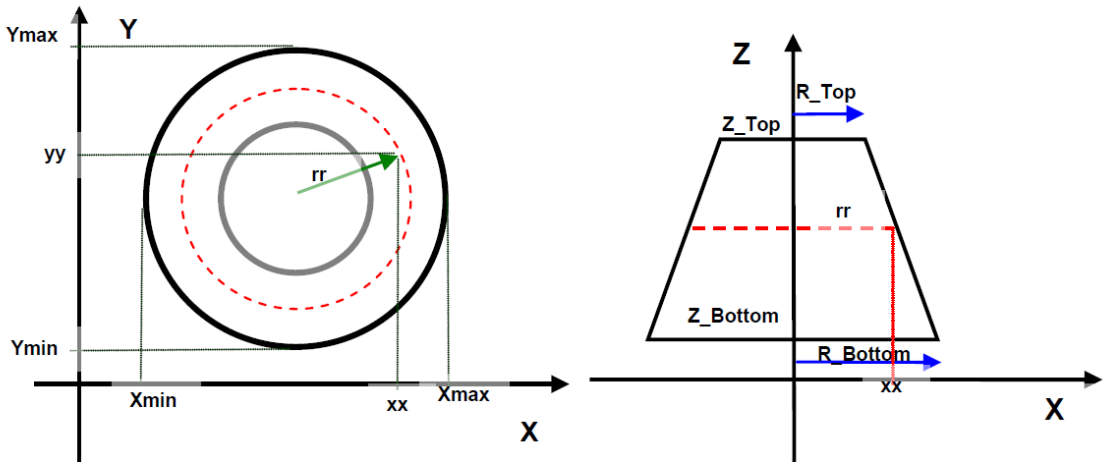

Figure 4.4.7 Geometrical scheme for ictop=5.

```
ictop
5
 Xmin    Xmax   Ymin   Ymax
100.0   900.0  50.0   850.0
npoigx    npoigy
 200        200
 R_top      R_bottom      Z_top      Z_bottom
 100.0        400.0       100.0        300.0
```

Figure 4.4.8 Topographical input file for ictop=5.

4.4.2.1.7 Topography obtained by a digital elevation model of the soil, *ictop=10*

Particularly when some real flow-like landslides take place, the event is recorded by a survey. The information about the topography, in these cases, are included in a DTM, so the nodes are expressed in terms of X, Y and Z coordinates. The "top" file is consequently completed writing the size of the mesh (deltax), the number of points included in the digital elevation model and all the coordinates obtained by the survey.

```
ictop
10
Number of points    deltax
      10200           10
Coordinate X     Coordinate Y     Coordinate Z
 1672006.72       5062875.00        548.21
 1672009.72       5062875.00        545.32
 1672012.72       5062875.00        543.10
 …                …                 …
 …                …                 …
 1669656.72       5065390.00        1224.33
```

Figure 4.4.9 Topographical input file for ictop=10.

4.4.2.1.8 Closing part of the topography file

Independently from the type chosen, it is possible to attribute different properties to the points, depending on the elevation of them. Two properties can be distinguished: the basal friction, indicating *basal type* equal to *1*, or erosion, indicating *basal type* equal to *2*. Once selected the properties, it has to be decided the law used. In Figure 4.4.10, for example, *type 1* means that Hungr erosional law (Hungr et al., 2005) has been selected. Finally, the altitude coordinates are explicated and the parameters imposed in those zones. All the variables g4-g16 are used to define different properties depending on the Z coordinate of the point.

```
terrain
 10
ntopo zones
 2
basal type  ZONE 1 -----------------
 2
basal law
 1
geomm:  type  Zmin     Zmax    g4  g5  g6
              1    750.00   859.99   0.  0.  0.
rheo:    Hungr  g9  g10 g11 g12 g13 g14 g15 g16
         0.0002 0    0     0    0    0    0    0     0
basal type  ZONE 2 -----------------
 2
basal law
 1
geomm:  type  Zmin      Zmax      g4  g5  g6
              1    860.00   2000.00    0.  0.  0.
rheo:    Hungr  g9  g10 g11 g12 g13 g14 g15 g16
         0.0005 0    0     0    0    0    0    0     0
```

Figure 4.4.10 Example of the closing part of the topography file.

4.4.2.2 Parameters file

This file contains all the parameters that are used to model the problem. In "dat" file you can find the type of particles and the parameters that govern the system. Generally speaking, this file contain allow you to impose the rheological law you want to use, to define the parameters and to explicate all the variables of the problem.

4.4.2.2.1 First part of the parameters file

The first index you have to write allows you to choose between two possibilities: the *ic_SW_Alg* index equal to *1* call the coastal SW algorithm, while imposing the value equal to *0* call the landslide algorithm.

If the particles are being injected through a hydrograph, it is necessary to identify the type of data, i.e., whether it is a sheet of water or a flow per unit length. In all the cases reported, the *nhist* index is imposed equal to *0*.

Ndim allows you to define if the problem you are studying is 1D or 2D depth-integrated.

It has to be explicated, then, the type of material involved in the motion. The indices *ic_soil* and *ic_water*, indicate the presence respectively of soil and water: you have to write *1* to include the material, otherwise *0*. If there are virtual particles, you have to write *1* in the *ic_vps* index. Finally, to switch on the boundary conditions you have to use the index *ic_abs*. Practically, you can impose null velocity perpendicularly to some segments, or define some absorbent boundary. If you write *ic_abs=1* it means that you turn on the absorbent boundary conditions, but not the conditions about

the velocities; *ic_abs=2* imposes both the conditions; *ic_abs=3* creates a condition on the velocities but not on the position of the particles.

```
1
test_01
ic_SW_Alg
   0
nhist
   0
ndim
   2
 ic_soil  ic_water  ic_vps  ic_abs
    1         0         0        0
```

Figure 4.4.11 First part of the parameters file.

4.4.2.2.2 Second part of the parameters file

The following part of the parameters file is used to define the type of source mass that will move during the landslide. The mass can have various shapes and changing the index *Soil_unkno* you can define the one you want to use. Basically, the options that can be selected are:

- *Soil_unkno=1* if the source mass is a cylinder or a cone;
- *Soil_unkno=2* if the mass can be represented with a multilinear shape depending on x;
- *Soil_unkno=3* to generate initial data in a 1D dam-break problem;
- *Soil_unkno=4* if the mass is a 3D cloud of points;
- *Soil_unkno=6* if the mass is contained in a external file, with extension ".pts";
- *Soil_unkno=9* if you are considering a sliding mass;
- *Soil_unkno=11* if the mass have a rectangular shape;
- *Soil_unkno=12* when the source is an ellipse.

Depending on this selection, you have now to indicate the geometrical characteristics of the mass or, if *Soil_unkno=6*, the name of the source mass file. Below there will be explained the case used in this thesis.

4.4.2.2.2.1 Cylinder or a cone source mass, *Soil_unkno=1*

In Figure 4.4.12 it is reported the case of a cylindrical source mass (*Soil_unkno=1*). *h_inf_SW* is the minimum depth of the flow, while the fourth line is used to define the position of the center of the circle which forms the base of the cylinder, the radius and the height of the mass.

icdens is used to distinguish between cone and cylinder: if you use a normal cylinder you have to write 0, if you want to include a cone you have to choose *1*, finally if you use value equal to *2* you want to include a second cylinder, inside the first, that has a different height.

The last line is used to define the number of circle along which the particles are distributed, *nlinep*, and the factor of smoothing of the kernel, *facthsml*.

```
Soil unkno  h_inf_SW
      1          0.001
 xp0   yp0    rp0      hp0   icdens
 0.3    0.3   0.029   0.081     0
nlinep  facthsml
  30         3
```

Figure 4.4.12 Second part of the parameters file with Soil_unkno=1.

4.4.2.2.2.2 Source mass contained in a external file, *Soil_unkno=6*

In this case, the characteristics of the source mass are contained in an external file, with the ".pts" extension. The way of composing this file will be explained in §4.4.2.3.

```
Soil unkno  h_inf_SW
      6          0.001
pts file name
  test_001
```

Figure 4.4.13 Second part of the parameters file with Soil_unkno=6.

4.4.2.2.3 Third part of the parameters file

This lines of the ".dat" are used to define, if the *ic_abs≠0*, the boundary conditions or, if *ic_vps=1*, the virtual particles.

If the virtual particles are included in the model, you have to decide if you want to explicit them as groups (*Vps_type=1*) or segments (*Vps_type=2*). Then you can the details of those conditions: if you choose option 1, you have to define the number of groups and, for each group

- the number of particles,
- the area covered by each group,
- the height of the particles,
- the smoothing length of each particle.

When *Vps_type=2* you need to write the number of segments you want to include and therefore, for each segment

- the initial and final x and y coordinates,
- the separation distance of the particles in the segment,
- the heights at the ends of the segment.

The two final lines define the variables that are used to calculate the repulsion force that the virtual particles make against the mass particles, to prevent that they break through the solid border. Practically, the value of *vp_r0* has to be similar to the separation distance of the particles defined above, *vp_D* has to be of the same magnitude of the motion velocity. *vp_n1* and *vp_n2* are the formulation exponents, which are typically equal to 12 and 4 respectively (Figure 4.4.14).

```
Vps_type
    2
N_segments
    2
SEG 1   x0       y0       xf       yf
        0.10    0.20    1.50    0.50
        ds_segm
         0.005
        h0      hf
       0.05   0.05
SEG 2   x0       y0       xf       yf
        0.10    0.00    1.50    0.10
        ds_segm
         0.005
        h0      hf
       0.05   0.05
vpr_0   vp_D   vp_n1   vp_n2
0.005   0.010    12        4
```

Figure 4.4.14 Third part of the parameters file.

Alternatively, if you impose the boundary conditions with *ic_abs≠0* you have to explicate the number of segments, which can be arcuate or linear, the x y coordinates, the separation distance between the particles and the height of the boundary.

```
narcs   nsegs info for Vn0
 0        2
 SEG 1   x0     y0      xf      yf  //   ds    Zext
          0.   0.345   2.56   0.345
       0.002  10
 SEG 2   x0     y0      xf      yf  //   ds    Zext
          0.   0.515   2.56   0.515
       0.002  10
```

Figure 4.4.15 Third part of the parameters file.

4.4.2.2.4 Fourth part of the parameters file

This section is common to all the types of analysis. The characteristics of the SPH approximation are here written (Figure 4.4.16).

pa_sph is the index used to select the approximation algorithm for the pressure discretization: *1* indicates third symmetrical formulation while *2* indicates the second symmetric formulation. Normally the chosen value is *2*.

nnps is used to the type of search, one applies the general method (all pair search) that is used just working with a low number of particles, *2* the temporary mesh method, link listed algorithm.

sle is the index that control the evolution of the smoothing length: *sle=0* imposes constant smoothing length, *sle=1* call the updating of the smoothing length using the equation proposed by

Benz (1990), *sle=2* uses a simples way of updating. The evolution of the smoothing length is extremely connected with the goodness of the approximations and normally is fixed equal to *2*.

The type of kernel used for the smoothing is decided using the variable *skf*: *1* indicates a cubic spline, *2* is used for the Gaussian formulation and *3* for the quintic spline.

The last line of this part contains some logic variables, which can be true or false:

- *sum_den* is true when the height of the particles is calculated by the method of summation, as the sum of the heights of neighboring particles, considering a particular weight. The false value indicates that the calculation is realized using a continuous function, in which the relative velocities between the considered particle and those close are considered.
- *av_vel* is true when the calculation of an average velocity is imposed to correct the real velocity of the particle considered, changing its value to a one closer to the neighbor particles. This help to avoid the risk of penetration of the particles in the virtual particles or in the boundary.
- *virt_part* is useless, so it is always false.
- *nor_dens* is useless, so it is always false.

```
pa_sph   nnps  sle   skf
   2        2     2     1
sum_den    av_vel    virt_part    nor_dens
   T          T          F            F
```

Figure 4.4.16 Fourth part of the parameters file.

4.4.2.2.5 Fifth part of the parameters file

This part is fundamental to define the material properties, the rheological parameters and the pore pressure condition. The first two values are the gravity acceleration and the material density. All the other variables are depending on the rheological laws used.

c3 is a constant that varies its role on the basis of the rheology chosen. With *rheol=1*, i.e. turbulent Newtonian model, *c3* is the Manning coefficient. When *rheol=1*, i.e. Bingham with evolution, *c3* represent the evolution variable. If we select a frictional model (*rheol=5, 6, 7, or 8*) and *c3* is not zero, this parameter becomes the turbulence coefficient described by Voellmy (1955).

c4 is the erosion rate, when this characteristic has to be included in the model. The value of erosion is the one proposed by Hungr (1995) and depends on the initial and final volume of material involved in the landslide and on the length of the flow. This index can be used with *rheol=3, 5, 6, 7, or 8*.

rheol is used to select the rheological model to be used. It can be chosen between the following values:

- *rheol=1*: turbulent Newtonian fluid,
- *rheol=2*: laminar Newtonian fluid,
- *rheol=3*: Bingham's fluid with evolution,
- *rheol=4*: exact Bingham's fluid,

- *rheol=5*: frictional fluid,
- *rheol=6*: frictional fluid with consolidation,
- *rheol=7*: frictional fluid influenced by the curvature,
- *rheol=8*: frictional fluid with consolidation influenced by the curvature,
- *rheol=9*: Bagnold's fluid.

c6 is used with Bingham's model and represents the yield stress of the material.

c7 is the viscosity of the fluid when *rheol=3 or 4*.

c8 is the Manning coefficient if you select Bingham's law with evolution (*rheol=3*).

When a frictional model is chosen, it has to be fixed the tangent of the friction angle. *c9* and *c12* are the tangent of the internal friction angle final and initial respectively.

c10 is the minimum thickness of the flow interested by shear stress or friction. This parameter is common to all the models and normally it is very small.

c11 is used when a turbulent Newtonian fluid is considered and becomes consequently equal to $7/3$.

c13 is the exponential damping factor with time of the friction angle for frictional fluids. It is used for frictional fluids and Bagnold's fluid. If the consolidation is included, this parameter is connected with the consolidation coefficient c_v by the relation $c13 = \pi^2 c_v/4$.

When the dissipation of the pore pressure is considered not instantaneous but due to consolidation, *c14* is used and it is normally equal to the ratio between the height that is subjected to shear stress and the total height of fluid. This index is selectable only with frictional models.

c15 is the minimum value that can be reached by the depth of the fluid. It should be kept small to avoid approximation errors.

Finally, *icpwp* is an index that control the interstitial pressure. If the pressure is dissipated this index is equal to *1*, if not is equal to *0*.

When *icpwp=1*, *pwprel* is the index that explicates the relation between the pressure and the liquefaction pressure. It has to be added just when the pressure is dissipated.

grav	dens	c3	c4	rheol	c6	c7	c8	c9	c10	c11	c12	c13	c14	c15
9.81	1400.0	0.0	0.0	-	0.0	0.0	0.0	0.0	0.001	0.0	0.0	0.0	0.0	0.001
icpwp														
0/1														

Figure 4.4.17 Fifth part of the parameters file.

4.4.2.2.5.1 Bingham model, *rheol=4*

Selecting exact Bingham's fluid, two parameters have to be included in the input file: the yield stress (*c6*) and the viscosity (*c7*).

grav	dens	c3	c4	rheol	Tauy0	mu	c8	c9	c10	c11	c12	c13	c14	c15
9.81	1400.0	0.0	0.0	4	24.2	0.05	0.0	0.0	0.001	0.0	0.0	0.0	0.0	0.001

Figure 4.4.18 Fifth part of the parameters file for Bingham rheology.

4.4.2.2.5.2 Voellmy model, *rheol=7*

This selection call the Voellmy's rheology, including erosional effects. The frictional model chosen imposed the definition of the tangent of the friction angle (*c9* and *c12*) and the turbulence coefficient (*c3*). If you consider also the erosion following Hungr's law, the erosion rate has to be written in *c4*.

The use of a frictional model requires to decide if you want to distinguish an active and passive earth pressure coefficients or not. If yes, you have to defines the two values.

grav	dens	turb	E	rheol	c6	c7	c8	tanfi1	c10	c11	tanfi0	c13	c14	c15
9.81	1400.0	200.0	0.002	4	0.0	0.0	0.0	0.20	0.001	0.0	0.20	0.0	0.0	0.001
K0 activated?														
0														

Figure 4.4.19 Fifth part of the parameters file for Voellmy rheology.

4.4.2.2.6 Sixth part of the parameters file

The last part of the parameters file contains the indices used to define the outputs you want to export from the model. Practically, if you write *1* to respective index, you include the variables in the output file.

You can export the height of material, the displacements, the velocities, the erosion height and other variable (Figure 4.4.20).

GID filter	1.hs	2.disp	3.v	4.Pw	5 eros	6.Z	7.hrel	8.hw	9.eta	10.hs+hw	11.	12.
	1	0	1	0	1	1	0	0	0	0	0	0

Figure 4.4.20 Sixth part of the parameters file, selecting of the output variables to export.

4.4.2.3 Source mass file (optional)

If *Soil_unkno=6*, the information about the source mass is contained in ad external file, with ".pts" extension.

npoin source	deltax	facthsml
9387	2	2
X	Y	h
1668194.505	5065168.5	2.52
…	…	…
…	…	…

Figure 4.4.21 Source mass file.

First of all, you have to indicates the number of points composing the mass, the size in x and y direction to generate the mesh (*deltax*) and the factor of smoothing of the kernel, *facthsml*.

Then you have to write the x y coordinates of the starting mass and the respective heights of material.

4.4.2.4 Master file

The last file used by the code to run the simulation is called master file. It contains the integration options, such as the integration time step and the total time for the simulation.

To run the SPH integration approximation you have to select *1* in the *if_sph* index. Then *SPH_problem_type=1* identify the shallow water conditions and *SPH_t_integ_Alg=4* defines the 4° order Runge Kutta algorithm for integrating in time.

Then you have to explicates the name of the parameters file and the time step *dt* for the integration, the end time for the simulation and the maximum number of increments of time step if it is chosen to use an adaptive time step.

The indices called *print_step*, *save_step* and *plot_step* are used to define the output time steps. With prin_step you define the time interval used by the code to print the results on the screen. The others two indices play a similar role and are used to determine the time interval to print the results on the output file.

Finally, *ic_adapt* is used to eventually to use an adaptive scheme for the determination of the time step, during the calculation.

```
1
test_001
if_sph if_gfl if_tgf
  1          0      0
SPH_problem_type   SPH_t_integ_Alg
            1                          4
sph problem name
test_001
dt         time_end    maxtimesteps
0.1         1350.00          27000
print_step   save_step   plot_step
   500           1000          1000
dt_sph  ic_adapt
   0.1         0
Ntime curves     max pts in them
       0                        6
dt   time_end   maxtimesteps
-1      2.00           100000
```

Figure 4.4.22 Master file.

4.4.2.5 Output files

Once completed the simulation, the code gives out some files containing the results. The main output file is the ".post.res" one, which includes the calculation results depending on the variables

you selected in the last part of the parameters file. The information are expressed indicating the number of node and the respective measurement.

The “post.msh” file contains the information about the geometry of the system, the number of nodes and elements in which the topography has been discretized and the relation between the x, y, z coordinates and the node index.

The “master.chk” file summarizes all the integration selections chosen. Finally, the “.chk” file includes all the boundary conditions selected and the variables that have to be exported by the calculation.

5 NATURAL PHENOMENA AND LABORATORY TESTS

5.1 INTRODUCTION

In literature, many experiments have been made to collect a useful quantity of information about the behavior of a flowing mass. Among all these tests, two main groups can be easily recognized: the small-scale and the full-scale ones. Obviously, these two categories present both advantages and disadvantages.

On one hand, a small apparatus is easy to use, just a few quantity of material has to be used in each test and many measurements are immediately obtained. The simpler is the experiment, the more you can easily repeat it and collect precise and reliable data. Major and Pierson used a wide-gap concentric cylinder viscometer to perform a huge quantity of tests and obtained interesting information about the debris flow rheology (1992). Other experiments concerning the collapse of a simple volume of material on a plane were made (Davidson et al., 2000; Lajeunesse et al., 2004; Gabrieli et al., 2013). Many authors used laboratory flume experiments to analyze the behavior of a flow-like landslide small scale, investigating the main geometrical characteristics and the rheological parameters obtainable (Bagnold, 1954; Mainali & Rajaratnam, 1994; Parsons et al., 2001; Egashira et al., 2001; Iverson et al., 2004; Barbolini et al., 2004; Kaitna et al., 2007; Cochard & Ancey, 2009; Haas et al., 2015; Hürlimann et al., 2015).

On the other hand, a second family of experiments is the full-scale one. In this case, the advantages consist in a greater similarity to a real case, reducing the scale-problems and taking into consideration boundary condition that are commonly find in field. However, a huge quantity of material has to be used for each test. It is difficult to have a full repeatability analysis and the costs concerned to the use of a similar apparatus are not negligible. Anyway, this kind of experiments have been used by some authors to compare various kinds of material used in big experimental apparatus to investigate the dependence of the behavior of the mass in motion on the material contents and on the boundary conditions of the system (Iverson et al., 2010; Iverson, 2015; Zhou et al., 2015).

In the following paragraphs a short overview of what has been done in the last decades will be presented.

5.2 SMALL-SCALE EXPERIMENTS

5.2.1 The role of granular and cohesive contents in a collapsing mass

The material contents governs the flow of a collapsing mass. Cohesive and granular materials cause different mechanisms of momentum exchange and therefore change the dynamical and geometrical characteristics of the motion.

Two simple cases are reported above to underline how the nature of the mass influences its behavior.

The first case considered concerns the experience of Lajeuness et al. (2004). Basically, a Plexiglas cylinder filled with a granular mass was suddenly lifted, causing the breakdown of the material. In

this way, the granular mass spreads on the horizontal plane until it comes to rest and forms a deposit.

The topic of this experiments lead to understand, in such a simple geometry, the role of the granular content in the deposit shape. The authors wanted to correlate some typical behavior of the material with the initial dimensions of the source mass.

In all other experiments, a fast camera was carefully aligned along the horizontal direction to acquire side views of the granular mass. The camera was then connected to a computer and the digitized images were processed in order to extract the profiles $h(r,t)$ of the granular mass throughout time t, h being the local thickness and r the radial distance to the axis of symmetry of the granular mass. As the granular mass spreads axis-symmetrically, its profile provides enough information to fully characterize its three-dimensional shape. A similar experiment represents the first case study considered in this thesis.

The simple scheme of the experimental apparatus can be understood in Figure 5.2.1. Several series of experiments were conducted: the main goal was the comprehension of the effect of different control parameters namely, such as the released mass M, the initial aspect ratio of the granular column defined as $a = H_i/R_i$, the properties of the substrate on which the beads are spreading and the bead size. Clearly, the variables H_i and R_i identify the geometrical characteristics of the column of material, being respectively the height and the radius of the *i*-case. The authors used different basal friction, changing the material on which the collapse took place. They considered also an erodible bed, composed by the same material that was contained in the cylinder, in order to identify the influence of granular material on the horizontal plane.

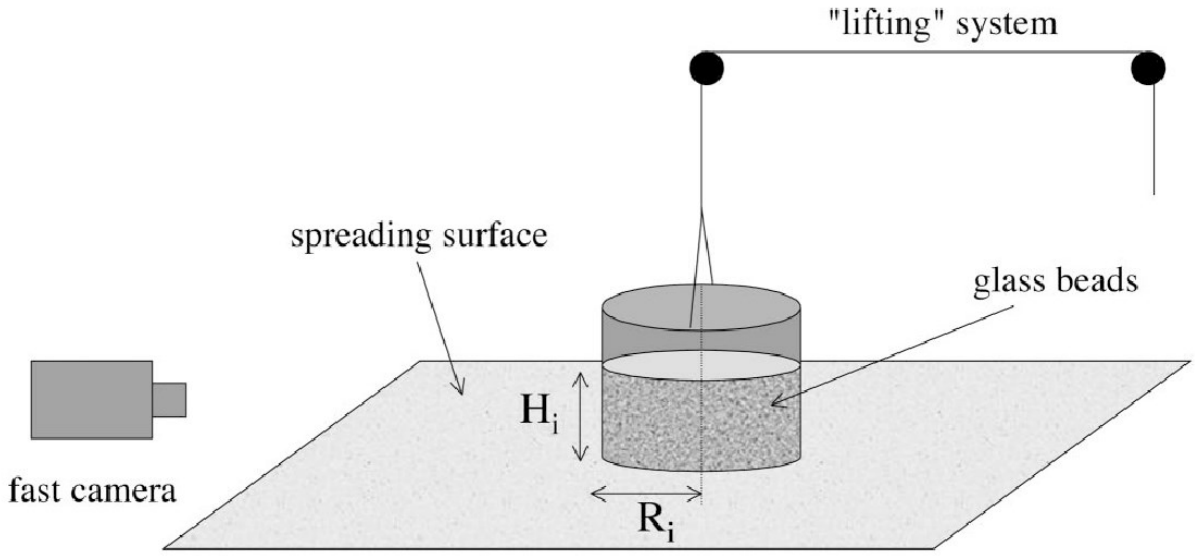

Figure 5.2.1 Scheme of the experimental setup of Lajeuness.

They considered mainly two regimes, function of the aspect ratio a. In the first regime, observed for $a \leq 3$, the granular mass spreads through an avalanche of its flanks dissipating only a fraction of the initial gravitational energy and producing either truncated cone or conical deposits. In the

second regime, observed for $a \geq 3$, the upper part of the column descends, conserving its shape, while the foot of the pile propagates radially outward. They also found that, for a given substrate and bead size, the flow dynamics and the shape of the obtained deposits are found to be independent of M but to vary only with the initial aspect ratio a.

The overall shape of the deposit depends only slightly on the substrate properties, smooth or rough, rigid or erodible and on the bead size when a is small. However, this dependency progressively increases with a to become eventually important in the second regime. The same dynamical regimes and deposit morphologies are recovered for the same range of a, independent of the substrate properties or the bead size. They attributed the independence of quantities such as the rescaled deposit radius R_f/R_i, the rescaled spreading velocity $v/\sqrt{gR_i}$, and the fraction of energy dissipated during the flow with respect to the substrate properties is due to the fact that the flow develops near the free surface of the granular pile. As a result, the flow dynamics is essentially controlled by grain/grain interactions independent of the underlying substrate properties.

The simple case reported is useful to understand some typical aspects of the behavior of a mass with respect to the materials content. The simplicity of the test on one hand allows to perform numerous repetitions and to collect a huge quantity of data. On the other hand, however, the more the system is simple, the less the material can be fully characterized.

The second case described wants to understand the role of a cohesive material insertion in mass flowing. To study this, Kaitna et al. (2007) considered the flow of artificial and natural mixtures of particles with different grain sizes and fluids of varying viscosity in a rotating drum. The experimental setup is slightly more complicated, but still maintains a simplicity that makes it possible to accurately control the phenomenon.

From these tests, it was possible to gain insight in the bulk flow behavior of the different mixtures ranging from dry solids and granular suspensions, to viscous fluids and to test the applicability of different modelling approaches to describe the identified flow regimes.

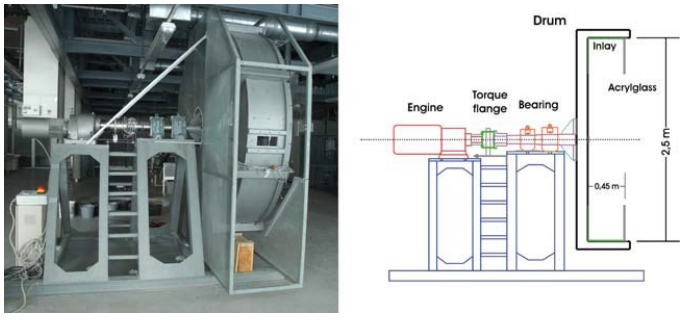

Figure 5.2.2 Left: side view of the rotating drum, right: cross section of the experimental setup

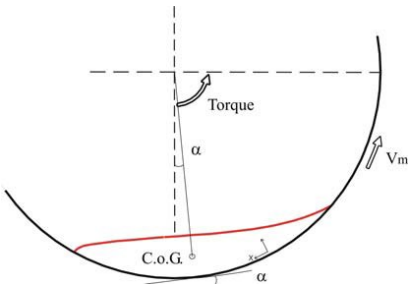

Figure 5.2.3 Sketch of deviation angle of centre of gravity (c.o.g.) from the vertical

A vertically rotating flume (Figure 5.2.2) has been constructed to study the flow of artificial and natural mixtures of particles with different grain sizes and fluids of varying viscosity. The advantage of such a setup is that observation of a stationary surge is possible over an extended period of time.

The experiments have been carried out in a rotating drum with a diameter of 2.46 m. The inner surface of the circumference is skimmed to avoid possible flow instabilities due to irregular bottom curvature. The channel section has a width of 0.45. The rectangular cross-section is confined on one side by stainless steel, on the other side by acrylic glass to allow observations from the side. In order to avoid slip at the flume bottom the inner circumference is roughened by a synthetic 5x5mm mesh of approximately 1mm height.

The total flow resistance of the mixture, i.e. bottom shear stress and lateral shear stress at the channel walls, has measured with a torque flange, which is directly installed at the rotation axis of the drum between the bearings and the engine. The average shear stress of the mixture exerted on the channel bottom may then be estimated by assuming a uniform distribution of bottom shear stress and a triangular shear stress distribution on the sidewalls. Surface velocity was finally determined from digital video analysis.

Practically, Kaitna et al. observed that rheological properties of a slurry flow are altered by addition of coarse particles to the 'viscous fluid'. Thus, rheological parameters determined for debris flow material of limited grain size do not represent the bulk rheological behavior of the complete natural material. For debris flow hazard assessment, based on viscoplastic rheological simulation models, it is necessary to know the rheological parameters of the prototype debris flow. They affirmed that for material mixtures with a high content of fines (particles smaller than 0.04 mm represented 9% of the total material) a rheological interpretation using the rotating drum was possible. It has to be noticed that these tests have been restricted to mixtures including sediment particles less than 5 mm in diameter. Finally, effects like settling and accumulation of coarse particles have been observed in the rotating drum for mixtures of low sediment concentration.

5.2.2 Flume experiments

Many researchers used a channel or a chute to study different issues concerning flow-like landslides. Using this type of setup, in fact, it is possible to evaluate various aspects that have to be considered in rapid landslides.

Authors have dealt characteristics such as erosion, slope changes and impact forces against structures. Furthermore, many researchers have also investigated the study of the correlation between the nature of the components of a mass flowing and its geometrical and dynamical behavior. Sometimes, the final goal is to obtain information in laboratory helpful to analyze then a real debris flow.

Actually, various strategies are used to understand as much as possible how the material components, the boundary conditions and the geometrical characteristics influence the motion of a mass.

5.2.2.1 Erosional aspects

Egashira et al. (2001) took into consideration the effect of the entrainment of bed material into debris flow. Their main goal was to propose an empirical formulation that allow you to include in a numerical model the effect of erosion during a flow. He performed many tests with a geometrically simple physical apparatus to understand the relationship between erosion and the sediment size.

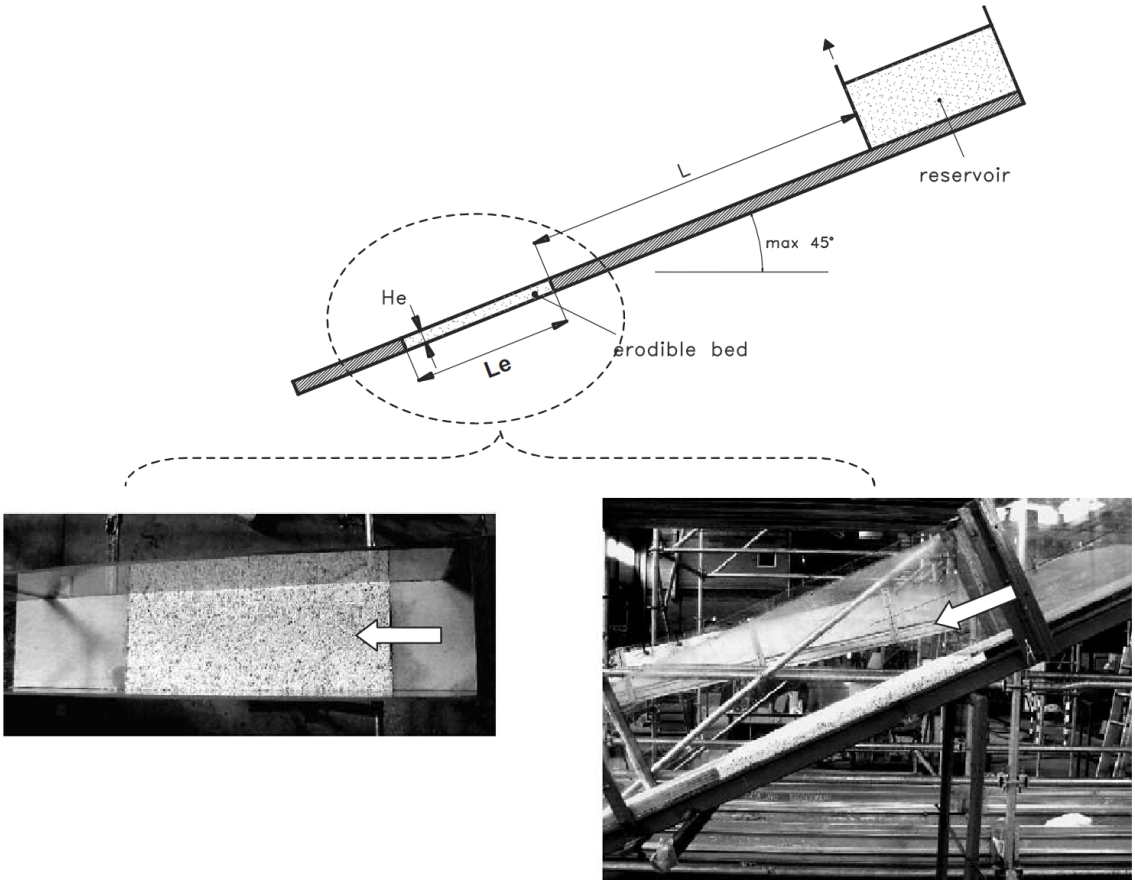

Figure 5.2.4 Barbolini's experimental setup, with close-up on the erodible part.

Barbolini et al. (2004) used a similar approach to study the mechanics of erosive processes characteristic of snow avalanche flows. In their experiments, a dry granular mass was instantaneously released on an inclined chute where an erodible portion of bed had been created. The distinction between the incoming flow and the erodible material was made easier using different colors for the related. When the granular flow arrived, it dived into the erodible bed and pushed it ahead. Consequently, the erodible mass progressively lost its structure and was mobilized and entrained into the flow particles. Their final goal was to calculate an erosion rate that was strictly connected with the inclination of the slope (Figure 5.2.4).

In their experiments, Barbolini et al. observed that ploughing at the front was the main mechanism responsible for the erosion of the bed material. Abrasion at the surface of separation between the incoming flow and the erodible layer was also observed, but this mechanism was mainly responsible for the inclusion of eroded particles into the moving material.

5.2.2.2 Impact forces against structure

An interesting theme often studied concerns the impact forces due to a debris flow impacting again a structure. Canelli et al. (2012) conducted some experimental tests with the use of a specifically created flume (Figure 5.2.5), in order to obtain detailed knowledge of the mechanical aspects, and to analyze the dynamics of the impact of a debris flow on different types of structures.

The tests conducted on rigid barriers have led to the conclusion that a debris flow thrust can be estimated using the equilibrium of the quantity of motion, corrected with a suitable safety factor that varies between 1.5 and 5.

This safety factor is connected to the possibility of the formation of a vertical jet-like wave after the impact. Although unlikely, the occurrence of such a phenomenon would lead to an underestimation of the design thrust value, and therefore to an incorrect design of the barrier. For this reason, the authors said that during the design phase, the type of flow (channelized, free surface) should be correlated to the type of barrier installed (rigid or filtering) and to the possibility of applying a homogeneous fluid scheme. The impact of single or multiple masses of large dimensions (boulders) could in fact generate impulsive forces on the barrier of some orders of magnitude higher than those estimated utilizing an equivalent fluid scheme.

5.2.2.3 Effects of material content changing and geometrical characteristics

Commonly, authors try to understand the effect of debris flow composition on his behavior. Practically they are interested in understanding how the runout, the depositional mechanisms, and the deposit morphology changes with the content of the material that flows. The more this can be understood, the more accurately a debris flow can be predicted and the unacceptable area of risk can be identified.

Mainali & Rajaratnam (1994), for example, generated a steady uniform flow of a highly concentrated sand-water slurry, initially, without mixing any clay or silt-size particles. The second phase of their study included silt- and clay-sized particles that could then be compared to the sand-water slurry flow to delineate the role of the fines in a debris flow. They collected a huge quantity of measurements in terms of velocity and concentration profiles. These measurements are compared with the predictions of dilatant fluid as well as laminar as turbulent Newtonian fluid models. The large values of Reynolds number observed an almost all the tests suggests that the flows are prevalently turbulent. Turbulent dispersion of particles is more pronounced for smaller grain sizes. The linear velocity profiles seem to suggest that the increase in shear with depths is the result of viscosity changes rather than changes in the velocity gradient as indicated by dilatant fluid models. For the larger particles there is a tendency toward stratification resulting in the suppression of turbulence.

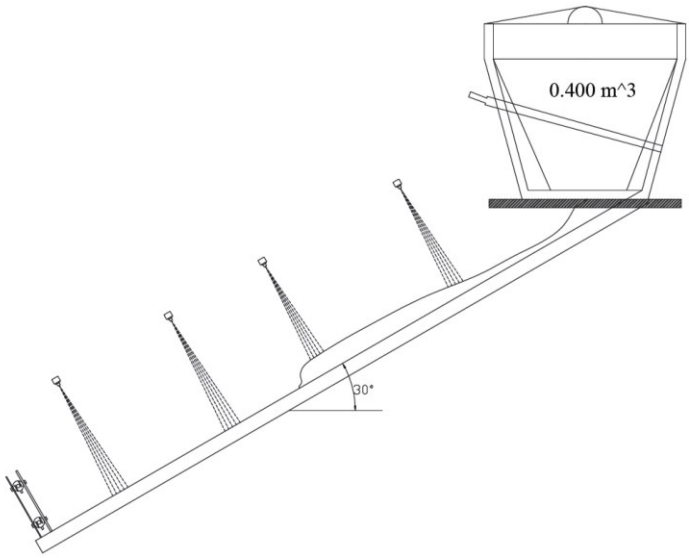

Figure 5.2.5 Schematic representation of the Canelli's flume.

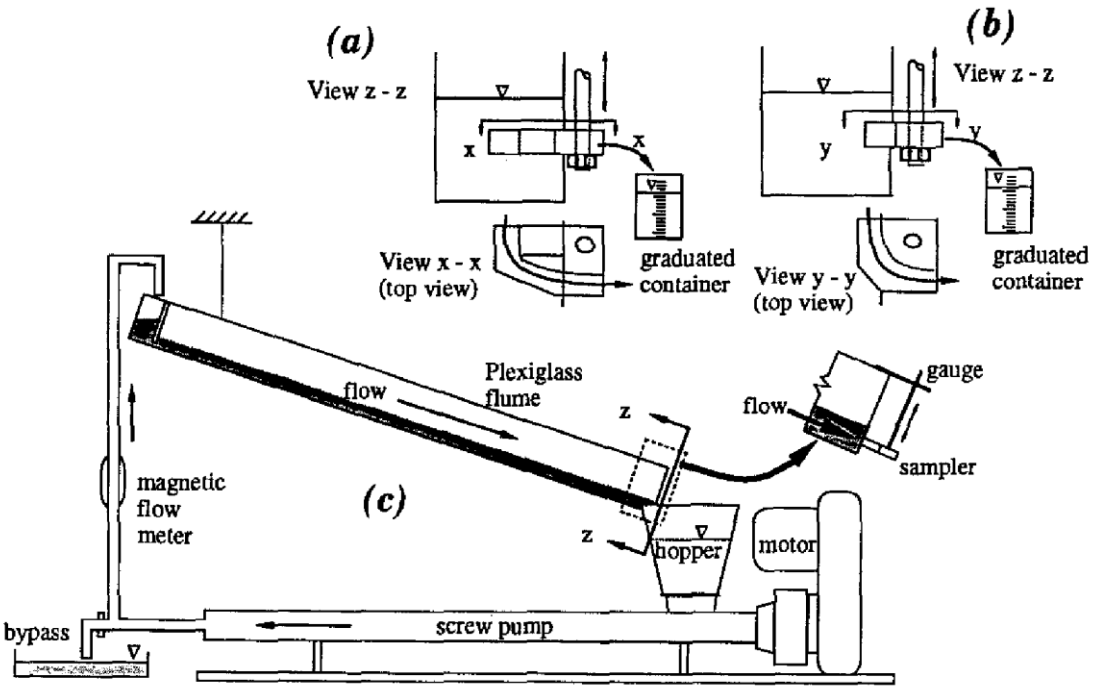

Figure 5.2.6 Mainali & Rajaratnam's experimental setup and sketch of samplers

Haas et al. (2015) experimentally created small-scale debris flows having self-formed levees and a marked depositional lobe, with flow behavior, deposit morphology, and sediment sorting that were similar to many natural debris flows (Figure 5.2.5).

The width-to-depth ratio of small-scale experimental debris flows was in the range of natural debris flows. Debris flow runout was also in the range of natural debris flows, but flows were relatively short due to high friction. The authors found that the composition plays a fundamental role on depositional mechanism, runout, and deposit geometry. For example, debris flow runout increases with an increase in channel slope and width, outflow plain slope, debris flow volume, and water fraction. Increasing coarse-material fraction increases runout, probably increased flow confinement by levee formation and grain collisional forces. However, too large coarse-material concentrations cause large frontal accumulations of coarse debris that reduce runout distance. An increase in clay fraction enhances runout, most likely because of better-retained excess pore pressures. However, too large proportions of clay (>0.22) make debris flows highly viscous so that runout is reduced. Deposition of clay-rich debris flows is likely mainly driven by viscosity and yield strength.

The debris flow composition strongly control the geometrical characteristics of the deposit. In fact, the coarse-grained, clay, and water fractions all have a profound effect on lobe height, lobe width, and levee height. On the other hand, effects of initial conditions of topography (i.e., outflow plain slope, channel slope, and width) and volume are negligible.

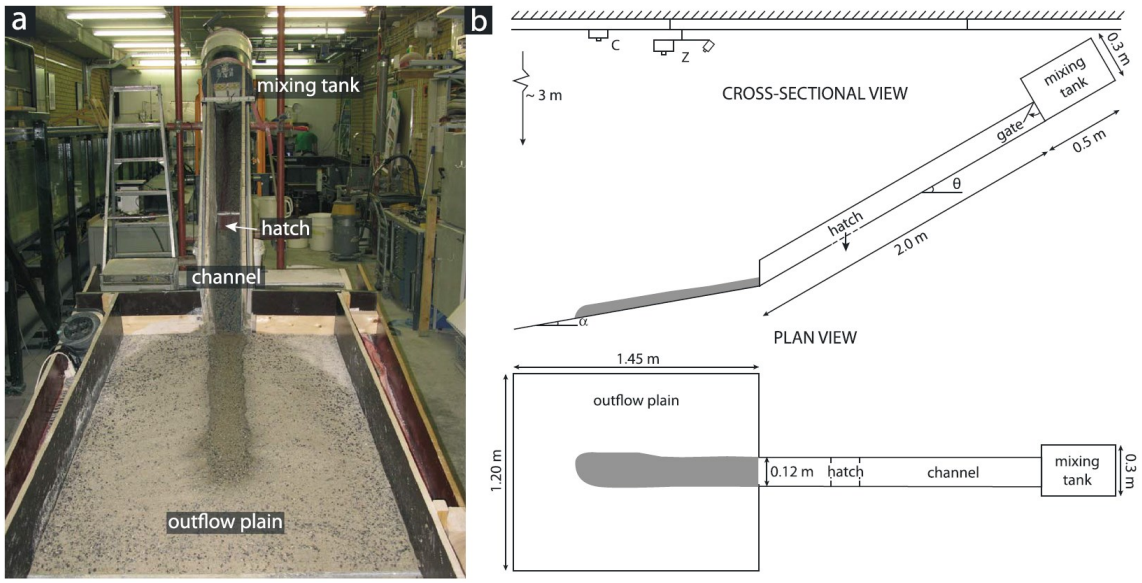

Figure 5.2.7 Experimental flume setup of Haas et al. (a) Photograph. (b) Schematic overview.

In 2009 other authors (Cochard & Ancey, 2009) analyzed dam-break problems for viscoplastic problems, changing the slope inclination from 0° to 18° and recording the behavior of the material in time. They used image processing technique o accurately reconstruct the free-surface evolution of fixed volumes of fluid suddenly released a plane. During their experiments, Cochard and Ancey worked with four concentrations of a viscoplastic material, with a rheological behavior that was closely approximated by a Herschel–Bulkley model for a fairly wide range of shear-rates. They confirmed first this point by some viscometer tests. They did not include any lateral boundary conditions so the material can flow freely on the inclined aluminium plate and then on the horizontal runout zone.

They observed that almost all the profiles they obtained were similar one another. Lateral spreading occurred in the first instants, in the inertia-dominated regime, then became negligible. Because of yield stress, part of the fluid was abandoned at the lateral margins and formed levees that confined the yielded region, giving the appearance of a self-channelized flow. Surprisingly enough, the free surface became increasingly corrugated over time owing to “valley” formation in the stream-wise direction.

5.2.2.4 Characterization of real debris flow material

To characterize a real debris flow, two main strategies may be used. On one hand, data collected from field observations are the basis for developing, testing, and improving predictive methods. On the other hand, laboratory tests on small-scale models are another suitable approach for studying debris-flow runout under controlled conditions and for developing predictive equations.

In that sense, some authors perform flume tests with material directly collected from real debris flows sites, to evaluate its behavior in small-scale and understand the main characteristics of the motion.

D'Agostino et al. (2010) were interested in the comprehension of the behavior of a real debris flow occurred in the Dolomites. They investigated the shape of the deposits of a rapid landslide depending on the slope of the experimental apparatus. The laboratory tests were carried out using debris-flow matrix collected from lobes in the Fiames fan area. They considered some tests performed on a 2m×1m tilting plane with an inclination between 0° and 38°, on which a steel tank with a removable gate was installed. A fixed horizontal plane 1m long, with an artificial roughness to simulate the natural basal friction, served as the deposition area (Figure 5.2.8). Dynamic fan formation was simulated using an artificial flume installed on the tilting plane.

The maximum runout distance and maximum lateral width of deposit were directly measured during the tests; the area of deposit was measured from orthophotos of the deposition area.

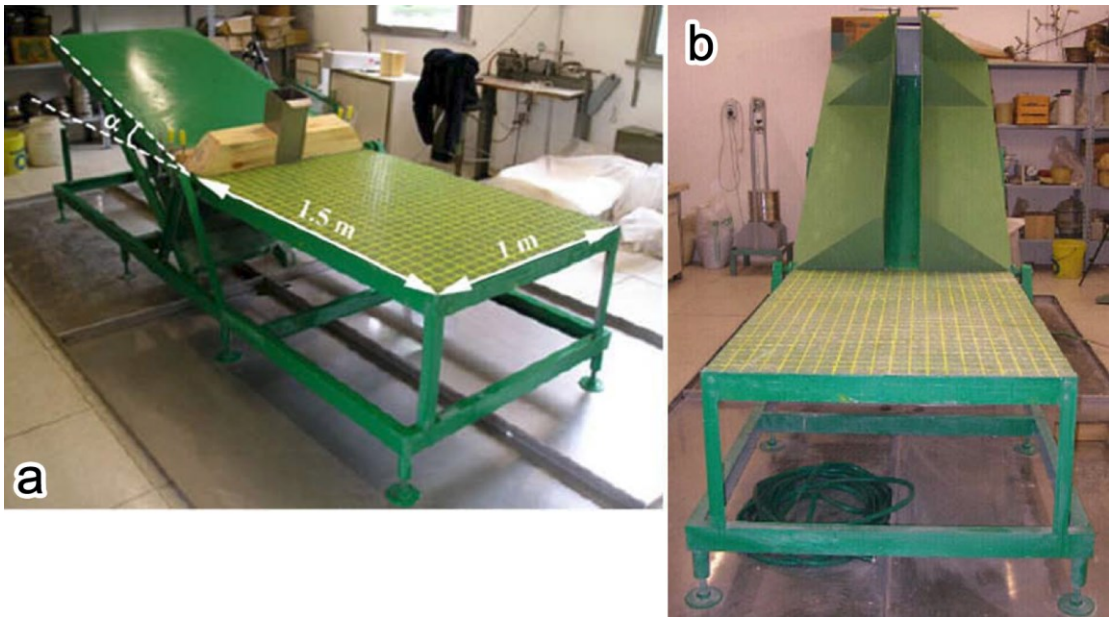

Figure 5.2.8 Experimental flume setup of D'Agostino et al. (a) Tilting-plane rheometer: set-up for quasi-static tests. (b) set-up for dynamic tests.

The topic of their work was to correlate factors such as the total drop, the runout distance, the upstream point of the mass and the angle of frictional energy line, with the slope inclination and various material content. The information about the behavior of this mass are then used to analyze the real debris flows. Although scale issues cause major problems in small-scale laboratory studies of debris flows, integrating laboratory tests with field documentation of debris flows proved promising for studying these hazardous phenomena.

The strategy of simplifying the case study, using the material of a real debris flows for simpler laboratory tests, is commonly applied.

Hürlimann et al. (2015) has recently performed something in that sense. They considered a debris flows occurred in Switzerland and performed some laboratory experiments to understand the dependence of the geometrical characteristics of the deposit on three different factors: soil-water content, grain-size distribution and mobilized volume.

The laboratory experiments revealed a strong influence of the water content on the runout distance of the hillslope debris flows. Even a very small increase of water content (e.g. 1–2%) markedly increased the runout distance because of the exponential relation between water content and runout. The effect of different grain-size distributions was also analyzed and showed that an increase of clay content (e.g. 5%) considerably reduced the maximum runout. A positive relation between bulk volume and runout was observed, but with a smaller influence than the other factors.

Finally, some authors used flume experiments to correlate the behavior of the flow with Bagnold, Savage and friction numbers, to eventually verify their applicability in the flow behavior prediction. Even if these numbers are sometimes difficult to evaluate in real phenomena, it can be useful to understand the eventual connection existing between these variables and the characteristics of the flow.

The results obtained by Bettella et al. (2012) suggest that these dimensionless numbers, calculated at the runout phase, are correlated to the deposit shape. On the other hand, their values calculated at the full motion phase are not always correlated to the flow characteristics during the runout phase and then caution is necessary to forecast the flow behavior at deposition. Volumetric concentration and grain size distribution are confirmed as key additional factors to classify and predict the flow behavior along with the three dimensionless parameters.

5.3 REAL-SCALE EXPERIMENTS

Sometimes authors found scale problems working with laboratory tests. Recently, Iverson took into consideration the crucial role in designing experiments aimed at understanding the behavior of landslides, debris flows, and other geomorphic phenomena involving grain-fluid mixtures played by scaling (Iverson, 2015). He noticed that commonly the goal of physics experiments is generally to distil a phenomenon to its simplest possible form. For that reason, such experiments usually employ grains consisting of identical rigid spheres or homogeneous material.

By contrast, in real landslides and debris flows the grains are typically composed of irregular rock fragments with sizes that span many orders of magnitude. An assemblage of incompressible spheres in contact with one another has no elastic component of compressibility because any volume change must be accommodated by irreversible slip at grain contacts. Furthermore, an assemblage of irregular, incompressible grains can exhibit a finite bulk elastic compressibility because some porosity change can be accommodated by elastic shear distortions of angular grain contacts.

Other difficulties in designing relevant landslide and debris-flow experiments arise as a result of the physical properties of the pore fluid. Sediment mixtures commonly undergo significant porosity changes as they are loaded or as they shear, and these porosity changes produce pore-pressure changes that are proportional to the pore-fluid viscosity.

Miniaturized experiments consequently exhibit pore-fluid pressure effects that are too small and pore-fluid shear resistance effects that are too large, relative to those exhibited in large-scale field phenomena. Iverson affirmed that even if small-scale experiments can contribute greatly to understanding of landslides and debris flows, experiments must be designed with care, and experimental results must be interpreted with a healthy dose of skepticism. In literature, some big-scale experiments are available, even if they are fewer. Iverson at al. (2010) collected an interesting

Figure 5.3.1 Photograph of a 10m^3 debris flow descending the USGS debris-flow flume at the H. J. Andrews Experimental Forest near Blue River, Oregon.

and big database of 28 large-scale experiments. They changed the basal boundary conditions and sediment mud contents.

Sensor measurements of evolving flow thicknesses, basal normal stresses, and basal pore fluid pressures demonstrate that debris flows in all subsets developed dilated, coarse-grained, high-friction snouts, followed by bodies of nearly liquefied, finer-grained debris.

Imposed differences in bed roughness and sediment mud content in the experiments cause systematic differences in flow dynamics, some expectable and some surprising. Debris flows on smooth beds travel about 30 percent faster but no further than flows on rough beds, and mud-rich flows run out nearly twice as far as mud-poor flows, even though both reach similar peak speeds. Mud reduces net flow resistance by promoting persistence of high pore pressures in flow bodies. Bed roughness increases flow runout by promoting development of coarse-grained flow fronts and gravel-rich lateral levees, which channelize flow and reduce loss of downslope momentum.

Grain-size segregation in debris flows is more than a source of distinctive morphological and sedimentological features. The large size of grains in flow fronts favors inertial grain collisions that increase frictional resistance, and the presence of large intergranular pores implies the existence of high hydraulic diffusivities. High diffusivities facilitate dissipation of excess pore fluid pressure and drainage of pores, adding further to local flow resistance.

Surface waves similar to classical roll waves occur in all of our experimental debris flows. They develop gravelly fronts resembling the main flow front, and also develop finer-grained trailing bodies.

Iverson et al. basically affirm that their data lead them to conclude that many textbooks misrepresent debris-flow mechanics almost entirely. They commonly attribute the distinctive behavior of debris flows to a fixed, non-Newtonian rheology and they generally assume that flows

are laminar and subject to no-slip boundary conditions, such that effects of bed roughness are negligible. In contrast, their data demonstrate that the central feature of debris-flow mechanics is heterogeneous two-phase flow, in which boundary friction is crucial and local flow resistance is a variable that evolves together with global flow dynamics. Reproducibility of this emergent behavior implies that, although debris-flow mechanics are complex, the notion of "perfect" debris-flow behavior is not entirely illusory.

Recently, Zhou et al. conducted some experimental tests to better understand the process of sediment erosion and entrainment on the channel bed and the formation of debris flows (Zhou et al., 2015). After the catastrophic debris flows that occurred in Wenjia Gully (Wenchuan Earthquake Area), China on August 13, 2010, they decided to investigate the role of erosion in the phenomenon, using a big scale apparatus. A large flume was constructed near the Dongchuan Debris Flow Observation and Research Station, in the Dongchuan District of Yunnan Province, China. The flume consists of a straight concrete channel 45 m long, 0.7 m wide and 1.4 m deep, inclined at 12° to the horizontal. At the lower end of the flume, the slope opened onto a horizontal concrete plane. The flume walls and runout area are constructed of smooth cement floors. A container with a capacity of 12 m^3 is connected to the top of the flume through a channel with two rows of saw-teeth, which dissipated any turbulent energy in the released upstream flows from the container and minimized turbulence effects on the downstream sediment erosion and entrainment.

Figure 5.3.2 Flume apparatus used by Zhou et al. (a) Picture of the experimental setup. (b) Entrainment of bed materials and formation of downstream debris-flow surges.

The authors found that with sediment fully blocking the sloping channel, upstream flows initially raise the water levels and inundate the upstream areas behind landslide dams. Overtopping of the water flows suddenly causes a failure of the crest of the landslide dam and then gradually mobilizes the dam body. Instability develops from the crest to the toe of the dams, and more and more coarse soil particles become entrained into the flows. Step-pools and rapid waves accompany these landslide dam failures, which move downstream and cause cascading failures of unstable landslide dams. Once the flows have successively destroyed the landslide dam, more granular materials in their experiments have been eroded and mixed with the flows.

Besides the overtopping by water flows, which gradually caused instability of a landslide dam, the flows through the narrow gap made by landslide dams are usually greatly accelerated. The increased flow velocities induce rapid and significant later erosion of the dam.

The experiments performed show that the failure by upstream flows of a landslide dam with a large downstream length creates a series of cascading failures of closely distributed small landslide dams. This induces significantly enlarged destructive debris flows downstream. Similar to most single landslide events, clusters of landslide dams can also act as a primary control on channel morphology and longitudinal river profiles, reducing or even enhancing a river's incision efficiency. However, the effects of cascading landslide dam failures can be more complicated.

Big-scale experiments have the advantage to better represent the real dimension of a debris flow, compared with small-scale tests. Unfortunately, the execution of this type of procedures can be very difficult and expensive. It is therefore true that the more complicated is the experimental apparatus, the more uncertainties remain about the data acquired.

It is evident that a flow-like landslide is a complicated phenomenon, in which many factors have to be considered and investigated, in order to fully characterize its dynamical and deposit aspects. Small-scale and big-scale experiments capture different aspects of the complexity of this natural hazard.

6 CALIBRATION PROCEDURE

6.1 INTRODUCTION

In this paragraph, the calibration procedure will be explain. To collect a big number of numerical results, a specific code has been implemented using *Matlab*. Basically, the main goal is to automatically compile the input files for the case study selected, to run a big number of simulations and finally to post-elaborate the results. In fact, it is necessary to make it easy to manipulate such a big number of information, in order to compare them with the respective physical measurements.

6.2 INPUT FILES PREPARATION AND SIMULATIONS RUNNING

As explained in §4.4.2, four types of input files have to be prepared for each simulation. This first step of the procedure can be summarize as follow:

- Creating a folder called "*Simulations*", containing for each numerical test one sub-folder;
- Giving the name to each sub-folder, named "*test_001*"…"*test_xxx*" depending on the number of simulations you want to obtain;
- In each folder "*test_xxx*", three sub-folders are created: one, named "*SPH*", in which the code will print the results; the second, named "*File_JPG*", that will contain some pictures of the results obtained; finally, a "*File_TXT*" folder will contain the measurements necessary to compare the numerical and the physical results;
- In the folder "*SPH*", a copy of the code and the four updated input files are placed;
- Finally, a simple *AutoIt v3* code is placed in "*test_xxx*" folder, to launch more than one simulation, in parallel.

6.2.1 Parameters file

The most important part of this first step consists in the definition of the physical and rheological parameters to use for the simulation, depending on the study case and the rheological model you want to consider.

Two strategies are applied to make the parameters varying, depending on the study case considered. With the two small-scale cases, the rheological parameters varies logarithmically between a minimum and a maximum values. For the last case, instead, a Montecarlo analysis has been applied, and consequently many random extractions are taken from the normal distribution assigned to each parameter.

Once decided the total number of simulations and created the same number of sub-folder, first of all the parameters file, described in §4.4.2.2, have to be compiled. Basically, the *Matlab* code creates a new file, called "*test_xxx.dat*" and save it in the respective "*test_xxx/SPH folder*". It writes all the invariable parameters, such as the first four parts of the file described in §4.4.2.2. Then it create, depending on the variation law decided and on the global number of simulations, an opportune quantity of combinations of parameters. These updated values are inserted in the fifth part of the "*.dat*" file and the file is saved again.

Finally, the file is completed with the last parts and definitively saved.

6.2.2 Master and topographical files

The master and the topographical files are filled, maintaining the same content. In fact, in all the simulations the same geometrical characteristics and the integration variables have to be the same.

The name of each file is updated, depending on the destination folder and all those files are saved.

6.2.3 Source mass files

When this kind of file is used, it has to be created. Obviously, because the geometrical characteristics of the initial mass are always the same, the upper part of the "*.pts*" file remains each time the same.

When many zones of parameters variability are provided, as it happens in the last case study, the information about the changes of these values have to be included. Consequently, the *Matlab* code update this part of source mass files with the opportune parameters, saves each file giving the right name and place it in the respective sub-folder.

6.2.4 Simulations launcher

Unfortunately, *Matlab* does not allow running more than one simulation at the same time. For this reason, it is necessary to use *AutoIt v3* software as launcher. *AutoIt v3* is a freeware BASIC-like scripting language designed for automating the Windows GUI and general scripting. It uses a combination of simulated keystrokes, mouse movement and window/control manipulation in order to automate tasks in a way not possible or reliable with other languages. For these reasons, it is particularly suitable for the purpose. Practically, it open a command window, write the command lines that allow to run the numerical code in a folder and select the input files to use in the calculation. As soon as the first script is finished, *Autoit v3* is suddenly run again from *Matlab*, to launch the next simulation. Depending on the number of processors of the computer used, it is possible to decide the number of simulations you can run at the same time.

To avoid overloading the CPU of the computer, a special pause between a group of simulations and the next is defined by controlling the size of the output file compiled by the SPH code.

6.3 POST-ELABORATING RESULTS

During the pause between two subsequent groups of simulations, some operations on the completed numerical results can be performed.

When the comparison between physical and numerical measurements are made just on the final heights of deposit, the code extracts from the "*.post.res*" files the data relating to the last time step. Instead, when also the kinetical measurements are considered, the code finds the requested nodes and saves the information, storing the time step reached, too.

The code stores all the measurements, with a unique reference system, in some matrices. In that way, it is possible to easily calculate the performance indices of each numerical test, compared with the respective case study considered.

Working with the last case study, the most complicate one, it was necessary to apply a statistical algorithm to improve the calibration procedure. The *Matlab* code implements also this algorithm, giving out the updated values of parameters.

Finally, all the performance indices, the summary files with the results reached and some useful graphs are automatically saved and placed in the "*File_TXT*" and "*File_JPG*" folders, respectively.

By the application of this procedure, it is possible to manipulate a big number of simulations in an orderly manner. The results are easily understandable and analyzable. The calculation of the performance of each numerical test allows unequivocally finding the best simulation depending on the variables you decide to consider.

6.4 CONSIDERATIONS

6.4.1 Calibration strategies in literature

The common technique used for calibrating a numerical model is based on the back-analysis. Basically, the variables to use for comparing the numerical and the physical data are decided. Among the simulations performed, it is identified the one that reaches the most similar value compared with the reference one.

Normally, two types of measurements are taken into consideration to identify the numerical results:

- the geometry of the deposit, consisting for example in quantities such as the runout, the spread, or the heights in characteristic sections;
- the kinematic measurements, such as the velocities in characteristic sections, or the heights varying during the flow.

It is evident that the more measurements you have available, the more precise and accurate the calibration will be. It is therefore opportune to consider also kinematic measurements, when available, to fully describe the phenomenon. Unfortunately, especially speaking of real flow-like landslides, rarely it happens that this type of information is accessible. In fact, when a debris flow or a mudflow suddenly happens, it is hard to collect velocities or heights versus time. The unexpected nature of this kind of phenomena limits the type of measurements collectable.

It is obviously different when we consider laboratory tests. In this case, in fact, the experimental apparatus may be constructed to save different kind of data, such as the velocities field or the variation of heights during time.

Hungr and Evans (1996) consider the runout as the variable to compare. They analyzed 23 case histories of rock avalanches, working with three alternative rheologies: frictional, Voellmy and Bingham. Each trial run was assessed by matching the following parameters to the actual values as determined from maps or from reports: total horizontal runout distance, length of the main deposit, mean thickness of debris in up to three location, flow velocities, where available and flow duration. Using these comparisons, the authors could identify the best combination of parameters for each case considered. A second criterion for comparing the results of modelling with actual observations is in terms of velocity and flow duration. They concluded that Voellmy rheological law has been the one that produces the most consistent results in terms of debris spreading and distribution as well as velocity data. The main deficiencies Hungr and Evan found speaking about the frictional model are the tendency to predict excessive thinning of the deposits in the distal part and to overestimates

velocities. This first paper shows how the calibration allows better reproducing some aspects of the rapid landslide, approximating others.

Bertolo and Wieczorek (2005) selected six streams with evidence of historical debris flows in the Yosemite Valley of California, USA. As a first step, they calibrated the parameters for two different numerical code, DAN and FLO-2D ones, through the back analysis of three debris- flows channels using a trial-and-error procedure starting with values suggested in the literature. In the second step, they applied the selected values to the other channels, in order to evaluate their predictive capabilities. They selected three rheological laws: they started with a frictional model, they tried then the Voellmy one and finally they worked with Bingham constitutive equation. They compared the velocities obtained by the two models and saw good agreements for all the selected rheologies, except for the Bingham model, where the low velocities cause a very long duration of the transport and the depositional stage, which seems not to be realistic for these coarse debris-flow events. They obtained accurate runout distances for the three test channels from the DAN model. The FLO-2D model creates an accurate representation of the material spreading on the fan and depicted where the channels split. Finally, even if they found that the calibration might give good results to estimate some characteristics of the flow, they observed that the calibrated values of the rheological parameters used in the models differ from one case to another. This demonstrate, again, how much the calibration depends on the variable considered.

Authors consider different aspects of flow-like landslides. They try to include in the model, for example, erosional effects. Consequently with this, they have to calibrate one or more parameters, depending on the erosional law they consider, as explained in the §3.3. Chen et al. (Chen et al., 2006) proposed a new concept of yield rate and establish the erosional relationship to bridge these two systems. They applied their method to analyze a recent debris flow event in northern Italy. The magnitude of a debris flow event is determined more by the volume of the material entrained along the runout path than by the initial volume. Although the evaluation of surface lowering is crucial in the erosion/entrainment process, field measurements of the likely erosion depth of a debris flow are very difficult to determine. Erosion evaluation is more meaningful and practical if measured in volume and area to be affected by erosion, which leads easily to the estimation of erosion rate. Two areas affected by erosion could have the same values of area but might produce debris accumulation at very different erosion rates. Chen et al. propose a new concept of yield rate based on the assumption that the volume eroded is proportional to the surface area to be affected and the material moving velocity. Defined in a dimensionless form, the yield rate can be rationally and conveniently estimated in the field, or measured in physical models. They wanted, in that way, to include more information about the phenomenon in the back-analysis procedure, to better identify the nature of the landslide.

The results obtained using different rheological laws are also common in literature. Pirulli and Mangeney (2008) using the numerical code RASH3D, based on a continuum mechanics approach and on the long wave approximation, back-analyzed two cases of rock avalanches: Frank (1903, Canada) and Val Pola (1987, Italy). Three alternative ‘‘rheologies’’ - frictional, Voellmy and Pouliquen - are used. Comparison among obtained results underlines that the validation of a ‘‘rheology’’ requires not only a good agreement between the numerical simulation results and the run out area boundaries but also in term of depth distribution of the mass in the deposit. In case of a Pouliquen

rheology, it is observed that the deposit tend to be short, as in case of a frictional rheology, while the distribution of the mass brings near the Voellmy profile. In case of a frictional rheology, it is the thin front that run up the opposite slope and then run back; while in case of a Voellmy rheology, it is the thick front that run up the opposite slope and then run back. Concerning the main aspects investigated, some approximations have to be tolerated.

Recently, Manzanal et al. (2016) tried to simulate rock avalanches using a depth integrated SPH model. Their aim was to compare the performance of different rheological models to reproduce the track, runout and depth of the final deposit for both, scale test and real events. In one of their cases, a small scale laboratory test is reproduced. The test consisted in releasing a dry granular mass on an inclined base of forex. Two different rheological models are considered: in first place, the frictional fluid with a single rheological parameter is established. As rheological parameter, they decided to consider the friction between the basal surface and the sliding sand, which is smaller than the internal friction angle of the sand. Second, the viscoplastic frictional model based on Perzyna law is applied. The results in terms of deposit depth are compared together with the isolines and the contour of spreading obtained by the laboratory tests. They observed that the two rheologies reproduce quite well the run out shape and the maximum run up. However, the computed maximum deposit height fluctuates slightly between the two rheologies. The comparison they performed was qualitative: they considered the maximum deposit height as indicator, without calculating any error index to evaluate objectively the results achieved.

6.4.2 Calibration steps

As observed, many authors use comparison about heights or deposit shape for deciding the best combination of parameters, which allow you to reproduce the flow-like landslide you are studying.

Commonly, various integration methods are chosen to solve the system equations. Some models consider the components of the flowing mass as a homogeneous material, assigning average rheological and physical properties. Some others, contrarily, leads to include all the components of the mixture in the equations governing the system.

The RASH3D and FLO2D numerical codes are both based on depth-averaged Eulerian flow models, but they differ in the technique adopted for the numerical implementation of the governing system of mass and momentum conservation: a finite volume scheme in RASH3D (Mangeney-Castelnau et al., 2003), and a finite difference scheme in FLO2D (O'brien et al., 1993).

TRENT2D (Armanini et al., 2009; Rosatti & Begnudelli, 2013) is also based on depth-averaged equations, assumed isotropy of normal stresses and adopt a finite volume scheme for the numerical implementation of balance equation, like RASH3D does. Anyway, TRENT2D and RASH3D are different under some aspects: in RASH3D the boundary of the source area, the geometry of the initial volume and the rheological parameters of the muss must be specified. In TRENT2D, an inflow flood hydrograph of the mixture is required, together with the local slope of the area and the initial section pf the flow.

The theoretical basis of DAN (Hungr, 1995) and DAN3D (Hungr & McDougall, 2009) is a system of depth-averaged governing equations derived from the principles of continuum mechanics. Both algorithms are designed to work within the semi-empirical framework of the ‘‘equivalent fluid’’

approach. This approach requires selection of material rheology and calibration of input parameters through back-analysis of real events. The two models are based on Lagrangian forms of the depth-integrated St. Venant equations, applied in curvilinear coordinates.

To predict motion of diverse grain-fluid masses from initiation to deposition, Iverson and Denliger (2001) develop a depth-averaged, three dimensional mathematical model that accounts explicitly for solid and fluid phase forces and interactions. Model input consists of initial conditions, path topography, basal and internal friction angles of solid grains, viscosity of pore fluid, mixture density, and a mixture diffusivity that controls pore pressure dissipation.

Others, contrarily, consider two different phases for representing the material. Pudasaini (2012) proposed a model that employs the Mohr-Coulomb plasticity for the solid stress, and the fluid stress is modelled as a solid-volume-fraction-gradient-enhanced non-Newtonian viscous stress. The generalized interfacial momentum transfer includes viscous drag, buoyancy, and virtual mass. The model includes also virtual mass induced by relative accelerations between the solid and fluid phases. Pudasaini leads to unify existing avalanche and debris flow theories, including the single-phase avalanche model of Savage and Hutter (1989), the debris-mixture model of Pudasaini et al. (2005), and the two-fluid debris flow model of Pitman and Le (2005).

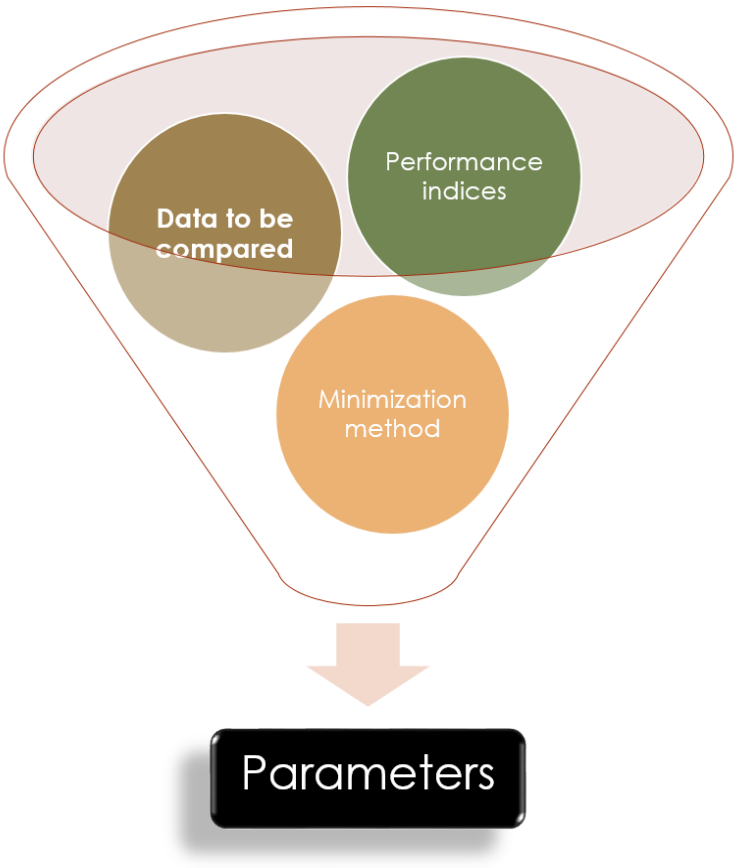

Figure 6.4.1 Calibration procedure's ingredients.

This is just a brief overview taken from an extensive amount of available models. Once you have decided the model to use for approximating the landslide, you have to identify which rheological law better describes the material you are working with. All these numerical models allow, in fact, including various rheological laws, such as Bingham, Voellmy or frictional. As described in §3.2, depending on the nature of the rapid landslide, you have to select the most suitable model among the ones available. Obviously, this choice involves the identification of the parameters to be then calibrated.

The present thesis used the GeoFlow-SPH code, already presented in §4. The main characteristics can be summarized in some points:

- the material is considered an “equivalent fluid” governed by simple rheological relationships (Bingham, Voellmy or Coulomb law) which can vary along the path according to the superficial material that is encountered;
- the model considers strain-dependent, non-hydrostatic, anisotropic internal stresses due to the 3D deformation of material with internal shear strength and the centripetal acceleration due to path curvature;
- the model simulates mass and momentum transfer due to entrainment and makes it possible to consider corresponding variations in flow rheology.

At this point, a critical point for the calibration procedure consists in the definition of the data to be compared. Depending on what you are interested in or on the data you have available, you can decide what variables have to be included in the comparison between the numerical model and the respective measurements.

Sometimes it happens that just few information about the rapid landslide are available, particularly speaking about real cases. Working with laboratory tests, on the contrary, usually you are able to decide which measurements you want to collect. If you have a huge quantity on data, you have to select the ones that are able to sufficiently describe the phenomenon. The compromise must lie in the choice of a quantity of information that are sufficiently descriptive, but that do not destabilize the calibration procedure, excessively increasing the demand of similarity.

It is important to remember that a numerical model aims to reproduce a complicated natural phenomenon, simplifying the system with many approximations. Working with the Geoflow-SPH model, for example, the material included in the simulation is single phase and has to include all the various content and the heterogeneity of the real mass flowing.

Asking too much precision to the numerical model may lead to unrealistic and inaccurate results.

Furthermore, if the goal of the calibration is to identify the deposit shape, without any interest in the reproduction of the kinematic characteristics of flow, it is better to neglect the measurements among time, such as the velocities.

Contrarily, if the velocities field or the behavior of the flow along the slope is the topic of the procedure, you have to give importance to this kind of measurements.

Often, the numerical model is used to reproduce the phenomenon in its entirety. In this case, the data to be compared should contain information about both the aspects: deposit shape and kinematic measurements.

The second important ingredient of a calibration procedure consist in the determination of the performance indices used to evaluate the numerical results achieved. Normally, in fact, many simulations are performed and it is necessary to objectively identify the ones that better reproduce the flow-like landslide considered. These performance indices are very useful to have a unique quantity that appraises the goodness of each numerical result.

Normally, different expressions of the error between measurements and numerical results are used as performance indices, capturing several aspects (Willmott & Matsuura, 2005).

Generally speaking, if the individual model-prediction errors are defined as $e_t = y_t - \hat{y}_t$, the average model-estimation error associated to an analysis obtained with the parameter set ϑ can be generically expressed as:

$$e(\vartheta) = \left[\frac{1}{n}\sum_{t=1}^{n}\left|y_t\,(\vartheta) - \hat{y}_t\right|^{\tau}\right]^{1/b} \qquad \textit{Equation 6-1}$$

where $b \neq 0$ and $\tau \geq 0$ are two coefficients and $y_t\,(\vartheta)$ expresses the values y_t obtained using the parameter set ϑ.

One of the simplest formulation uses the average error to understand how the numerical model differs from the case study. In fact, one simple relation, assessed with $b = 1$ and $\tau = 1$, gives the average error or Mean Absolute Error (MAE), according to:

$$MAE = \frac{1}{n}\sum_{t=1}^{n}\left|y_t\,(\vartheta) - \hat{y}_t\right| = \frac{1}{n}\sum_{t=1}^{n}|e_t| \qquad \textit{Equation 6-2}$$

in which the absolute value of individual error is adopted in order to remove the error sign influence from the computation.

Another commonly defined index is the Root Mean Square Error (RMSE) which is derived from Equation 7-2 with $b = 2$ and $\tau = 2$. It is formulated as:

$$RMSE = \left[\frac{1}{n}\sum_{t=1}^{n}\left|y_t\,(\vartheta) - \hat{y}_t\right|^{2}\right]^{1/2} = \left[\frac{1}{n}\sum_{t=1}^{n}|e_t|^{2}\right]^{1/2} \qquad \textit{Equation 6-3}$$

where, again, the stated rationale for squaring each e_t is to avoid the influence of the error sign. In this case, each error influences the total error in proportion to its square: as a result, large errors have a relatively greater influence on the RMSE with respect to smaller ones, meaning that the RMSE grows as the error is concentrated within a decreasing number of increasingly large individual errors.

The MAE and RMSE have the same units as the variable of interest but they do reflect the relative error size. To deal with this problem, the Mean Absolute Percentage Error (MAPE) is defined as:

$$MAPE = \frac{100}{n}\sum_{t=1}^{n}\frac{\left|y_t\,(\vartheta) - \hat{y}_t\right|}{\hat{y}_t} \qquad \textit{Equation 6-4}$$

In this way, MAPE makes it possible to compare forecasts of different series in different scales.

Finally, when the calibration leads to understand the parameters for complicated cases, such as the real ones, some helpful tool can be found to improve the identification of the parameters combinations that minimizes the performance index chosen.

Different minimization methods are available to help the calibration procedure. In literature, it is rarely possible to find the application of statistical algorithm to the calibration of flow-like landslides. In my work, I decided to use the Ensemble Smoother (Evensen, 2003). This strategy will be explained in §7.3.4. To capture the high content of details contained in the third case study with a numerical

model that tends to simplify as much as possible all the aspects of the phenomenon, it was necessary to increase the number of parameters. This choice made it hard to apply a normal calibration procedure, based on the repetition of some simulations and the simple choice between them.

The algorithm is useful to reduce the uncertainty of the parameters, limiting the errors that can be done with an inexact selection of rheological variables.

7 CASE STUDIES

7.1 SPREADING OF A COHESIVE MATERIAL COLUMN

7.1.1 Introduction

The first case study that is interesting to take into account is the collapse of a cylindrical mass on a plane. The simplicity of the geometry, the knowledge of the material characteristics and the repeatability of the experiment make this case a perfect candidate with whom start the calibration of this model.

Different content of materials are included in the initial volume of mass. Water, kaolin and sand are mixed to obtain an almost homogeneous blend that is put inside a Plexiglas cylinder leaning on a plane. Suddenly this cylinder is vertically raised and the mass start to collapse. The behavior of this simple case depending on the density and the characteristic of the mixture is really interesting to evaluate. The calibration of a numerical model that leads to reproduce this phenomenon should give out a starting point to construct a table of parameters depending on the material you are taking into account.

7.1.2 Experimental setup and procedure

A cylinder on inner radius R1, placed on a horizontal 40cm X 40cm Plexiglas plane, composes the experimental setup. The Plexiglas tube is partially filled with a mixture composed by kaolin, sand and water, in different percentage. Two dimensions of cylinder were used for these experiments: the first has an inner diameter of 9.3cm, while the second one of 5.8cm. In all the tests, the height of material is maintained constant equal to 8cm.

A twine passing throw two pulleys connect the cylinder to some weights, supported on a movable shelf. As soon as this shelf is released, the weights fall down putting in traction the twine and raising in this way the cylinder. There are two pierced wooden boards through which the cylinder flows when it is lifted. Practically, this help to reduce as much as possible all the lateral movements and all the oscillations of the Plexiglas body during the test. The experiment consist in the lift of this cylinder, partially filled with cohesive or granular material, partially saturated.

Figure 7.1.1 First step of the experiment: view of the material into the cylinder for the WK1 big cylinder test (t=0.00s).

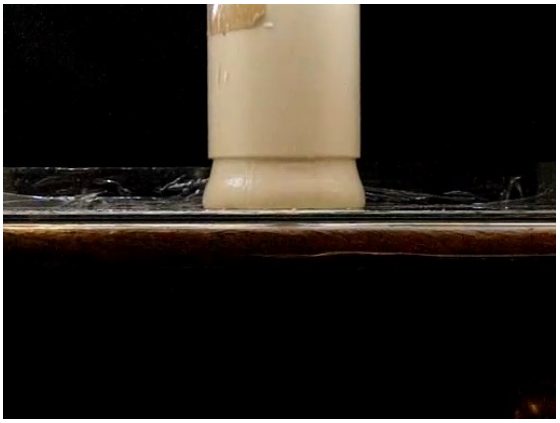

Figure 7.1.2 View of the lifting of the tube for the WK1 big cylinder test (t=0.15s).

Figure 7.1.3 Initial release of the material for the WK1 big cylinder test (t=0.30s).

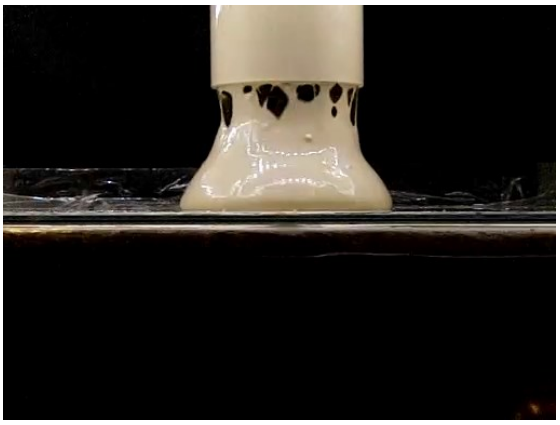

Figure 7.1.4 Full release of the material for the WK1 big cylinder test (t=0.45s).

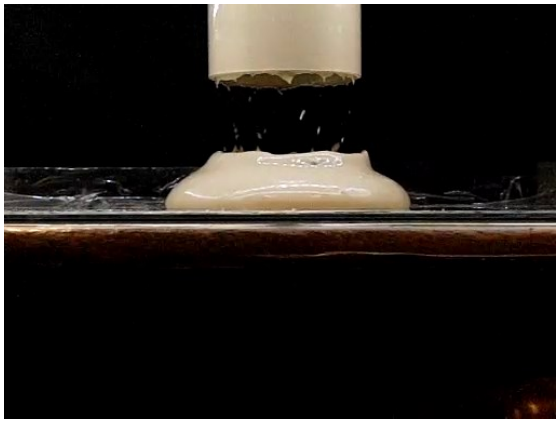

Figure 7.1.5 Deposit and identification of the final profile for the WK1 big cylinder test (t=0.60s).

The rising phase must be as vertical as possible not to influence the measurements and consequently the final profile of the mixture. The boundary conditions have to be maintained the same to make it possible to have a reliable comparison among all the experiments performed. No change in the position of the image acquisition system or the experimental apparatus is made during the entire duration of the tests.

To ensure reproducible initial conditions, the tube is always filled following the same procedure: the mixture is prepared paying close attention to the mixing phase, then it is gradually inserted inside the cylinder and the test is performed as soon as possible, to reduce maximally the deposition. It is necessary to notice that just the volume of the material was checked. It was not included any checkup of the weight inserted in the cylinder. This fact limits somehow the quality of the results.

The experimental procedure simply consists in quickly removing the tube by means of a lifting system made of rope and pulleys. After it is released, the material mass spreads on the horizontal plane until it comes to rest and forms a deposit.

To capture instant by instant the various stages of collapse of the columns of material, it is used a digital camera in high speed video mode. The images recording is performed by a CASIO® EXILIM EX-F1, positioned on a tripod with adjustable circular level, which allows you to horizontally place the acquisition apparatus and acquire side views of the moving mass. The camera is controlled by remote, to avoid interference by the operator in time to start or stop recording. The time evolution of the system is measured by acquiring 300 images per second, with a resolution of 2816x2112 pixels digital camera acquiring.

The camera is connected to a computer and the digitized images are processed in order to extract the profiles $h(r,t)$ of the granular mass throughout time t, being h the local thickness and r the radial distance to the axis of symmetry of the mass. Thanks to the axial symmetry of the system, the material profile provides enough information to fully characterize its three-dimensional shape.

7.1.3 Pictures elaboration

After having performed all the tests, a post elaboration of the acquired images is required. It has to be underlined that the choice to acquire 300 photograms per second leads to obtain the profiles of all these time steps. On the other hand, this selection limits the quality of the images in terms of resolution. As the relief of the profiles is handmade, for now, it was possible to work only on the final pictures of each test. The reliability of the data obtained is strictly connected with the resolution of the photograms. Furthermore, only one repetition of each test was performed, so it is not available a repeatability evaluation.

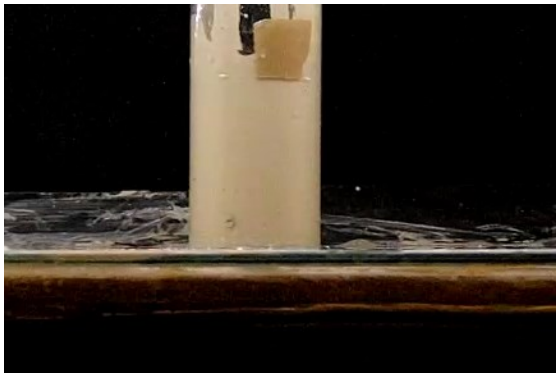

Figure 7.1.6 First photogram of the movie of the WK4 mixture, small cylinder.

Figure 7.1.7 Photogram of the final deposit of the WK4 mixture, small cylinder.

From the video of the experiment, the first and the last photograms were taken out. The first image is necessary to calibrate the procedure of acquisition: in fact the conversion from pixels to meters has to be performed starting from a well-known measure easily recognizable on the screen and the external diameter of the cylinder (6.5cm and 10.0cm respectively) is used to understand the scale of the image. The second picture has to be analyzed using a special software, *ImageJ* specifically, that helps us to pick up as many points as necessary to characterize the shape of the deposit.

In the first photo, it is possible to identify the two points of contact of the cylinder with the support plan. This first passage allows you to understand in addition to the scale factor, as already said, even if there is any rotations or distortions in the shooting direction. Then, working with the second image, it is possible to mark enough useful points to make it possible a clear identification of the profile.

It is important to note that some errors can characterize the experimental tests in question and this fact must be taken into the mind in order to evaluate the reliability of the experimental results in the subsequent calibration phase.

First, even if two pierced wooden boards are used to lift more vertically as possible the cylinder, its lifting is not perfectly vertical. Some oscillations happened during the experiments and this modify the way in which the material exits from the cylinder. That is way, even if the problem should be axial-symmetric, the profiles obtained are often asymmetrical.

Then it has to be considered that the filling phase of the cylinder was not always perfect: especially working with dense mixtures, it was difficult to verify the accuracy in the volume definition.

Finally, the resolution of the images obtained is not very high. This caused inevitably some uncertainty in reconstructing the profiles from the images with the software.

7.1.4 Experimental results

Totally, 36 experiments are made, changing the content of kaolin and sand in respect to the water one. The compositions of the mixtures are described in Table 7.1.1. Six tests considered sand-water mixtures varying from the dry sand (WS1-6) to a wet sand with a water content equal to 1.2%. This water content leads to a saturation state that is defined pendular. The domain gaseous is connected, there are liquid bridges shared between pairs of particles but the water does not completely fill the empty space between the grains. This regime is mainly characterized by gravity, capillary and contact forces (Gabrieli, 2009; Gabrieli et al., 2013). Six tests considered kaolin-water mixtures (WK1-6) with a water content varying from 43.5% to 52.6%. It has to noticed that in the most liquid WK test completed with the big cylinder, the material flowed out from the recording area, due to the high mobility of this mixture. For this reason, the profile of the WK6 test performed with the big tube cannot be considered reliable at all.

Finally, 7 tests were performed with mixture of sand, kaolin and water (WSK1-7): in this case, the strategy adopted is to maintain constant the percentage of kaolin in respect to the water, the same adopted in WK5 mixture, and then to add varying quantities of sand. The main goal is to understand the differences on the final shape of deposit given by the inclusion of different percentage of granular material.

Each test has been performed using both the cylinders.

Water & Sand Mixtures			**Water & Kaolin Mixtures**			**Water, Kaolin & Sand Mixtures**			
name	*water (%)*	*sand (%)*	*name*	*water (%)*	*kaolin (%)*	*name*	*water (%)*	*sand (%)*	*kaolin (%)*
WS1[a,b]	0.0	100.0	*WK1*[a,b]	43.5	56.5	*WSK1*[b]	40.1	10	49.9
WS2[a,b]	0.3	99.7	*WK2*[a,b]	45.5	54.5	*WSK2*[a,b]	35.5	20	44.4
WS3[a,b]	0.5	99.5	*WK3*[a,b]	46.7	53.3	*WSK3*[a,b]	31.2	30	38.8
WS4[a,b]	0.8	99.2	*WK4*[a,b]	48.1	51.9	*WSK4*[a,b]	26.7	40	33.3
WS5[a,b]	1.0	99.0	*WK5*[a,b]	49.5	50.5	*WSK5*[a,b]	22.3	50	27.7
WS6[a]	1.2	98.8	*WK6*[a,b]	52.6	47.4	*WSK6*[a,b]	17.8	60	22.2
						WSK7[a,b]	13.4	70	16.6

Table 7.1.1 Content of components of the mixtures used for the experiments: [a] small cylinder, [b] big cylinder.

The volume of material used is respectively 0.465liters and 0.211liters for the big and the medium cylinders. The horizontal plane is made by glass, so the basal friction is extremely slight.

Thanks to *ImajeJ*, it is possible to have exact measurements of the final deposit of each mixture. In fact, from the identification of the position of some characteristic pixels in the picture, applying the right scale factor and the necessary transformation, a list of xyz coordinates are immediately obtained, allowing the identification of the behavior of each test. The reference system is maintained the same for all the elaborations in order to makes it possible to compare the results of the different laboratory trials.

In this way, 36 profiles are easily drawn. It can be immediately noticed that it is not drawn the WK6 profile made using the big cylinder. In fact, the material was too liquid and it went out from the basal plane. Consequently, any reliable profile could not be obtained.

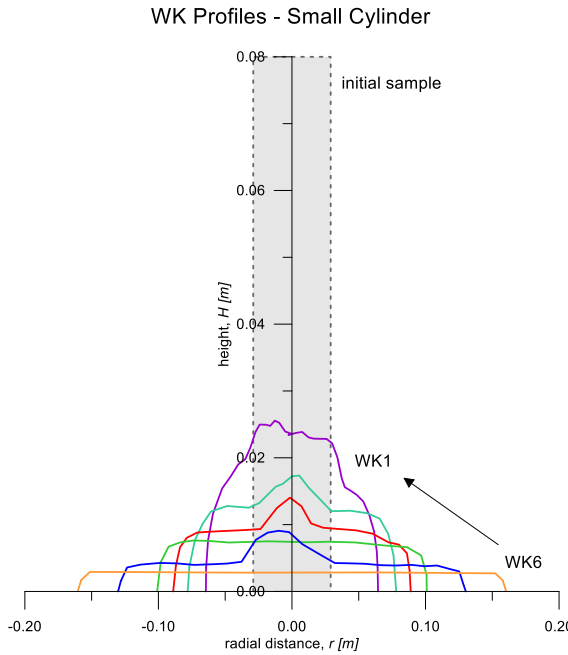

Figure 7.1.8 Profiles of the WK mixtures, small cylinder.

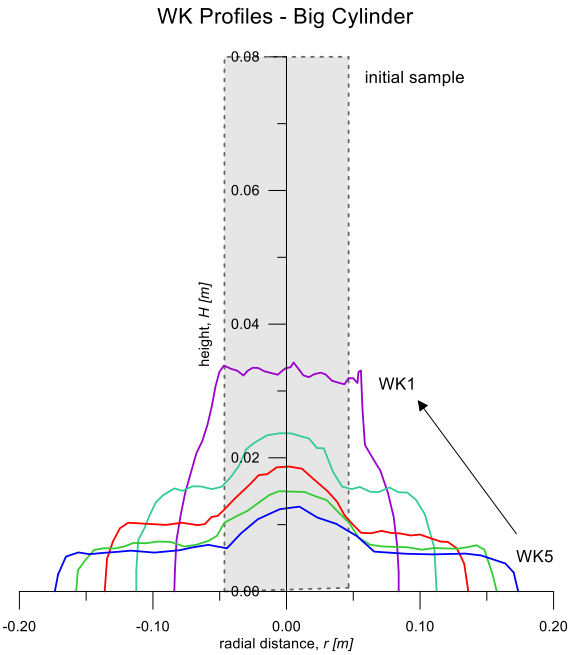

Figure 7.1.9 Profiles of the WK mixtures, big cylinder.

Speaking about the WK mixtures, it can be notice that an increment of the kaolin content increases the maximum height, while decreases the runout of the deposit. The results of the tests seem to be consistent among them because the variation of runout distance with the kaolin content shows a congruent monotonic trend in relation with the water content.

In all the experiments, the mass tends to form a disk with vertical lateral border and a uniform height. On this issue, it has to note that the disk has not a uniform height due to the presence in the final profile of a central part higher than the lateral parts (Figure 7.1.8 and Figure 7.1.9). This effect does not seem due to the real behavior of the material, but an effect due to the procedure adopted in the experiment. In fact, the adhesion of the material to the inner cylinder surface caused a momentary confinement of the upper part of the volume that received a pushing upwards (Figure 7.1.10), while the outside material could more free expand laterally. In the sequence of images

below (Figure 7.1.10) it is evident the presence of a thin layer of material in contact with the internal perimeter of the cylinder, due to the boundary conditions of the tests.

The behavior of the WS mixtures (Figure 7.1.11 and Figure 7.1.12) shows how an increase of the water content gives an apparent increment of the internal friction angle. In fact, particularly with the big cylinder, the tests with higher W present higher angles of final slopes. In effect, this result is surely related to the capillary bonding forces due to the presence of capillary water bridges among the solid particles (Gabrieli et al., 2013; Artoni et al., 2013).

In any case, the final profile of WS mixtures is similar to a conical shape with an angle varying from 10° to 80° according with the water content, but still less than the 90° angle observed in WK tests.

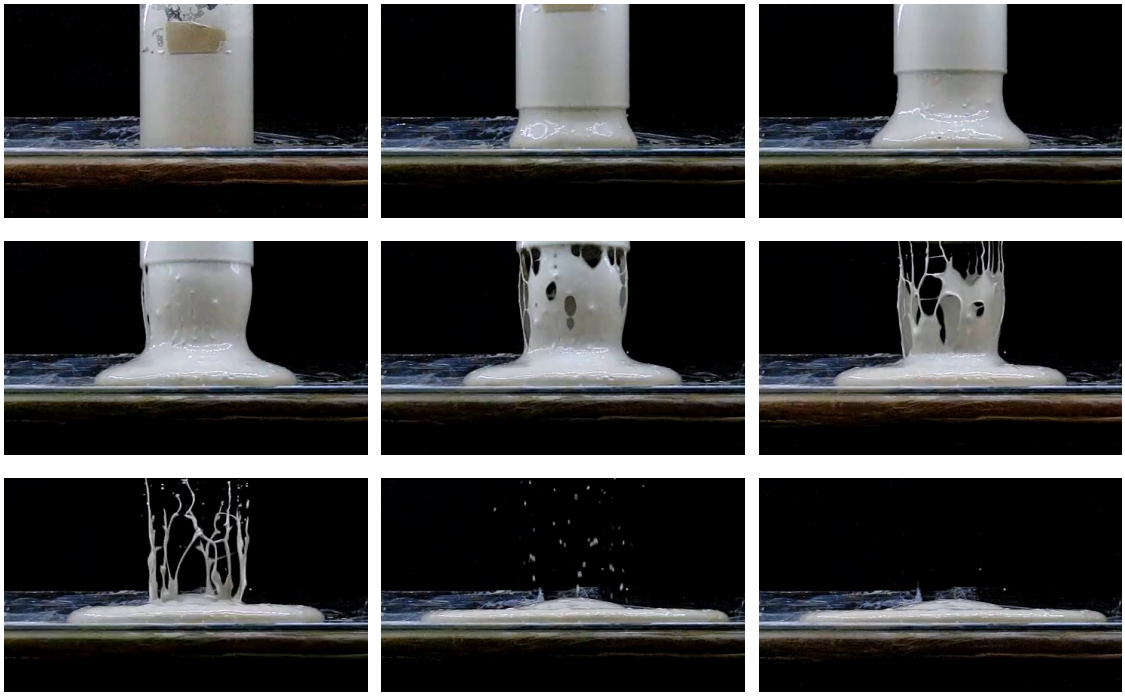

Figure 7.1.10 Sequence of screenshots of a test: the role of the boundary conditions.

The runout decreases with the increment of sand, while the maximum height increase. This fact is consistent with what observed in the WK mixtures, even if here it is slightly less evident. Note that the WSK5 and the WSK6 made with the big cylinder have probably not to be considered because the profiles are not congruent with the other tests, showing that those tests were probably affected by some execution.

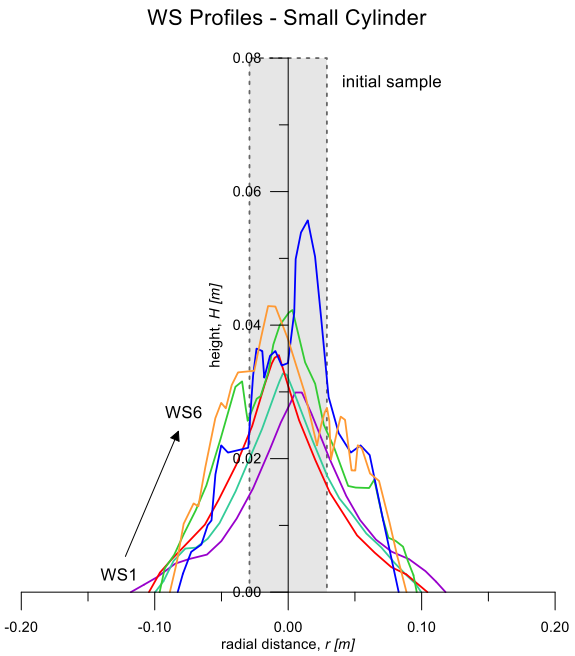

Figure 7.1.11 Profiles of the WS mixtures, small cylinder.

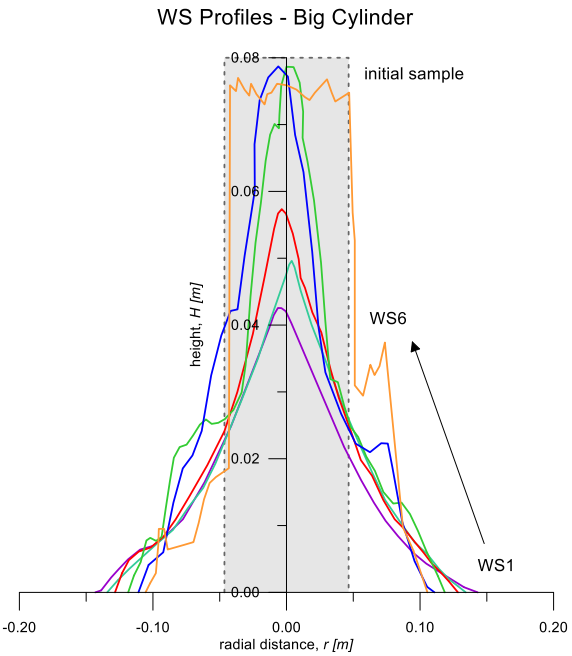

Figure 7.1.12 Profiles of the WS mixtures, big cylinder.

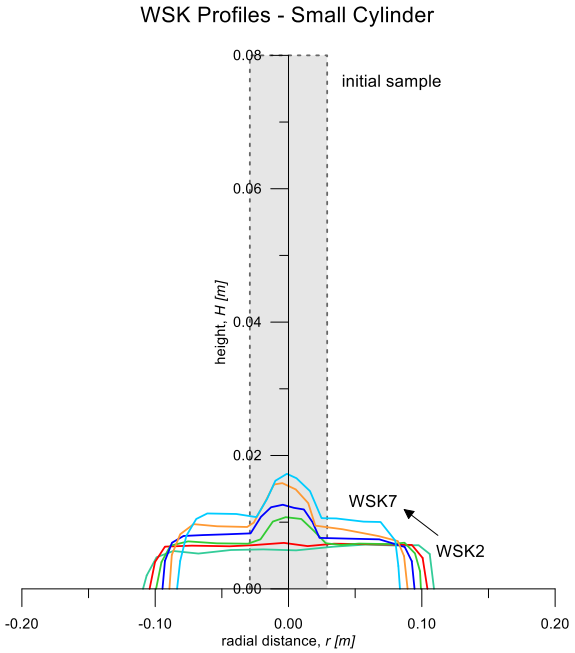

Figure 7.1.13 Profiles of the WSK mixtures, small cylinder.

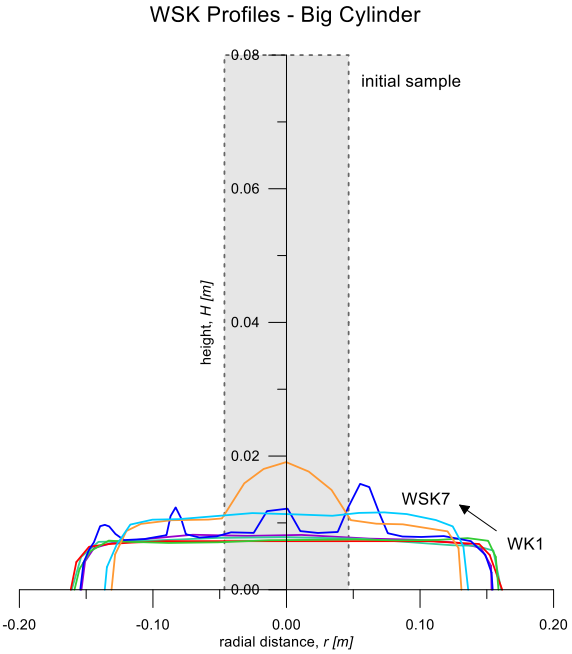

Figure 7.1.14 Profiles of the WSK mixtures, big cylinder.

Initially, the values of runout and maximum height were used as parameters to identify the shape of the studied profile. The runout is an essential information about the deposit, but, as said before, due to the particular retention effect of the central part, the maximum height cannot be considered the best parameter to identify the shape of each profile and it can sometimes lead to some errors

in the following calibration procedure. Therefore, it was necessary to consider more heights to characterize each shape. For this reason, two more heights were taken into account, at $\pm 1/6$ of the total runout distance ($H1$ and $H2$).

Furthermore, a quantity that gives out an indication of the reliability of each profile is the volume. The basis of the collection of measurements is the axial-symmetry of the system. The data acquired in fact consider just the central section of the deposit. Consequently, if the final shape is not axial-symmetric, the profile is not reliable. By the calculation of the volume stopped on the plane, based on the spatial integral of the deposition area, the axial-symmetry of the test can be understood. In fact, the initial volume of material inserted in the cylinder is well-known and this value can easily be compared with the results of the calculation described above. It is evident that this strategy brings some errors and approximations, but anyway it helps us in the understanding of the goodness of each test, both talking about the execution of the test, both the post-processing of images.

If we consider the final shape of a test, it can be easily approximated with the sum of many rectangles. The more regular is the profile, the less number of subdivisions are necessary. At this point, the volume can be calculated, considering the axial-symmetry of the system as follow:

$$V_{calc} = \sum_{i=1,n} A_i \pi \, h_i \qquad \textit{Equation 7-1}$$

where A_i and h_i are the area and the height respectively of the *i*-element, among the n rectangles in which the deposit profile can be subdivided.

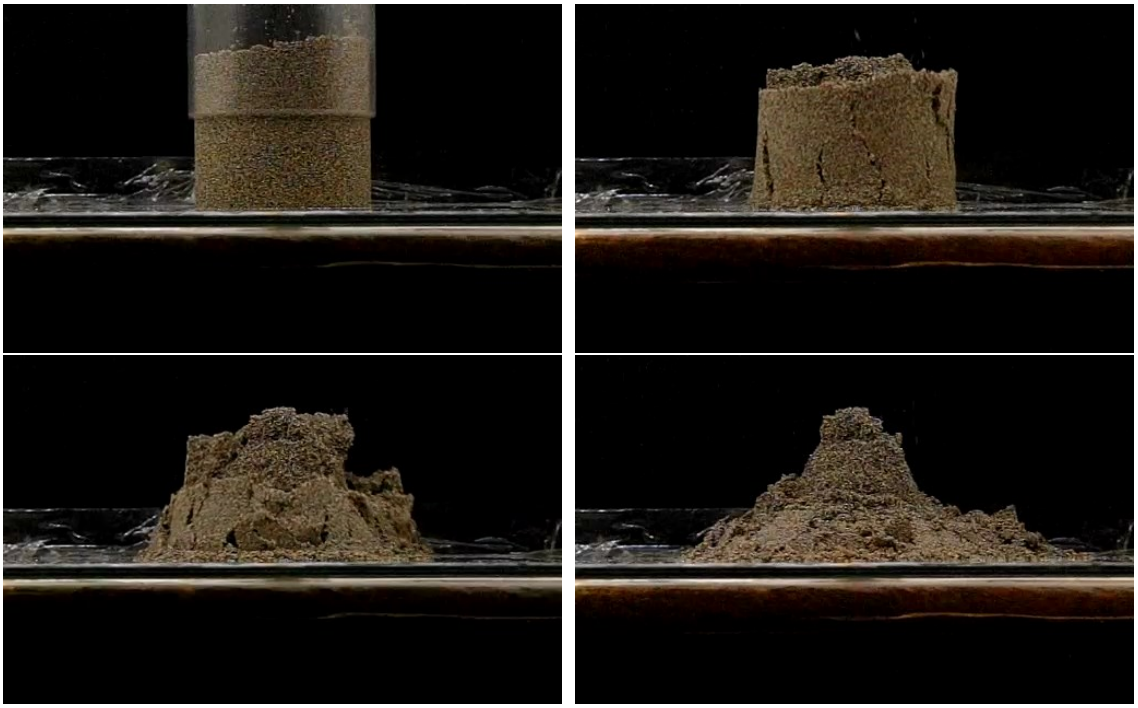

Figure 7.1.15 Sequence of screenshots of a WS test.

This formulation is realistic only when the basal assumption of axial-symmetry of the phenomenon is assured.

By the comparison of these calculated values with the theoretical volumes included in the experiments, it is possible to make some considerations about the tests reliability. It is evident that the profiles obtained from the WK tests are quite good. The deposit shape is effectively axial-symmetric and there is a good agreement between the real volume and the one calculated. The WSK mixtures have a good reliability, too.

Contrarily, the WS mixtures present big values of volume errors. The main reason for this can be explained looking at the behavior of this mixtures (Figure 7.1.15). It is evident that the final shape cannot be represented just by the central section profile. This test, in fact, needs more information that can characterize the three dimensional shape of the deposit. It is therefore clear that by the analysis of the videos acquired, approximate values can be extracted and this fact leads to big errors comparing the volume calculated with the initial one. The more is not axial-symmetric the final shape, the bigger is the error in the approximation of the studied phenomenon with just the section measurements.

In Table 7.1.2 - Table 7.1.7 all the characteristics of the deposit shapes are inserted.

WK mixtures									
Mixture	***Kaolin***	***runout***	***H_{max}***	***h1***	***h2***	***h***	***volume***	***Δ volume***	**Small cylinder**
	%	*[m]*	*[m]*	*[m]*	*[m]*	*[m]*	*[mc]*	*%*	
WK1	*56.5*	0.129	0.026	0.025	0.023	0.024	2.16E-04	2.4	
WK2	*54.5*	0.156	0.017	0.013	0.013	0.013	2.11E-04	0.4	
WK3	*53.3*	0.178	0.014	0.009	0.009	0.009	2.08E-04	1.5	
WK4	*51.9*	0.202	0.008	0.007	0.007	0.007	2.16E-04	2.3	
WK5	*50.5*	0.260	0.009	0.004	0.004	0.004	2.16E-04	2.0	
WK6	*47.4*	0.321	0.003	0.003	0.003	0.003	2.09E-04	1.0	

Table 7.1.2 Characteristics of the physical tests made with the WK mixtures and the small cylinder.

WK mixtures									
Mixture	***Kaolin***	***runout***	***H_{max}***	***h1***	***h2***	***h***	***volume***	***Δ volume***	**Big cylinder**
	%	*[m]*	*[m]*	*[m]*	*[m]*	*[m]*	*[mc]*	*%*	
WK1	*56.5*	0.168	0.034	0.033	0.033	0.033	5.26E-04	3.2	
WK2	*54.5*	0.225	0.024	0.018	0.017	0.018	5.77E-04	6.1	
WK3	*53.3*	0.272	0.019	0.013	0.011	0.012	5.43E-04	0.1	
WK4	*51.9*	0.315	0.015	0.008	0.009	0.008	5.42E-04	0.3	
WK5	*50.5*	0.347	0.013	0.007	0.007	0.007	5.45E-04	0.3	

Table 7.1.3 Characteristics of the physical tests made with the WK mixtures and the big cylinder.

WS mixtures									
Mixture	**Sand**	**runout**	**H_{max}**	**h1**	**h2**	**h**	**volume**	**Δ volume**	**Small cylinder**
	%	*[m]*	*[m]*	*[m]*	*[m]*	*[m]*	*[mc]*	*%*	
WS1	*100.0*	0.236	0.030	0.011	0.016	0.014	2.75E-04	30.2	
WS2	*99.7*	0.199	0.033	0.018	0.016	0.017	2.65E-04	25.3	
WS3	*99.5*	0.209	0.036	0.021	0.014	0.017	2.74E-04	29.5	
WS4	*99.2*	0.193	0.042	0.028	0.023	0.025	4.15E-04	96.2	
WS5	*99.0*	0.166	0.056	0.029	0.035	0.032	3.67E-04	73.5	
WS6	*98.8*	0.177	0.043	0.033	0.027	0.030	4.39E-04	107.8	

Table 7.1.4 Characteristics of the physical tests made with the WS mixtures and the small cylinder.

WS mixtures									
Mixture	**Sand**	**runout**	**H_{max}**	**h1**	**h2**	**h**	**volume**	**Δ volume**	**Big cylinder**
	%	*[m]*	*[m]*	*[m]*	*[m]*	*[m]*	*[mc]*	*%*	
WS1	*100.0*	0.286	0.043	0.022	0.020	0.021	5.80E-04	6.7	
WS2	*99.7*	0.269	0.050	0.023	0.031	0.027	6.40E-04	17.8	
WS3	*99.5*	0.257	0.057	0.026	0.027	0.027	6.53E-04	20.1	
WS4	*99.2*	0.237	0.079	0.027	0.031	0.029	7.60E-04	39.8	
WS5	*99.0*	0.222	0.079	0.042	0.029	0.036	7.30E-04	34.3	
WS6	*98.8*	0.211	0.077	0.077	0.074	0.075	8.82E-04	62.3	

Table 7.1.5 Characteristics of the physical tests made with the WS mixtures and the big cylinder.

WSK mixtures									
Mixture	**Sand**	**runout**	**H_{max}**	**h1**	**h2**	**h**	**volume**	**Δ volume**	**Small cylinder**
	%	*[m]*	*[m]*	*[m]*	*[m]*	*[m]*	*[mc]*	*%*	
WSK2	*20.0*	0.218	0.007	0.006	0.006	0.006	2.09E-04	1.3	
WSK3	*30.0*	0.208	0.007	0.006	0.007	0.007	2.08E-04	1.4	
WSK4	*40.0*	0.199	0.011	0.007	0.007	0.007	2.01E-04	4.8	
WSK5	*50.0*	0.189	0.013	0.008	0.008	0.008	2.09E-04	1.2	
WSK6	*60.0*	0.179	0.016	0.009	0.009	0.009	2.16E-04	2.0	
WSK7	*70.0*	0.167	0.017	0.011	0.011	0.011	2.16E-04	2.4	

Table 7.1.6 Characteristics of the physical tests made with the WSK mixtures and the small cylinder.

WSK mixtures									
Mixture	**Sand**	**runout**	**H_{max}**	**h1**	**h2**	**h**	**volume**	**Δ volume**	**Big cylinder**
	%	*[m]*	*[m]*	*[m]*	*[m]*	*[m]*	*[mc]*	*%*	
WSK1	*10.0*	0.168	0.034	0.008	0.008	0.008	5.26E-04	3.3	
WSK2	*20.0*	0.225	0.024	0.008	0.008	0.008	5.47E-04	0.6	
WSK3	*30.0*	0.272	0.019	0.007	0.007	0.007	5.40E-04	0.7	
WSK4	*40.0*	0.315	0.015	0.007	0.008	0.007	5.40E-04	0.6	
WSK5	*50.0*	0.347	0.013	0.008	0.014	0.011	6.13E-04	12.7	
WSK6	*60.0*	0.262	0.019	0.012	0.012	0.012	5.37E-04	1.2	
WSK7	*70.0*	0.272	0.012	0.011	0.011	0.011	5.74E-04	5.6	

Table 7.1.7 Characteristics of the physical tests made with the WSK mixtures and the big cylinder.

7.1.5 Considerations

The runouts d, the average heights h and the calculated volumes are put in relation with kaolin content for the WK texts (Figure 7.1.16 - Figure 7.1.18) or the sand percentage for WS (Figure 7.1.19 - Figure 7.1.21) and WSK texts (Figure 7.1.22 - Figure 7.1.24).

Some general observations can be made on these relations. It is evident in texts WK how the runout linearly decreases with the increase of the kaolin content (Figure 7.1.16). This happens for both the cylinders used and the behaviors are quite the same. All the reference heights increases equally linearly. The average height h (Figure 7.1.17) decreases exponentially with the kaolin content. The comparison between the theoretical and the calculated volumes (Figure 7.1.18) suggests the reliability of the measurements obtained. While considering the presence of some inaccuracies, it is considered that these tests can be used as case studies for the next calibration of the numerical SPH-model described in this thesis.

The simplicity of the system is not only relative to the geometric characteristics of experimental apparatus. The collapse of the material of the cylinder has obviously characteristics of simplicity in the evolution of the motion. The symmetry of the system in fact only allows movement in the radial direction, while the transversal speeds to this direction are negligible.

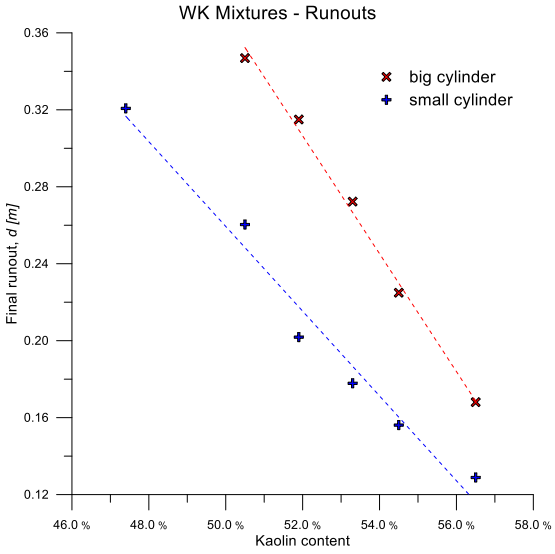

Figure 7.1.16 Runouts of the WK mixtures.

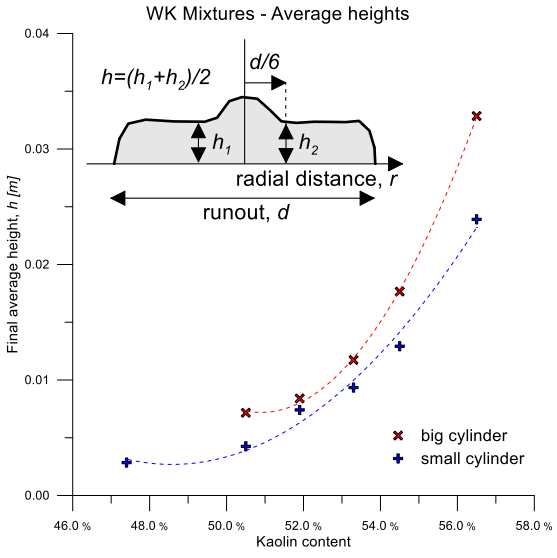

Figure 7.1.17 Average heights of the WK mixtures.

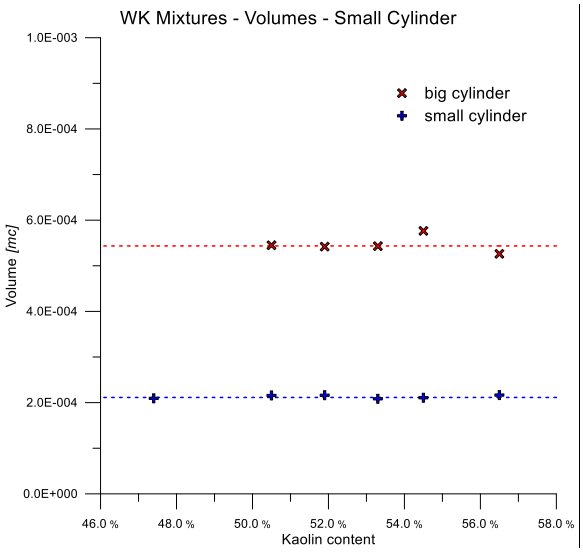

Figure 7.1.18 Volumes of the WK mixtures.

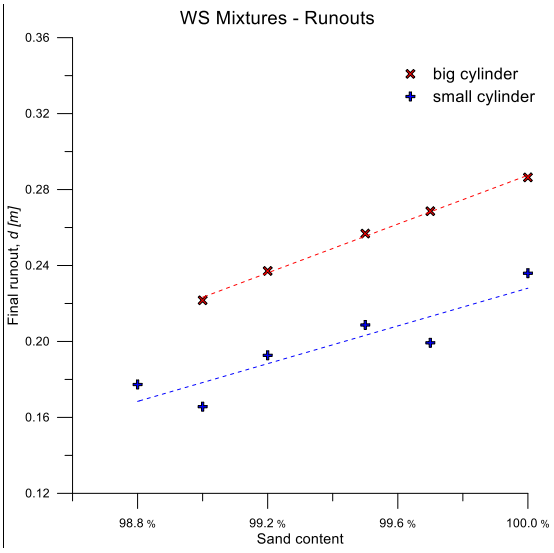

Figure 7.1.19 Runouts of the WS mixtures.

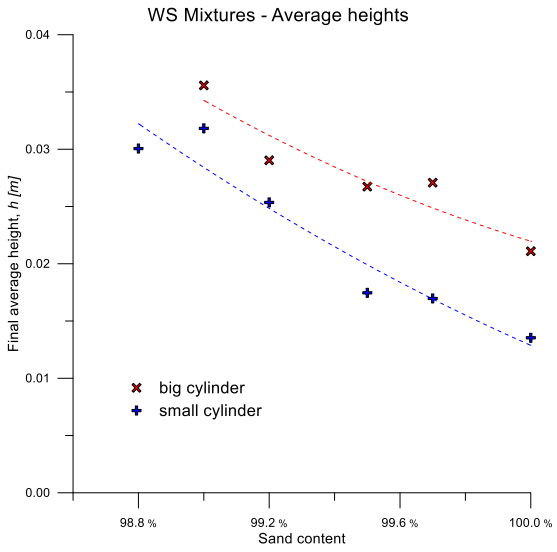

Figure 7.1.20 Average heights of the WS mixtures.

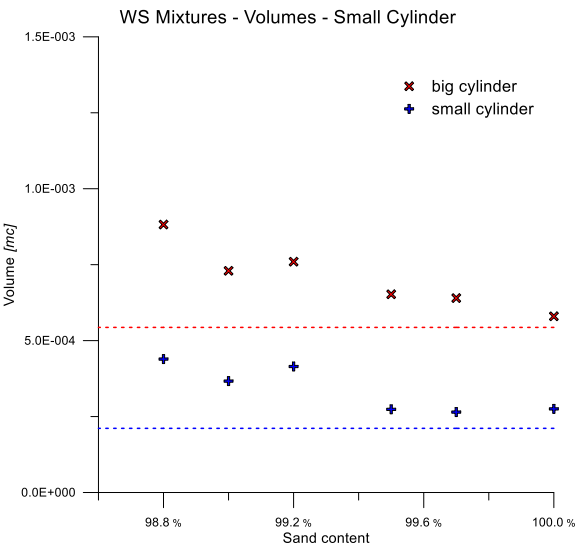

Figure 7.1.21 Volumes of the WS mixtures.

For the WS mixtures, the tests show that the runouts are directly proportional to the sand content. The big cylinder gives out more homogeneous data, even if both the lines included in Figure 7.1.19 are quite coherent. Anyway, the variations of the runouts are very mild, compared with the ones of the WK mixtures.

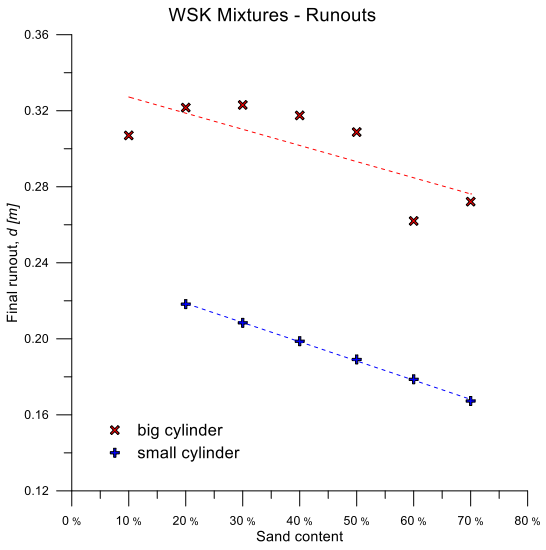

Figure 7.1.22 Runouts of the WSK mixtures.

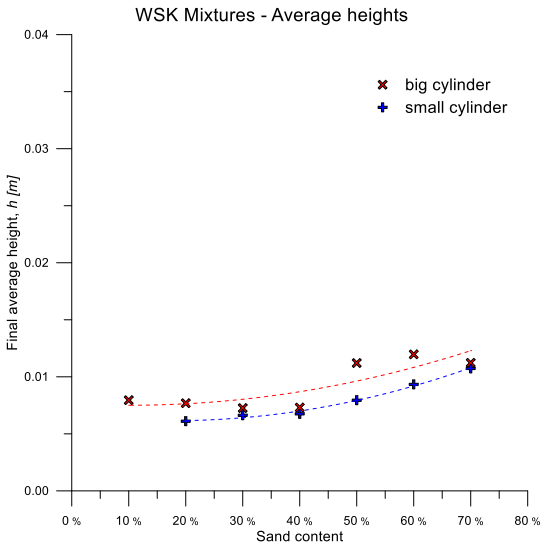

Figure 7.1.23 Average heights of the WSK mixtures.

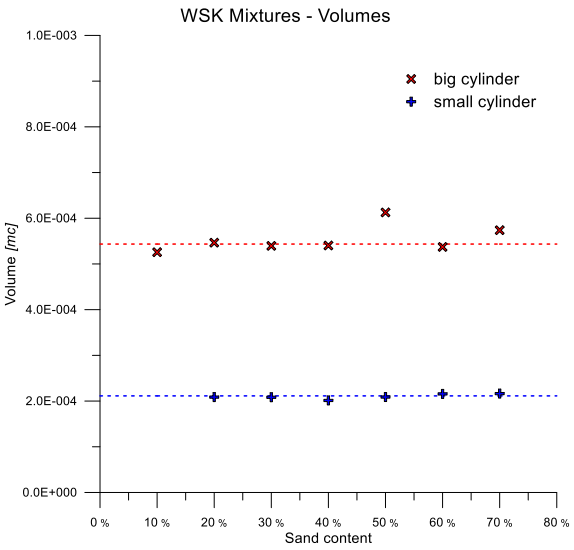

Figure 7.1.24 Volumes of the WSK mixtures.

It is evident that a high content of sand means that there is no water in the material. When the mass is completely dry, there is an evident difference between the central heights and the others taken into consideration. Increasing the water content, there is an increment in the apparent internal friction angle and accordingly it happens that the mass, instead of completely collapse, maintains a shape close to the initial cylindrical shape.

The data of volume reported in Figure 7.1.21 show the non-homogenous collapse that characterizes the WS mixtures. Especially for the texts with high amount of water, the differences between calculated and theoretical volumes demonstrate how the deposit shapes obtained from these tests is not axisymmetric at all. For that reason, it is believed that these tests are not suitable to be used for the numerical modeling. In fact, the mathematical model, for obvious reasons, can provide only axisymmetric results, considering that it simulates a homogenous single-phase material, while, probably, in the experimental texts the behavior is surely affected by also small non-homogeneity of water content.

As said before, it is quite evident how the behavior of the WSK tests is strictly connected with the cohesive matrix. The volumes comparison gives out good results, particularly with the medium cylinder and with the low amount of sand.

It can be noticed that Figure 7.1.22 shows a regular behavior of the collapse. The runout linearly increases with the increase of the density of the mixture, but does not change evidently its magnitude. The behavior of the big cylinder, instead, describes a less reliable comportment of the results. Even if a linear tendency of the runout on the sand content is still visible, it is evident that some irregularities are present. Especially speaking about the WSK1, WSK2 that have a runout smaller than WSK3, and WSK6, which has a too low value of runout compared with the others, it can be noticed that not all those results can be considered for the next calibration procedure.

Looking at Figure 7.1.24, it is evident that the problems of the WSK tests performed with the big cylinder presents some inaccuracies related to the axial-symmetry of the deposit. The comparison between the physical and the calculated volumes, in fact, leads to low values of errors.

Evidently, some problems in the material preparation and in the test execution led to inconsistent and therefore unreliable results.

Anyway, it is interesting to consider the WSK cases performed using the small cylinder, which are steadier and so can be considered to apply the next calibration strategy.

7.1.6 Numerical model construction

7.1.6.1 Introduction

The main goal of this phase is the calibration of the SPH-model, in order to identify the most reliable combinations of parameters you have to use considering the case you are simulating. The procedure is defined starting from the WK mixtures, and it is therefore extended to the WSK cases, small cylinder.

As mentioned in §6.4.2, it is opportune to identify some overall performance indices that are useful for the evaluation of the likelihood of each simulation. In fact, the calibration procedure produces a huge number of numerical results and it is required a simple and descriptive factor that provides the assessment of each one of those.

In the following paragraphs, the numerical code input files will be described. Furthermore, the way of preparing such a big number of input files, of running all the simulations and automatically of taking out the results will be presented below.

For all those simulations, Bingham rheological law is considered and the viscosity μ and the limit stress τ_0 have to be calibrated.

7.1.6.2 Input files

The Geoflow-SPH model needs some input files to run the simulations. All the characteristics of the geometry of the experimental apparatus, of the physical properties of the material and all the indications concerning the integration time steps have to be included in those files.

Particularly, for this case study this code subdivides the necessary information in three input files:

- "top" file: in this file all the geometrical information about the topography are included;
- "dat" file: this file contains the geometrical information of the source mass; it therefore includes the rheological parameters to calibrate and some others to impose. Finally, in this file the output variables are indicated;
- "MASTER.dat" file: this file is used to explicit the integration time steps, the total time of each simulation and the frequency with which the results are exported.

7.1.6.2.1 "top" file

The first information included in the "top" file indicates the geometry of the basal topography. *Ictop=1* means that you are working with a plane that has a constant elevation (Figure 7.1.25). The basal topography basically consists in a square of side 0.6m, equally subdivided in the two directions by 301 points. It means that the size of each element of the topography is 0.002m.

7.1.6.2.2 "dat" file

This is the most important file for defining the characteristics of the material. It includes the information about the dimensions of the cylinder. Practically, in this files the radius and the position of the base of the solid, the height of the cylinder and the number of element of elements with which discretize the mass are indicated. The cylinder is located in the center of the basal plane, has a radius respectively of 0.0465m and 0.0290m depending on which case study you are considering (Figure 7.1.26). The difference existing between the theoretical and the calculated volumes could lead to inaccurate results. For this reason, the height of material is varied depending on the case studied. Practically, the calculated volume is divided by the basal area of the cylinder and the theoretical height is therefore updated.

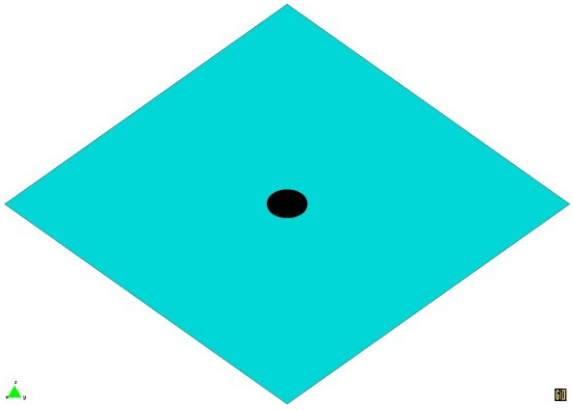

Figure 7.1.25 Topography of the system.

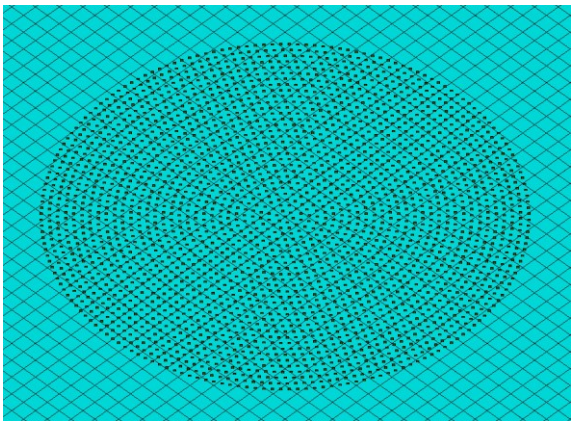

Figure 7.1.26 Disposition of the source mass.

The "dat" file, among other things, defines the rheological and physical parameters. In this file the density, the rheological law you want to use and, consequently to this, the rheological parameters of each simulation have to de expressed. In our case, as said before, Bingham's law is considered and the viscosity μ and the limit stress τ_0 are insert in the specific positions.

Finally, it is possible to indicate which kind of output variables you want to obtain. Heights, displacements, velocities and others can be included in the output file. In this case study, we are mostly interested in the comprehension of the heights of material when the flow is finished.

7.1.6.2.3 "MASTER.dat" file

In this file, it is imposed the total time of each flow, which is 0.5s. This decision allows the material to stop and, at the same time, restricts the collection of useless information that would unnecessarily large the output file. For the same reason, even if the calculation time step is fixed to 10^{-4}s, it is defined that the results have to be printed out just once every fifty.

7.1.6.3 Calibration strategy

The idea of the calibration strategy is to obtain a procedure that automatically composes the input files with the required information, runs the defined number of simulations you want to obtain and takes out from the output files of the program the useful information you need to analyze.

This strategy allow you to obtain a huge number of simulation that has to be a compromise that allows you to cover a sufficiently wide range of parameters without enlarging excessively the computational costs. In our cases, 100 simulations for each test are performed. For that reason, a variation range for each parameter is defined and therefore 100 combinations of parameters are obtained and included in the "dat" files. Each parameter varies between the minimum and the maximum value user defined with a logarithmic law, to cover a wider range, but to have at the same time a greater frequency around the most likely values.

The procedure can be summarize as follow, for each test:

- An opportune folder is created, in which the simulation, the output and the images folders are included.
- In the simulations folder, 100 different folders are created, containing the same "top" file and the same "MASTER.dat" file.
- The "dat" files are automatically updated with the right value of density, considering the test you are considering; the cylinder height is therefore corrected; finally, the 100 combinations of parameters are tidily placed in the files.
- 100 *Autoit v3* scripts are composed to subsequently run all the simulations. It is important to notice that the procedure thus constructed allow to run many simulations in parallel, depending on the number of processors your computer have. This drastically reduces the computational time required.
- 100 simulations are launched; from each of these, the data about the central section are extracted. The results of the last time step are plotted within the experimental data of the case study considered.
- The runouts, the maximum heights and the heights at the first and the second-third of the total runout are automatically obtained. These values will be used as performance indices for evaluating the likelihood of the results.
- The errors of the runouts, the maximum heights and the ones at the first and the second-third of the total runout between the simulated and the physical values are calculated. Finally, the best simulation is identified.

7.1.6.4 Output and costs

Using the postprocessor *GID*, the results versus time are viewable. As shown in Figure 7.1.27, the contour fill of the heights are easily exported and the behavior of the column is then clear. The gradual decrease of the maximum height takes place simultaneously with the collapse of the material, with an axial-symmetric increase of the runout.

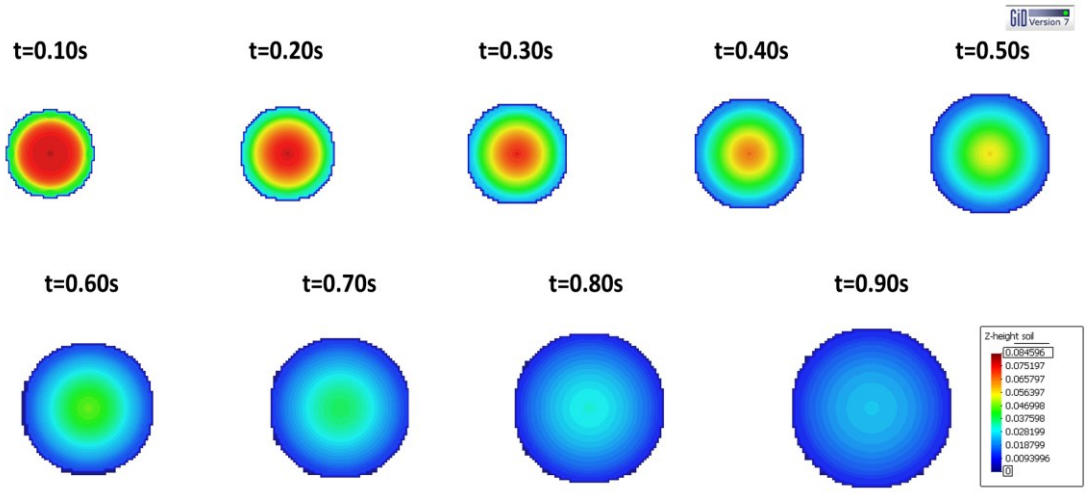

Figure 7.1.27 Countur fill of the heights of material during one simulation.

Finally, the cost of a similar procedure of calibration has to be considered. With the integration option imposed, one simulation can be completed in almost 3 minutes. The output files has then to be processed by *Matlab*, to export the desired information. This activity takes less than one minute each. An interesting detail that has to be underlined is the possibility to run at the same time as many simulations as many processors your computer has. With respect to the simulations of these paragraphs, 50 tests were performed simultaneously. Consequently, the total time required to complete 100 numerical calculations is less than 10 minutes. For the post elaboration of the output files, the total time necessary is about one hour.

7.1.6.5 Simulations of the WK mixtures, small cylinder

The minimum and maximum values of under-calibration parameters, τ and μ, adopted for the six groups of simulations (100 simulations for each laboratory WK text in one cylinder) are reported in the Table 7.1.8.

After having performed all the 600 simulations, it is possible to compare for each WK mixture, the physical data with the simulated ones. In Figure 7.1.28 - Figure 7.1.33 the physical profiles obtained by the experimental tests is drawn with the black line. Using colored lines, the results of all the simulations are also drained. The first thing is important to notice is that the spread of the simulations well cover the experimental data: it means that the variation ranges given to the parameters were acceptable.

While the numerical results are always symmetric, the laboratory results are not. Anyway, it is possible to recognize a similar behavior that suggests that the actual model is able to correctly simulate the case study.

WK Mixtures, small cylinder				
Mixture	*Kaolin %*	*Density [kg/m³]*	*Variation range of τ [Pa]*	*Variation range of μ [Pa s]*
WK1	*56.5*	1533.3	20.00 ÷ 200.00	0.50 ÷ 50.00
WK2	*54.5*	1505.3	20.00 ÷ 100.00	0.50 ÷ 50.00
WK3	*53.3*	1487.7	20.00 ÷ 30.00	0.50 ÷ 2.00
WK4	*51.9*	1469.6	20.00 ÷ 30.00	0.50 ÷ 2.00
WK5	*50.5*	1450.8	5.00 ÷ 30.00	0.05 ÷ 2.00
WK6	*47.4*	1411.4	1.00 ÷ 20.00	0.05 ÷ 2.00

Table 7.1.8 Density and variation ranges for the parameters for WK mixtures, small cylinder.

Among all the 100 simulations, it is important to find the way to identify the ones that better reproduce the experimental results. As said before, the indices used to define each profile and to compare the results are the runout and the heights. It is decided not to consider the maximum heights because the behavior of both the simulations and the experimental results shortly describe the form of the deposit and they would risk misleading the evaluation.

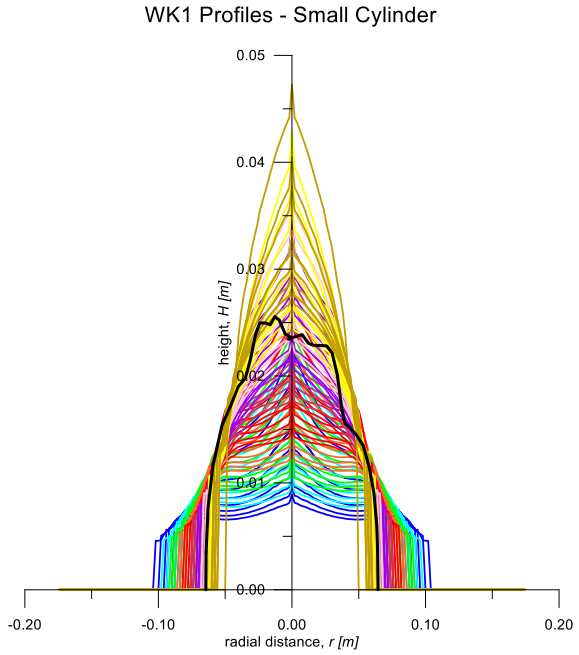

Figure 7.1.28 Profiles of the WK1 mixture compared with the simulations, small cylinder.

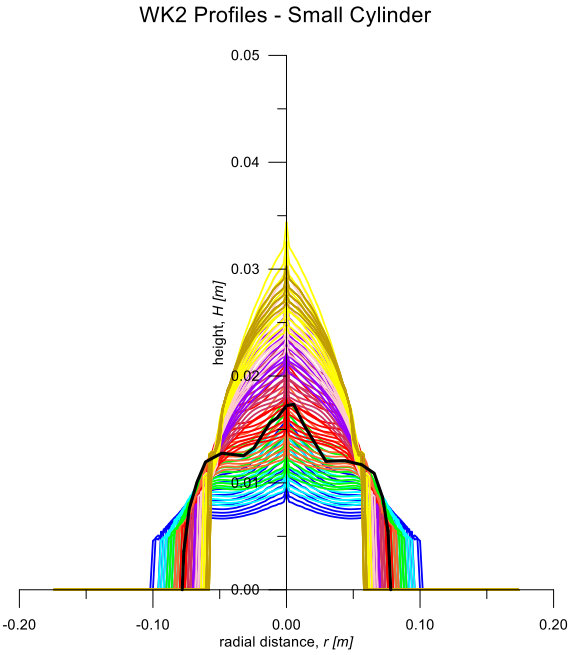

Figure 7.1.29 Profiles of the WK2 mixture compared with the simulations, small cylinder.

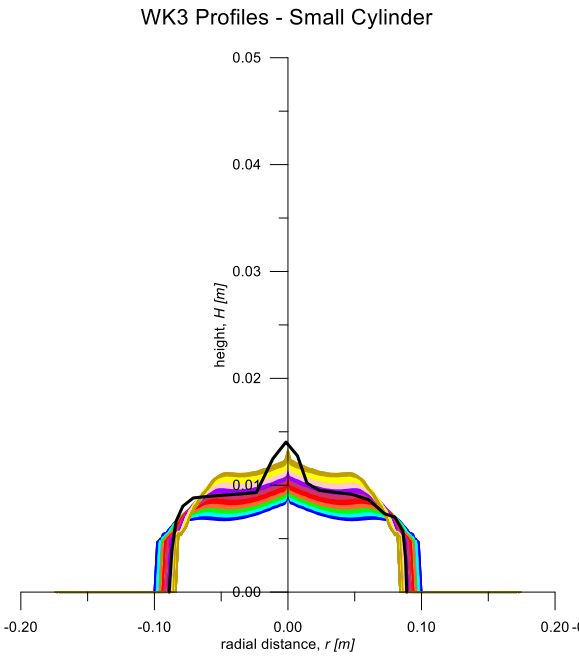

Figure 7.1.30 Profiles of the WK3 mixture compared with the simulations, small cylinder.

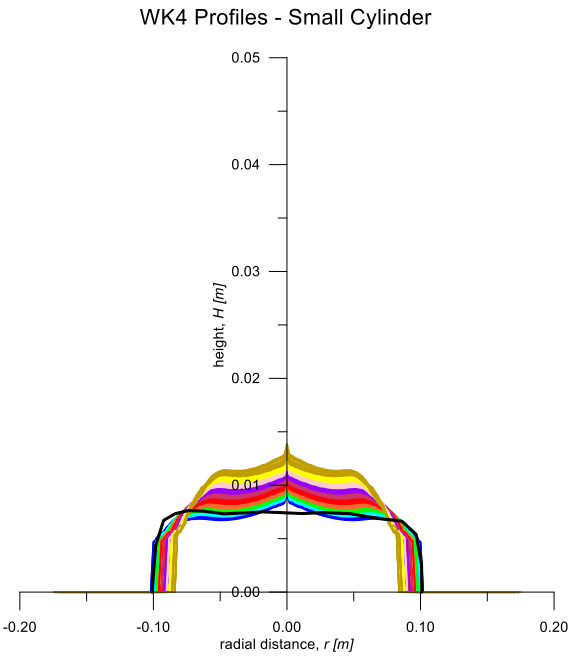

Figure 7.1.31 Profiles of the WK4 mixture compared with the simulations, small cylinder.

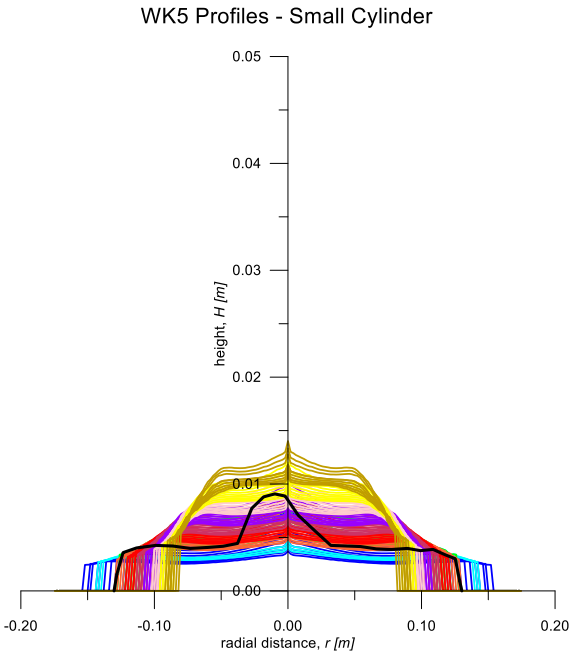

Figure 7.1.32 Profiles of the WK5 mixture compared with the simulations, small cylinder.

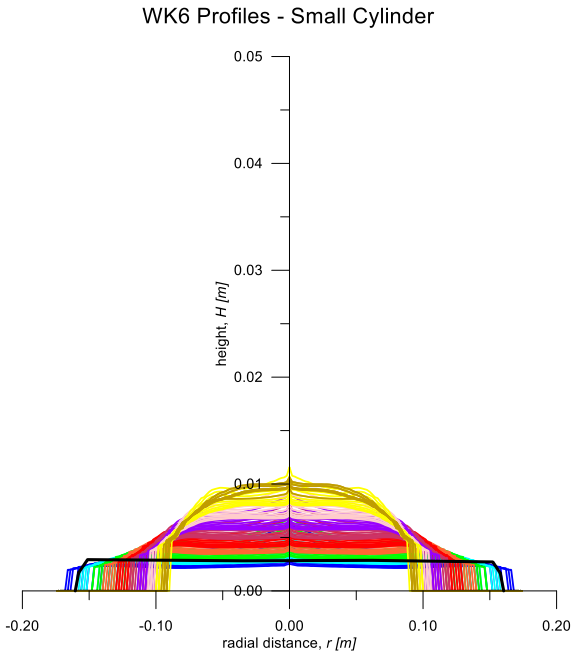

Figure 7.1.33 Profiles of the WK6 mixture compared with the simulations, small cylinder.

Considering the percentage error of each simulation compared with the experimental data, it is possible to calculate a performance index correlate to the runout and one for each height considered. A global index is therefore defined as follow:

$$E^{\%}_{total} = 0.50\ E^{\%}_{runout} + 0.25\ E^{\%}_{height\ 1} + 0.25\ E^{\%}_{height\ 2} \qquad \textit{Equation 7-2}$$

This formulation gives a different weight to the percentage error of the runout with respect to the ones to the heights. Basically, $\mathrm{E}^{\%}_{\mathrm{runout}}$ is considered with the same importance that has the summary of the two $\mathrm{E}^{\%}_{\mathrm{height}}$. The performance index so defined allows identifying the most similar simulation among all the available ones, without looking at them one by one.

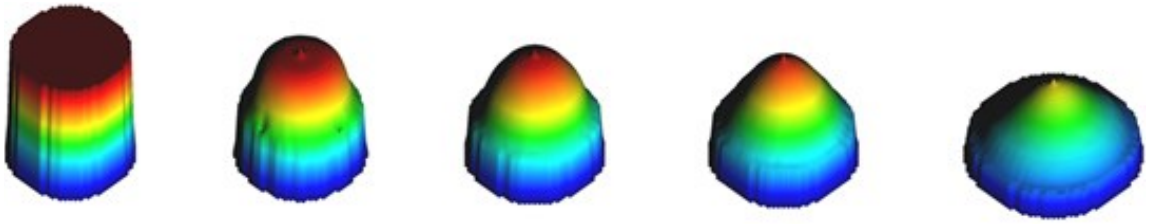

Figure 7.1.34 Contour fill of the output of one simulation in different time steps.

Looking at the numerical profiles, it is interesting to notice the central tip always present. The reason of this phenomenon has probably to be attributed to the confinement of the central point of the source mass (Figure 7.1.34). Due to the axial-symmetry of the system, the central point is in fact surrounded on all sides by points that move deforming at the same time in equal measure. Also for this reason, the maximum height is not considered as a reliable value for purposes of comparison between simulated and measured results.

Analyzing the errors distribution obtained for each test, it is possible to identify the simulation that reach the lowest value of $E^{\%}_{total}$. It is interesting to evaluate the likelihood of the results achieved comparing the deposit profiles of the laboratory test and of the best simulation respectively.

In Figure 7.1.35 - Figure 7.1.40 those results are outlined. It is evident how the numerical code is able to reproduce with high quality all the WK tests performed with the small cylinder. In all the figures, the simulation copy exactly the runout of the physical test and the requirement of likelihood on the H1 and H2 reference heights is always largely satisfy.

Some differences in the behavior can be noticed in the central part of the deposit. Anyway, it is assumed that this variables are not so descriptive of the event, because of irregularities of both the numerical model and the experimental test results in this position.

After all, it can be said that the model is able to reproduce the case study in a more than satisfactory way.

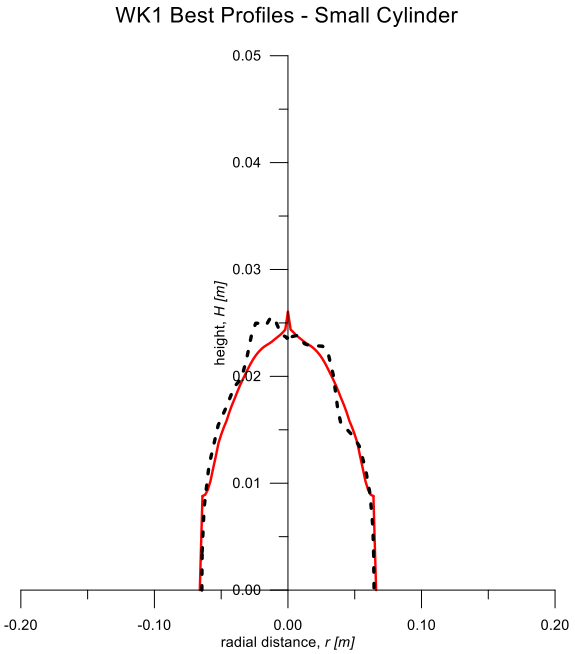

Figure 7.1.35 Profiles of the best simulation for the WK1 mixture, small cylinder.

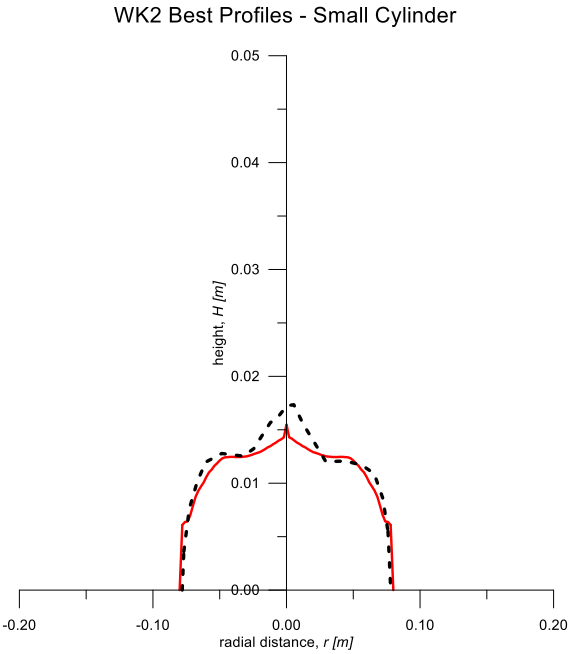

Figure 7.1.36 Profiles of the best simulation for the WK2 mixture, small cylinder.

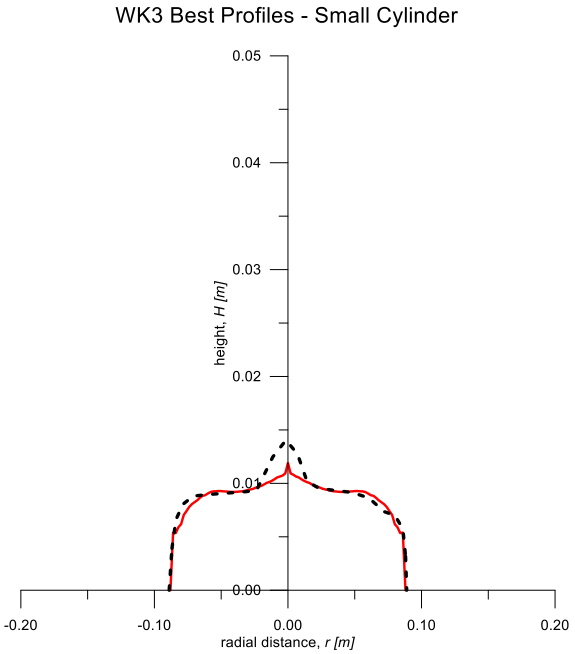

Figure 7.1.37 Profiles of the best simulation for the WK3 mixture, small cylinder.

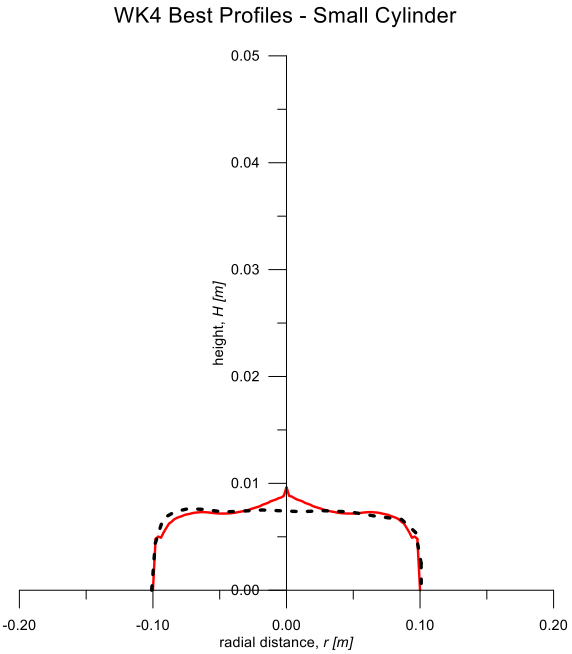

Figure 7.1.38 Profiles of the best simulation for the WK4 mixture, small cylinder.

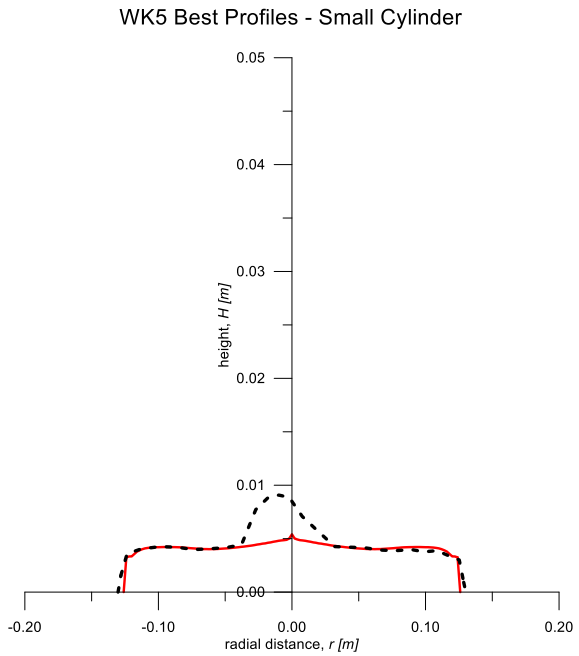

Figure 7.1.39 Profiles of the best simulation for the WK5 mixture, small cylinder.

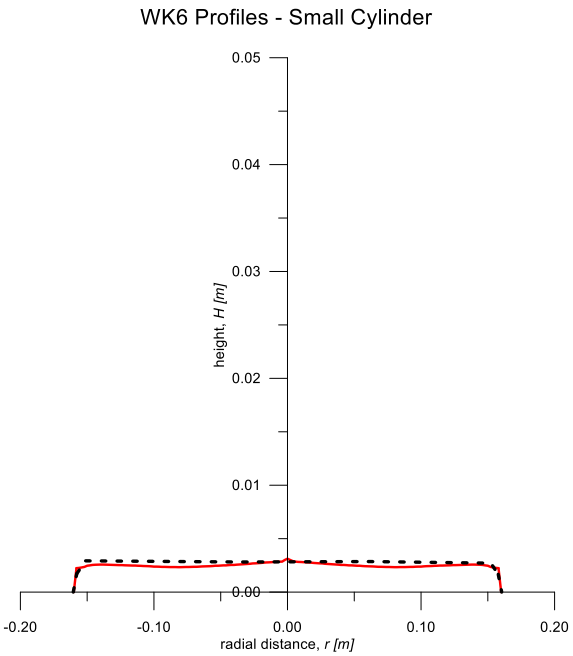

Figure 7.1.40 Profiles of the best simulation for the WK6 mixture, small cylinder.

It is interesting to look at the values of the parameters obtained by this calibration procedure and the values of the percentage errors for those simulations (Table 7.1.9).

The total error is always lower than 8% and, if we neglect the last test, it is even smaller. This control allows us to confirm with what we have previously stated about the goodness of the numerical results.

WK Mixtures, small cylinder								
Mixture	*Kaolin %*	c_v	τ *[Pa]*	μ *[Pa s]*	$E^{\%}_{runout}$	$E^{\%}_{height\ 1}$	$E^{\%}_{height\ 2}$	$E^{\%}_{total}$
WK1	*56.5*	*0.33*	71.88	10.77	1.0%	10.5%	2.2%	3.7%
WK2	*54.5*	*0.32*	40.90	2.32	0.4%	3.4%	0.6%	1.2%
WK3	*53.3*	*0.31*	27.42	1.08	1.4%	0.6%	1.3%	1.1%
WK4	*51.9*	*0.29*	21.89	0.58	3.2%	0.4%	0.5%	1.8%
WK5	*50.5*	*0.28*	7.45	0.17	5.1%	3.4%	1.1%	3.6%
WK6	*47.4*	*0.26*	2.71	0.05	1.8%	13.2%	13.7%	7.6%

Table 7.1.9 Parameters obtained from the calibration procedure and relative errors.

In this table, c_v expresses the volumetric solid content, calculated by the ration between the solid volume and the total volume of the mixture.

We can now plot the parameters obtained from the calibration procedure with respect to this volumetric solid content and notice that they have exponential trends, which is coherent with literature (Kaitna et al., 2007).

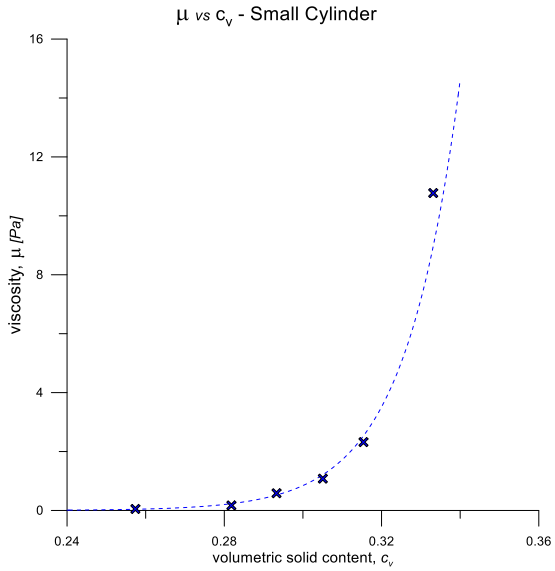

Figure 7.1.41 Behavior of μ with respect to the c_v of the WK mixtures, small cylinder.

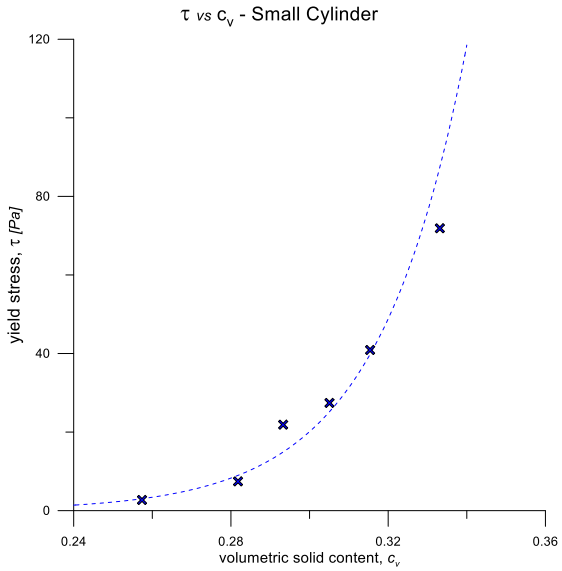

Figure 7.1.42 Behavior of τ with respect to the c_v of the WK mixtures, small cylinder.

7.1.6.6 Simulations of the WK mixtures, big cylinder

WK Mixtures, big cylinder				
Mixture	*Kaolin %*	*Density [kg/m³]*	*Variation range of τ [Pa]*	*Variation range of μ [Pa s]*
WK1	*56.5*	1533.3	25.00 ÷ 200.00	5.00 ÷ 50.00
WK2	*54.5*	1505.3	20.00 ÷ 100.00	1.00 ÷ 50.00
WK3	*53.3*	1487.7	15.00 ÷ 50.00	0.50 ÷ 10.00
WK4	*51.9*	1469.6	10.00 ÷ 40.00	0.10 ÷ 5.00
WK5	*50.5*	1450.8	5.00 ÷ 30.00	0.05 ÷ 5.00

Table 7.1.10 Rheological parameters range for WK mixtures, big cylinder.

The procedure described above is now repeated for the second case study. The five tests made with water and kaolin using the big cylinder are in this paragraph dealt.

In Table 7.1.10, the densities and the range of variation of each parameters are explicated. Compared to what was done with the case of the medium cylinder, in this case the parameters are varied in a more various ways. The minimum and maximum values are decided taking into account the results obtained previously, but trying to get a trend more orderly.

As made before, 100 simulations are performed again, including the geometrical dimension of the experimental apparatus now used. The same strategy to judge the tests is here again adopted. Among all the profiles extracted from the output files of the numerical code, it is possible to identify the most similar ones to the experimental results.

In the WK1 profile (Figure 7.1.43 and Figure 7.1.44) is evident the influence of the boundary conditions of the experiment.

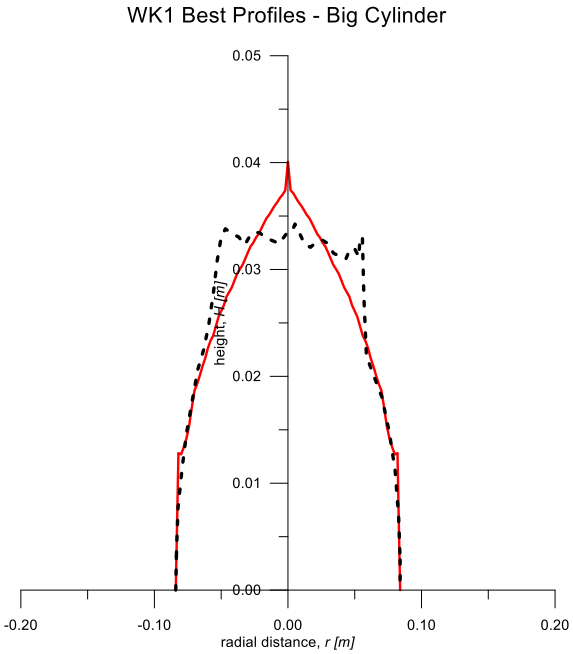

Figure 7.1.43 Profiles of the best simulation for the WK1 mixture, big cylinder.

Figure 7.1.44 Picture of the WK1 deposit.

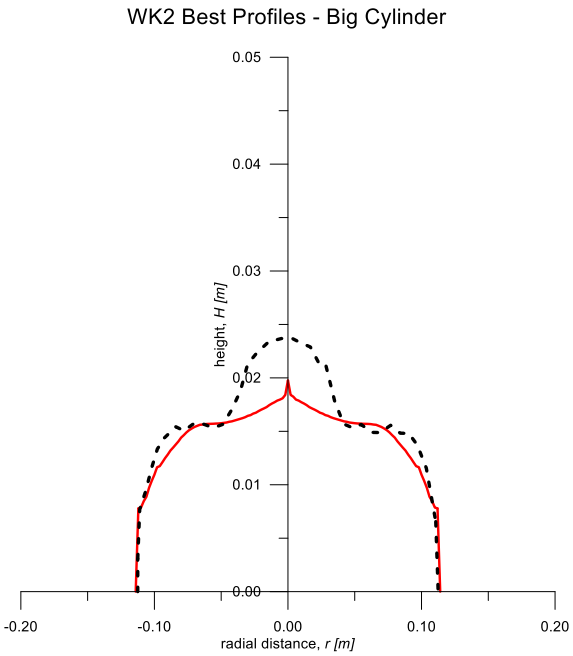

Figure 7.1.45 Profiles of the best simulation for the WK2 mixture, big cylinder.

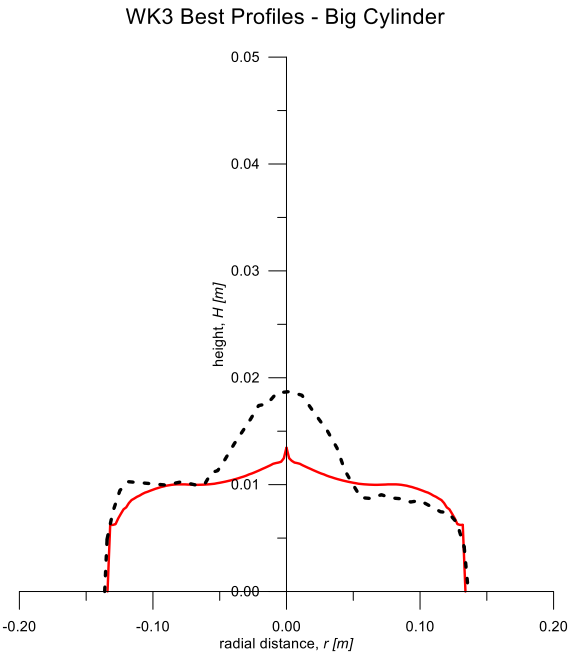

Figure 7.1.46 Profiles of the best simulation for the WK3 mixture, big cylinder.

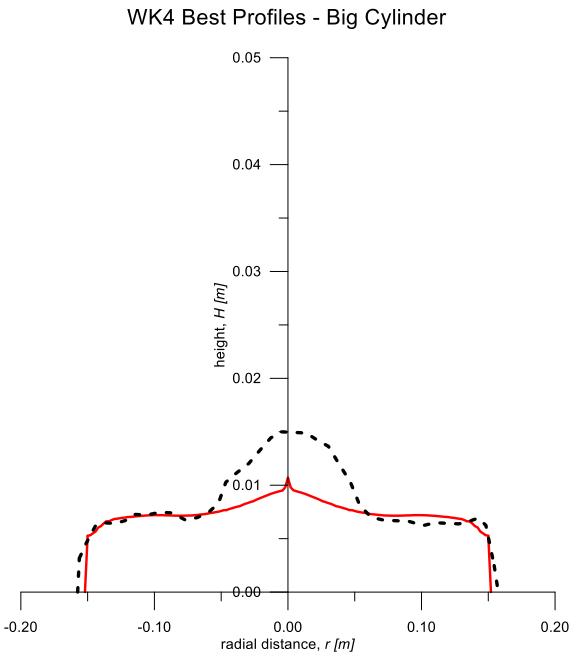

Figure 7.1.47 Profiles of the best simulation for the WK4 mixture, big cylinder.

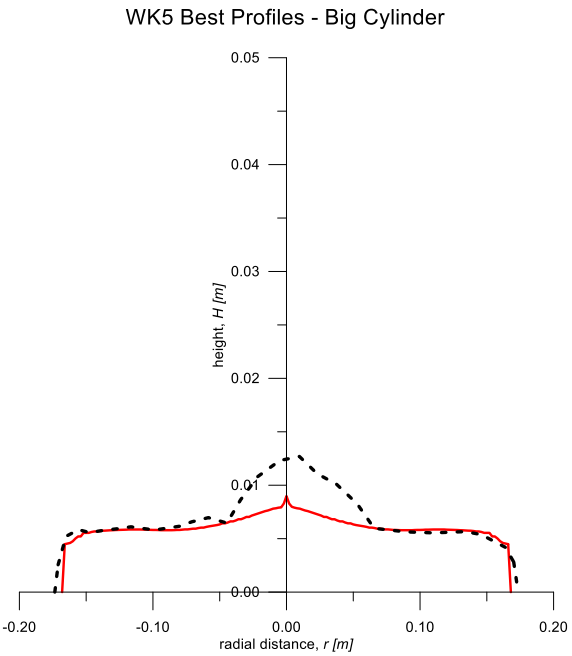

Figure 7.1.48 Profiles of the best simulation for the WK5 mixture, big cylinder.

In almost all the experimental profiles, an extra accumulation in the central part of the deposits is evident. It is not easily possible to reproduce this behavior because it is mainly due to the procedure adopted for the laboratory tests. Anyway, the likelihood of the numerical results is absolutely appreciable.

The runouts in all those cases are always very close to the measured ones. In fact, the errors on these values (Table 7.1.11) is less than 5%. The errors of the heights are a little higher and reach the value of 18%. It has to be underlined, anyway, that this fact happens with just one of the two heights considered. While the simulations gives always-symmetric values, the experimental data are commonly non-symmetric due to the imperfect conditions of the experimental apparatus.

The overall error remains in all the cases under the value of 10%. That result confirms the good ability of the numerical model to reproduce such a similar collapse and allows considering reliable the parameters obtained by this calibration.

Again, the graphs of the rheological parameters with respect to the coefficient of solid volume content are drawn. As sawn in the previous case, the behavior of these values follows again an exponential trend.

Because the work was carried out with both cylinders using the same mixtures, it is interesting now to compare the parameters obtained from the calibration of the two groups of case studies. In Figure 7.1.51 and Figure 7.1.52 all the results obtained are plotted.

WK Mixtures, big cylinder								
Mixture	*Kaolin %*	*cv*	τ *[Pa]*	μ *[Pa s]*	$E^{\%}_{runout}$	$E^{\%}_{height\ 1}$	$E^{\%}_{height\ 2}$	$E^{\%}_{total}$
WK1	*56.5*	*0.33*	79.37	23.21	2.7%	0.6%	1.1%	1.8%
WK2	*54.5*	*0.32*	40.90	2.39	0.7%	11.9%	5.5%	4.7%
WK3	*53.3*	*0.31*	25.61	0.70	3.4%	17.7%	6.2%	7.7%
WK4	*51.9*	*0.29*	21.60	0.24	5.1%	9.3%	11.8%	7.8%
WK5	*50.5*	*0.28*	16.51	0.14	4.6%	11.4%	16.6%	9.3%

Table 7.1.11 Parameters obtained from the calibration procedure and relative errors.

Considering that both μ and τ increase with the cohesive behaviour of the material, for higher values we expect shorter runout distances and higher final heights as observed in the previous experimental data.

It is evident from Figure 7.1.51 and Figure 7.1.52 that a good agreement is observable between the calibrated Bingham's parameters of the two cylinder sizes especially for lower volumetric solid content (more liquid mixtures). A greater difference is recognizable for WK1 (the most cohesive mixture), particularly about viscosity value. The reason of this discrepancy can be attributed to the boundary conditions, which are unavoidable in the laboratory tests and instead were necessary neglected in the simulations. In the experimental setup, the cylinder used for collapse tests is lifted, dragging the external thin layer of material in touch with the inner surface of the tube. Supposing the thickness of this layer dependent on the material viscosity, we can assume that the boundary effect of the cylinder is stronger for smaller cylinders and high value of μ.

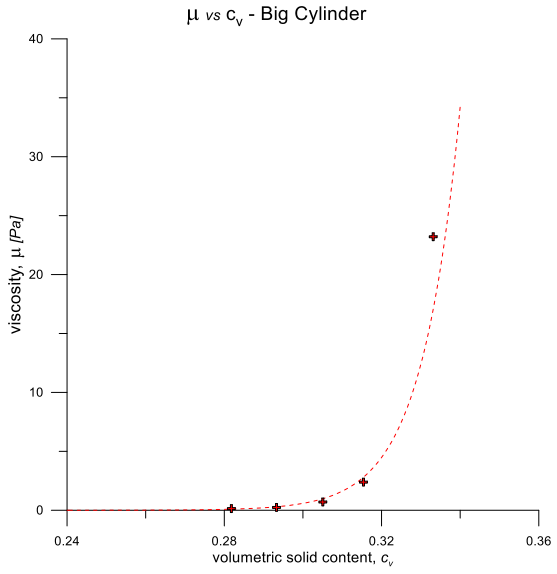

Figure 7.1.49 Behavior of μ with respect to the c_v of the WK mixtures, big cylinder.

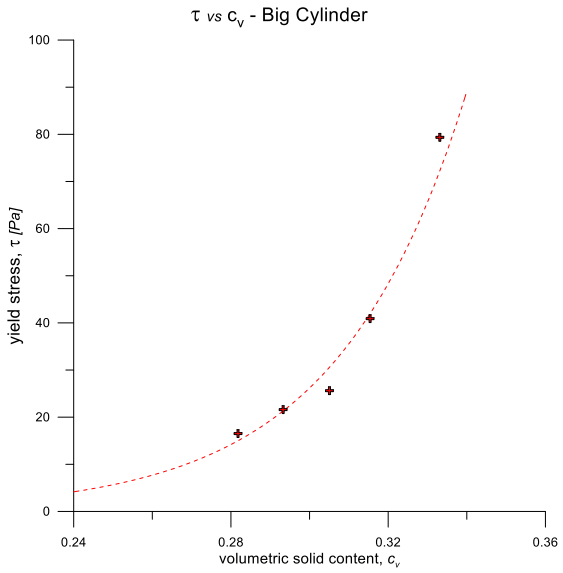

Figure 7.1.50 Behavior of τ with respect to the c_v of the WK mixtures, big cylinder.

On the other hand, SPH simulations are obtained with a depth integrated equation system with boundary conditions, which are partially unable to represents the initial lifting phase.

From the analysis of the video sequences of the two WK1 mixtures with different cylinders, two different behaviors were observed in the initial phase: the radial spreading of the material for the small diameter starts with a certain delay which is due to the stronger dragging effect on the inner mass. As consequence, the mass accumulates more potential energy, which leads to higher radial velocities of the flow and a larger final runout. In the calibration phase, this effect produces an underestimation of the viscosity value.

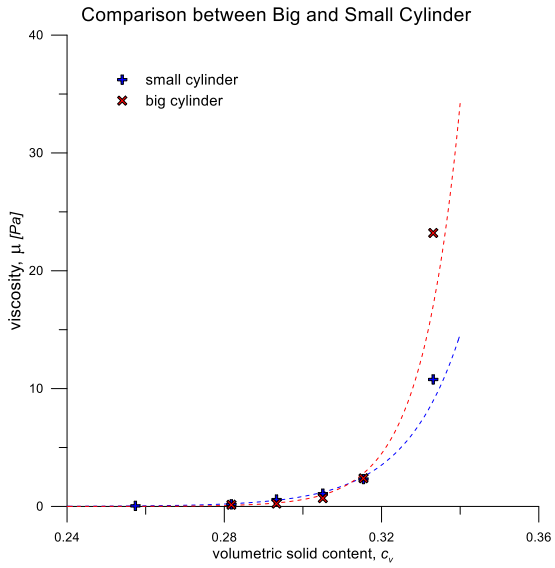

Figure 7.1.51 Comparison of the parameter μ obtained respectively with the small and the big cylinder.

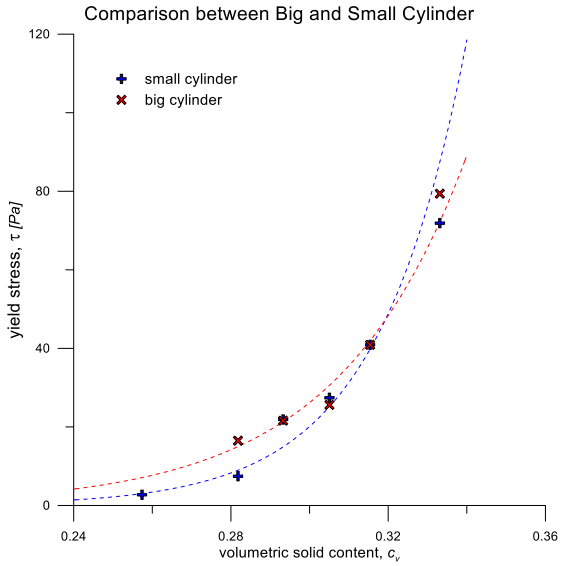

Figure 7.1.52 Comparison of the parameter τ obtained respectively with the small and the big cylinder.

7.1.6.7 Simulations of the WSK mixtures, medium cylinder

WSK Mixtures, small cylinder				
Mixture	*Kaolin*	*Density*	*Variation range of* τ	*Variation range of* μ
	%	*[kg/m³]*	*[Pa]*	*[Pa s]*
WSK2	*20.0*	1478.395	10.00 ÷ 50.00	0.01 ÷ 5.00
WSK3	*30.0*	1492.575	10.00 ÷ 70.00	0.01 ÷ 5.00
WSK4	*40.0*	1507.030	10.00 ÷ 90.00	0.01 ÷ 6.00
WSK5	*50.0*	1521.767	10.00 ÷ 100.00	0.01 ÷ 6.00
WSK6	*60.0*	1536.796	20.00 ÷ 110.00	0.05 ÷ 10.00
WSK7	*70.0*	1552.124	20.00 ÷ 120.00	0.05 ÷ 10.00

Table 7.1.12 Density and variation ranges for the parameters for WSK mixtures, small cylinder.

Above all the other tests described in §7.1.4, after having calibrated the WK tests, the mail goal is to try to repeat the same strategy with the WSK mixtures. The intention is to understand the role that the introduction of granular material plays in the parameters behavior, depending on the sand content included.

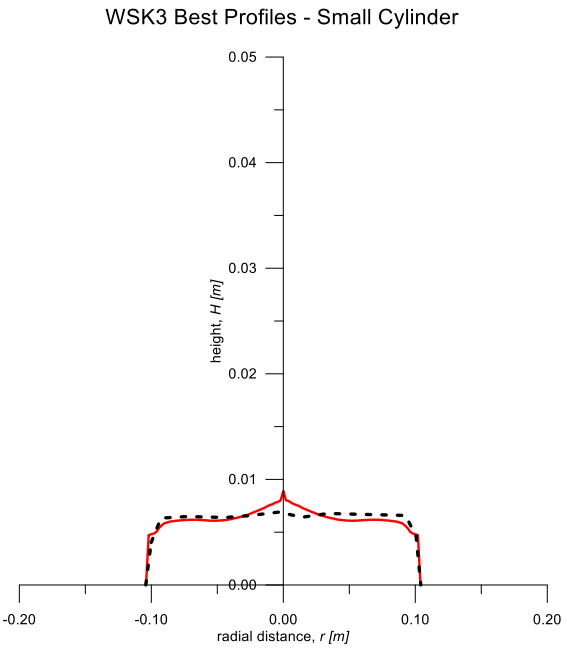

Figure 7.1.53 Profiles of the best simulation for the WSK2 mixture, small cylinder.

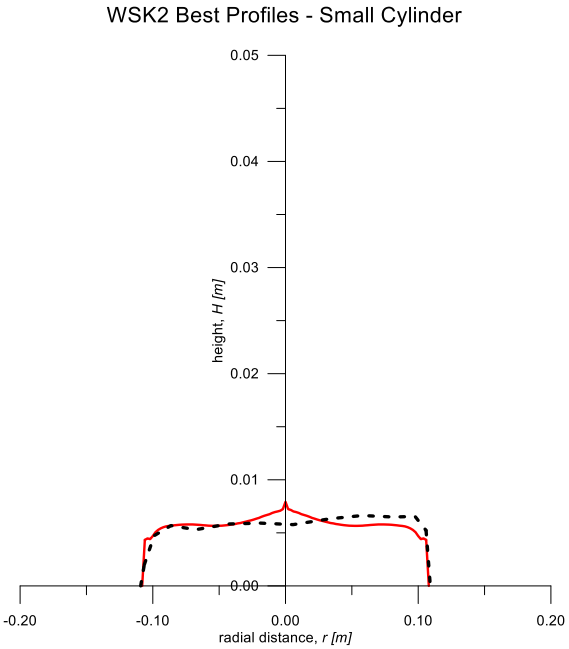

Figure 7.1.54 Profiles of the best simulation for the WSK3 mixture, small cylinder.

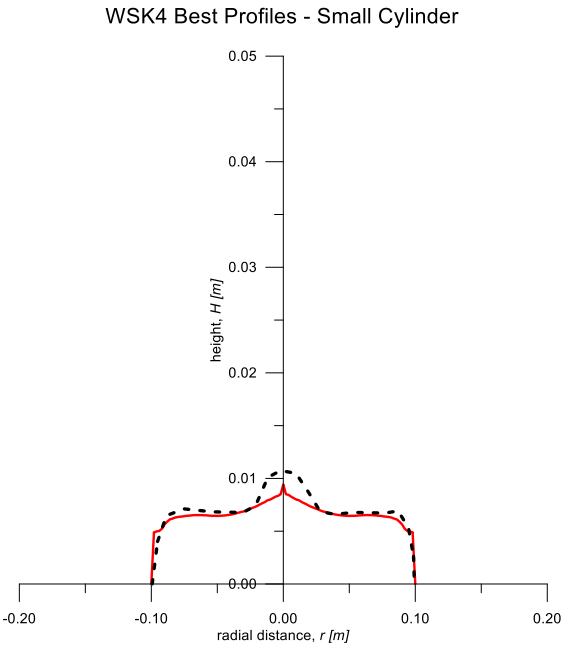

Figure 7.1.55 Profiles of the best simulation for the WSK4 mixture, small cylinder.

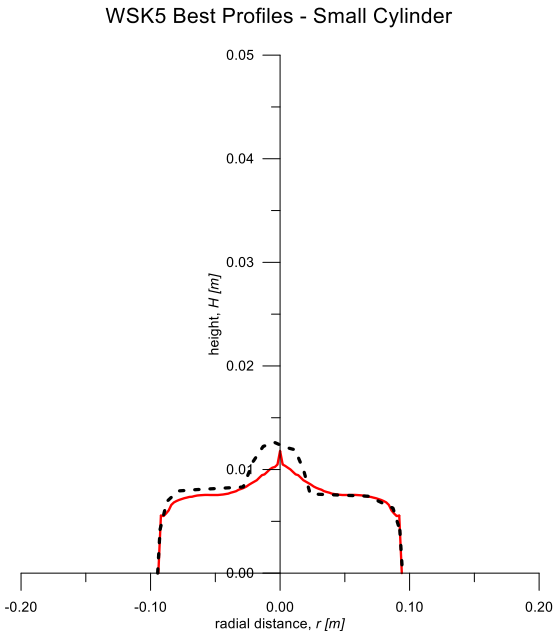

Figure 7.1.56 Profiles of the best simulation for the WSK5 mixture, small cylinder.

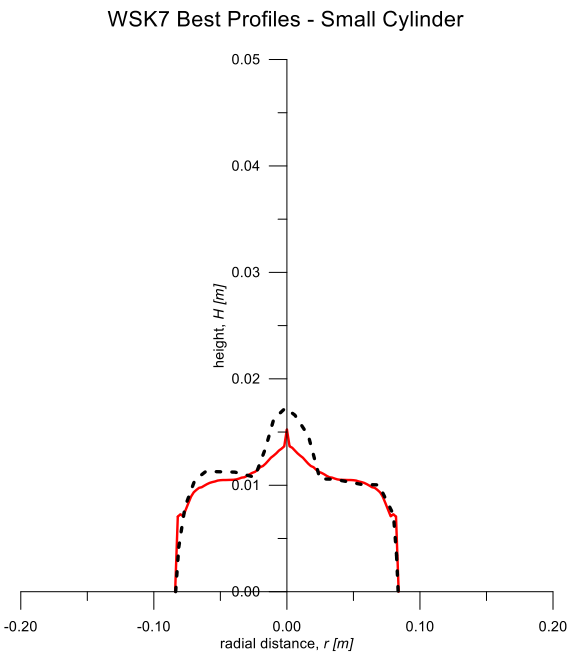

Figure 7.1.57 Profiles of the best simulation for the WSK6 mixture, small cylinder.

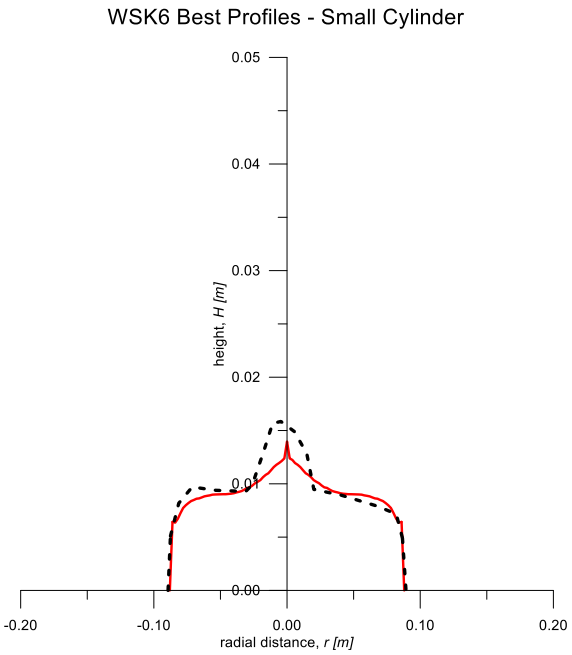

Figure 7.1.58 Profiles of the best simulation for the WSK7 mixture, small cylinder.

It is opportune to notice that the experimental data about the case of the big cylinder are not so reliable. Probably, it would be appropriate to repeat some tests, such as the WSK5 and WSK6, in which the presence of lumps has made the material not homogeneous and therefore not regular. The cause of this is probably linked to an incorrect procedure of preparation and mixing of the material. For all these reasons, just the small cylinder cases were taken into account for the application of the procedure of calibration so prepared. In Table 7.1.12, the main parameters of the WSK case studies are explicated.

WSK Mixtures, small cylinder									
Mixture	*Sand %*	*Density [kg/m³]*	c_v	τ *[Pa]*	μ *[Pa s]*	$E^{\%}_{runout}$	$E^{\%}_{height\ 1}$	$E^{\%}_{height\ 2}$	$E^{\%}_{total}$
WSK0	*0.0*	1450.80	0.32	7.45	0.17	5.1%	3.4%	1.1%	3.6%
WSK2	*20.0*	1478.39	*0.41*	17.10	0.32	3.2%	0.4%	7.6%	3.6%
WSK3	*30.0*	1492.57	*0.46*	23.75	0.32	2.4%	1.6%	5.8%	3.1%
WSK4	*40.0*	1507.03	*0.52*	33.89	0.35	1.2%	10.8%	2.6%	3.9%
WSK5	*50.0*	1521.77	*0.58*	46.42	0.35	3.0%	2.7%	6.1%	3.7%
WSK6	*60.0*	1536.79	*0.65*	62.32	0.53	4.1%	1.9%	4.3%	3.6%
WSK7	70.0	1552.12	0.72	80.59	0.95	2.3%	1.5%	4.2%	2.6%

Table 7.1.13 Parameters obtained from the calibration procedure and relative errors.

It has to be noticed that performing 100 simulations with the variation ranges decided means to choose 10 values for each parameters. The viscosity and the yield stress contribute both to increase the total stress, so it can happen that different combinations of parameters lead to similar results.

Among the values included in the numerical model, the values the better reproduce the laboratory cases are reported in Table 7.1.13.

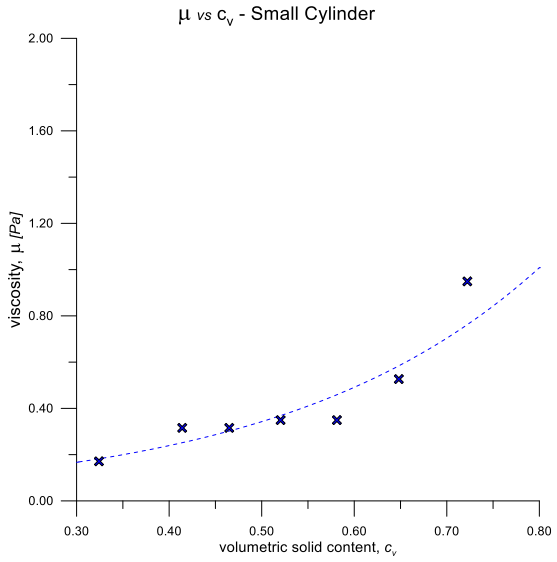

Figure 7.1.59 Behavior of μ with respect of the c_v of the WSK mixture, small cylinder.

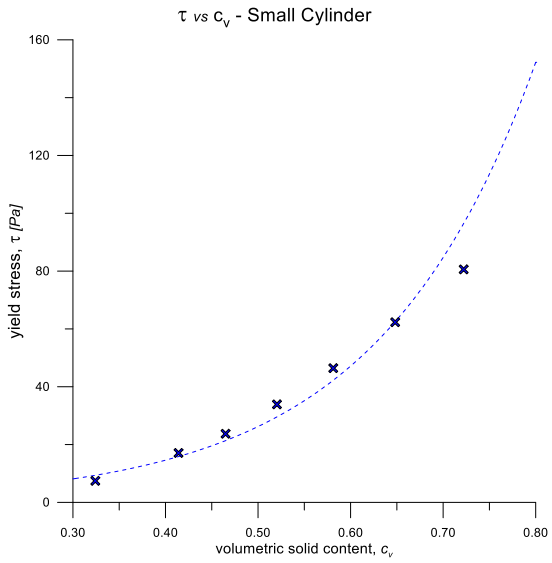

Figure 7.1.60 Behavior of τ with respect of the c_v of the WSK mixture, small cylinder.

It is interesting to look at the behavior of those calibrated parameters depending on the volumetric content of solid. It is evident that increasing the sand fraction for a constant water-kaolin ratio gives rise to an increase of the calibrated μ and τ to fit a more sticky and cohesive behaviour of the WKS mixtures. The variation due to the adding of sand is larger for the yield stress, which presents values varying from 10 to 80 Pa (an increase of 800% respect the value obtained for WK5 mixture). The variation of viscosity is only 500% that is not very large if compared with the viscosity variation observed in relation to the solid concentration in the WK mixtures (as reported in Table 7.1.9 and Table 7.1.11, the viscosity in WK tests increases quite 2 orders of magnitude).

Figure 7.1.59 shows that the values of μ obtained for the WSK2 and WSK3, and for WSK4 and WSK5 are respectively equal one another. This fact can be explained considering that the parameters used for the simulations are logarithmically distributed to increase the frequency of the most reliable values, but each parameter varies just ten times. A higher value of the viscosity imposed in the model for the WSK3 and the WSK5 mixtures, or a lower for the WSK2 and WSK4 ones could rise to more regular results.

Anyway, the total percentage errors suggest that all the results obtained are reliable and therefore accettable.

7.1.7 Conclusions

The laboratory results underlined how kaolin content change the behavior of the collapse. The runout is in fact directly dependent on this cohesive fraction.

The introduction of granular material caused changes in the final shape of the mass flowing, even if the entity of these variations is little compared with the one caused by the kaolin content.

Finally, the water-sand experiments cannot be sufficiently characterized by the acquisition of the diametric profile. These tests needs a three-dimensional survey of the deposit to be described. Anyway, the application of the calibration procedure is prevented by the non-axial symmetrical nature of these cases. It would be necessary to use a 3D numerical model to capture their heterogeneous behavior.

The model is able to reproduce the case collapse of a column of cohesive material, in terms of final deposit shape. The choice of the performance index to use in the calibration procedure expresses a good ability to fully characterize the phenomenon.

Among all the simulations performed, the identification of the most similar one was easily and automatically obtainable. At the same time, the couple of parameters that better behaves in the reproduction of the laboratory result is immediately available.

Unfortunately, it is not possible to compare the calibrated rheological parameters with the physical ones. Anyway, the exponential dependency of the viscosity and the yield stress on the volumetric solid content is coherent with what expected.

Therefore, similar parameters have been obtained changing the dimension of the collapsing mass. This confirm the strength of the results achieved.

It is true that the case study is simple and probably this fact helped the goodness of the calibration procedure. In any case, it has to be noticed that some approximations are still present, such as the different boundary conditions between the physical and the numerical model, which influence the initial period of the collapse.

The likelihood between laboratory measurements and numerical results is evident looking at the comparison of the respective profiles. The calculation of the error objectively confirms the good agreement achieved.

To improve the calibration procedure, some simulations could be performed again, reducing the variation range of each parameter and further decreasing the uncertainty in the determination of the optimum rheological variables.

Even if the runout numerical model adopted for the simulation of the experimental tests is based on a simplified representation of the real phenomena, it seems sufficiently reliable for the analysis of this simply test. Moreover, the Bingham law seems to well describe the behavior of WSK mixtures even when the sand fraction is very large (around 80% of the total weight).

7.2 SMALL-SCALE FLUME EXPERIMENTS

7.2.1 Introduction

The good results achieved in the §7.1 suggests to apply the calibration procedure for a case of more complex study. A fundamental requirement also in this second case, however, must be the precise knowledge of the experimental apparatus geometry and the material used. More in fact turn out to be the uncertainties during the test execution and data capture, less reliable will be the measurements obtained.

In collaboration with the University of Vienna (Universität für Bodenkultur Wien), many flume test are carried out. The materials used are again water, kaolin and sand and many information about the behavior of the moving mass are obtained. The experimental apparatus maintains fairly simple geometric characteristics and is composed of an inclined plane connected to a horizontal deposit area. The slope of the channel is 19 degrees, a value that allows an evolution of motion such that the moving mass can acquire an inertial speed sufficient to reach the zone of deposit. The channel has not been more inclined to avoid the onset of excessive speed. It is therefore interesting to note that the speeds achieved in tests are included in a range between 1.8m/s and 4m/s. In literature these values of velocities are commonly present (Costa, 1984; Coussot & Meunier, 1996). Many authors distinguish the type of hazard according to the typical speed. For values between 0.5m/s and 10m/s debris flows are identified, while when the velocity exceeds the value of 10m/s they speak about debris or rock avalanches.

The mass collapse is triggered by rapidly pulling forward a bulkhead; the same mechanical system starts the data acquisition of three laser sensors located along the channel for the recording of the flow height with time. Finally, many measurements about the deposition area are procured using photogrammetry and laser scanning. A high quality camera in fact takes many pictures of the mass at the end of the movement and a dense cloud of points is in that way is obtained. Finally a laser scanner is used to acquire the same information with a different technique, so you can compare the results obtained in two different ways.

Figure 7.2.1 Bohlin Visco 88 Viscometer.

7.2.2 Material characterization

In order to understand and interpret laboratory tests on physical models, which will be described in the next paragraph, it is necessary, first, to describe the nature and the mechanical properties of the soil involved in the experiment. This characterization is essential to ensure the repeatability of the experiments, as well as to be able to make a significant correlation between the specific characteristics of the terrain and its behavior during the tests. Two type of kaolin are used in these flume experiments, called type A and type B respectively.

The *Bohlin Visco 88* (Figure 7.2.1) is a portable, easily handled viscometer for laboratory, plant and field use. It includes a software for the calculation of torque [mNm], shear rate [1/s], shear stress [Pa], viscosity [Pas], temperature [°C] and rotational speed [HZ]. This viscometer features eight rotational speed settings in geometric progression from 20 to 1000rpm. The calculated shear rate, shear stress and viscosity are based on Newtonian liquid properties. When non-Newtonian liquids are studied, it is possible to calculate the true shear rate, etc. by using the rotational speed and torque readings.

The *Bohlin Visco 88* uses coaxial cylinder geometry. The inner cylinder rotates and the torque measurements are made on the same axis. It includes three different couples of cylinders, which have to be used depending on the viscosity of the material. If you work with liquid material, to have reliable results it is better to use the biggest one, in order to include as much material as possible in the space between the two cylinders. On the contrary, if the material is dense, you need to choose the smallest cylinders, to limit the quantity of material inserted, and consequently the friction the material causes to the rotation.

Nine mixtures are used with this experimental apparatus for kaolin A (Table 7.2.1), while just eight mixtures with kaolin B were studied (Table 7.2.2). Initially, the densities are measured, filling a well-known volume and weighting it. Then, the same values are calculated with the following equation:

$$\rho_{mix} = \rho_{kaol} \cdot c_v + \rho_w (1 - c_v) \qquad \textit{Equation 7-3}$$

Basically, the mixture is prepared, taking care to reach a perfect mixing level. Then the density is measured, as described above. Then the material is inserted in the cavity between the coaxial cylinders and the test is started.

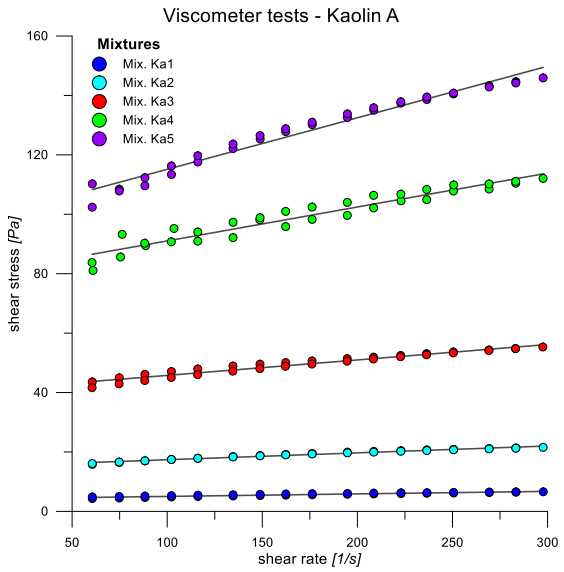

Figure 7.2.2 Results obtained by the viscometer tests for the mixtures from K_A1 to K_A5.

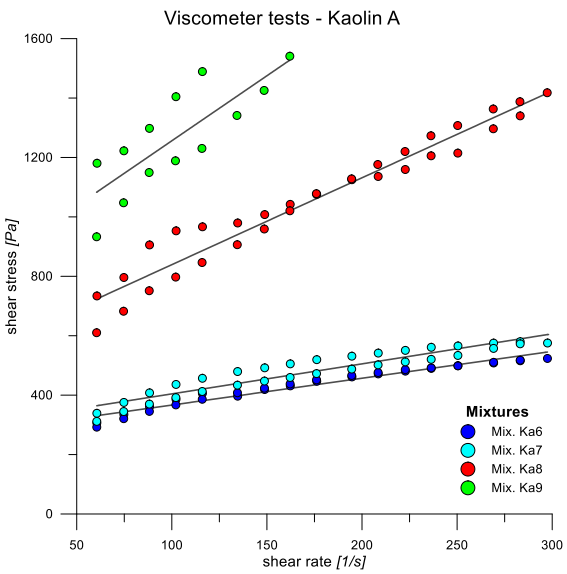

Figure 7.2.3 Results obtained by the viscometer tests for the mixtures from K_A6 to K_A9.

In all the experiments, a cycle of load and unload is applied. The shear rate is imposed with a range value from 14.4s^{-1} to 300s^{-1}. Each step is reached in 5s and kept for 5s. Once reached the

maximum shear rate, the velocity of the inner cylinder decreases, repeating the same steps of the load. Totally 40 measurements are obtained by each mixture and it is therefore possible to plot the results on a shear stress-shear strain plane.

Fitting the measurements obtained with a line, it is possible to find the Bingham parameters μ and τ. The intercept and the angular coefficient of those lines identify in fact the viscosity and the yield stress described by Bingham.

Kaolin -A-						
Mixture	***c_v***	***measured density***	***calculated density***	***density error***	***μ***	***τ***
		kg/m³	*kg/m³*	*%*	*Pa s*	*Pa*
Mix K_A1	*0.13*	1188.68	1213.33	2.0%	0.009	4.188
Mix K_A2	*0.19*	1325.47	1300.00	2.0%	0.024	14.906
Mix K_A3	*0.23*	1389.15	1376.47	0.9%	0.055	39.975
Mix K_A4	*0.28*	1455.19	1444.44	0.7%	0.124	77.451
Mix K_A5	*0.32*	1515.00	1505.26	0.6%	0.170	98.546
Mix K_A6	*0.35*	1675.00	1560.00	7.4%	0.764	307.540
Mix K_A7	*0.38*	1615.38	1609.52	0.4%	1.851	436.800
Mix K_A8	*0.41*	1661.54	1654.54	0.4%	2.759	583.080
Mix K_A9	*0.43*	1707.69	1695.65	0.7%	4.627	789.670

Table 7.2.1 List of mixtures used with viscometer test, kaolin A.

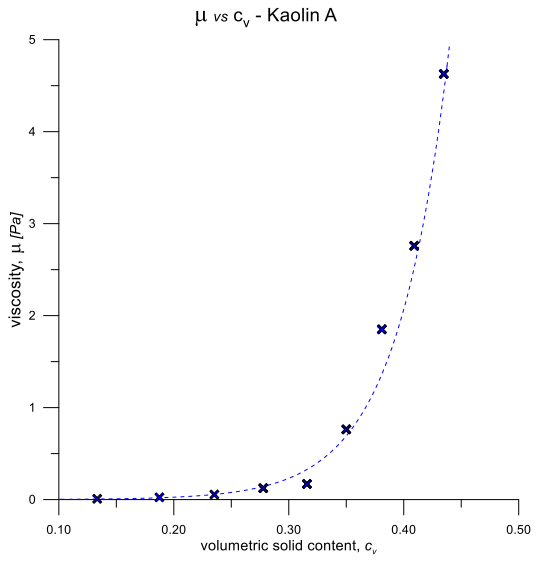

Figure 7.2.4 Viscosity μ vs c_v for the kaolin A.

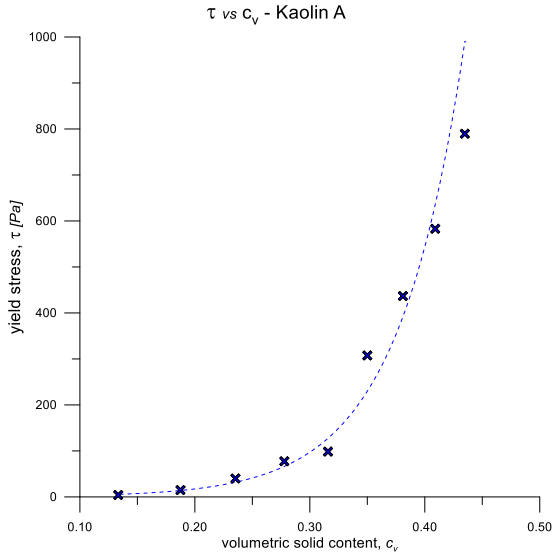

Figure 7.2.5 Yield stress τ vs c_v for the kaolin A.

Table 7.2.1 and Table 7.2.2 contain the measured and calculated densities for kaolin A and B respectively. The errors observed between these values assure a good accuracy in the material mixing.

Now it can be drawn the graphs of the parameters that characterize kaolin A and B, depending on the solid volumetric coefficient c_v (Figure 7.2.4 and Figure 7.2.5).

The data acquired are fitted with an exponential line in order to evaluate their tendency.

Kaolin -B-						
Mixture	***c_v***	***measured density***	***calculated density***	***density error***	***μ***	***τ***
		kg/m³	*kg/m³*	*%*	*Pa s*	*Pa*
Mix K_B1	0.14	1208.73	1218.18	0.8%	0.017	8.428
Mix K_B2	0.19	1293.07	1292.73	0.0%	0.043	28.488
Mix K_B3	0.22	1331.32	1310.91	1.6%	0.109	73.683
Mix K_B4	0.24	1367.28	1360.91	0.5%	0.139	88.527
Mix K_B5	0.28	1433.07	1407.27	1.8%	0.354	136.880
Mix K_B6	0.32	1491.80	1449.09	2.9%	0.964	222.350
Mix K_B7	0.36	1544.55	1484.55	4.0%	2.222	312.130
Mix K_B8	0.39	1592.19	1520.91	4.7%	3.970	440.870

Table 7.2.2 List of mixtures used with viscometer test, kaolin B.

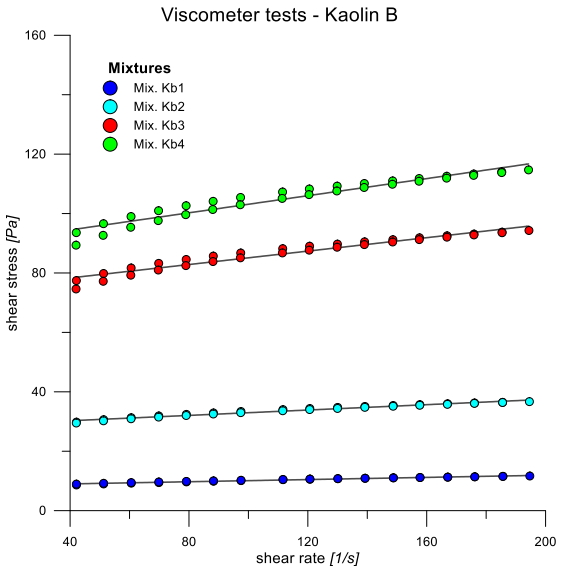

Figure 7.2.6 Results obtained by the viscometer tests for the mixtures from K_B1 to K_B4.

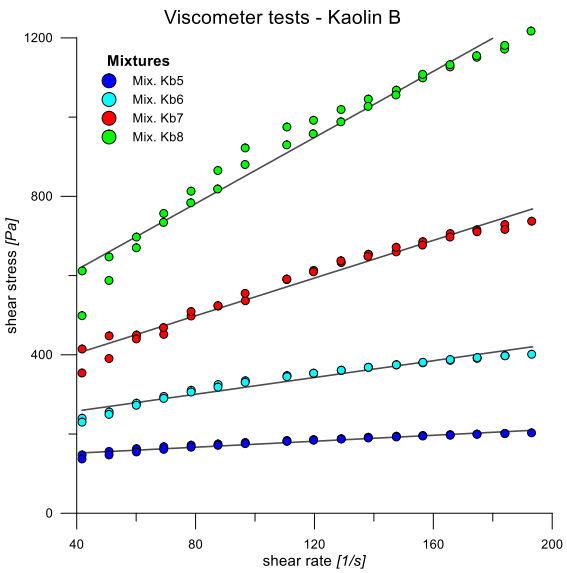

Figure 7.2.7 Results obtained by the viscometer tests for the mixtures from K_B5 to K_B8.

Finally, it is interesting to compare the behavior of the two materials. To do this, the data acquired by the viscometer have been plotted in two graphs.

Figure 7.2.10 underlines similar behavior just for low solid content. In these cases, probably the mixture is prevalently dominated by the liquid phase, and the kaolin content does not increase the viscosity appreciably. When c_v increases, contrarily, it can be noticed some differences: kaolin B in fact becomes more viscous and evidently increases the parameter μ.

Something similar can be observed in Figure 7.2.11, even if the effect of the increase of the solid content in less evident. Kaolin B has higher values of yield stress with respect to kaolin A, but this happens slightly.

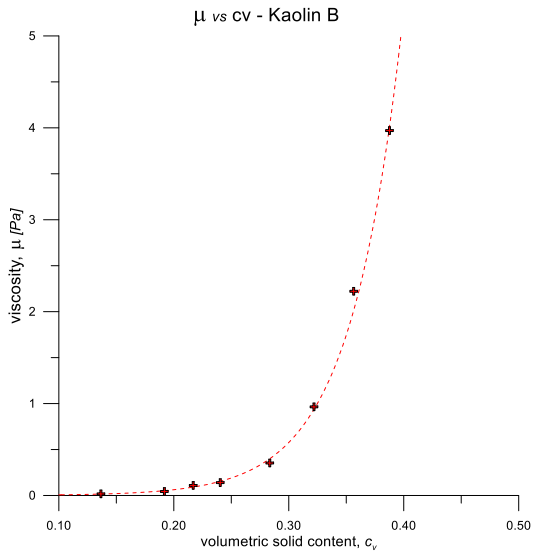

Figure 7.2.8 Viscosity μ vs c_v for the kaolin B.

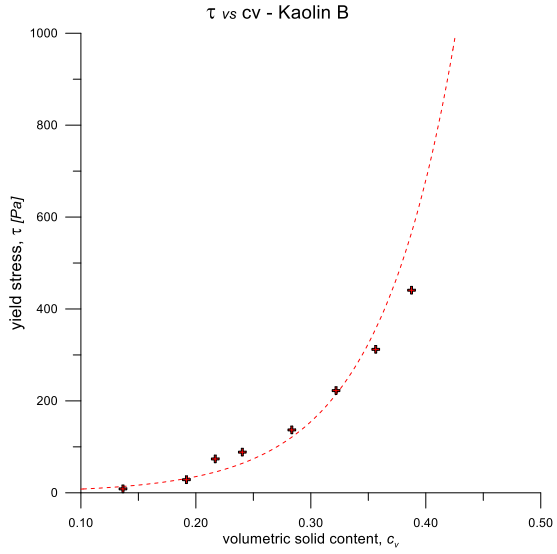

Figure 7.2.9 Yield stress τ vs c_v for the kaolin B.

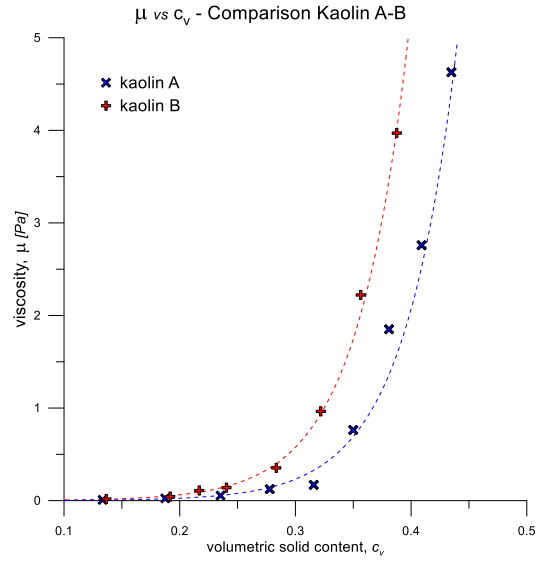

Figure 7.2.10 Comparison of the viscosities μ vs c_v for the kaolin A and B.

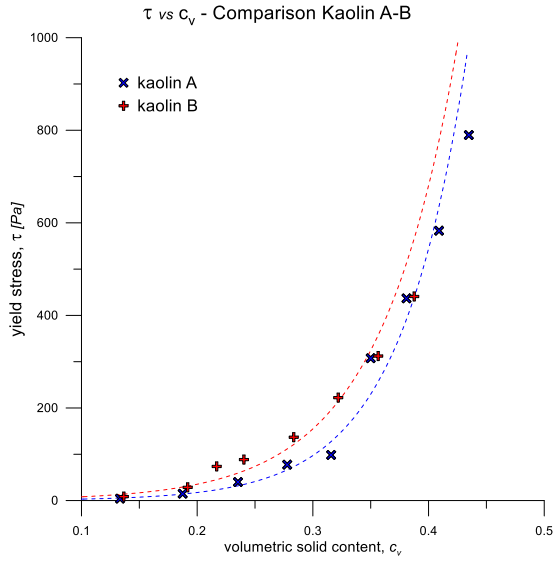

Figure 7.2.11 Comparison of the Yield stresses τ vs c_v for the kaolin A and B.

After all, it is expected that experiments performed with kaolin A will be less cohesive compared with similar mixtures containing kaolin B. It is interesting to study the effect of these viscosities on the behavior of the material during the laboratory tests.

7.2.3 Experimental setup

A prismatic container that discharges the material inside a channel 2.5m long and 0.16m large composes the experimental apparatus. The shape of the detachment volume is a simple trapezoid prism. At the end of the slope, a horizontal plane let the material stop its movement (Figure 7.2.13). It is evident in Figure 7.2.12 that all the chute base of the experimental apparatus is roughened by glued sand.

Figure 7.2.12 Picture of the experimental apparatus.

Three laser sensors are fixed along the channel to measure the heights of material in time. The acquisition system is directly connected with the triggering mechanism. The setup decided allows to obtain one datum every 0.0025s. As shown in Figure 7.2.13, the first sensor is 102cm distant from the detachment zone. The second and the third lasers are placed with a spacing of 34.2cm. The direction of the measurements obtained is vertical: the main goal is to get data comparable with those obtained from the numerical code, which are along the vertical too.

A load cell is placed just under the tested point of the third laser sensor. It measures the weight of mass passing on.

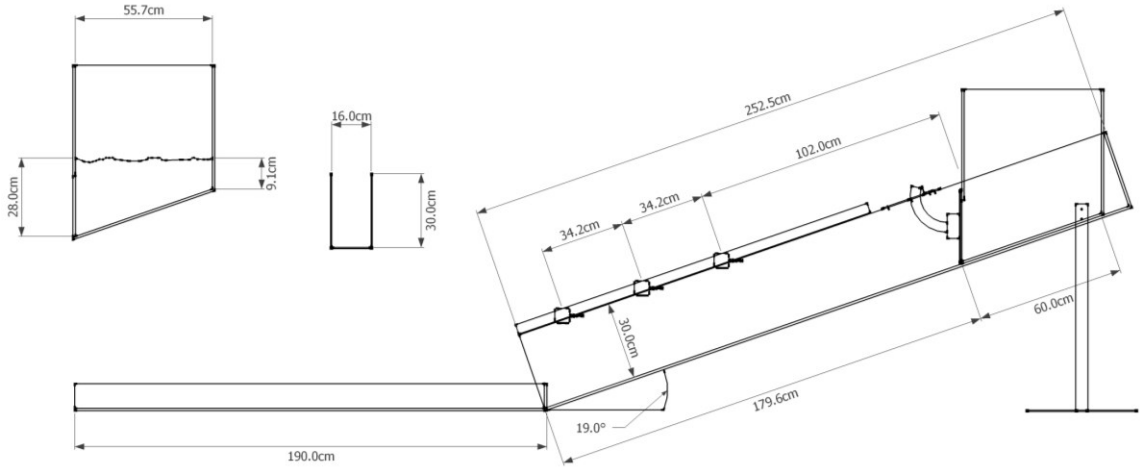

Figure 7.2.13 Experimental apparatus scheme.

A camera is located in front of the apparatus, to record all the experiments. As shown in Figure 7.2.14, the behavior of the mass is evidently visible. The material increases its velocity along the slope. The flux in the channel is almost homogeneous, even if a small transversal gradient of velocity due to the boundary conditions is present. The lateral walls of the apparatus decelerate the flow, while the central part of the material can move freely.

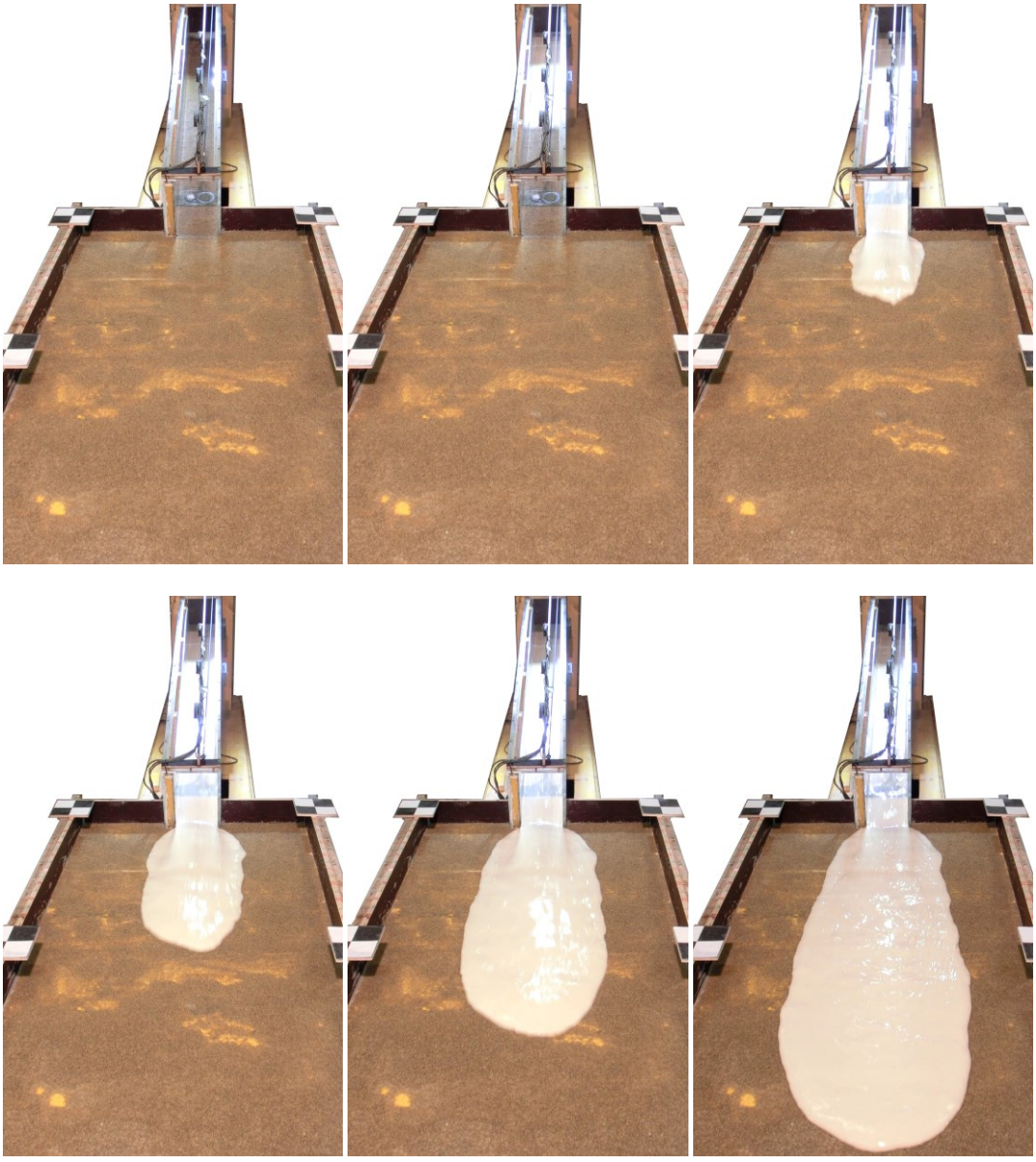

Figure 7.2.14 Pictures extracted from the video recorded by the frontal camera.

When the material reaches the horizontal plane, initially it slightly increases its width. Then, the arrival of the rest of the mass make the runout start to increase. Obviously, the lateral spread and the runout of the flow are strictly dependent on the characteristics of the mixture. The main goal of

the following paragraphs is to analyze the behavior of those flows depending on the percentage of sand water and kaolin included in the initial mass.

At the end of the test, about 50 pictures are taken using a high quality camera. These images are then processed using the software *VisualSFM* to obtain the cloud of points of the deposit. The 3D model is therefore elaborated using the software *CloudCompare* to resize and align the cloud with the reference system decided. Finally, a 3D laser scanner is used to record the same data, in order to compare the quality and the precision of these two acquisition methods.

7.2.4 Experiments list and procedure

Globally 15 different mixtures are tested with the channel. Initially, the mass is composed by kaolin and water and five experiments are performed (Table 7.2.3).

WK_A mixtures								
Mixture	***Water***	***Kaolin***	***Density***	***Volume***	***Weight***	$c_{v,K}$	μ	τ
	%	*%*	*kg/m³*	*L*	*kg*		*Pa s*	*Pa*
WK_A1	*55.6%*	*44.4%*	1376.47	15.00	20.65	0.235	0.052	40.578
WK_A2	*54.1%*	*45.9%*	1394.20	15.00	20.91	0.246	0.064	46.230
WK_A3	*52.6%*	*47.4%*	1411.43	15.00	21.17	0.257	0.080	57.690
WK_A4	*51.3%*	*48.7%*	1428.17	15.00	21.42	0.268	0.098	71.543
WK_A5	*50.0%*	*50.0%*	1444.44	15.00	21.67	0.278	0.114	79.623

Table 7.2.3 WK_A mixture characteristics.

Some of these tests are repeated many times, in order to assure the repeatability of the results. WK_A1 and WK_A3 mixtures are used twice, while WK_A5 is tested three times. Table 7.2.3 contains the main characteristics of the material used. The values of the rheological parameters described in §7.2.2 are also reported.

WSK_A mixtures									
Mixture	***Water***	***Kaolin***	***Sand***	***Density***	***Volume***	***Weight***	$c_{v,K}$	$c_{v,S}$	c_v
	%	*%*	*%*	*kg/m³*	*L*	*kg*			
WSK_A1	*41.7%*	*41.7%*	16.7%	1552.07	15.00	23.28	0.249	0.105	0.353
WSK_A2	*38.5%*	*38.5%*	23.1%	1597.87	15.00	23.97	0.236	0.149	0.385
WSK_A3	*35.7%*	*35.7%*	28.6%	1639.33	15.00	24.59	0.225	0.189	0.415

Table 7.2.4 WSK_A mixture characteristics.

WSK_B mixture - group 1									
Mixture	***Water***	***Kaolin***	***Sand***	***Density***	***Volume***	***Weight***	$c_{v,K}$	$c_{v,S}$	c_v
	%	*%*	*%*	*kg/m³*	*L*	*kg*			
WSK_B1	*50.0%*	*40.0%*	10.0%	1440.36	15.00	21.61	0.222	0.058	0.280
WSK_B2	*41.7%*	*33.3%*	25.0%	1548.14	15.00	23.22	0.198	0.156	0.355
WSK_B3	*35.7%*	*28.6%*	35.7%	1635.56	15.00	24.53	0.180	0.236	0.416

Table 7.2.5 WSK_B mixture characteristics, group 1.

WSK_B mixture - group 2									
Mixture	*Water*	*Kaolin*	*Sand*	*Density*	*Volume*	*Weight*	$c_{v,K}$	$c_{v,S}$	c_v
	%	*%*	*%*	*kg/m³*	*L*	*kg*			
WSK_B4	*45.5%*	*45.5%*	9.1%	1501.23	15.00	22.52	0.262	0.055	0.318
WSK_B5	*41.7%*	*41.7%*	16.7%	1552.07	15.00	23.28	0.249	0.105	0.353
WSK_B6	*38.5%*	*38.5%*	23.1%	1597.87	15.00	23.97	0.236	0.149	0.385
WSK_B7	*35.7%*	*35.7%*	28.6%	1639.33	15.00	24.59	0.225	0.189	0.415
WSK_B8	*33.3%*	*33.3%*	33.3%	1677.04	15.00	25.16	0.215	0.226	0.441

Table 7.2.6 WSK_B mixture characteristics, group 2.

Subsequently, three tests are made with the same kaolin A, starting from the WK_A5 mixture, including different content of sand. It is evident that the rate between water and kaolin is always equal to one, while the quantity of sand increases gradually. The kaolin has been therefore changed and eight more tests are performed. Two groups of experiments can be recognized: the first group keeps a rate of 5 to 4 between water and kaolin, increasing the sand content (Table 7.2.5). The second group takes place starting from a matrix containing the same quantity of water and kaolin (Table 7.2.6). In this last set of tests, the WSK_B4, WSK_B5 and WSK_B7 are performed twice each.

A comparison between two mixtures containing the same percentage of materials, but with a change in the kaolin used, is finally performed.

The material is homogeneously mixed using an electric drilling machine (Figure 7.2.15). Then, it is weighed and inserted in the prismatic container. The acquisition system is switched on and the camera begin recording. The gate is suddenly opened, starting at the same time the laser sensors functioning.

At the end of the flow, using a reflex the pictures are collected. Then the *Sense 3D Scanner* allows directly to obtain a 3D model of the deposit.

Finally, some hand-made measurements are collected to have later on an evaluation of the error of the photogrammetric technique and to compare it with the error of the laser scanning.

Figure 7.2.15 Preparation of the material.

At the end of each test, mainly two types of information are available:

- Data in time, collected by the laser sensors along the channel and by the load cell.
- Data at the end of the phenomenon, obtained with two different technique.

From the first group of information, it is possible to evaluate the height of material moving down in the channel during the test. It is therefore possible to estimate the average velocities between the sensors and to define the exact starting time.

A huge quantity of measurements are obtained about the deposit. In fact, on one hand the 3D scanning of the horizontal plane rises to have about 20000 measurements, while on the other hand using the post elaboration of the pictures, it is possible to collect about 200000 data.

7.2.5 Output obtained

Initially the material used contains just water and kaolin, in five different percentage. The material is perfectly mixed and inserted in the prismatic container. After having completed the test, the measurements collected can be analyzed.

Firstly, the data acquired by the laser sensors are imported in Excel and elaborated to obtain some interesting information. Looking at Figure 7.2.16, it is possible to notice the wave of material reaching respectively the first, the second and the third sensor. It is interesting to analyze the delay between the three graphs to understand velocity of the flow along the channel.

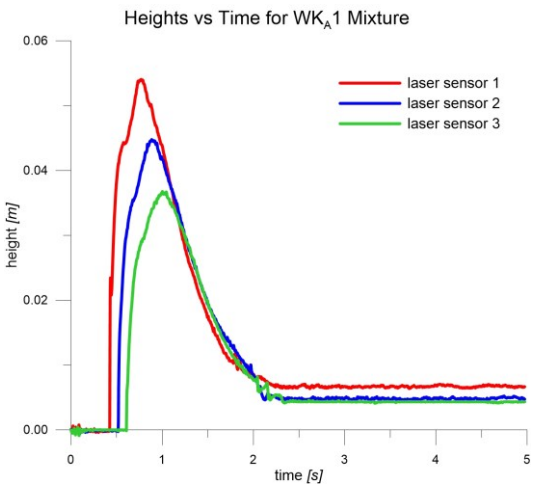

Figure 7.2.16 Laser sensors measurements acquired for the WK$_A$1 mixture.

In fact, it is possible to calculate the mean values of velocity between a pair of sensors, considering the time that is necessary to run from one sensor to the next one. By the analysis of these two values of velocities, it is therefore interesting to understand if the flow is increasing or decreasing its speed.

Secondly, the maximum heights of those three waves are directly connected with the characteristics of the material used. Consequently, also this information are extracted from the output files.

As noted above, two techniques are used to get measurements about the deposits. On one hand, a high quality camera allows to take about fifty pictures of the horizontal plane, covered by the flow. VISUALSFM is a GUI application for 3D reconstruction using structure from motion. The first thing to note of importance is that photogrammetry is a scale-less method. Unlike laser scanning, the resultant point cloud has no absolute scale. As such, it is imperative that an object of known dimensions (e.g. a scale bar) is present next to the subject being photographed, and that photographs incorporate this known scale are taken as part of the process, so that the scale ends up in the final 3D model.

In order for any given point to be represented in the final 3D model, it must be present in at least three photographs, preferably many more. As such, when taking photos, ensure considerable overlap between images. Include overview shots of the entire subject [if possible] and closer shots that can be located in the overview. Taking shots as you move closer to the subject allows the software to make the links easier.

First, the pictures are added into the *SFM* workspace. Then a special command is launched, to run feature detection and full pairwise image matching. The time taken at this stage increases exponentially as more photos are used – 10 photos will take seconds, 100 photos minutes, and 1000 can take days. After this step, you have to run sparse reconstruction. Finally, dense reconstruction is requested to build the cloud desired. Figure 7.2.17b show the result obtained after the reconstruction. The cloud contains about 600.000 points.

The second technique that is used is the 3D laser scanning (Figure 7.2.17c). The Sense 3D scanner gives you the ability to observe a scene in three dimensions and then translates the observations into a 3D model. The scanning takes few minutes and let you obtain the cloud in less than five minutes. For the same case study, the number of points is about of 25.000.

All the results achieved by these two techniques have to be scaled. In Figure 7.2.17a, some useful targets are present for this goal. It is known, in fact, the relative positions of the targets and it is consequently possible to attribute to the models the correct size. All the results are then cropped, considering the data just on the deposition plane, as shown in Figure 7.2.17.

From the analysis of these models, many useful information are therefore taken. The runouts, the spreads and the heights of the deposits are immediately obtained. Thanks to this, all the tests can be characterized giving information in time and at the end of the phenomenon and this leads to the creation of a database full of reliable information.

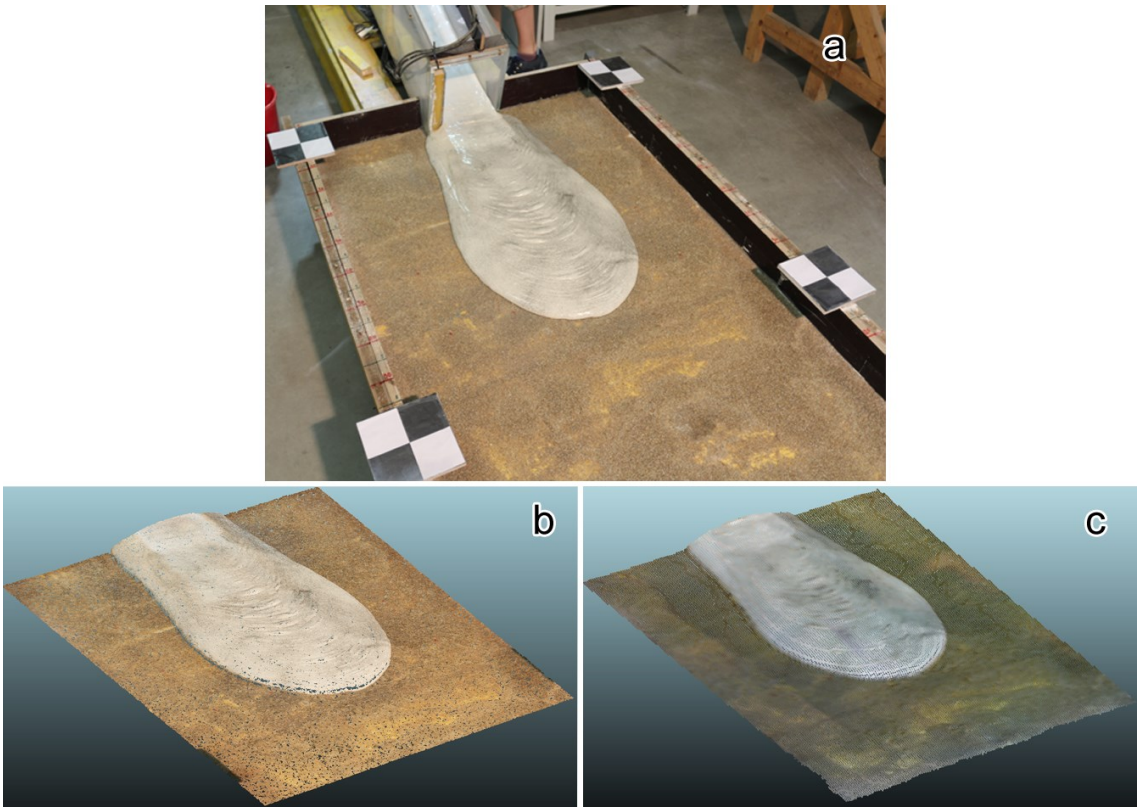

Figure 7.2.17 a) Picture of the deposit area; b) Cloud obtained by photogrammetry; c) Cloud obtained by laser scanning.

7.2.6 WK_A Mixtures

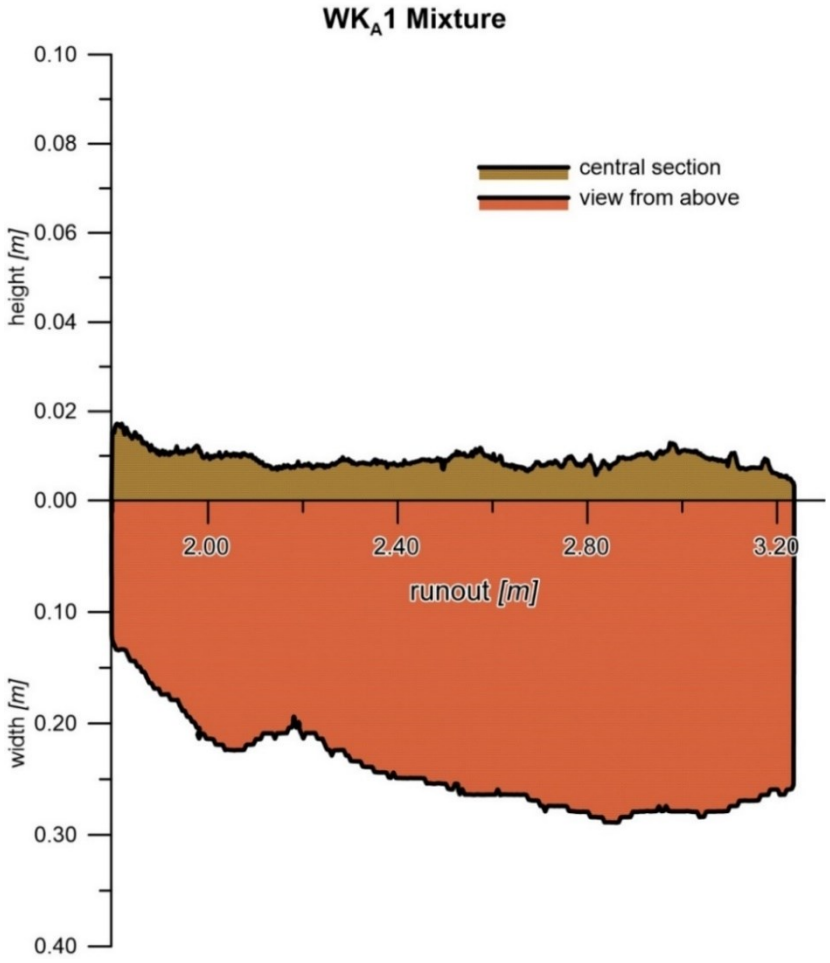

Figure 7.2.18 Central section and view from above for the WK_A1 mixture.

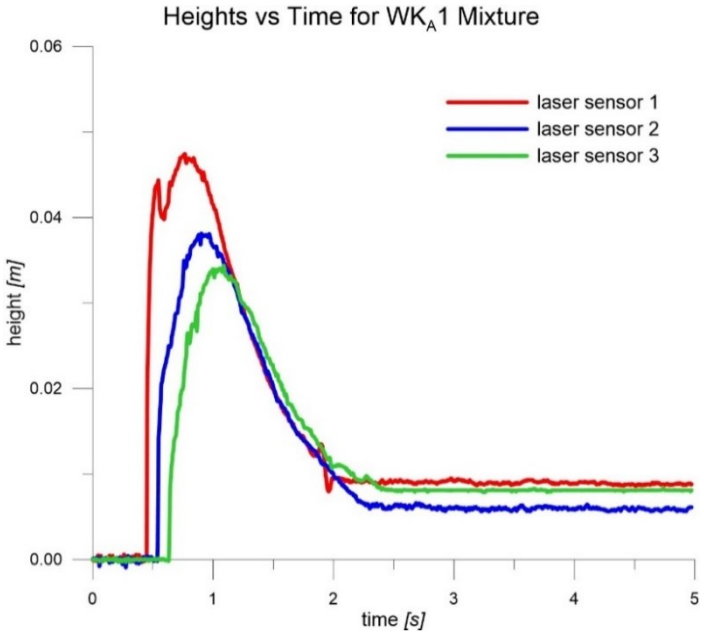

Figure 7.2.19 Heights of material vs time for the test.

Mixture WK_A	
name	**WK_A1**
kaolin	**$c_{v,K}$**
%	-
44.4	0.235
Runout	**Spread**
m	*m*
3.236	0.698
Velocity 1	**Velocity 2**
m/s	*m/s*
3.697	3.508

Table 7.2.7 Characteristics of the test.

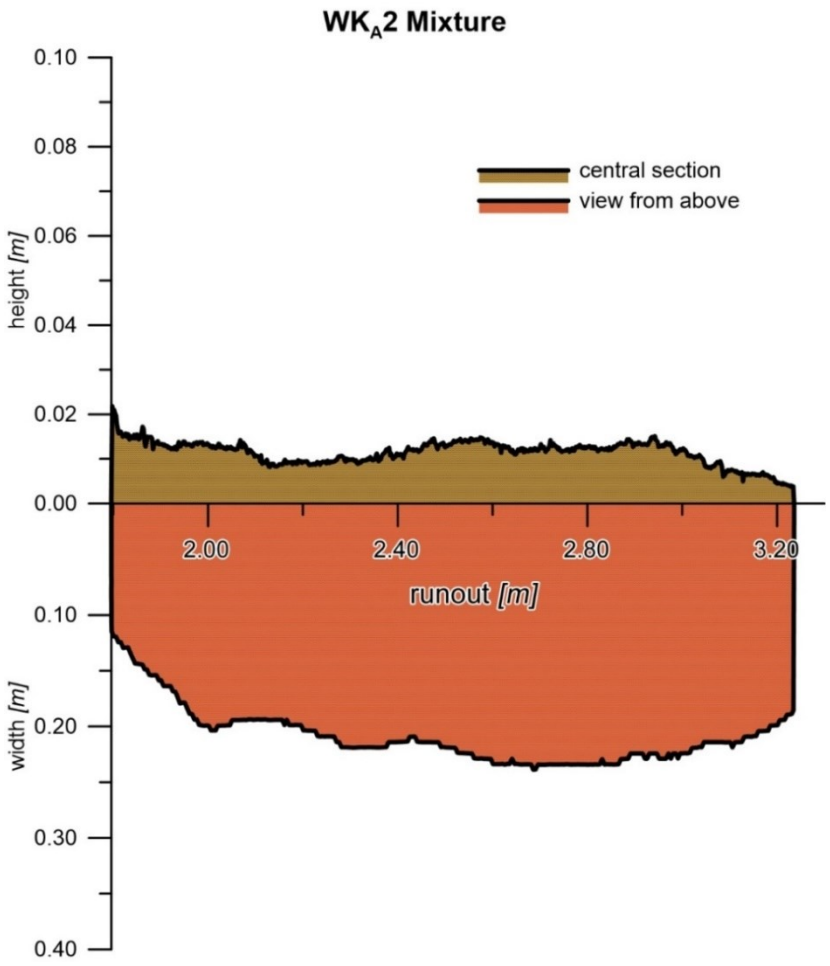

Figure 7.2.20 Central section and view from above for the WK$_A$2 mixture.

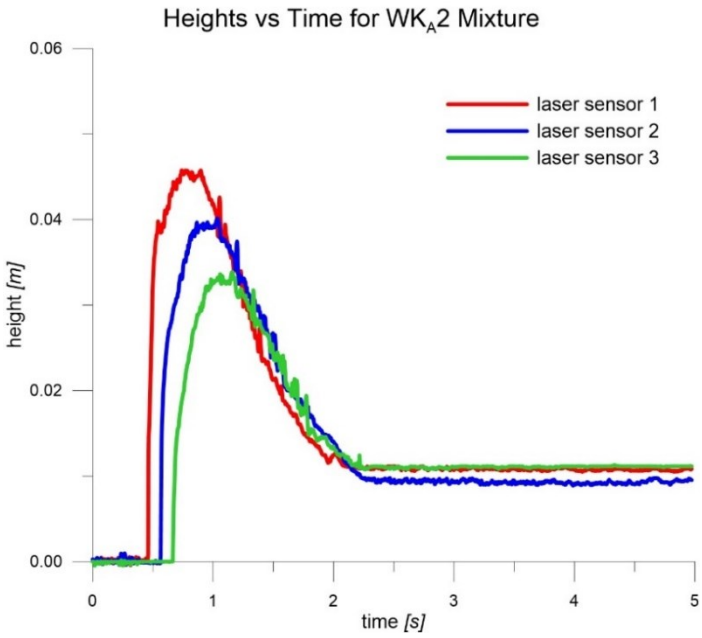

Mixture WK$_A$	
name	**WK$_A$2**
kaolin	**$c_{v,K}$**
%	-
45.9	0.246
Runout	**Spread**
m	*m*
3.236	0.493
Velocity 1	**Velocity 2**
m/s	*m/s*
3.257	3.257

Table 7.2.8 Characteristics of the test.

Figure 7.2.21 Heights of material vs time for the test.

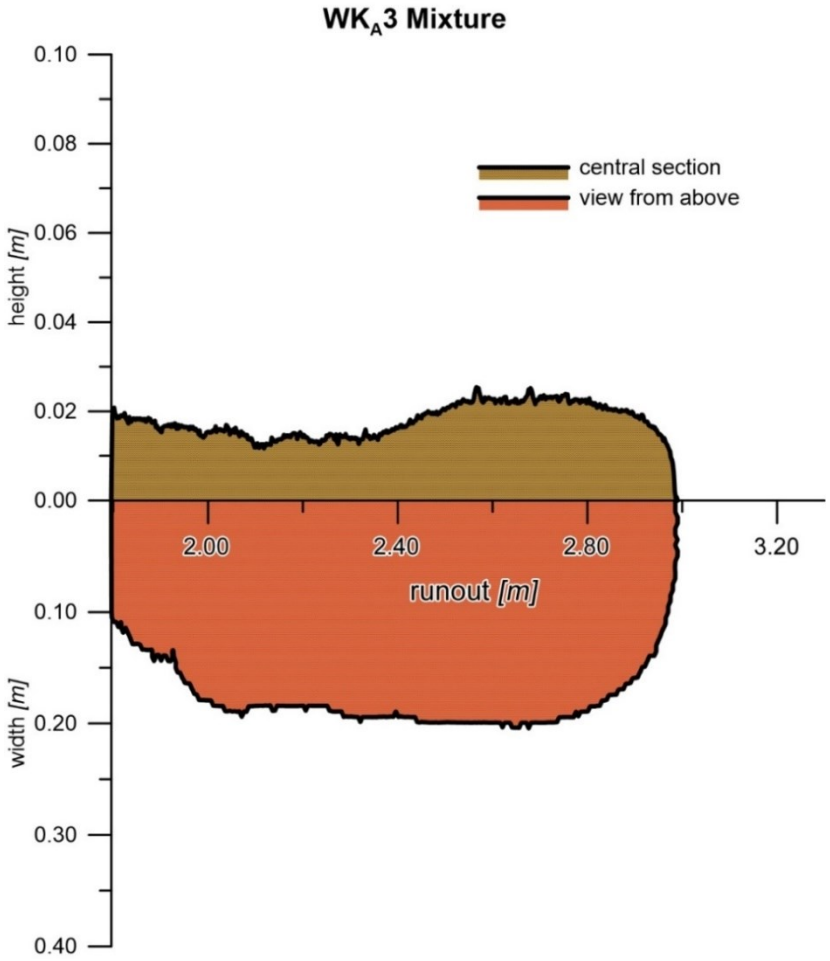

Figure 7.2.22 Central section and view from above for the WK$_A$1 mixture.

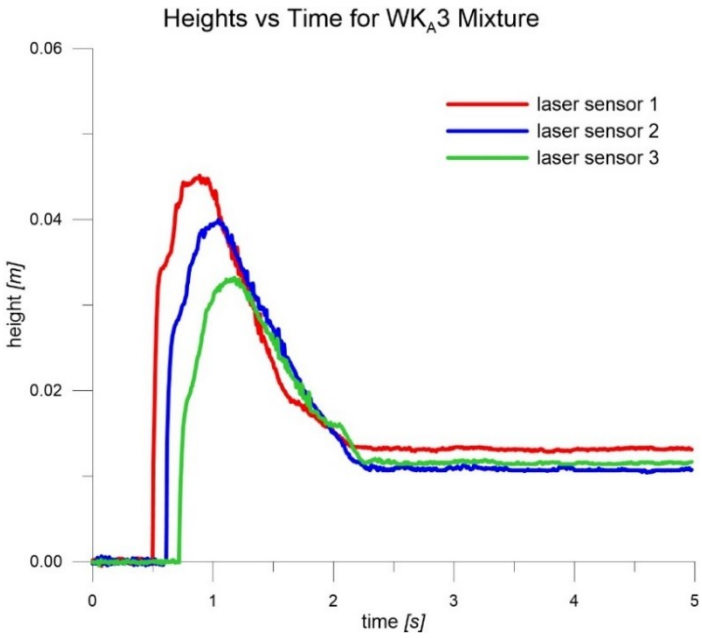

Mixture WK$_A$	
name	**WK$_A$3**
kaolin	**$c_{v,K}$**
%	-
47.4	0.257
Runout	**Spread**
m	*m*
2.990	0.433
Velocity 1	**Velocity 2**
m/s	*m/s*
3.040	3.181

Table 7.2.9 Characteristics of the test.

Figure 7.2.23 Heights of material vs time for the test.

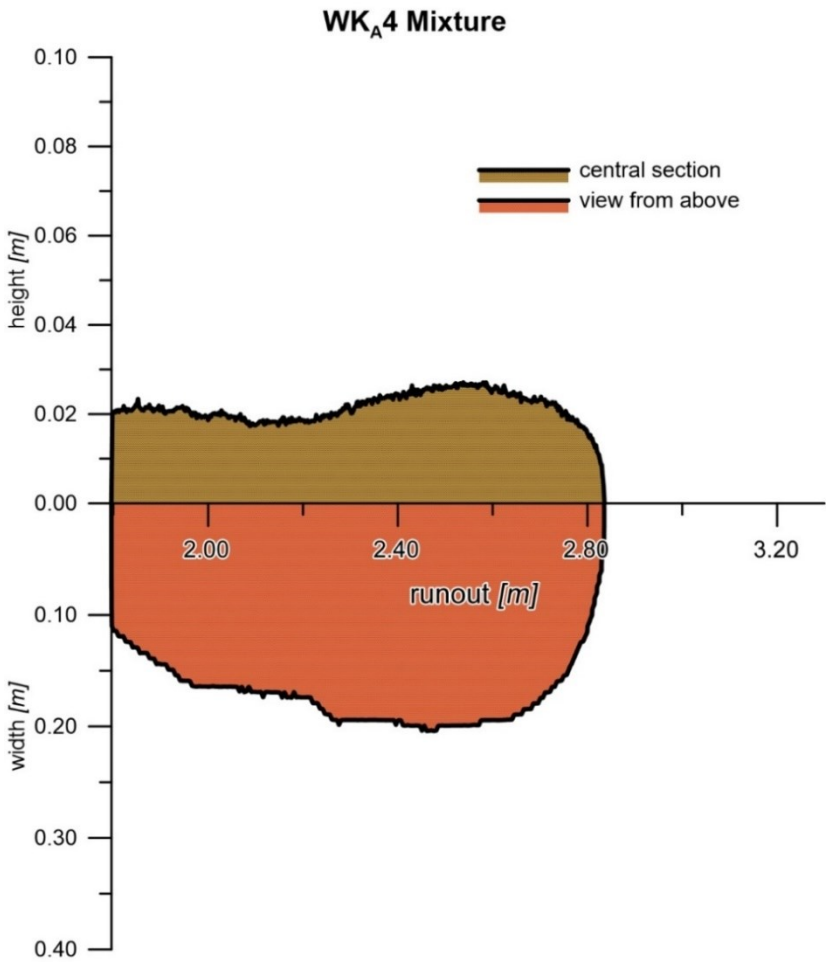

Figure 7.2.24 Central section and view from above for the WK$_A$1 mixture.

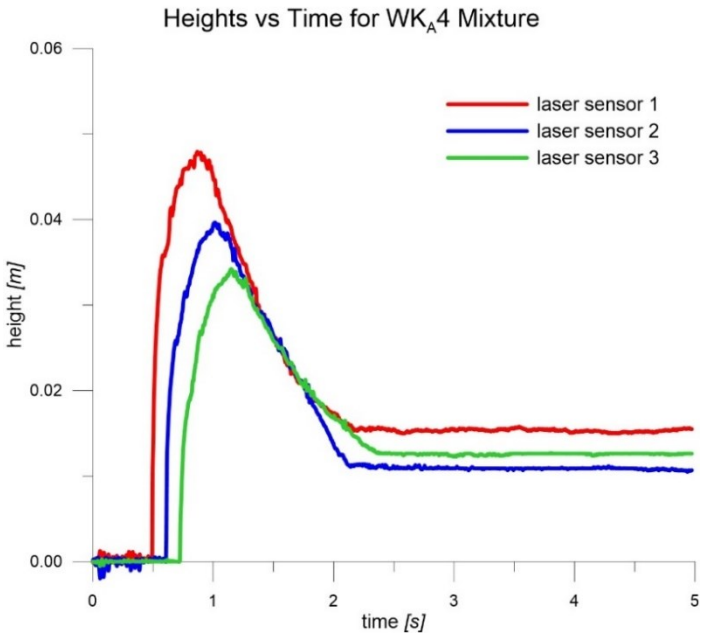

Figure 7.2.25 Heights of material vs time for the test.

Mixture WK$_A$	
name	**WK$_A$4**
kaolin	**$c_{v,K}$**
%	-
48.7	0.268
Runout	**Spread**
m	*m*
2.835	0.427
Velocity 1	**Velocity 2**
m/s	*m/s*
2.911	2.911

Table 7.2.10 Characteristics of the test.

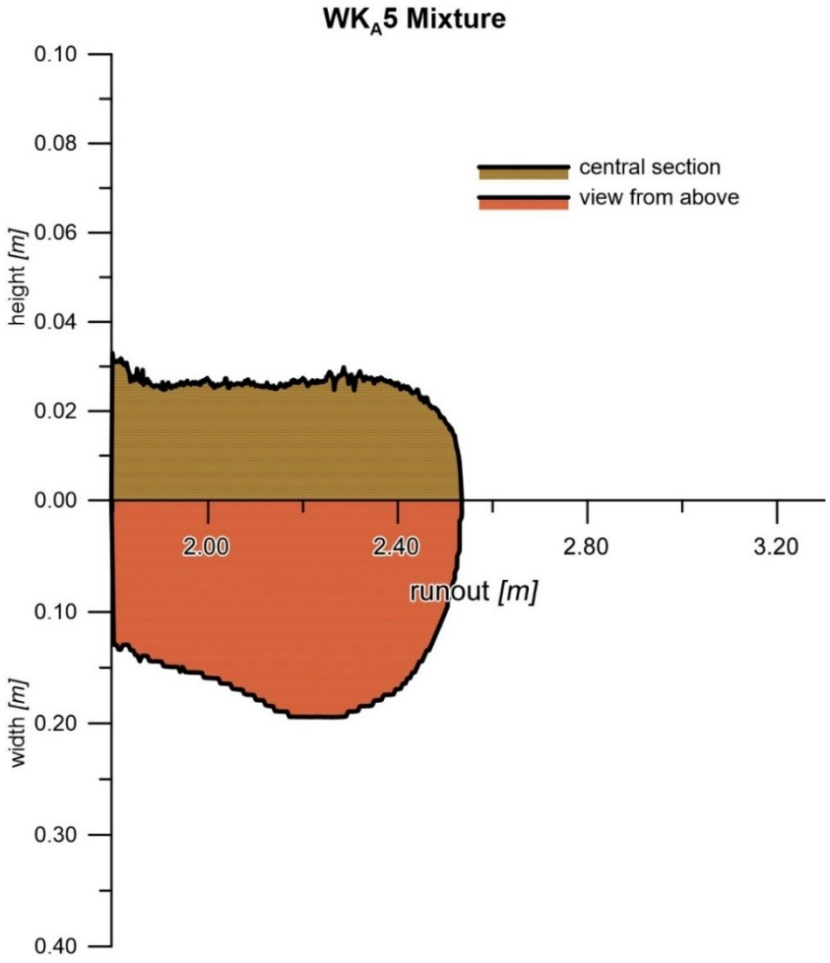

Figure 7.2.26 Central section and view from above for the WK$_A$1 mixture.

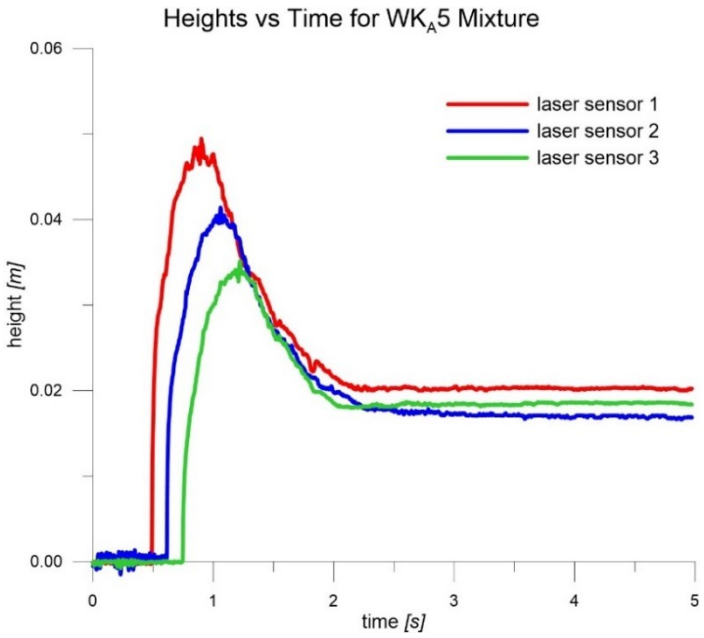

Mixture WK$_A$	
name	**WK$_A$5**
kaolin	**$c_{v,K}$**
%	-
50.0	0.278
Runout	**Spread**
m	*m*
2.535	0.403
Velocity 1	**Velocity 2**
m/s	*m/s*
2.736	2.533

Table 7.2.11 Characteristics of the test.

Figure 7.2.27 Heights of material vs time for the test.

7.2.6.1 Repeatability of the WK_A tests

Some of the experiments were performed twice, to check the reliability of the results. The WK_A5 mixture was used three times because the second try gave too different data compared with the first one.

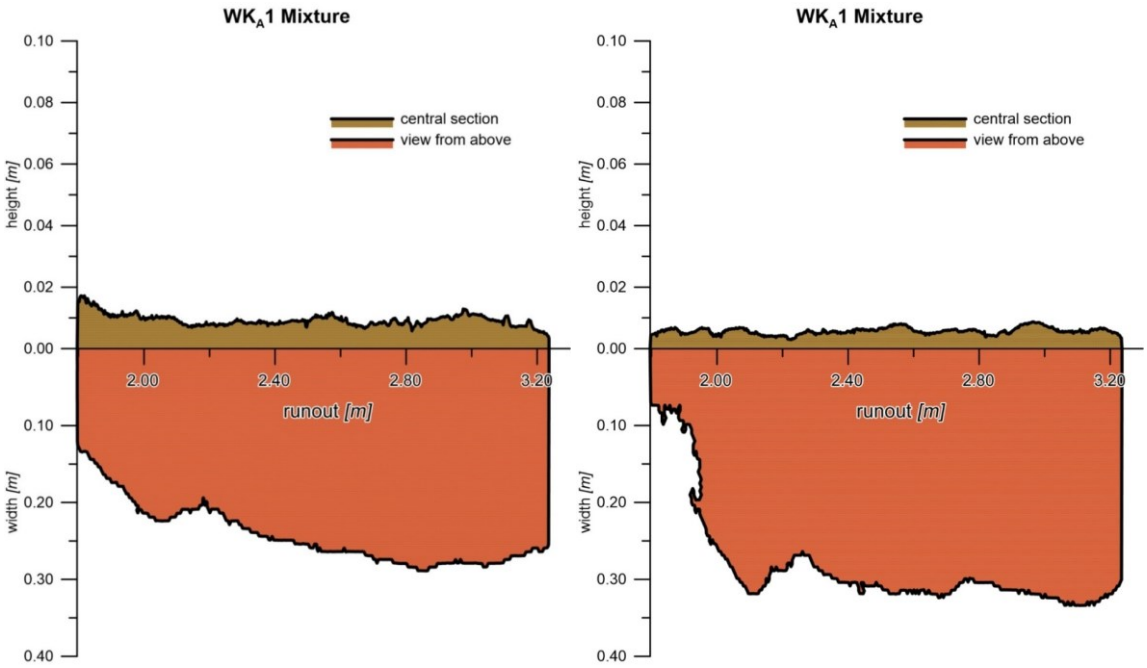

Figure 7.2.28 Comparison of the results for the WK_A1 tests.

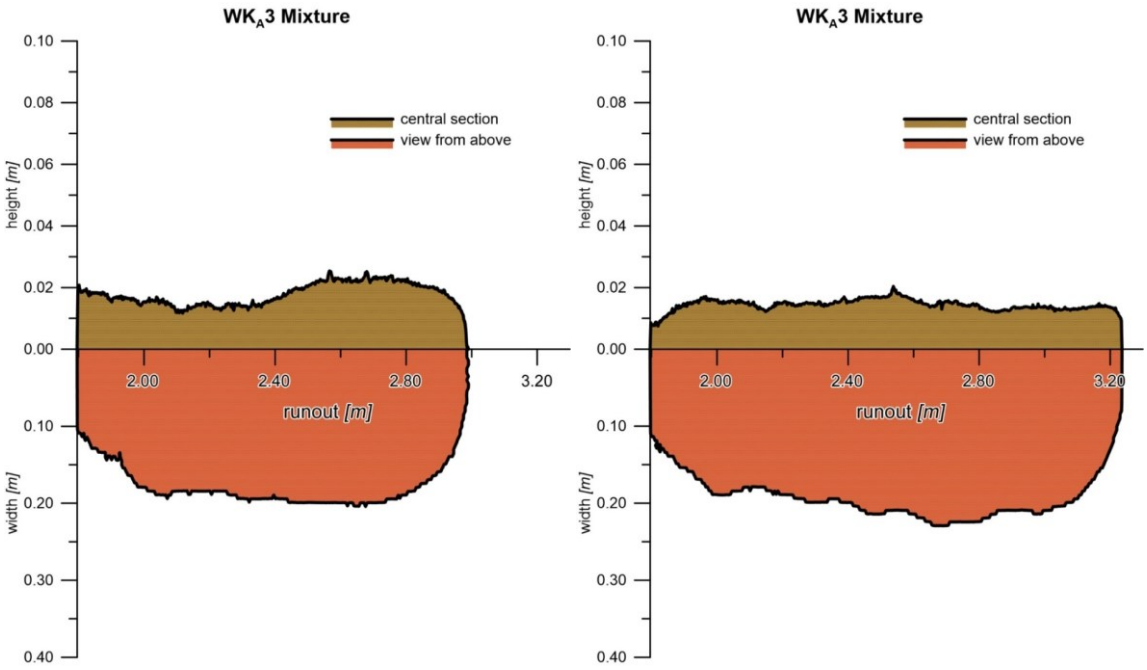

Figure 7.2.29 Comparison of the results for the WK_A3 tests.

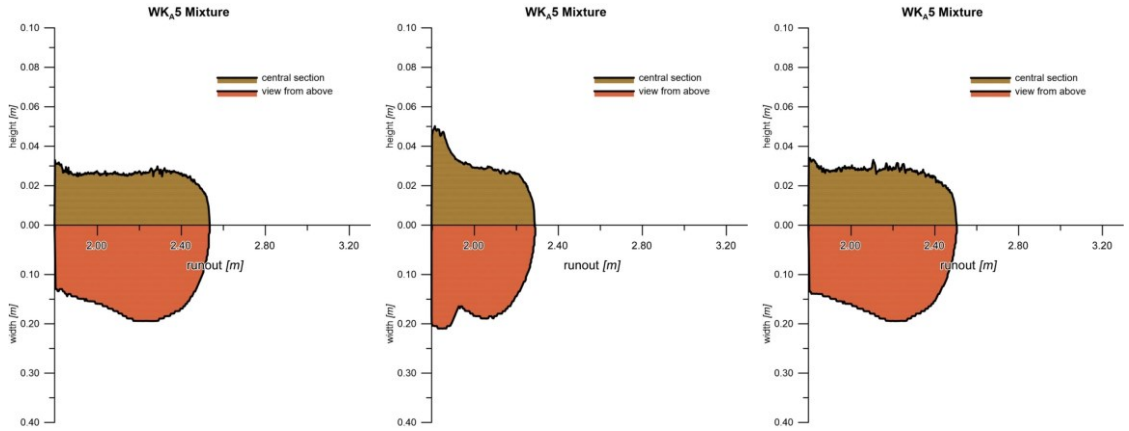

Figure 7.2.30 Comparison of the results for the WK$_A$5 tests.

Figure 7.2.28 shows a similar behavior for the two repetitions. The material reach the end of the horizontal plane, while the spread is slightly bigger. The velocities of the second try are similar to those of the first attempt: v_1 and v_2 are in fact equal to 3.6m/s and 3.8m/s respectively, compared to 3.3m/s measured in both the sections in the first test.

Figure 7.2.29 underlines how the second experiment performed with the WK$_A$3 mixture is slightly more liquid than the first. In fact, the runout is 3.24m, instead of 2.99m and the velocities are 3.11m/s and 3.20m/s, instead of 3.04m/s and 3.18 respectively. The spread does not change significantly.

The summary of the repetition of the experiment performed with the WK$_A$5 mixture is showed in Figure 7.2.30. It is evident that the second try is not coherent with the others and probably some inaccuracies happened during the execution of the test. All the velocities in this second case are lower than the others, especially speaking about v_2. The differences of the behavior are underlined by the runouts, which are 2.53m and 2.51m for the first and the last tries, while 2.29m for the second. The material is characterized by a more viscous behavior and suddenly decelerate on the deposit plane. Two successive waves are recognizable in the second repetition that create a strange and not reliable deposit shape.

7.2.6.2 Considerations on the WK$_A$ experiments

It is possible to plot the mean velocities depending on the percentage of kaolin contained in the mixture.

If we fit the reference tests with a line, it is interesting to see that the angular coefficient of the fitting line of the first velocities is almost equal to the one of the second velocities. This fact means on one hand that increasing the kaolin content, the material decreases linearly its velocity. On the other hand, the decrease of velocity along the channel remains the same for all the cases.

Another thing that is evident from Figure 7.2.31 is that while the repetitions of the WK$_A$1 test gives similar results in term of velocity, one of the WK$_A$5 experiment is quite different from the others. Particularly, it has both the velocities evidently lower than the other cases. This fact underlines how the environmental conditions and the way of preparing the material can lead to

error. For this reason, this test has been made three times, to understand the more reliable behavior for this mixture.

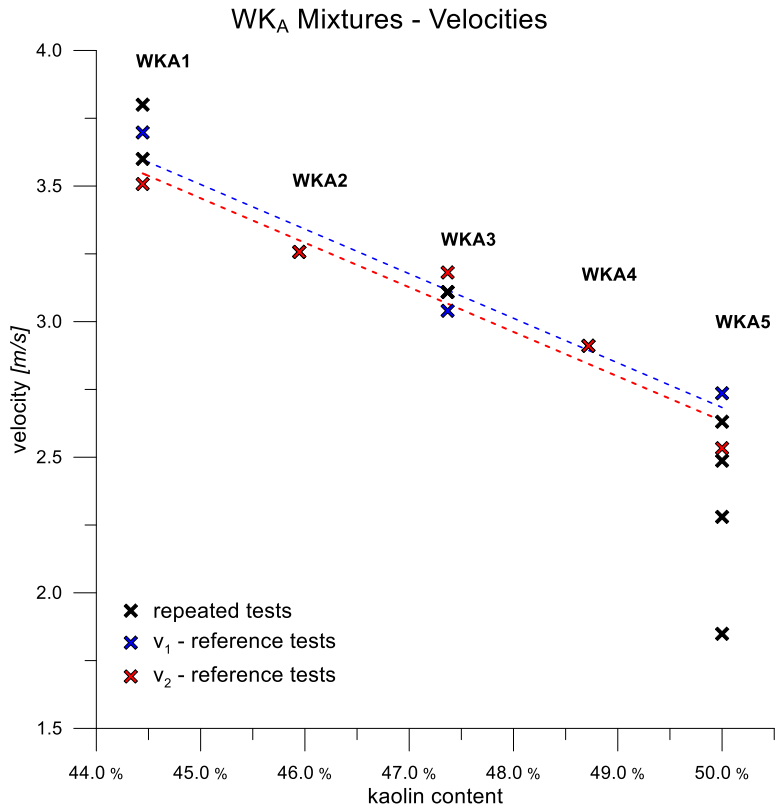

Figure 7.2.31 Comparison of the velocities between the WK$_A$ tests.

A second interesting graph that can be drawn is the one in Figure 7.2.34. The runouts and the spreads of all the WK$_A$ tests can be therefore compared, depending on the kaolin content. It is evident that the runout decreases linearly with the increase of kaolin included in the flowing mass. It has to be noticed that the maximum length of the horizontal plane is 2.326m, distance that is reached by WK$_A$1, WK$_A$2 and one of the tests made with WK$_A$3. Also in this graph it can be seen that one of the repetition of the WK$_A$5 definitely untrustworthy.

In the same figure, the spreads of all the experiments is evident. With the increase of the kaolin content, the spread slightly increases. The angular coefficient of the red line is lower than the one of the blue line. In fact, it happens that, while the runout is extremely dependent on the fluidity of the mixture, directly connected to the solid content in the mass, the spread remains closer to a mean value, even working with liquid mixtures.

Studying the video of the experiments (Figure 7.2.33), it is observed that as soon as the mass comes out from the channel, it increases it spread. From this moment, the central part of the flow continues to keep a high velocity, due to the inertia stored along the slope. The lateral part of the flow, conversely, decreases suddenly its velocity and stop. The creation of this kind of track makes the runout increase and keep almost constant the spread. Probably this behavior is due to the

anisotropy of the material that makes the mass run differently in the transversal direction compared with the longitudinal one.

A similar behavior was observed by Azimi et al. (2016). They performed some laboratory experiments to understand the dynamics of gravity-driven free surface flow of multi-phase viscoplastic fluids. Foam and sand–foam mixtures were employed to represent multi-phase yield stress fluids.

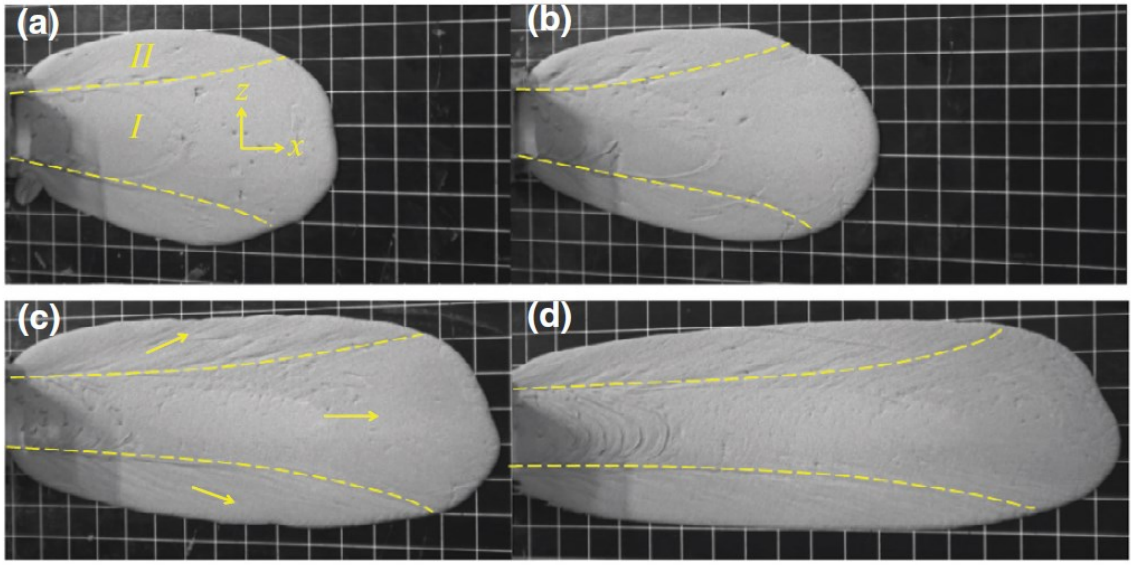

Figure 7.2.32 Snapshot images of the spreading of sand–foam mixtures 30s after the beginning of the test for various

Experimental observations on the flow and spread of this material indicated that the mixtures remained homogeneous during the plane tests and no discontinuity occurred. Spreading on an inclined plane was divided into two regions. Region *I* shows the main flow along the longitudinal axis and Region *II* shows the lateral spreading of the mixtures with an angle from the x axis (Figure 7.2.32).

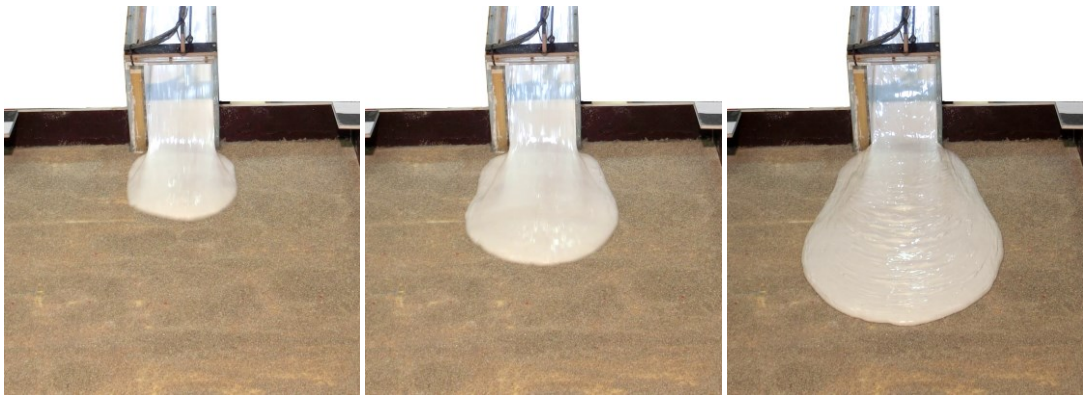

Figure 7.2.33 Pictures extracted from the video recorded by the frontal camera.

It is evident how the runouts increase without changing the lateral spread. The central part of the

material continues to flow undisturbed, while the lateral regions decrease soon their velocities and stop.

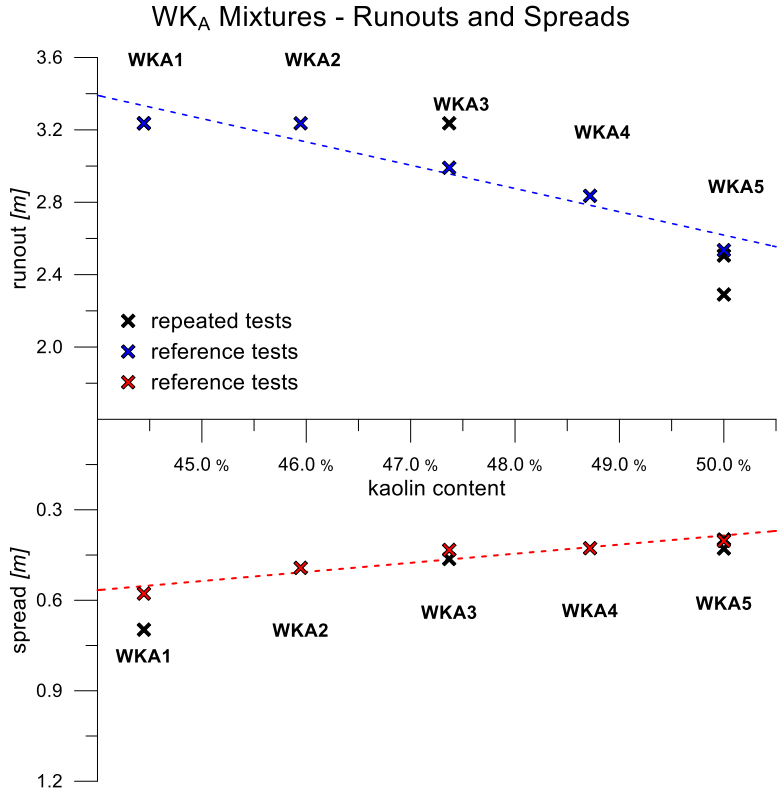

Figure 7.2.34 Comparison of the runouts and the spreads between the WK$_A$ tests.

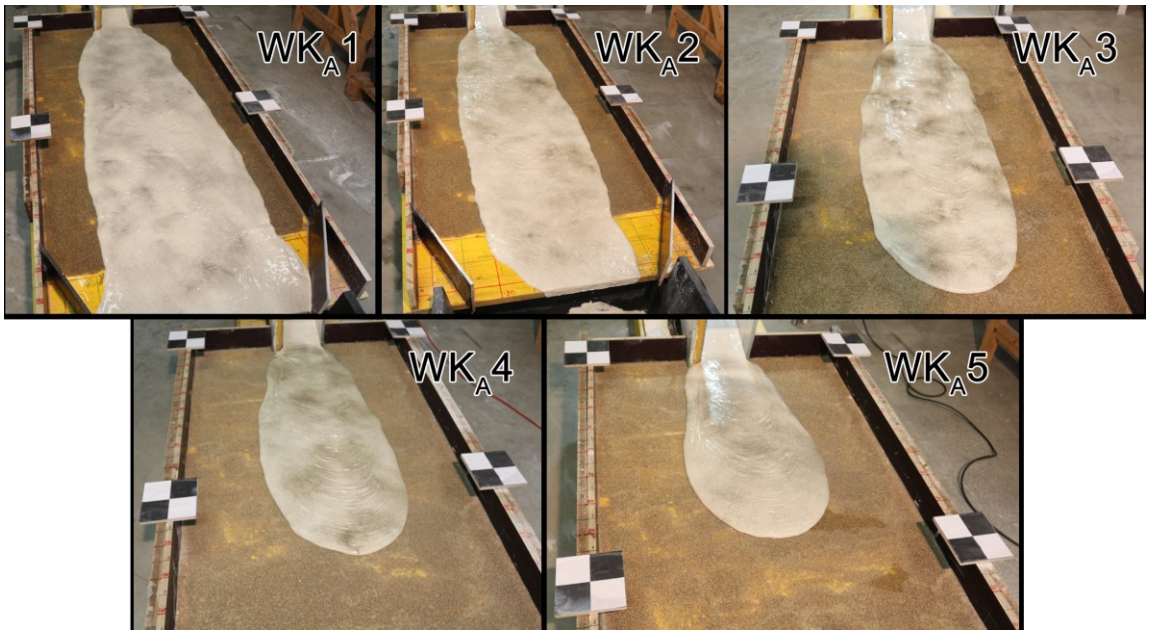

Figure 7.2.35 Pictures of all the deposits for the WK$_A$ experiments.

7.2.7 WSK_A Mixtures

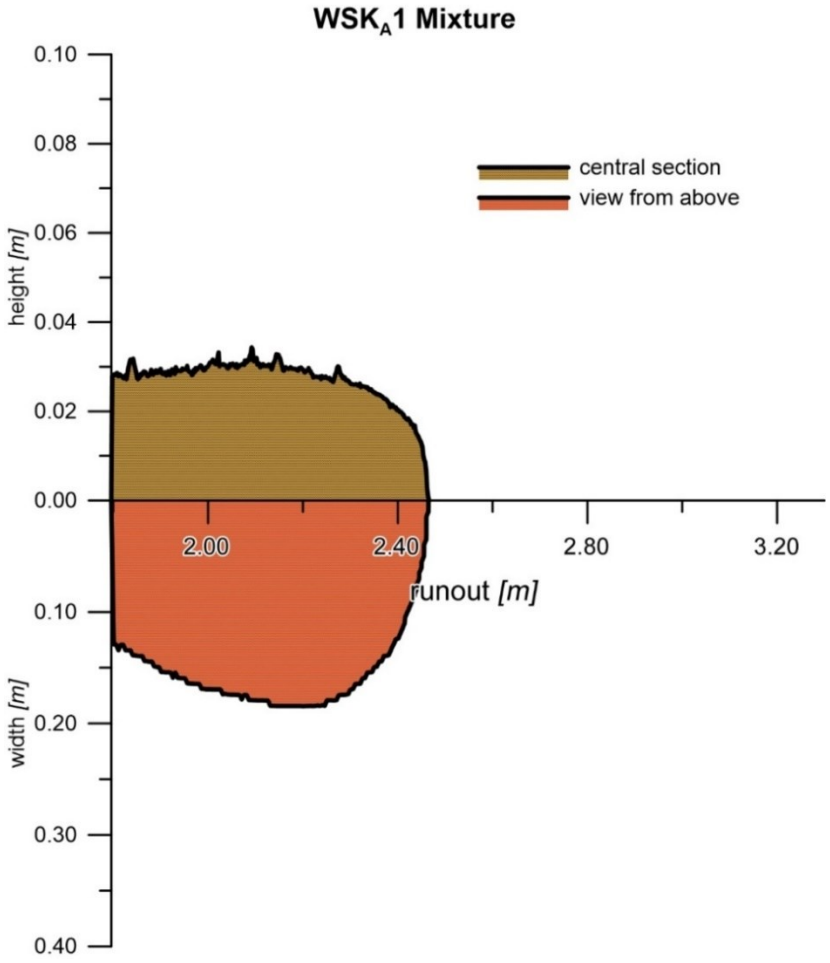

Figure 7.2.36 Central section and view from above for the WSK_A1 mixture.

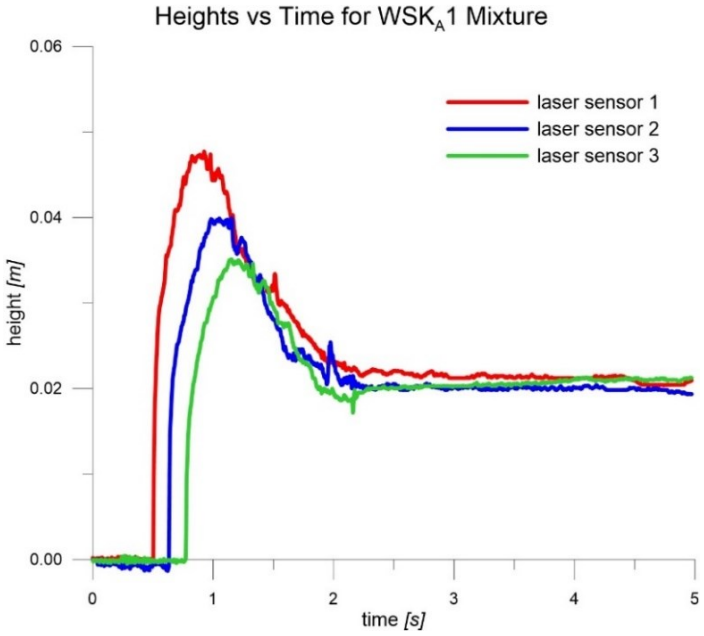

Figure 7.2.37 Heights of material vs time for the test.

Mixture WSK_A	
name	**WSK_A1**
sand	**$c_{v,tot}$**
%	-
16.7	0.353
Runout	**Spread**
m	*m*
2.465	0.379
Velocity 1	**Velocity 2**
m/s	*m/s*
2.631	2.443

Table 7.2.12 Characteristics of the test.

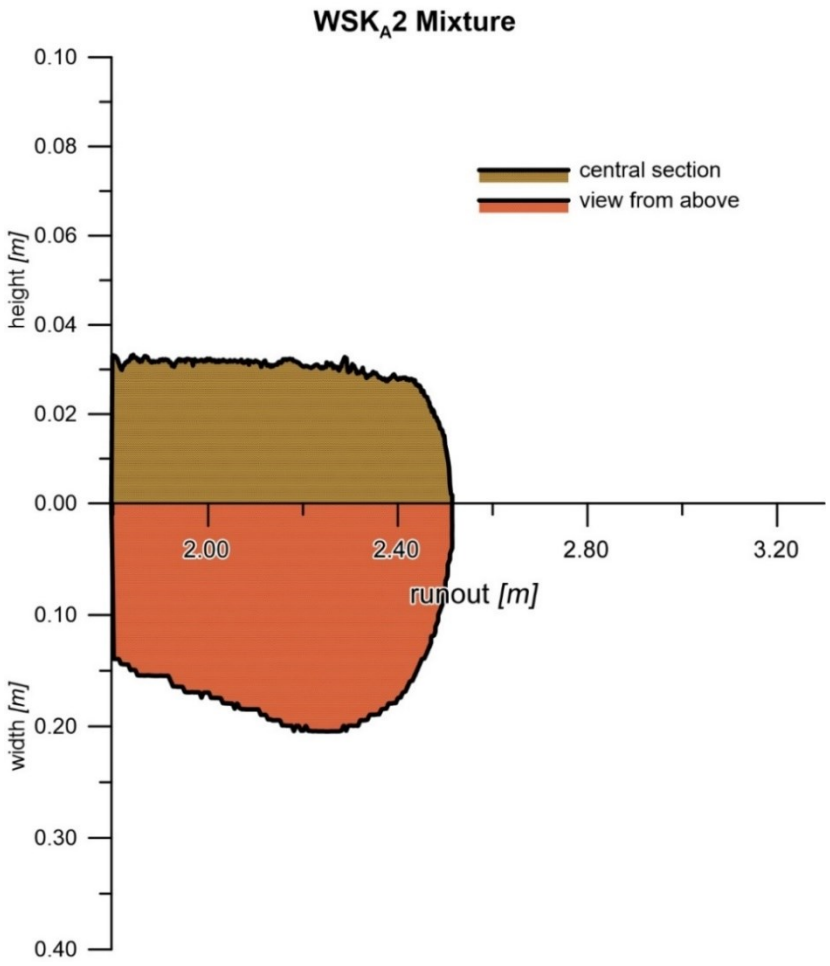

Figure 7.2.38 Central section and view from above for the WSK$_A$2 mixture.

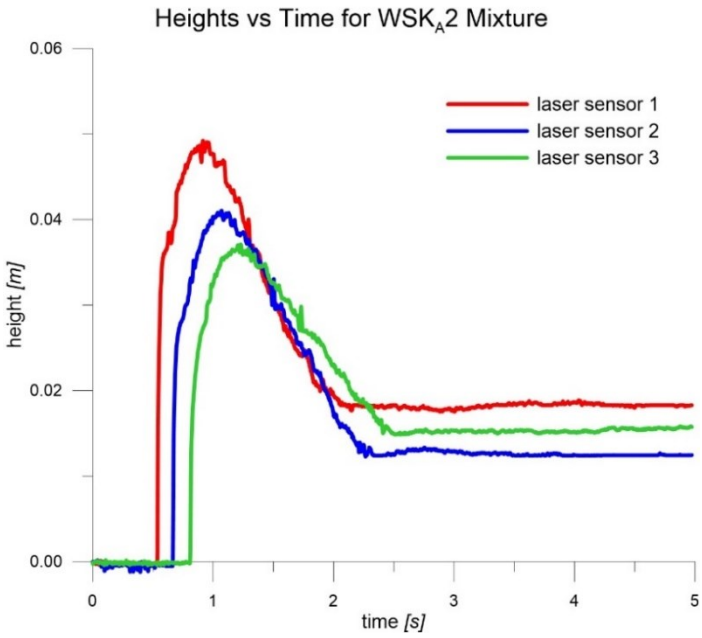

Mixture WSK$_A$	
name	**WSK$_A$2**
sand	**$c_{v,tot}$**
%	-
23.1	0.385
Runout	**Spread**
m	*m*
2.515	0.404
Velocity 1	**Velocity 2**
m/s	*m/s*
2.631	2.400

Table 7.2.13 Characteristics of the test.

Figure 7.2.39 Heights of material vs time for the test.

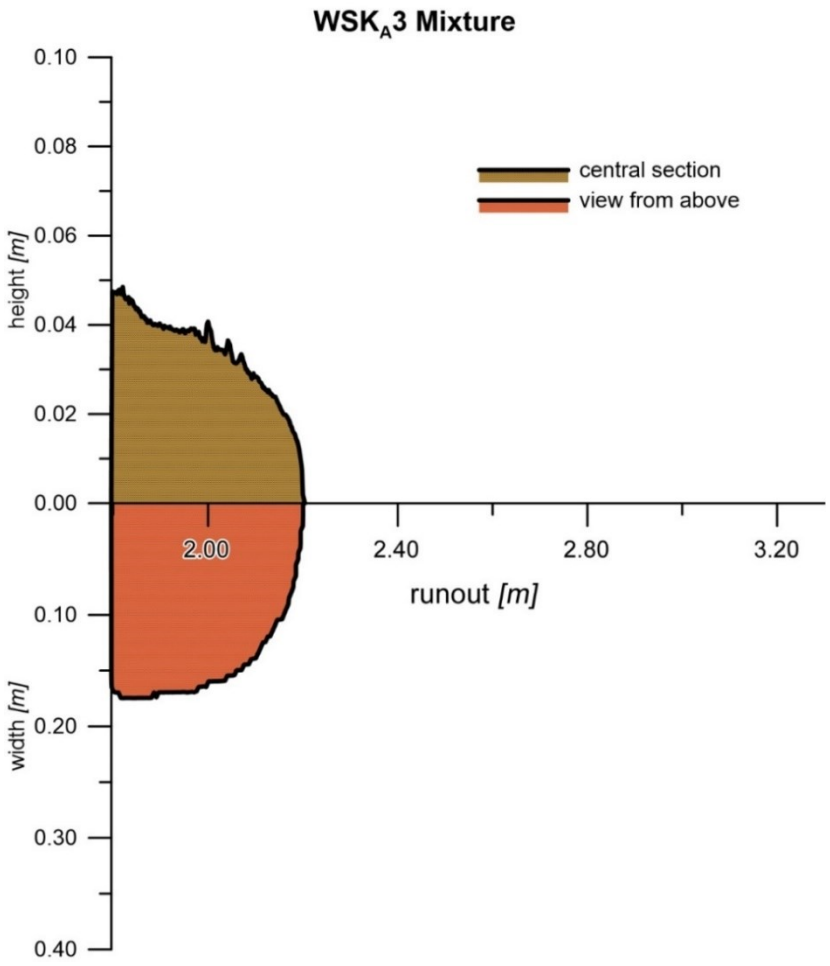

Figure 7.2.40 Central section and view from above for the WSK$_A$3 mixture.

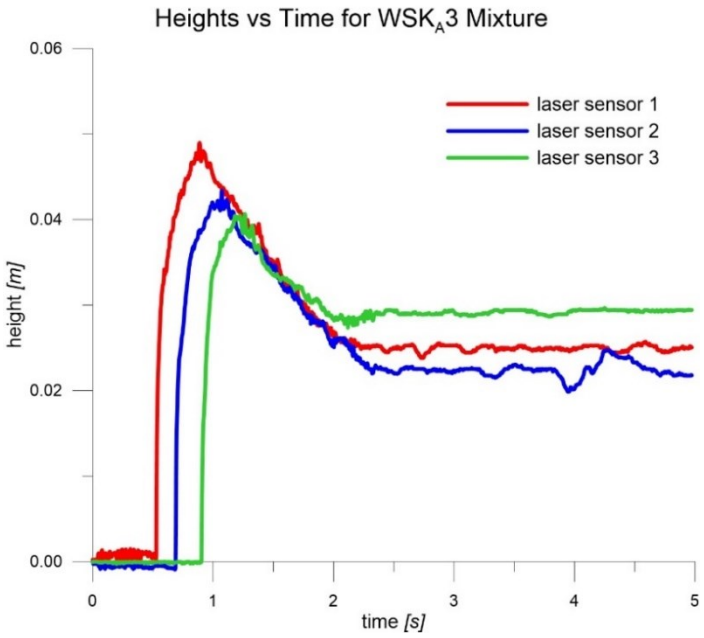

Mixture WSK$_A$	
name	**WSK$_A$3**
sand	**$c_{v,tot}$**
%	-
28.6	0.415
Runout	**Spread**
m	*m*
2.205	0.379
Velocity 1	**Velocity 2**
m/s	*m/s*
2.105	1.591

Table 7.2.14 Characteristics of the test.

Figure 7.2.41 Heights of material vs time for the test.

The same quantities of water and kaolin are inserted in the WSK_A mixtures, so the ratio between these two components is fixed equal to one. The sand content is therefore varied three times, from 16.7% to 28.6%.

The main goal of these tests consists in the comprehension of the influence of the sand in a viscous matrix. Each experiment was performed just once, so the considerations have to consider this fact.

Figure 7.2.42 Pictures of all the deposits for the WSK_A experiments.

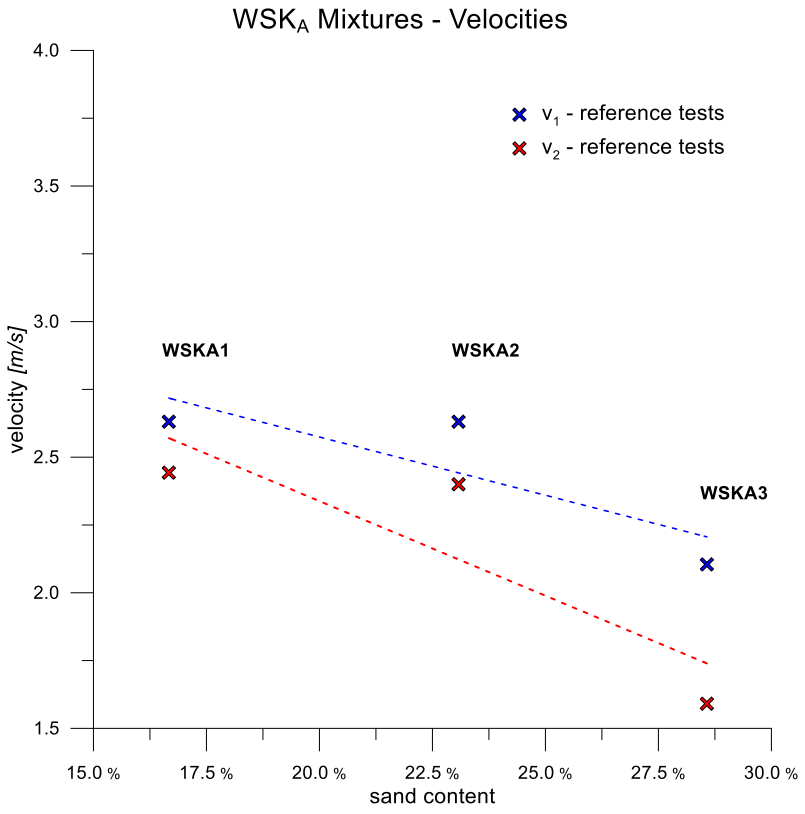

Figure 7.2.43 Comparison of the velocities between the WSK_A tests.

The runout initially increases with the increase of the sand content, then decreases. Probably the second test include a quantity of sand that is sufficient to raise the gravity load, increasing the density. The grains are suspended in the viscous matrix and are not able to perform friction.

Increasing the granular content, after a limit level, the flow start to depend on friction mechanism of momentum exchange. Consequently, the velocities decrease (Figure 7.2.43) and the runout makes the same.

It has to be noticed that again the spread of the deposits remain almost constant, confirming what observed working with water-kaolin mixtures (Figure 7.2.44).

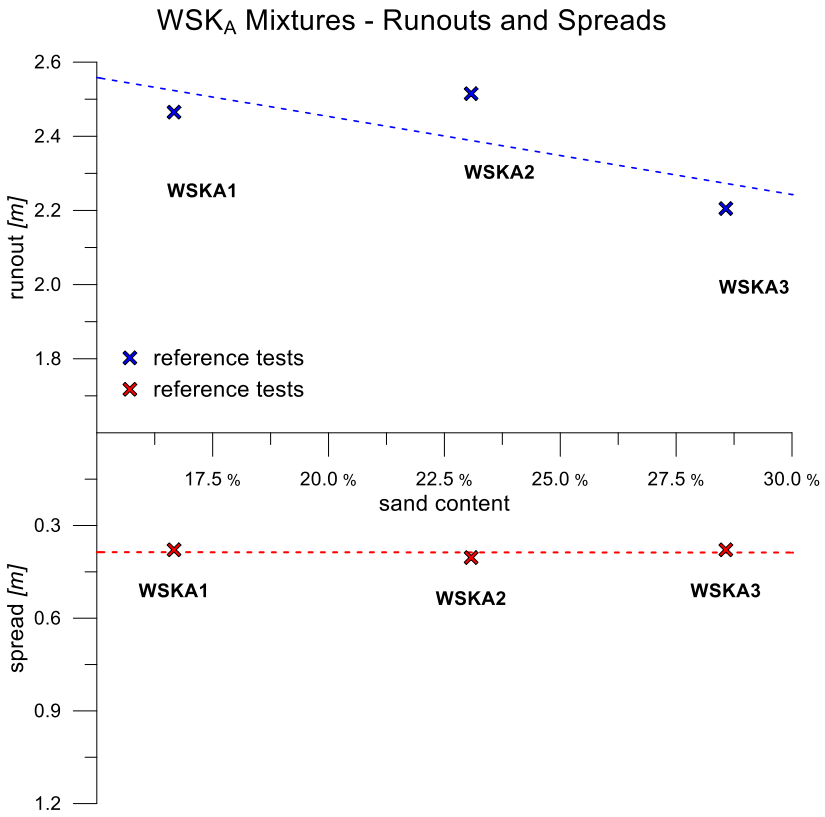

Figure 7.2.44 Comparison of the runouts and the spreads between the WSK$_A$ tests.

7.2.8 WSK_B Mixtures, first group

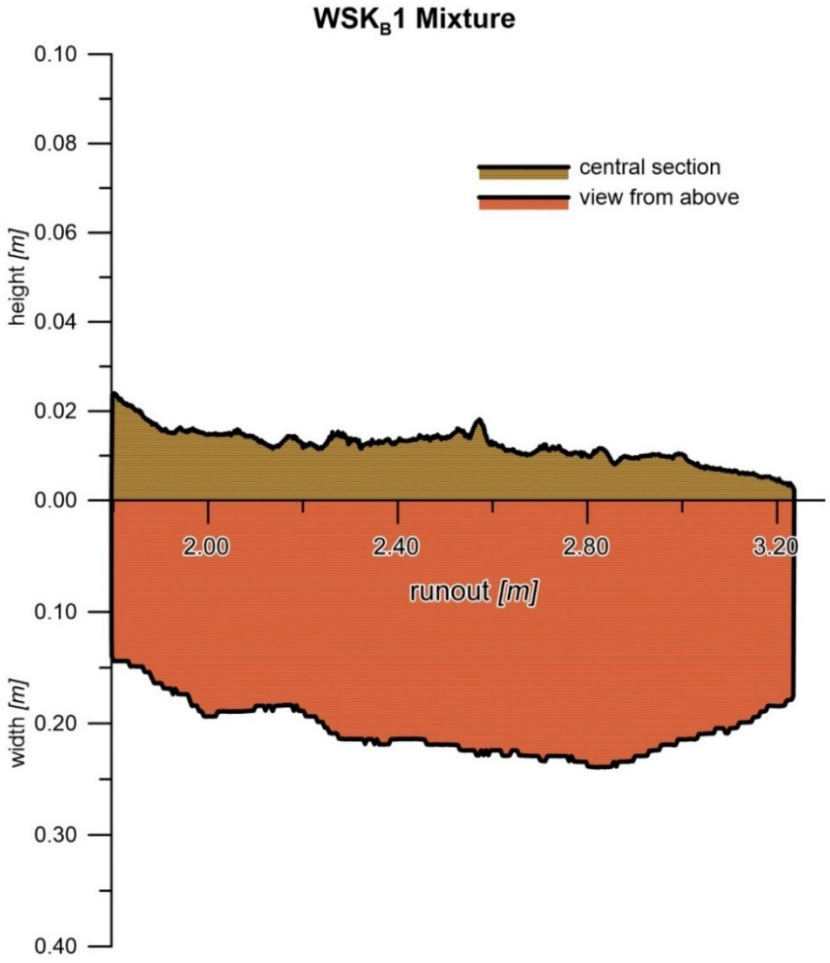

Figure 7.2.45 Central section and view from above for the WSK_B1 mixture.

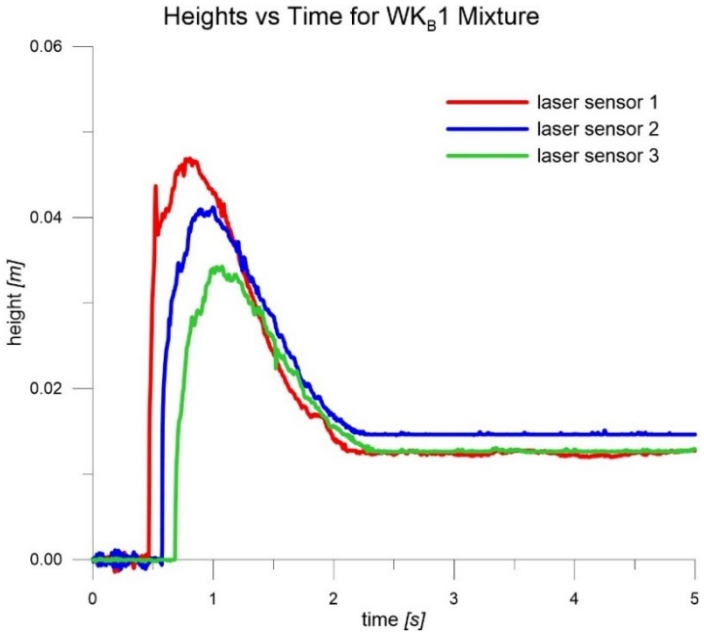

Figure 7.2.46 Heights of material vs time for the test.

Mixture WSK_B	
name	**WSK_B1**
sand	**$c_{v,tot}$**
%	-
10.0	0.280
Runout	**Spread**
m	*m*
3.236	0.493
Velocity 1	**Velocity 2**
m/s	*m/s*
3.109	3.109

Table 7.2.15 Characteristics of the test.

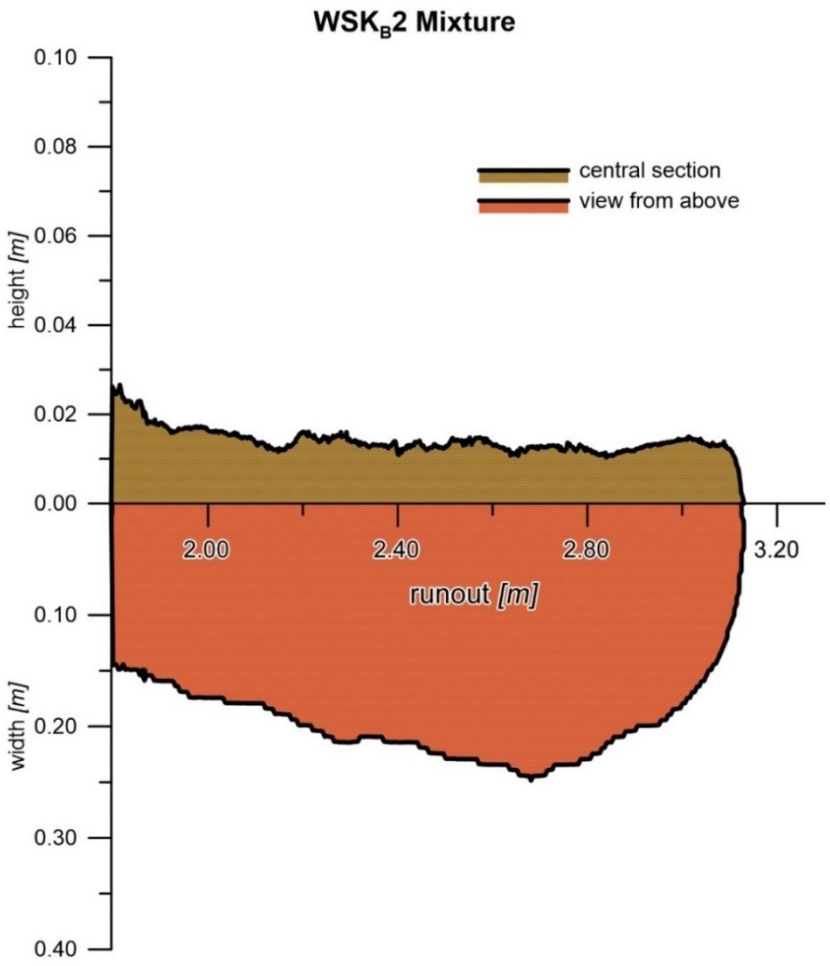

Figure 7.2.47 Central section and view from above for the WSK$_B$2 mixture.

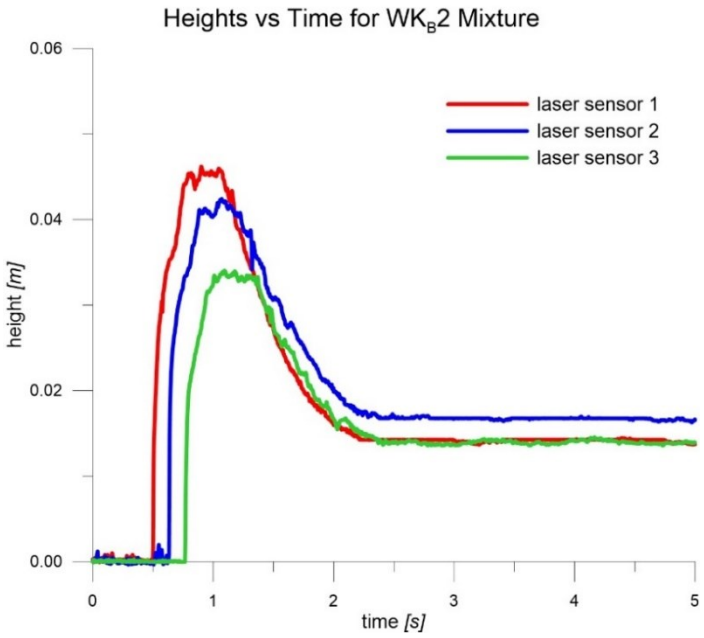

Mixture WSK$_B$	
name	**WSK$_B$2**
sand	**$c_{v,tot}$**
%	-
25.0	0.355
Runout	**Spread**
m	*m*
3.130	0.497
Velocity 1	**Velocity 2**
m/s	*m/s*
2.581	2.533

Table 7.2.16 Characteristics of the test.

Figure 7.2.48 Heights of material vs time for the test.

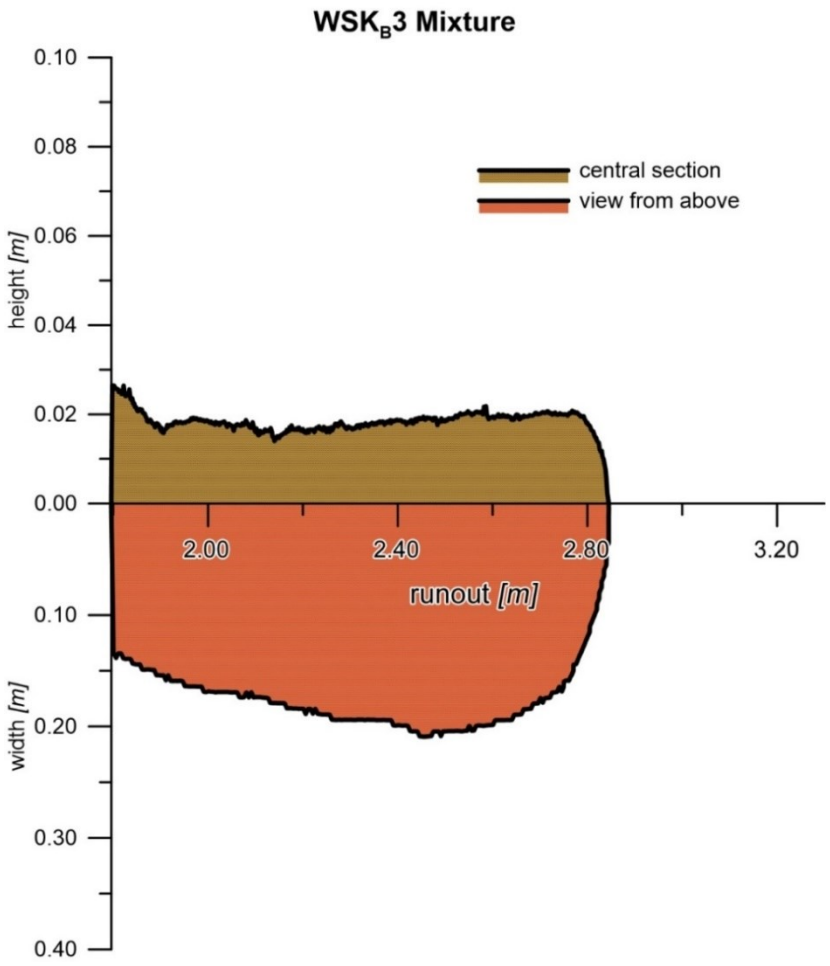

Figure 7.2.49 Central section and view from above for the WSK$_B$3 mixture.

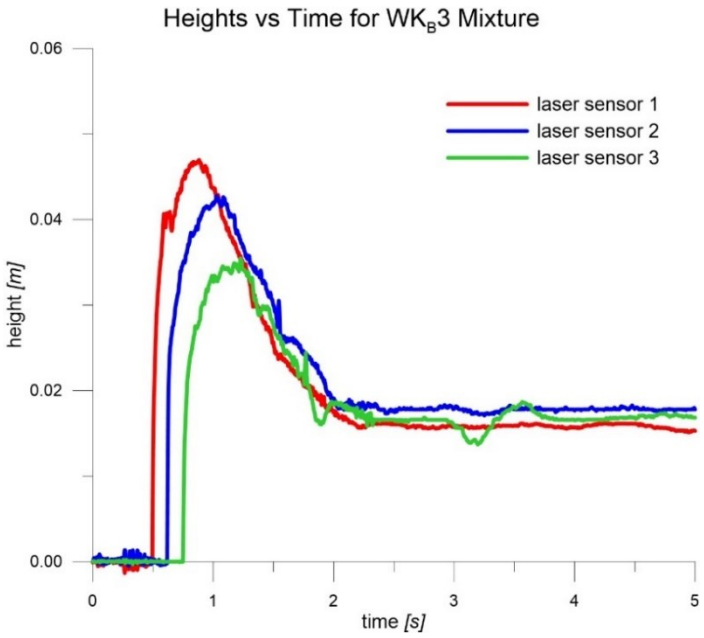

Mixture WSK$_B$	
name	**WSK$_B$3**
sand	**$c_{v,tot}$**
%	-
35.7	0.416
Runout	**Spread**
m	*m*
2.845	0.427
Velocity 1	**Velocity 2**
m/s	*m/s*
2.792	2.581

Table 7.2.17 Characteristics of the test.

Figure 7.2.50 Heights of material vs time for the test.

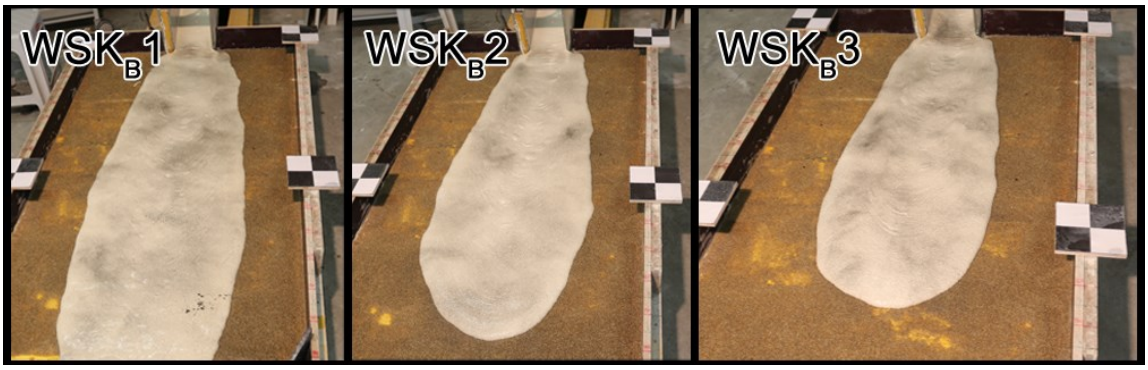

Figure 7.2.51 Pictures of all the deposits for the WSK_B experiments.

Starting from a mixture that contains 50% of water and 40% of kaolin, a crescent quantity of sand has been included in the flowing mass. The first test contains just 10% of sand, which is likely transported by the water-kaolin matrix. In the second test the sand content reaches the value of 25%, while the last test arrive at the value of 36%. In this case, the starting mixture is very liquid.

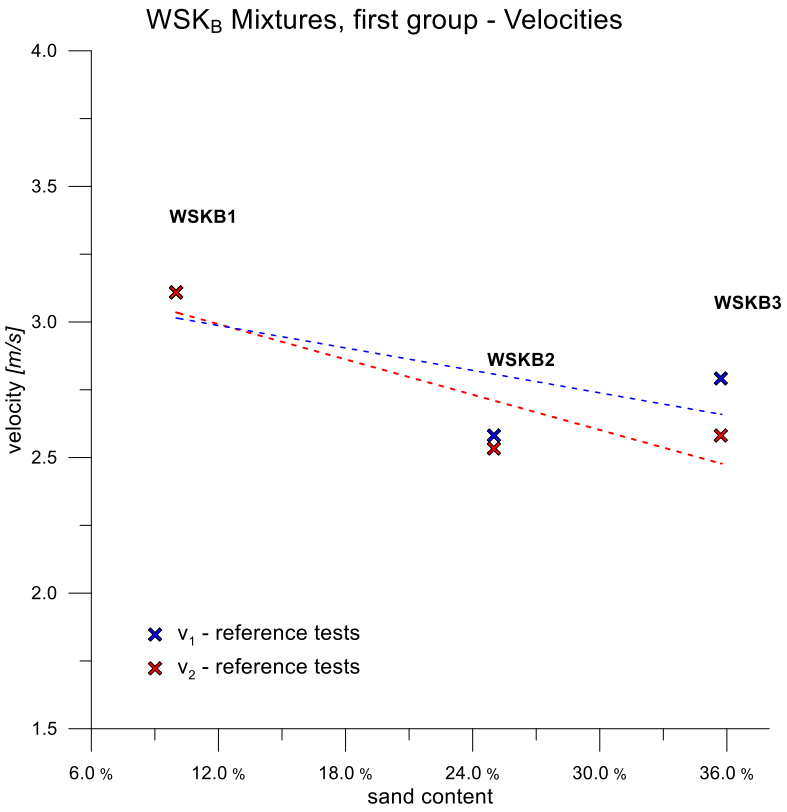

Figure 7.2.52 Comparison of the velocities between the WSK_B tests, first group.

Figure 7.2.52 shows that while there is not acceleration for the WSK_B1 mixture passing from the first part of the channel to the second, the same does not happen for WSK_B2 and WSK_B3. The material slows down more when the sand content grows.

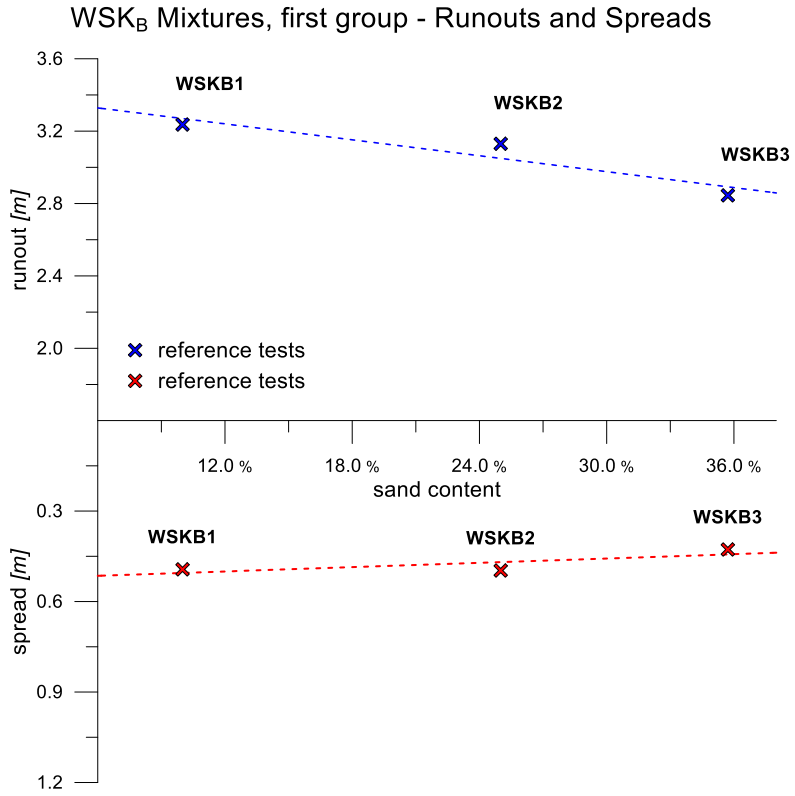

Figure 7.2.53 Comparison of the runouts and the spreads between the WSK_B tests, first group.

If we compare the runouts of these three tests, it can be said that the runouts decrease with the granular material added to the mixture (Figure 7.2.53). The distance traveled by the first case should be higher, considering the fact that the material has reached and exceeded the total length of the horizontal plane.

The spread remains almost constant, confirming the fact that the material has a different behavior longitudinally with respect to how it acts transversely.

7.2.9 WSK_B Mixtures, second group

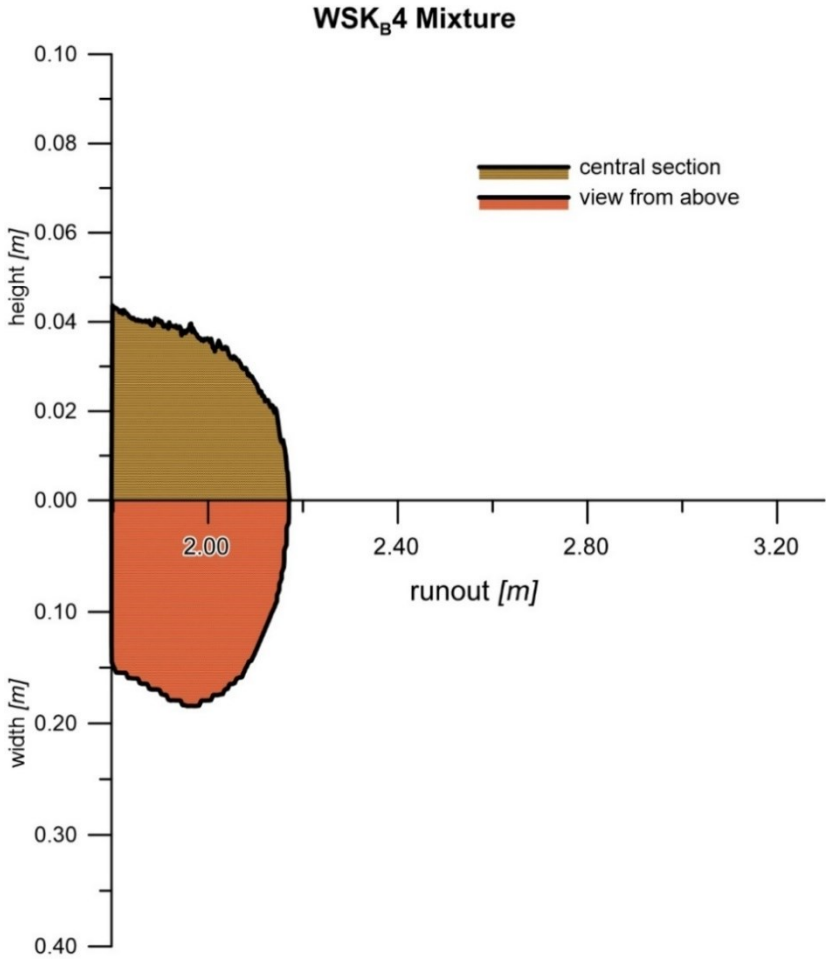

Figure 7.2.54 Central section and view from above for the WSK_B4 mixture.

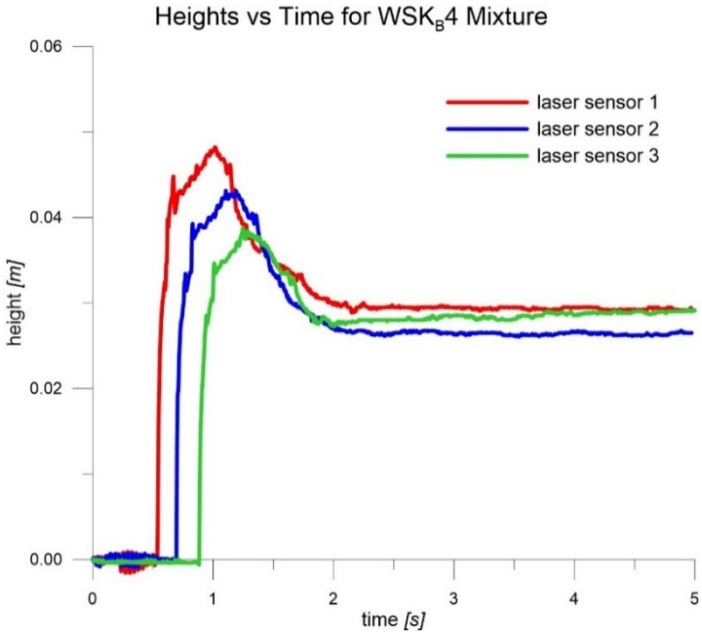

Figure 7.2.55 Heights of material vs time for the test.

Mixture WSK_B	
name	**WSK_B4**
sand	**$c_{v,tot}$**
%	-
9.1	0.318
Runout	**Spread**
m	*m*
2.171	0.368
Velocity 1	**Velocity 2**
m/s	*m/s*
2.206	1.800

Table 7.2.18 Characteristics of the test.

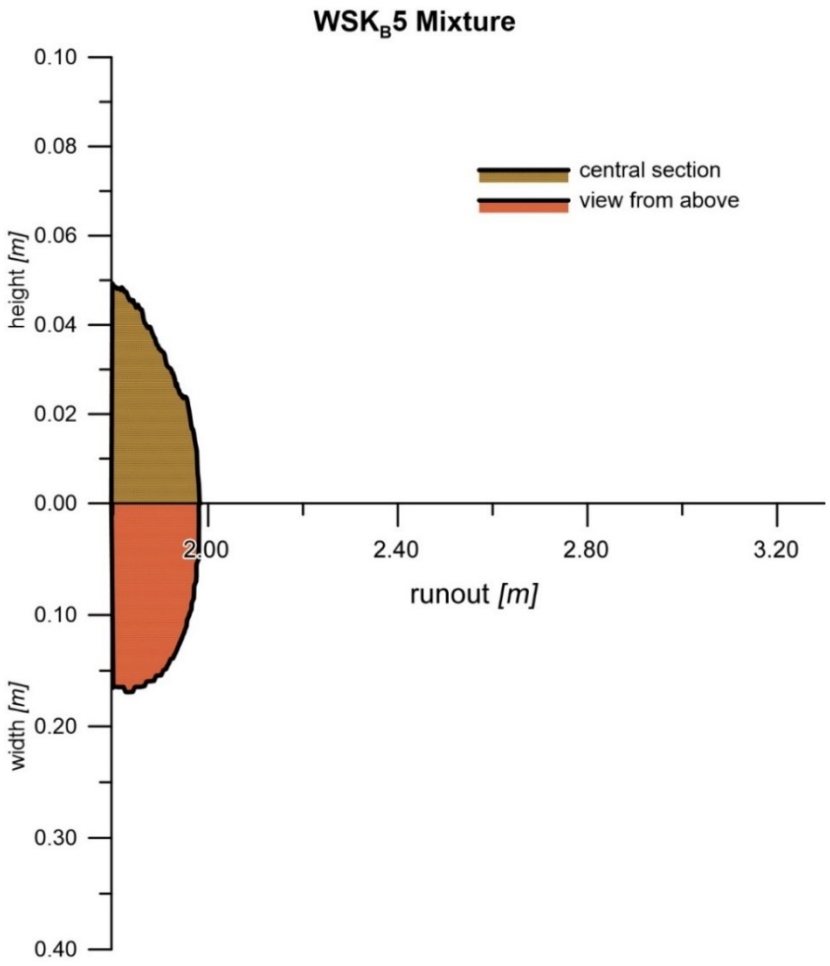

Figure 7.2.56 Central section and view from above for the WSK$_B$5 mixture.

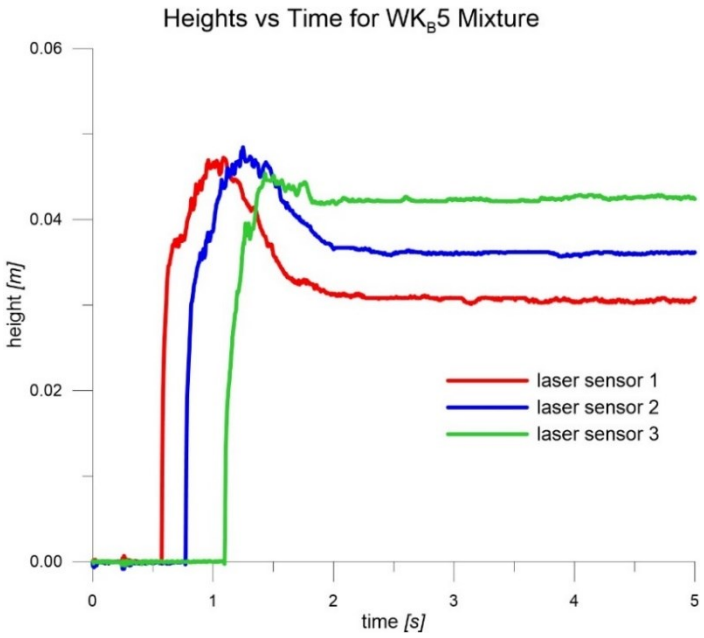

Figure 7.2.57 Heights of material vs time for the test.

Mixture WSK$_B$	
name	**WSK$_B$5**
sand	**$c_{v,tot}$**
%	-
16.7	0.353
Runout	**Spread**
m	*m*
1.981	0.348
Velocity 1	**Velocity 2**
m/s	*m/s*
1.732	1.052

Table 7.2.19 Characteristics of the test.

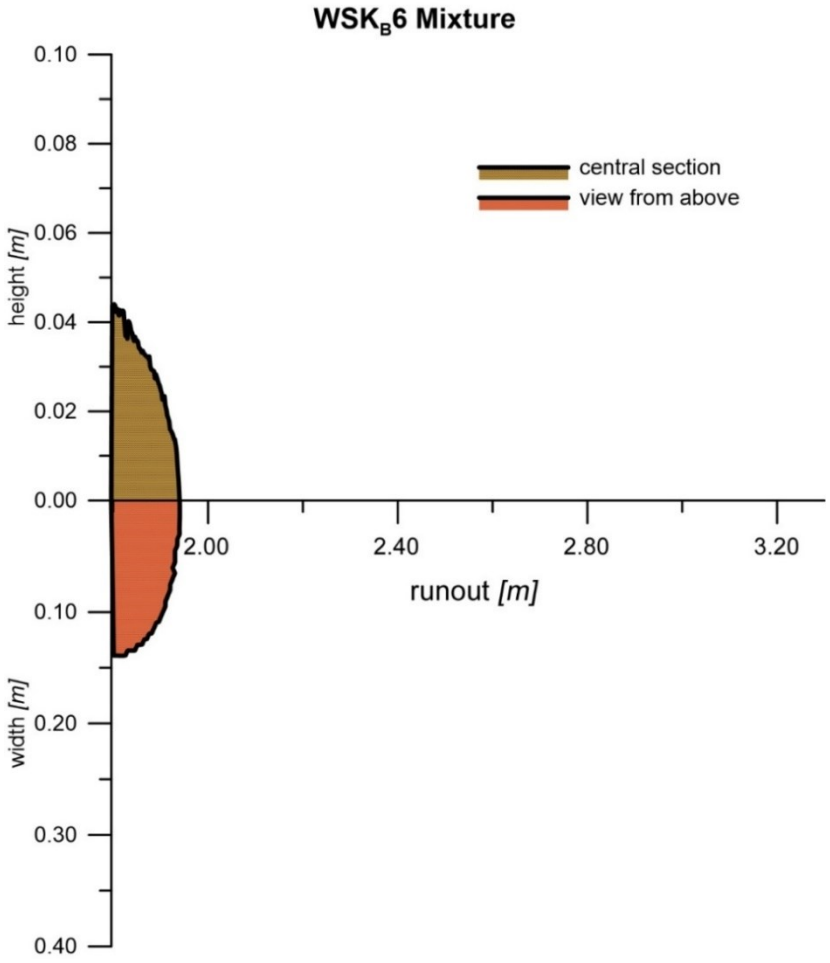

Figure 7.2.58 Central section and view from above for the WSK$_B$6 mixture.

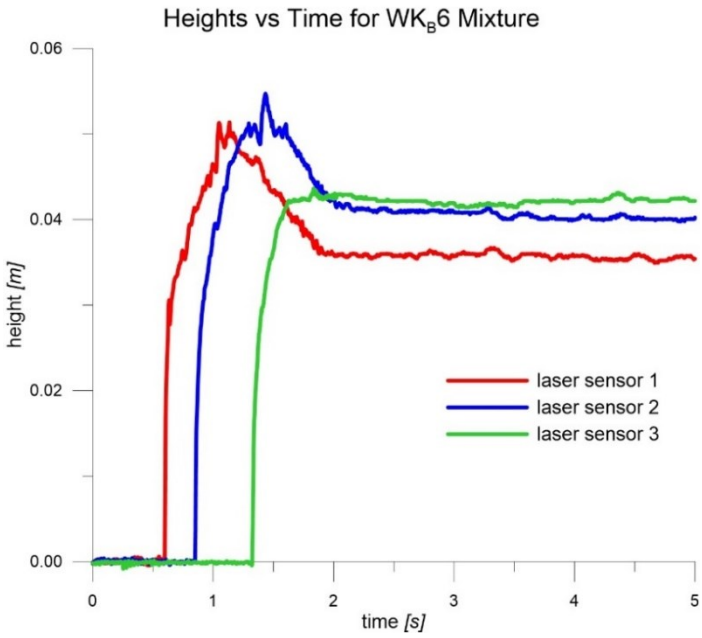

Figure 7.2.59 Heights of material vs time for the test.

Mixture WSK$_B$	
name	**WSK$_B$6**
sand	**$c_{v,tot}$**
%	-
23.1	0.385
Runout	**Spread**
m	*m*
1.940	0.294
Velocity 1	**Velocity 2**
m/s	*m/s*
1.341	0.720

Table 7.2.20 Characteristics of the test.

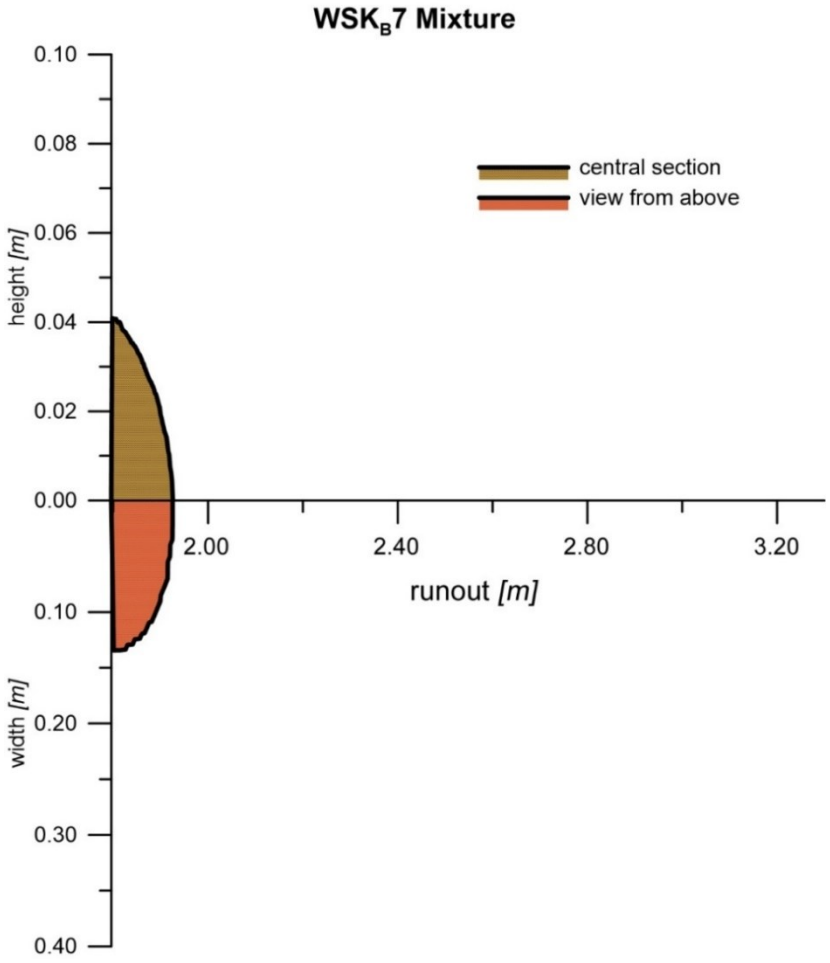

Figure 7.2.60 Central section and view from above for the WSK$_B$7 mixture.

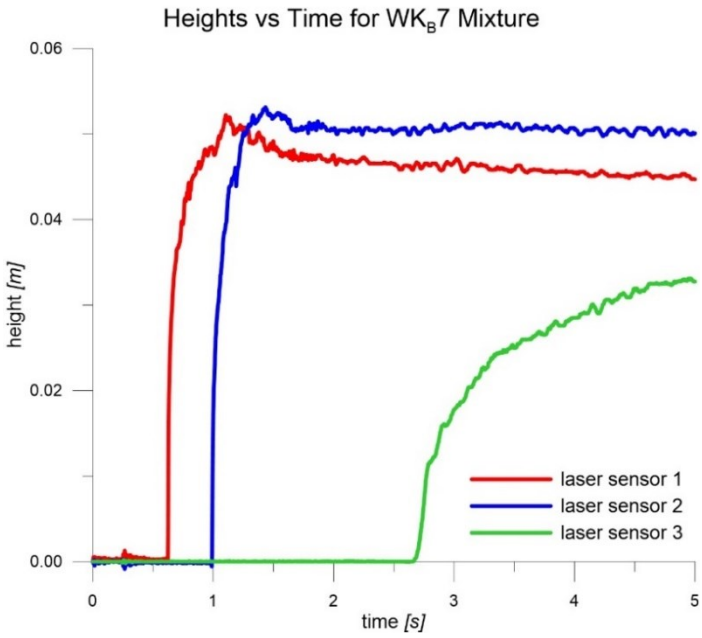

Figure 7.2.61 Heights of material vs time for the test.

Mixture WSK$_B$	
name	**WSK$_B$7**
sand	**$c_{v,tot}$**
%	-
28.6	0.415
Runout	**Spread**
m	*m*
1.925	0.279
Velocity 1	**Velocity 2**
m/s	*m/s*
0.937	0.196

Table 7.2.21 Characteristics of the test.

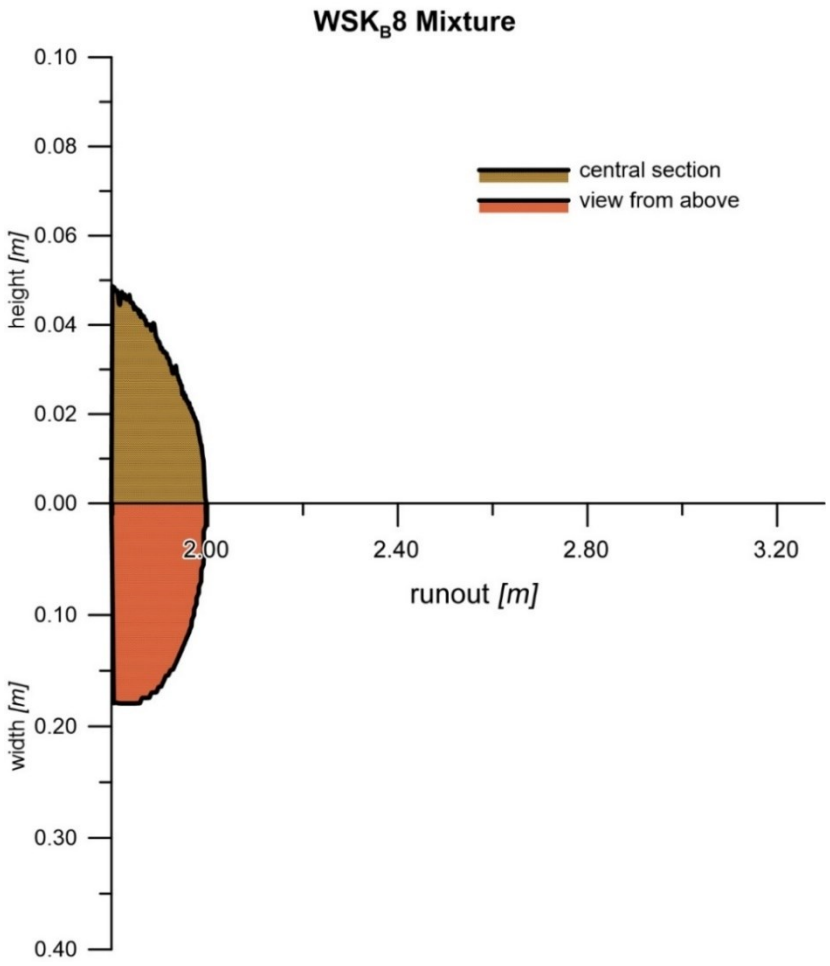

Figure 7.2.62 Central section and view from above for the WSK$_B$8 mixture.

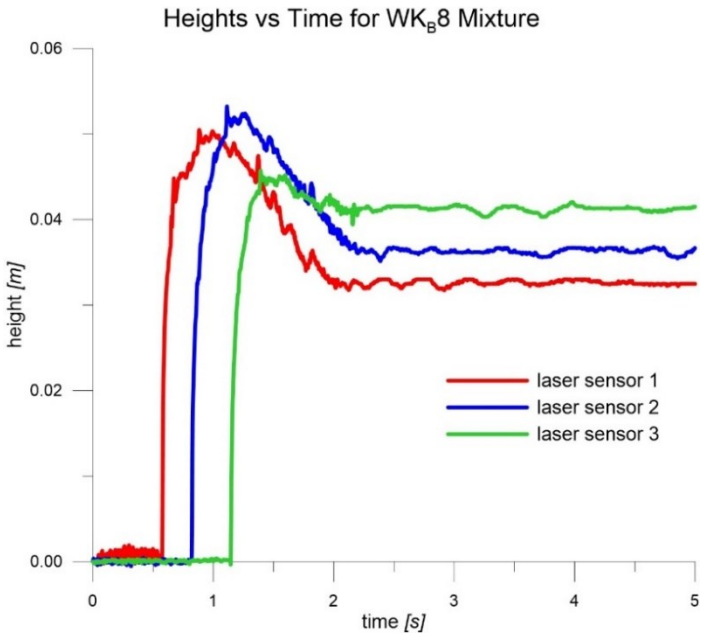

Figure 7.2.63 Heights of material vs time for the test.

Mixture WSK$_B$	
name	**WSK$_B$8**
sand	**$c_{v,tot}$**
%	-
33.3	0.441
Runout	**Spread**
m	*m*
1.995	0.369
Velocity 1	**Velocity 2**
m/s	*m/s*
1.396	1.044

Table 7.2.22 Characteristics of the test.

7.2.9.1 Repeatability of the WSK_B tests

Again, among all the WSK_B experiments, it was decided to repeat twice three test. It is evident that the second try with the WSK_B4 mixture gives unreliable results. This is evident also comparing the velocities of the two experiments: v_1 and v_2 of the second try are 1.20m/s and 0.78m/s respectively, which means that the flow was evidently slower, known that v_1 and v_2 of the first test are 2.21m/s and 1.80m/s respectively. The deposit shape also underlines the inaccuracies that characterize this second try (Figure 7.2.64).

Results that are more similar are obtained with the others two mixtures considered. Figure 7.2.65 makes it clear how the deposits in both of the WSK_B5 tests are similar. The runouts differ for less than 1cm and the spreads also are very comparable. Looking at the velocities, it is evident a good repeatability because v_1 is 1.73m/s for the first try and 1.65m/s for the second one, while v_2 goes from 1.05m/s to 0.87m/s.

Good agreements is also present in the two experiments performed with the WSK_B7 mixture. Even if the second velocity slightly differs, passing from 0.20m/s to 0.52m/s, all the other variables are almost identical. The first test has in fact a runout of 1.92m, a spread of 0.28m and a velocity v_1 equal to 0.94m/s and the second has 1.92m, 0.28m and 1.07m/s respectively.

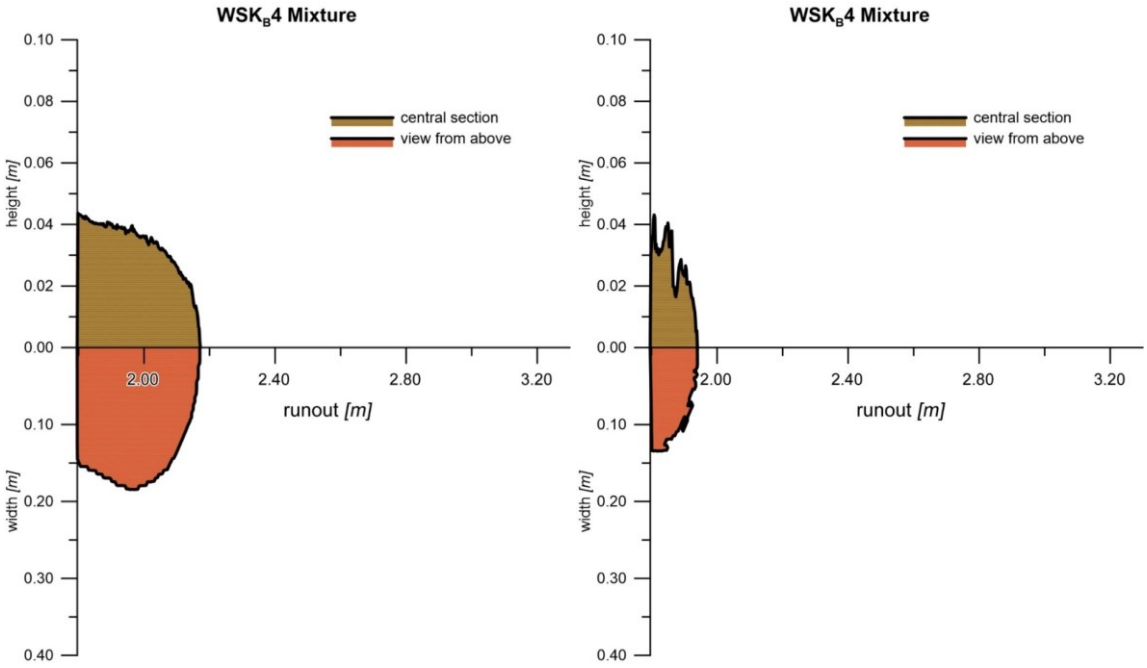

Figure 7.2.64 Comparison of the results for the WSK_B4 tests.

The difference observable in the first comparison are probably due to some inaccuracies during the preparation and the execution of the tests. Even if all the operations have been repeated with attention, some environmental conditions, such as the temperature and the humidity may have influenced the material during the mixing operations.

Anyway, all the rest of the tests leads to coherent and stable results that assure the reliability of the measurements. Speaking about the WSK_B4 experiments, it is evident that the try to neglect is the second one. It gives data that do contrast with all the others of the WSK_B series.

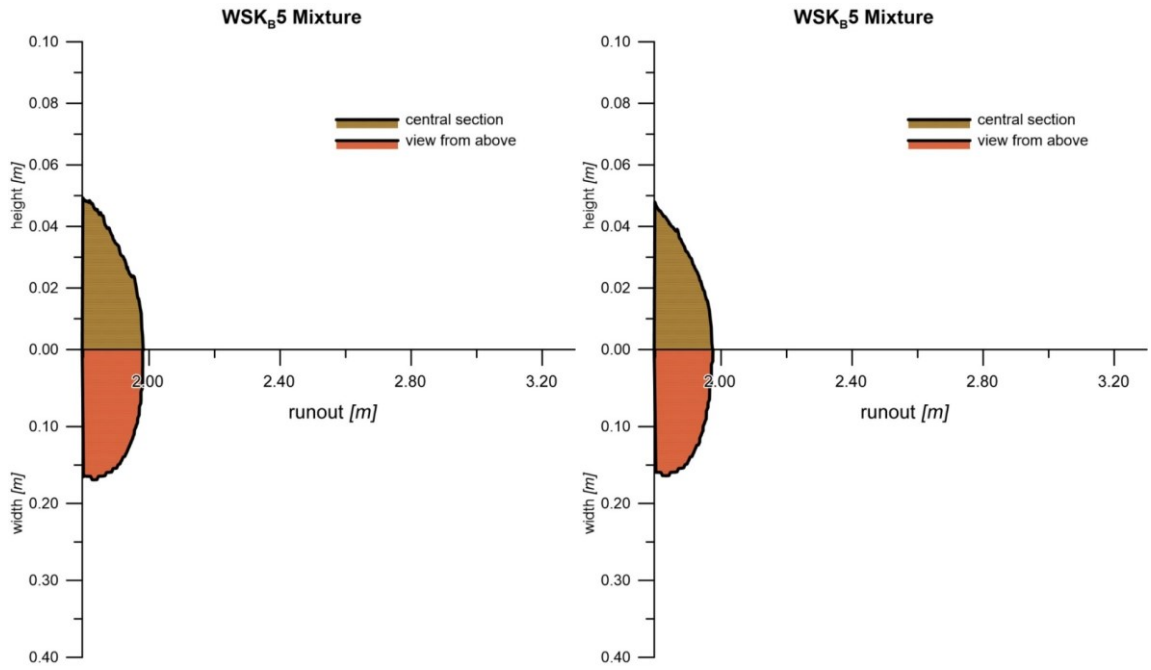

Figure 7.2.65 Comparison of the results for the WSK_B5 tests.

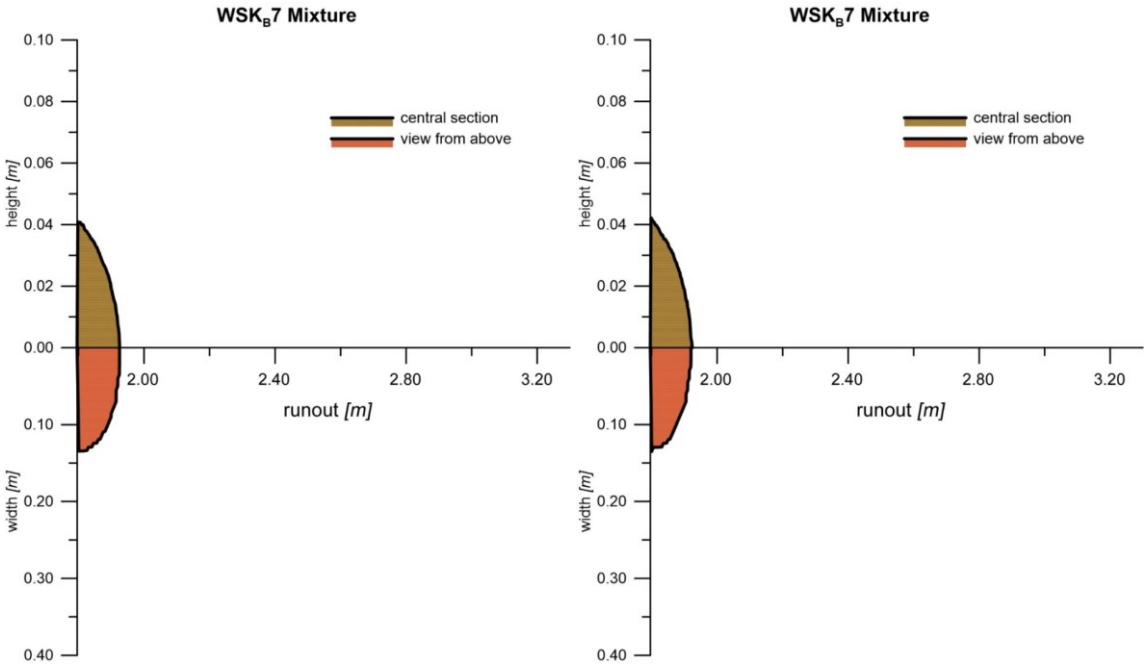

Figure 7.2.66 Comparison of the results for the WSK_B7 tests.

7.2.9.2 Considerations on the WSK_B experiments

In all the repetition is always observable how the material slows down along the channel. The high viscosity of the mixtures causes an average difference of 0.6m/s between v_1 and v_2 (Figure 7.2.67). The fact the two interpolating lines in Figure 7.2.67 are parallel means that the deceleration can be considered almost invariable even varying the sand content. The mass, after the initial acceleration phase, starts to slow down. In all the WSK_B4- WSK_B8 tests the material hardly reaches the deposit plane (Figure 7.2.68).

The material in all this series of experiments are extremely viscous. Along the channel, at the end of the flow, a huge quantity of mixture remains. Just a little part of the initial mass succeeds to reach the deposit plane.

The spreads are almost the same for all these experiments (Figure 7.2.69), while the runout slightly decreases increasing the sand content. The first test has the highest runout among all those experiments. The increment of sand makes the density of the mixture increasing, but causes also a decrease in the velocities and in the runouts. Frictional effects between the grains probably influence the motion.

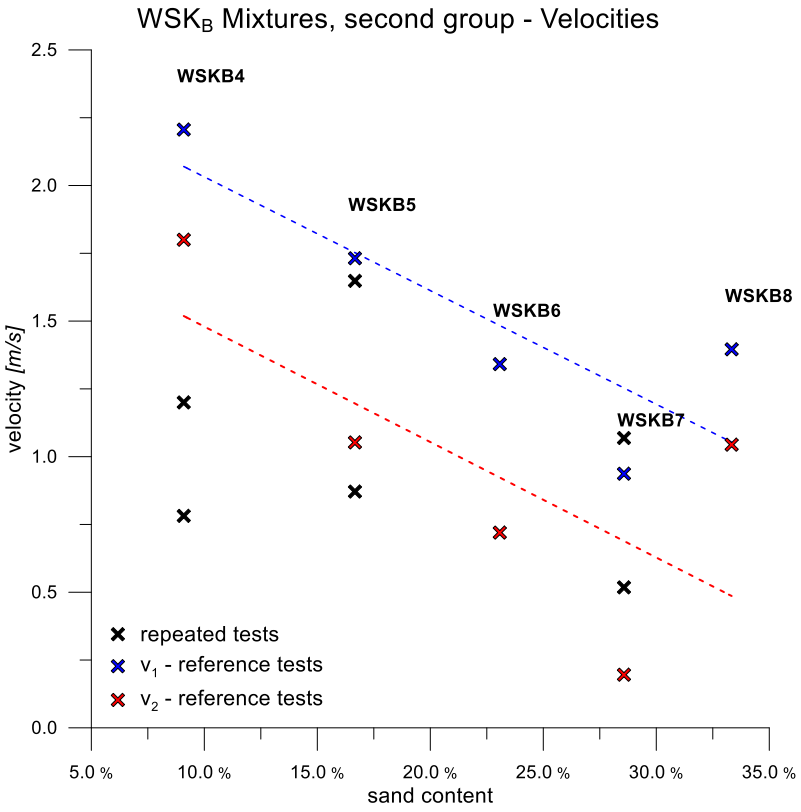

Figure 7.2.67 Comparison of the velocities between the WSK_B tests, second group.

It has to be noticed that the WSK_B8 has the values of runouts, spreads and velocities that are in contrast with the rest of measurements. The almost linear dependence of the runout on the sand content is not confirmed by this test. Anyway, the differences are extremely small and this fact can

be attributed to some inaccuracies on the test execution. Unfortunately it is not available any second try with this mixture.

Figure 7.2.68 Pictures of all the deposits for the WSK$_B$ experiments.

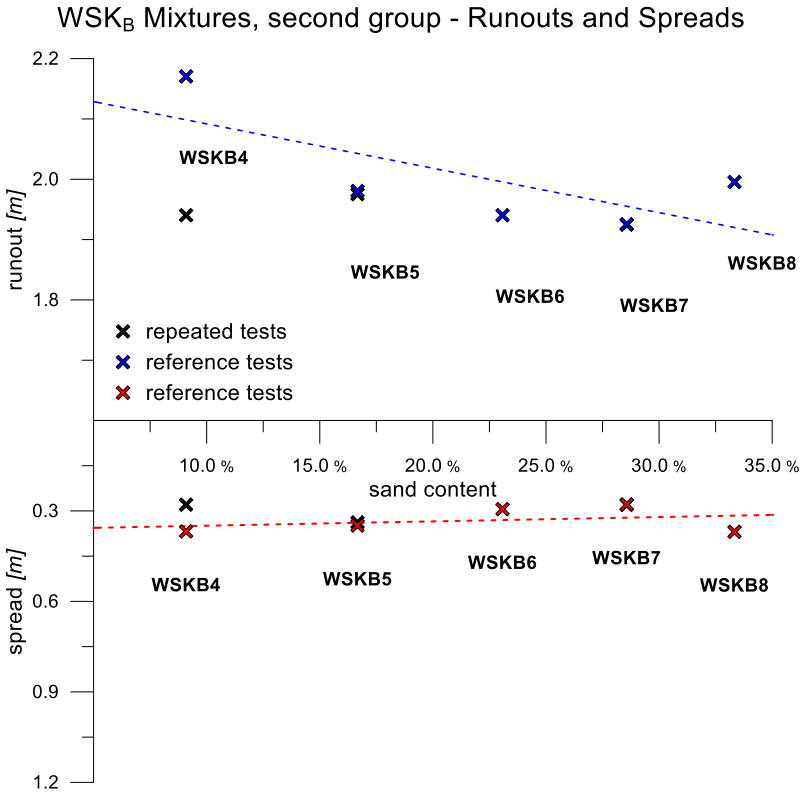

Figure 7.2.69 Comparison of the runouts and the spreads between the WSK$_B$ tests, second group.

7.2.10 Comparison between WSK_A and WSK_B Mixtures

The two mixtures contain 40% of kaolin, 10% of sand and 50% of water each. The difference, in this case, consist in the type of kaolin used. It is evident that the behavior is quite similar for both the tests. The material, in fact, reaches the end of the horizontal plane, creating an analogous shape.

If we look at Figure 7.2.72, we can see that the runouts are theoretically the same. This can be explained considering that 2.263m is the total length of the deposition plane. In the same figure, the spreads are also plotted. The less fluidity of the kaolin B reduces the width of the final shape of 6cm. Looking at the central section of the deposit (Figure 7.2.70), it can be underlined that higher heights of material are present along all the horizontal plane, especially on the left side, just after the change of slope. The more viscous nature of kaolin B measured in §7.2.2 influences the test, even if the mixture is very liquid.

To compare the behavior of the material along the channel, we can consider now how the velocity change passing form v_1 to v_2. First of all, the high liquidity of the mass makes it happens that the motion almost keeps the same velocity along the channel. Light differences can be noticed for WSK_A case, where v_1=3.60m/s and v_2=3.51m/s. For WSK_B mixture, the two velocities are identical and equal to 3.11m/s.

A second consideration confirm the effect of the higher viscosity of kaolin B compared to kaolin A. If we compare the velocity range of the WSK_A test with the one of WSK_B, it can be noticed that the B kaolin makes the flow slower.

Finally, Figure 7.2.71 underlines the higher viscosity of the test performed with kaolin B, compared to the one achieved with kaolin A.

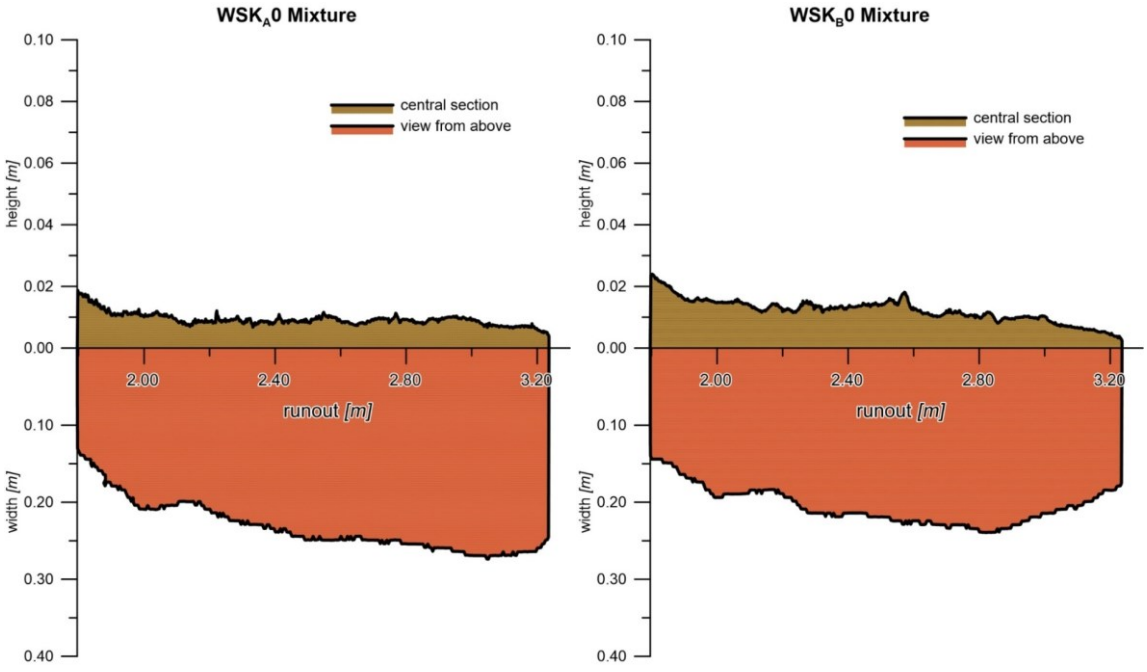

Figure 7.2.70 Comparison of the results obtained using kaolin A and kaolin B.

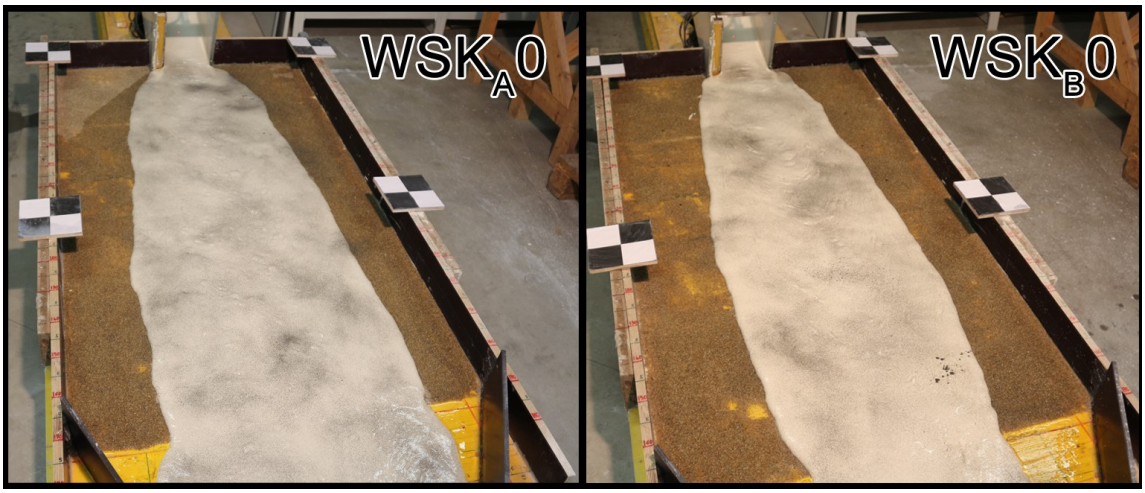

Figure 7.2.71 Pictures of all the deposits of the WSK$_A$0 and WSK$_B$0 experiments.

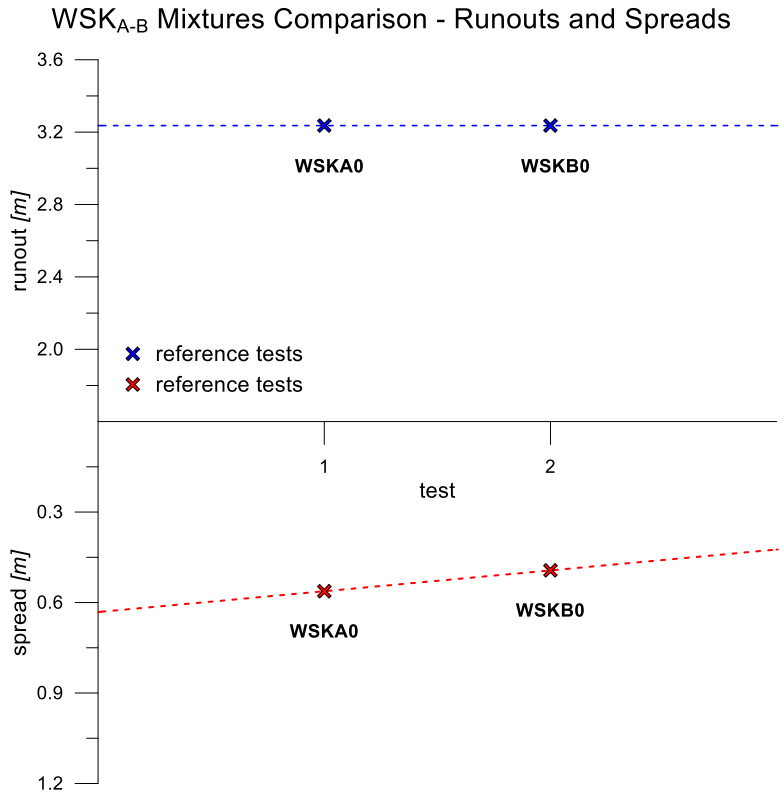

Figure 7.2.72 Comparison of the runouts and the spreads between the WSK$_A$ and WSK$_B$ tests.

7.2.11 Numerical simulations of the flume tests

The calibration technique applied for the first case studies can be now applied to the flume tests. The geometry of the system is still simple and well known, even if the cases are quite more complicated with respect to the spread of a cylinder on a plane.

First, the strategy of calibration has to be explained. Secondly, it is important to define what performance index can be used to identify the most reliable simulations among the huge number of tests performed. Finally, the behavior of the parameters depending on the properties of the mixtures considered has to be analyzed.

Two different rheological laws are included in the model, with the purpose to understand which is between the two, the best to reproduce the experimental result. Initially, Bingham's parameters has to be calibrated and therefore it is necessary to define the range of variation of those. Then, the same procedure is repeated with the turbulent coefficient and the internal friction angle that characterize the Voellmy rheological law. Each parameter is varied 20 times, with a logarithmic distribution between a maximum and a minimum value. All the combinations between these values are tried. At this point, the input files are automatically filled by a *Matlab* function and the simulations can be performed.

For each rheological law, 400 simulations are run. The strategy is slightly different from the one described in §0, where for each case, 100 tests were performed, including the exact value of density and changing the parameters range. In fact, a mean density is now fixed and, with just one group of simulation, all the laboratory tests are reproduced. The range of variation of the parameters has to be defined to cover all the cases.

In all the simulations, the density is fixed to $1400kg/m^3$. Depending on the rheological parameters, the variation ranges decided are the following:

- For Bingham law, τ is varied from *10Pa* to *200Pa*, while μ from $0.05Pa \cdot s$ to $15Pa \cdot s$.
- For Voellmy law, ξ is varied from $10m \cdot s^{-2}$ to $1000m \cdot s^{-2}$, while $cos\phi$ from *0.01* to *0.40*.

To decide the variation range of viscosity and yield stress, the results described in §7.2.2 are considered. Speaking about Voellmy rheology, instead, the literature suggested some typical values, already reported in §3.2.1.2.

7.2.11.1 Input files

7.2.11.1.1 "top" file

The first information included in the "top" file indicates the geometry of the basal topography. *Ictop=11* means that you have to explicit the x y z coordinates of all the points composing the basal topography. (Figure 7.2.73). The basal topography basically consists in an inclined part followed by an horizontal plane. The size of the mesh is composed by square of side 0.005m.

7.2.11.1.2 "dat" file

In this files all the rheological parameters defined above are written. In "dat" file the boundary conditions are therefore formalized. Basically two segments 2.56m long are identified and it is imposed zero speed in a direction perpendicular to these lines. These conditions lead to some errors in the approximation of the flow. The simulated velocities along the slope are transversally

homogeneous. On the contrary, it is evident, looking at the laboratory results, that the central part of the material flows faster than the lateral sides.

Finally, it is possible to indicate which kind of output variables you want to obtain. Heights, displacements, velocities are indicated as output of the numerical code.

7.2.11.1.3 "MASTER.dat" file

In this file, it is imposed the total time of each flow, which is 3s. It was in fact noted that this time allows the material to reach the horizontal plane and stop its movement. To limit the dimension of the output files, the calculation time step is fixed equal to 10^{-3}s and it is defined that the results have to be printed out just once every fifty.

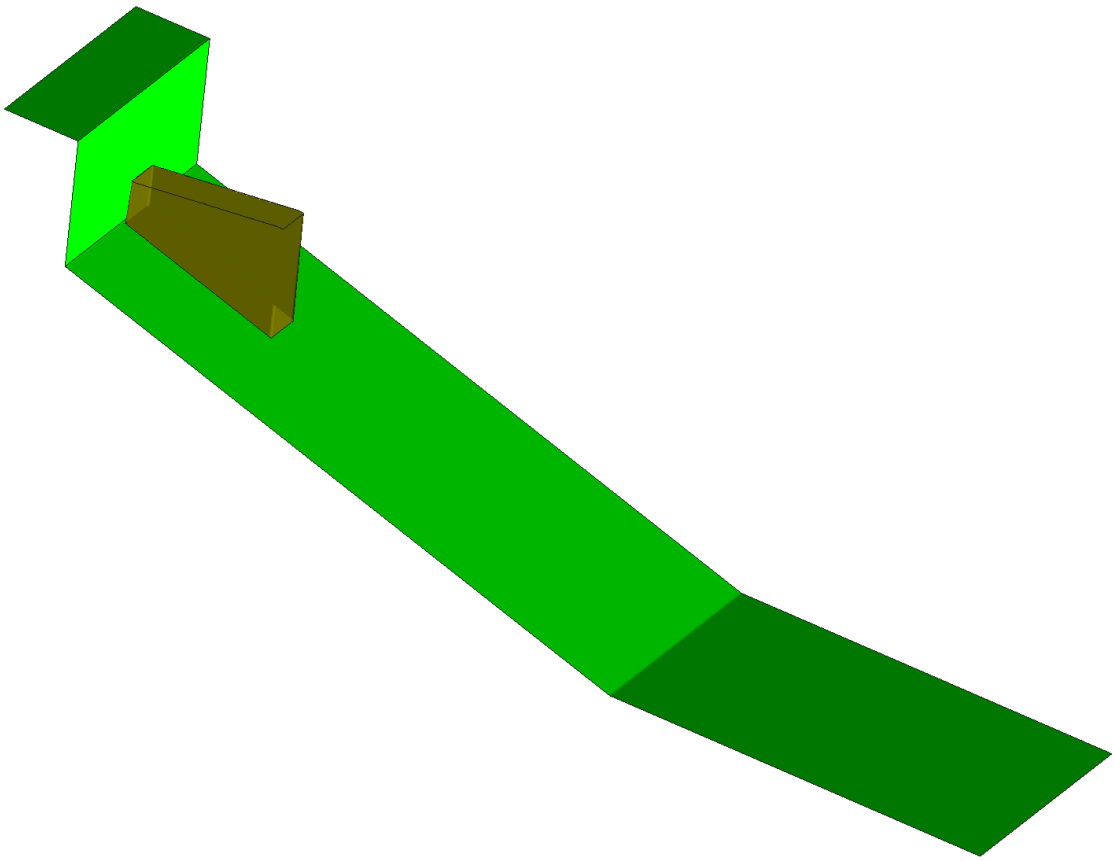

Figure 7.2.73 Topography of the system.

7.2.11.1.4 "pts" file

This file contains the information of the starting mass. The x y z coordinates of the points composing the source of material are written and the dimension of the kernel parameter is explicated. It is decided to fix this value equal to *3* that allows to obtain reliable results.

7.2.11.2 Calibration strategy

As said before, it is necessary to define the way for evaluating the numerical results. Particularly, it has to be defined some index, in term of error between numerical and experimental results.

The runout is absolutely an important characteristic of the flow, but it gives too few information. The huge number of information collected in the tests described in §7.2.6/§0 allows you to use much more measurements to calibrate the model.

Mainly two groups of data are used to understand the best way to reproduce the laboratory experiments. On one hand, in fact, all the data obtained by the laser sensors are compared with the heights of material passing on the corresponding sections. On the other hand, the central sections of the deposits are used to understand which simulations give out the most similar shapes, looking the material stopped on the horizontal plane.

In that way, for each laboratory test two pairs of parameters are obtained, using these two performance indicators. This strategy is then repeated for the second rheological law used.

The first performance index expresses the deposit errors as follow:

$$E_{dep} = \frac{1}{n} \sum_{i=1}^{n} \frac{\left| h_i^{sim} - h_i^{exp} \right|}{h_i^{exp}} \qquad \text{Equation 7-4}$$

where n is the number of points to compare between the simulated and the measured values, h_i^{sim} and h_i^{exp} are the deposit height of the node i for the simulation and the experiment, respectively.

The index that considers the dynamical characteristics of the flow takes into account the information obtained by the three laser sensors and expresses a global formulation of error:

$$E_{time} = \frac{1}{3m} \left(\sum_{t=1}^{m} \frac{\left| h_t^{1,sim} - h_t^{1,exp} \right|}{h_t^{1,exp}} + \sum_{t=1}^{m} \frac{\left| h_t^{2,sim} - h_t^{2,exp} \right|}{h_t^{2,exp}} + \sum_{t=1}^{m} \frac{\left| h_t^{3,sim} - h_t^{3,exp} \right|}{h_t^{3,exp}} \right) \qquad \text{Equation 7-5}$$

where m is the number of points to compare between the simulated and the measured values for each sensor, $h_t^{1,sim}$ and $h_t^{1,exp}$ represent the simulated and measured heights passing in correspondence of the first sensor. The same calculation is repeated to consider also the information of the second and third sensors.

All the indices described are dimensionless and normalized, expressing in that way a relative error.

Finally, the overall error is obtainable by the sum of E_{dep} and E_{time}:

$$E_{overall} = \frac{E_{dep} + E_{time}}{2} \qquad \text{Equation 7-6}$$

This formulation allows to identify the simulation that is a compromise between the one that better reproduce the deposit behavior of the rapid landslide and the one that better replicate the dynamical characteristics of the flow.

7.2.11.3 Simulations of the WK_A tests using Bingham rheology

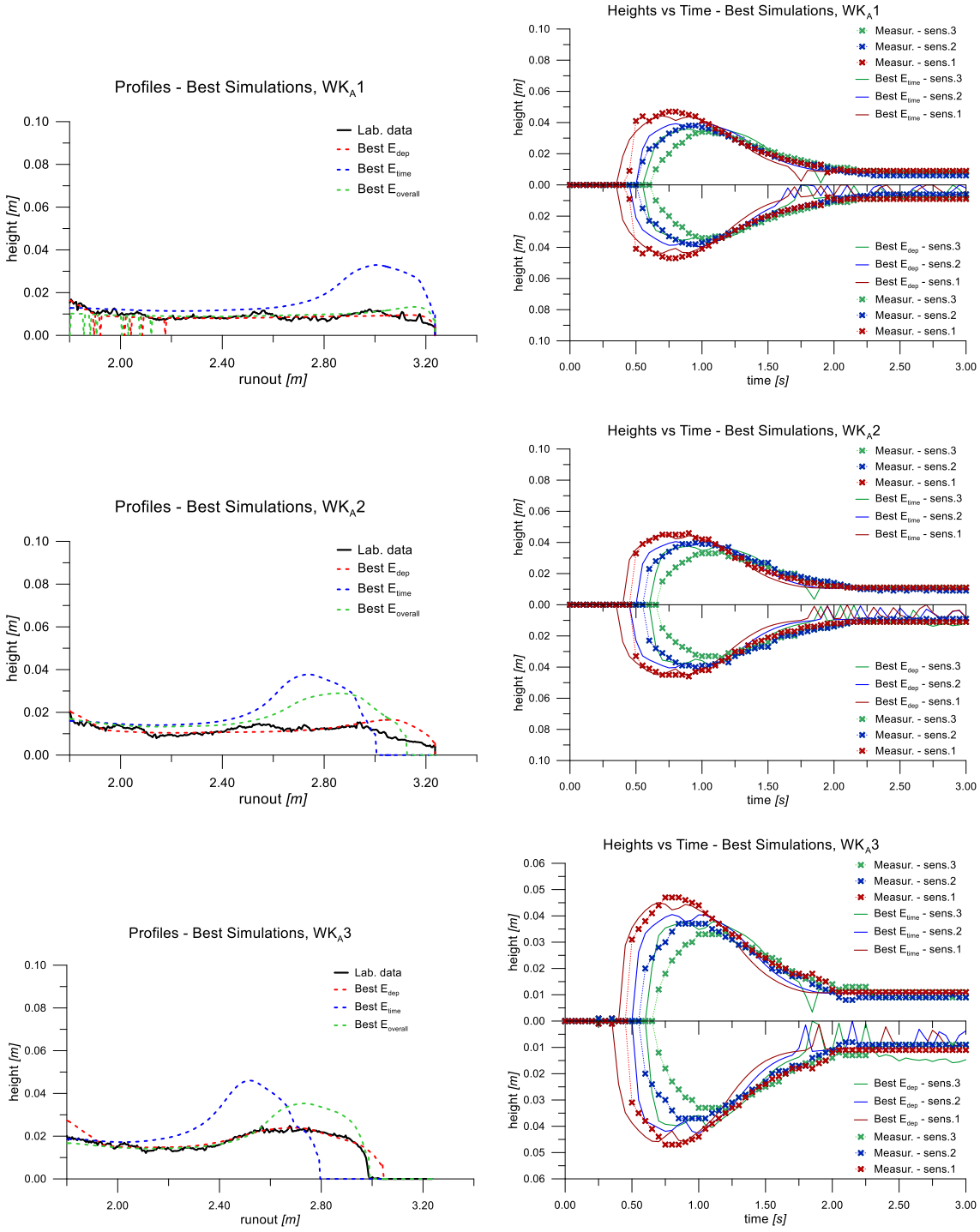

Figure 7.2.74 Profiles of the deposit of the best simulations for the WK_A tests, considering the likelihood of the profile and the laser measurements - Bingham rheology (part 1).

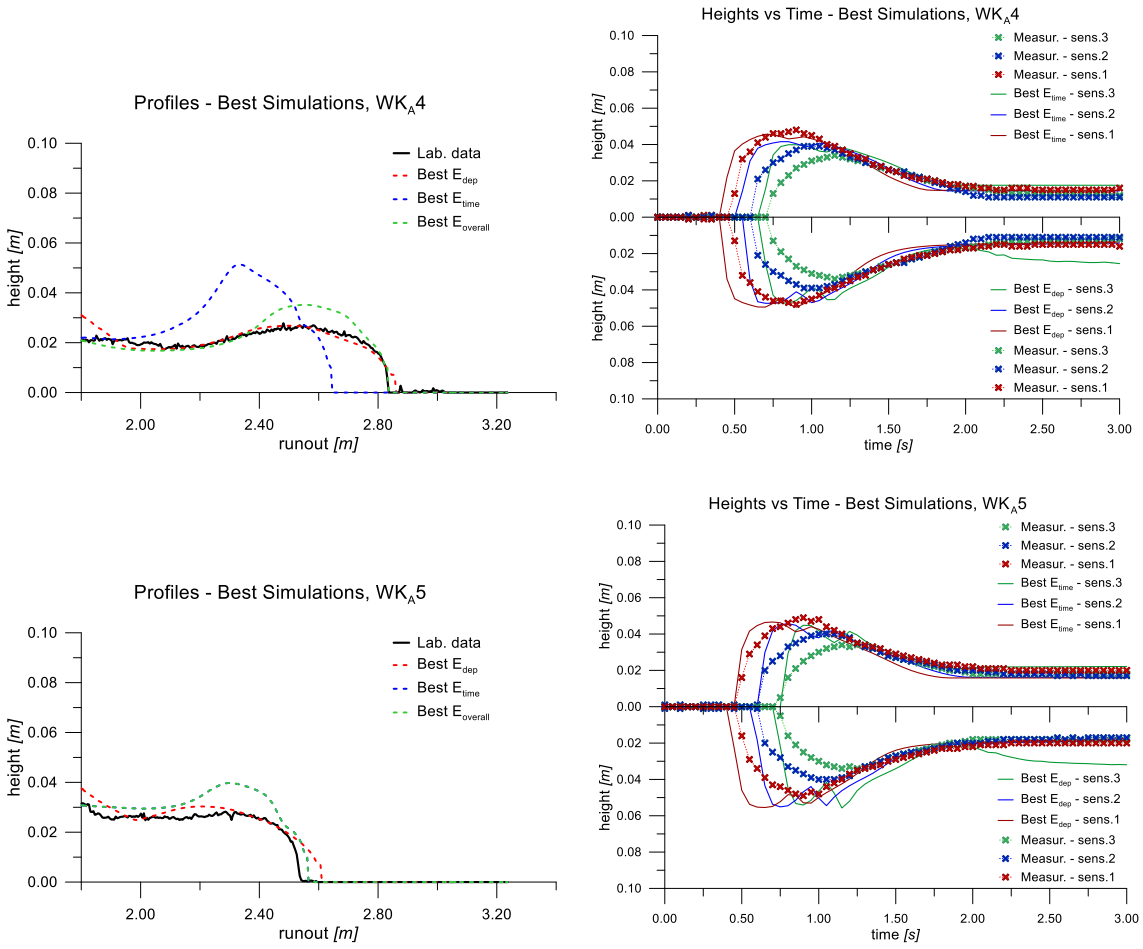

Figure 7.2.75 Profiles of the deposit of the best simulations for the WK_A tests, considering the likelihood of the profile and the laser measurements - Bingham rheology (part 2).

Figure 7.2.74 and Figure 7.2.75 show the profiles of the simulations that have the lowest values of error, considering the measurements of the deposit – red line – and the heights of material passing under the laser sensors – blue line. It is evident that the first simulation reproduces with high quality the laboratory case. The runouts of both the simulations obtained reach the end of the horizontal plane, but the red line better allows obtaining the heights of material throughout the deposit plane.

It is therefore interesting to look at the right graphs of Figure 7.2.74 and Figure 7.2.75. In this graphs, the behavior of the material along the slope is underlined. The laboratory measurements are compared with the corresponding information obtained by the numerical code. The lower figure shows the comparison with the simulation that better reproduce the profile on the plane, while in the upper one it is visible the same graph for the simulation has the lowest vale of error about heights in time. For this first case, it has to be noticed that the two numerical results leads to similar data in time, even if the deposit shape is quite different.

The same analysis is then repeated for the WK_A2 mixture. The mean error of the blue line is 0.008m, while the best simulation that minimizes the difference between experimental and numerical heights on the horizontal plane reaches the value of 0.001m.

Even if the arrival on the first laser sensor of the simulation has a delay compared with the measurements recorded in laboratory, it can be noticed that the mean velocities of the simulation are similar to the ones of the physical model. The mean velocity between the first and the second sensors for the "best profile" simulation is about 3.40m/s, that is quite similar to the 3.26m/s obtained by the experimental apparatus. The velocities remain the same also between the second and the third laser sensors, for both the numerical and physical model.

In almost all the WK_A cases, it can be noticed that while the model can accurately reproduce the shape of material stopped on the horizontal plane, the comparison between the data collected in time is less meticulous.

Particularly, the simulated material arrive to the first sensor always before compared with what happens in the real cases. Anyway, all the velocities obtained by the model are between 3.40m/s and 1.70m/s that are absolutely coherent with what observed during the laboratory tests.

To evaluate the goodness of the simulations, the mean errors between the measurements and the heights obtained by the model are calculated. It is interesting to notice that, for all the WK_A cases, the errors is always less than 0.003m.

Basically, depending on what is the main goal you want to obtain, you can have different combinations of parameters. If you want to accurately reproduce the flow of material along the slope, you can minimize the error between the laser sensors measurements and the respective data obtained by the simulations. On the contrary, if you want the model to give you out the most similar runout and deposit shape, you have to find the simulation that maximally reduces the respective error.

Among all the simulations, if you reduce the error that take into account both the information, in time along the slope and at the end of the phenomenon on the horizontal plane, you can find the most similar simulation. It has to be said that many combinations of parameters leads to similar errors. Consequently, the choice of one simulation defined as best one is quite reductive.

Looking at Figure 7.2.75, after all, it is evident that there is a good agreement of the kinetic data, even for the simulations the minimize the deposit errors.

Anyway, if we consider the parameters used to obtain these three types of best simulations, we can analyze the behavior of the calibrated ones compared to what we obtained by the viscometer.

Figure 7.2.76 summarizes all the calibration results. It is interesting notice that the choice of the data to compare evidently influences the parameters obtained.

The behavior of the calibrated viscosity is quite different compared with the measured one. Minimizing the error relative to the profile heights leads to higher value of μ, even if the exponential tendency is still present. Even the overall index of performance allows obtaining values of viscosity more elevated, even if less than the previews ones. Some similarity may be found in the parameters

obtained by the minimization of the last performance index. The viscosity plays an important role when the flow velocity is high. The request of likelihood in terms of heights versus time gives high weight to the kinetical characteristics of the phenomenon. Probably, that is way the best similarity is observable using this error formulation.

Something different happens looking at the yield stress. It is evident that the calibrated parameters obtained by the "best profile" and the "best heights vs time" indices basically underestimate and overestimate the measured ones respectively. The overall index mediates these two effects, leading to stresses similar to the physical ones.

It has to be said that both the parameters increase the shear stress. Consequently, different combinations of μ and τ can minimize the performance index used. This can gives unreliable results, such as the ones obtained for the most viscous material by the minimum research of the overall error. Figure 7.2.76, in fact, shows a too much high value of μ and a too small value of τ, compared with the rest of the results. Probably, a combination of parameters more coherent with the other would have had similar quantity of error. Finally, the more the material is viscous, the less mass reaches the deposit plane. It happens then that few data about the deposit are used to the calibration procedure, giving more importance to the kinetic information of the flow. This can interfere in the calibration.

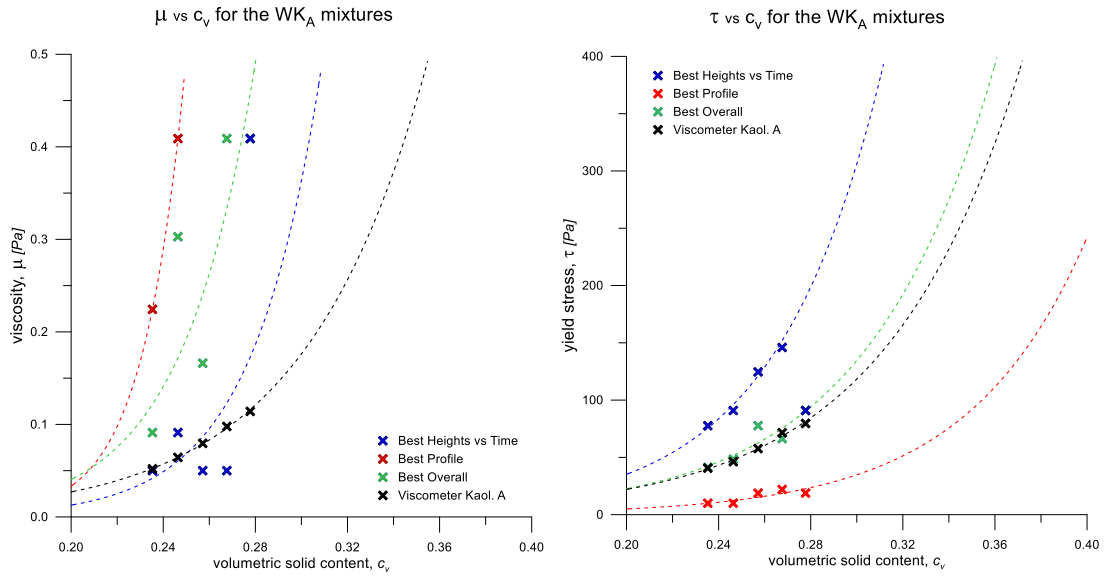

Figure 7.2.76 Comparison between the calibrated parameters with different performance indices and the viscometer measurements.

7.2.11.4 Simulations of the WSK$_A$ tests, using Bingham rheology

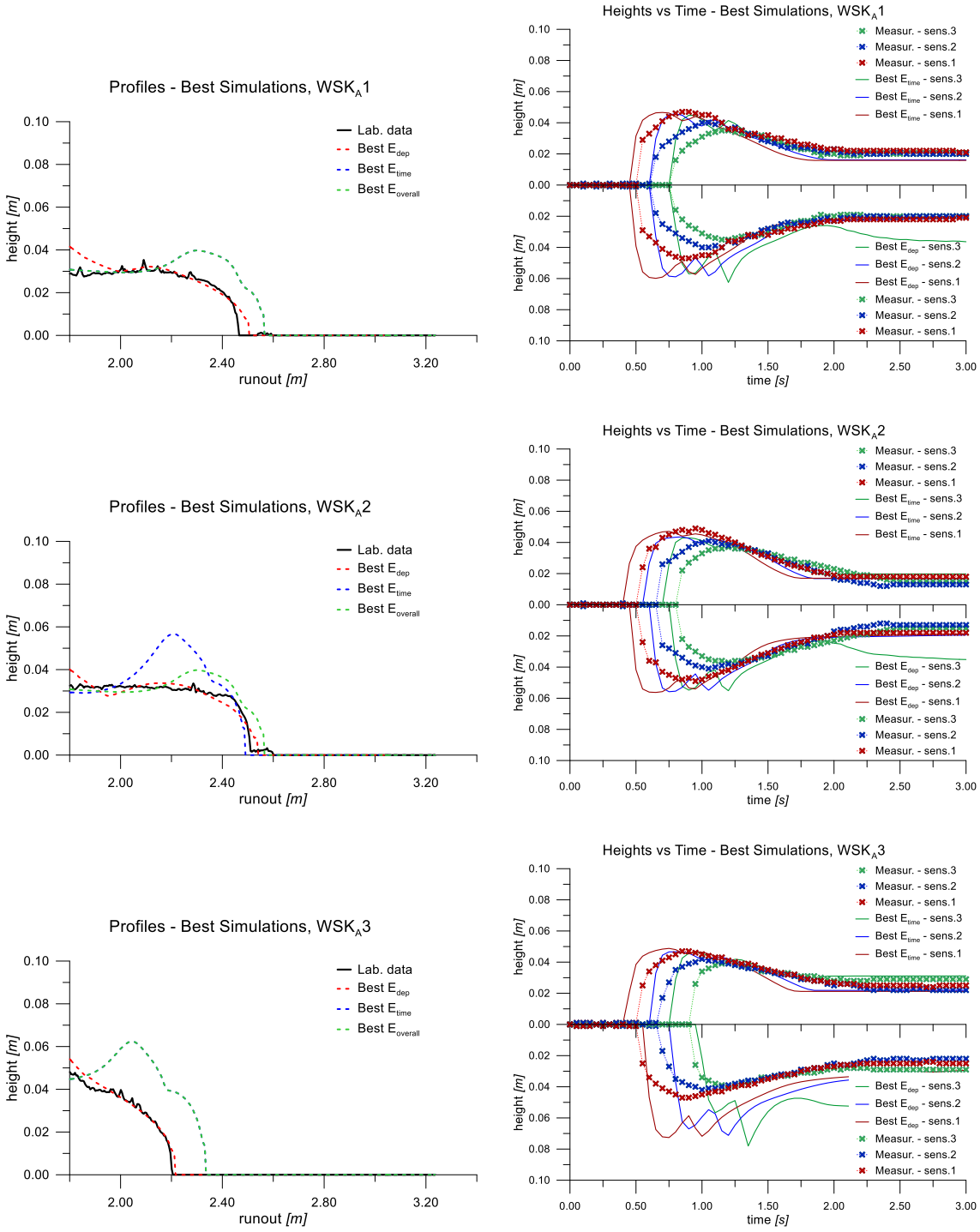

Figure 7.2.77 Profiles of the deposit of the best simulations for the WSK$_A$ tests, considering the likelihood of the profile and the laser measurements - Bingham rheology.

The same procedure has been applied to the WSK$_A$ tests. Figure 7.2.77 shows the result achieved, underlying the behavior of the numerical results with respect to the performance index considered.

The numerical model is able to catch both the aspects considered, i.e. the kinematic and the deposit data. Again, looking at the profiles, it is possible to notice the higher likelihood of the simulation that minimize the "profile" error. The runout is precisely predicted and there is a good accordance in the heights of material stopped on the horizontal plane.

The simulations that minimize the kinetic index of performance, on the contrary, overestimate the runout. In all these simulations, an extra accumulation of material is present, increasing the heights of deposit.

If we look now at the "Heights vs Time" graphs, it is also evident how the dynamics of the phenomenon is captured in a better way if it minimizes the kinetic error. Many differences are appreciable in the behavior of the heights versus time for the "Best profile" simulations. Particularly, it can be said that these simulations overestimate the maximum values reached by the waves of material flowing.

Practically, if the request of likelihood concerns the trend of the heights versus time, the material accumulate too much speed, reaching high values of runout. Contrarily, if we want to reproduce the deposit shape, the behavior along the channel presents some approximations.

Totally, anyway, it can be noticed a good ability of the numerical model to reach the goal desired.

7.2.11.5 Simulations of the WSK_B tests, first group, using Bingham rheology

This group of laboratory tests includes mixtures with a medium viscosity, able to deposit appreciable quantity of material on the plane. In this case, it is even more evident how the performance index chosen to evaluate the simulations influences the calibration.

While the dynamic behavior is overall well reproduced by all the best simulations, evident differences are appreciable looking at the deposit plane. The approximation of the heights during the flow concerns principally the moments when the material reaches the three sensors, and consequently the velocity field. The height of the waves of material are absolutely comparable with the laboratory measurements.

More differences that are important can be noticed comparing the profiles of the calibrated tests with the physical one. The simulations that minimize the deposit errors index are able to reproduce the heights of material stopped on the plane and, with some approximations, the runouts. Contrarily, it is evident that the likelihood of the simulations that better fit the dynamic measurements of the test is not satisfactory with reference to the deposit. The runouts are evidently underestimates and the accumulation of material gives shape different compared with the observed data.

For the WKS_B3 mixture, the overall index represents a kind of mean of the others two indices. The "Best overall" simulation, in fact, is a compromise between the two likelihood requests. In the rest of the WKS_B tests the simulation that minimizes the overall error, minimizes also the dynamic error.

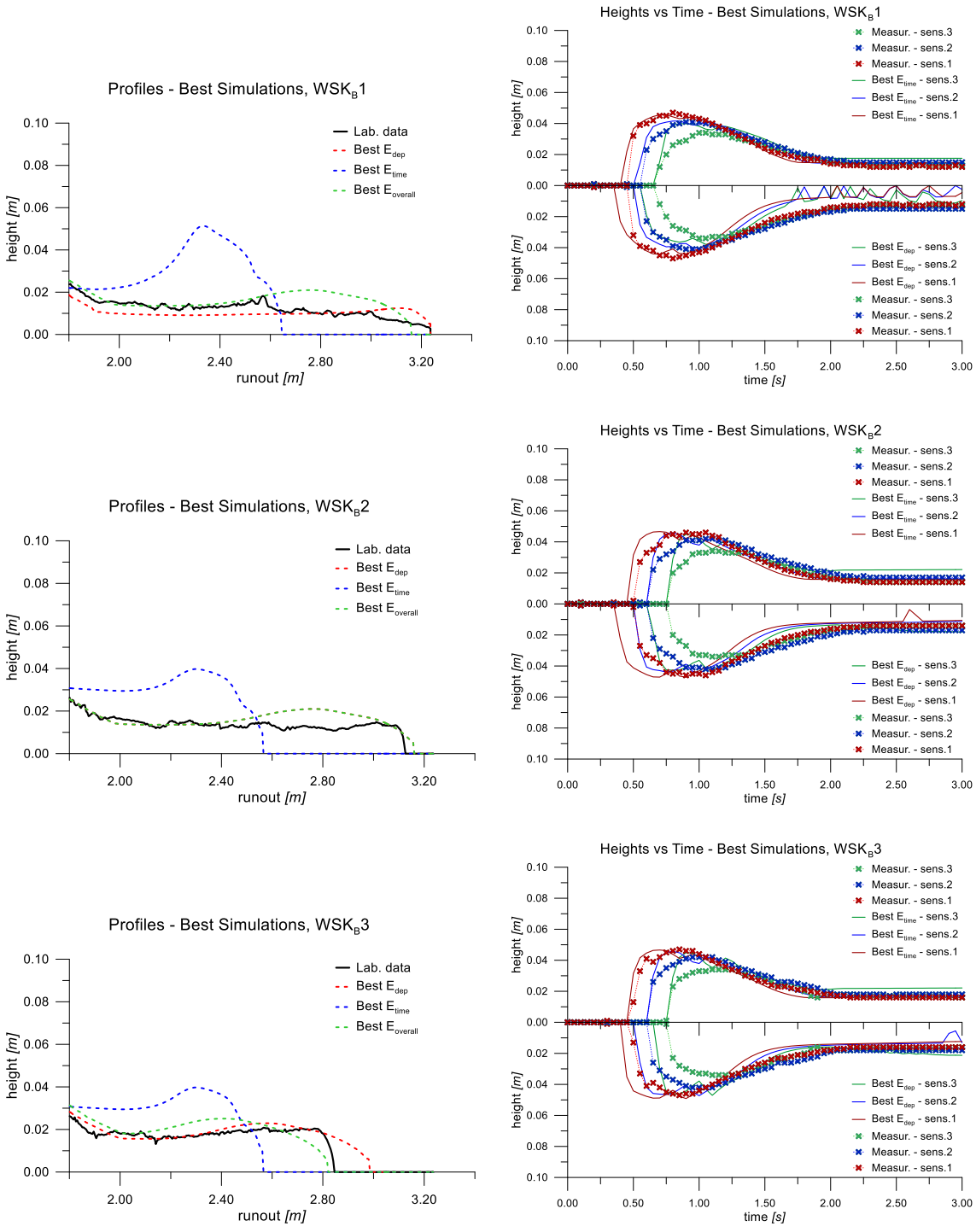

Figure 7.2.78 Profiles of the deposit of the best simulations for the WSK$_B$ tests (first group), considering the likelihood of the profile and the laser measurements - Bingham rheology.

7.2.11.6 Simulations of the WSK$_B$ tests, second group, using Bingham rheology

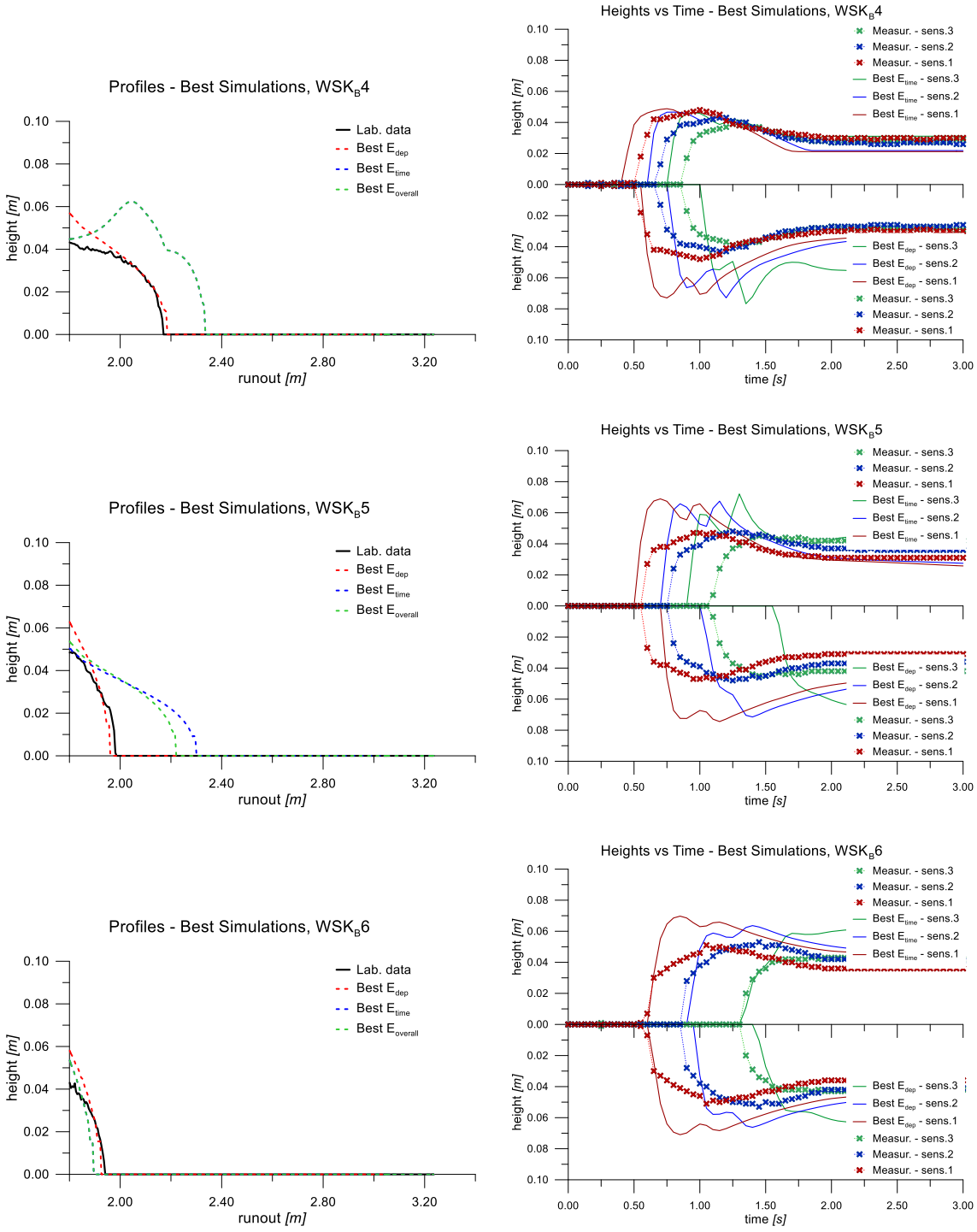

Figure 7.2.79 Profiles of the deposit of the best simulations for the WSK$_B$ tests (second group), considering the likelihood of the profile and the laser measurements - Bingham rheology (part 1).

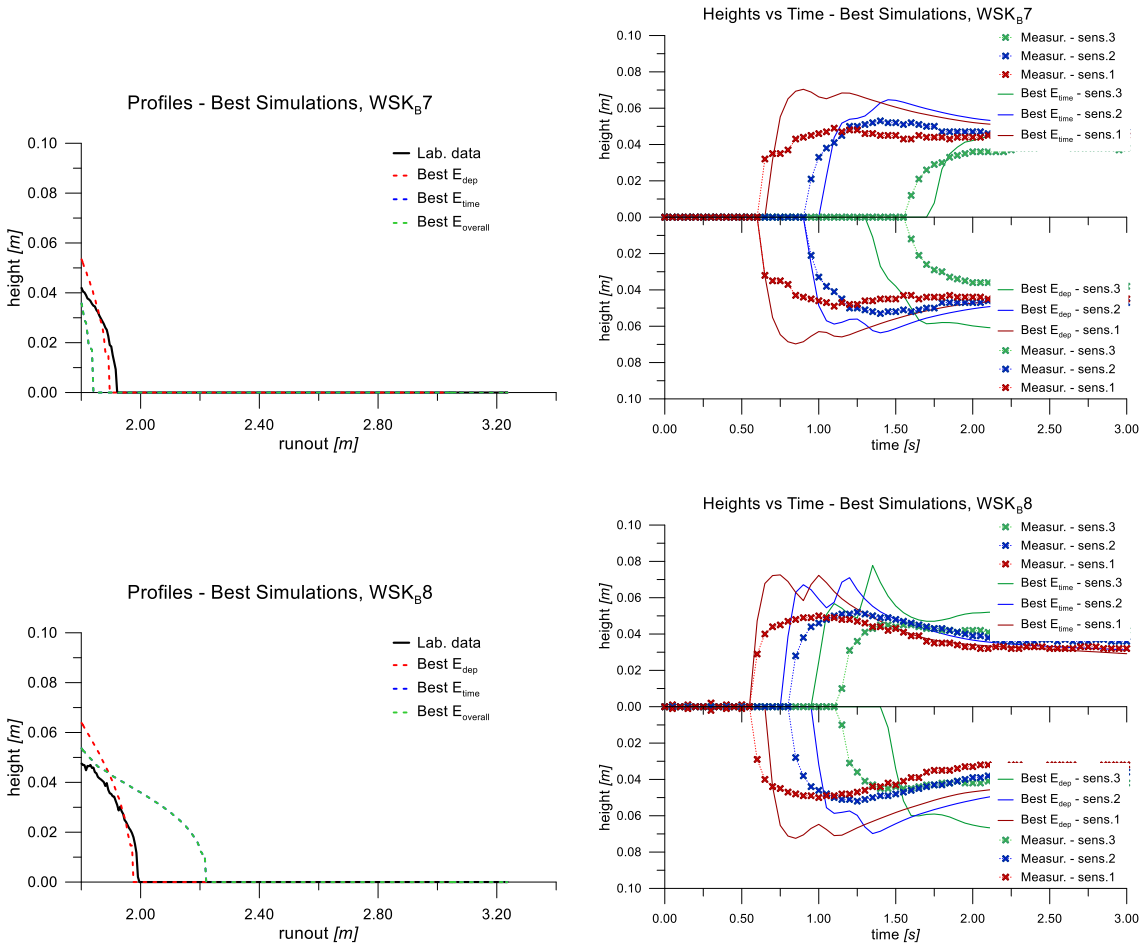

Figure 7.2.80 Profiles of the deposit of the best simulations for the WSK$_B$ tests (second group), considering the likelihood of the profile and the laser measurements - Bingham rheology (part 2).

Finally, the second group of WKS$_B$ tests are used for the application of the calibration technique. The material in these experiments hardly reaches the deposit plane, so the runout are always low values. This means that few data are used for the calculation of the deposit error and that is why the best overall simulation always coincides with the “Best heights vs time” one.

As already observed, minimizing the dynamic error, the runouts are not precise. It has to be noticed that, even if the deposit shapes are obtained with a good agreement, the model commits many approximations trying to reproduce the behavior of the material along the channel.

7.2.11.7 Considerations about the calibrated Bingham parameters

All the results achieved are inserted in the tables below. Depending on the solid content, the viscosities and the yield stresses obtained by the various calibrations are reported.

WK_A Mixtures										
Mixture	*Kaolin*	c_v	μ_{prof}	τ_{prof}	μ_{h_time}	τ_{h_time}	$\mu_{overall}$	$\tau_{overall}$	$\mu_{viscometer}$	$\tau_{viscometer}$
	%		*[Pa s]*	*[Pa]*	*[Pa s]*	*[Pa]*	*[Pa s]*	*[Pa]*	*[Pa s]*	*[Pa]*
WK_A1	**44.4**	*0.235*	0.224	10.000	0.050	77.657	0.091	41.331	0.052	40.578
WK_A2	**45.9**	*0.246*	0.409	10.000	0.091	90.919	0.303	48.390	0.064	46.230
WK_A3	**47.4**	*0.257*	0.745	18.789	0.050	124.625	0.166	77.657	0.080	57.690
WK_A4	**48.7**	*0.268*	1.006	21.998	0.050	145.908	0.409	66.329	0.098	71.543
WK_A5	**50.0**	*0.278*	1.834	18.789	0.409	90.919	0.409	90.919	0.114	79.623

Table 7.2.23 Parameters obtained from the calibration procedure for the WK_A mixtures, Bingham rheology.

WSK_A Mixtures										
Mixture	*Kaolin*	*Sand*	c_v	μ_{prof}	τ_{prof}	μ_{h_time}	τ_{h_time}	$\mu_{overall}$	$\tau_{overall}$
	%	*%*		*[Pa s]*	*[Pa]*	*[Pa s]*	*[Pa]*	*[Pa s]*	*[Pa]*
WSK_A1	**41.7**	**16.7**	*0.353*	2.477	16.048	0.409	90.919	0.409	90.919
WSK_A2	**38.5**	**23.1**	*0.385*	1.834	30.153	0.050	170.826	0.409	90.919
WSK_A3	**35.7**	**28.6**	*0.415*	6.095	11.708	0.068	200.000	0.068	200.000

Table 7.2.24 Parameters obtained from the calibration procedure for the WSK_A mixtures, Bingham rheology.

WSK_B Mixtures – first group									
Mixture	*Kaolin*	*Sand*	c_v	μ_{prof}	τ_{prof}	μ_{h_time}	τ_{h_time}	$\mu_{overall}$	$\tau_{overall}$
	%	*%*		*[Pa s]*	*[Pa]*	*[Pa s]*	*[Pa]*	*[Pa s]*	*[Pa]*
WSK_B1	**40.0**	**10.0**	*0.280*	0.303	10.000	0.050	145.908	0.745	10.000
WSK_B2	**33.3**	**25.0**	*0.355*	0.745	10.000	0.409	90.919	0.745	10.000
WSK_B3	**28.6**	**35.7**	*0.416*	1.006	10.000	0.409	90.919	1.359	10.000

Table 7.2.25 Parameters obtained from the calibration procedure for the WSK_B mixtures, Bingham rheology.

WSK_B Mixtures – second group									
Mixture	*Kaolin*	*Sand*	c_v	μ_{prof}	τ_{prof}	μ_{h_time}	τ_{h_time}	$\mu_{overall}$	$\tau_{overall}$
	%	*%*		*[Pa s]*	*[Pa]*	*[Pa s]*	*[Pa]*	*[Pa s]*	*[Pa]*
WSK_B4	**45.5**	**9.1**	*0.318*	6.095	21.998	0.068	200.000	0.068	200.000
WSK_B5	**41.7**	**16.7**	*0.353*	8.229	106.446	4.514	13.707	6.095	10.000
WSK_B6	**38.5**	**23.1**	*0.385*	4.514	170.826	3.344	200.000	3.344	200.000
WSK_B7	**35.7**	**28.6**	*0.415*	3.344	200.000	6.095	200.000	6.095	200.000
WSK_B8	**33.3**	**33.3**	*0.441*	6.095	124.625	6.095	10.000	6.095	10.000

Table 7.2.26 Parameters obtained from the calibration procedure for the WSK_B mixtures, Bingham rheology.

The results collected leave some doubts in terms of the best strategy to adopt to calibrate the numerical model. As anticipated in §6.4.2, the determination of the data to compare is a fundamental but critical point of the back-analysis. Probably, it is reductive to look for a unique combination of parameters considered the best one. Some interpretations are necessary to reach a satisfactory level of approximation.

The minimization of an index, sometimes, leads to the neglect some parameters combinations that cause slightly higher errors, but still small, and perhaps are better in some ways. It is therefore hard to decide which aspect of the rapid landslide is better to precisely reproduce, and which can present errors.

It is interesting to understand the behavior of the performance indices, depending on the parameters used. For this reason, in

Figure 7.2.81 the contours of the errors are represented. Basically, for each combination of viscosity and yield stress used, the three formulations of error are calculated.

The yellow areas underlines the parameters that produce simulations with high values of error. On the contrary, the blue areas identify the zones containing the parameters that are able to better reproduce the laboratory result.

The first column of graphs shows the trend of the profile error. The blue zone is located in the lower part of the contours, where the parameters have small values. It can be seen that increasing the kaolin content, the blue band moves slightly to higher value. It is also evident that while a variation in the viscosity causes big effects in the error calculation, the sensibility of the model to the yield stress is less important. The black point in the graph identify the combination that minimize this formulation of the error.

The second column of Figure 7.2.81 represents the behavior of the performance index that evaluate the dynamical likelihood between numerical and physical results. First of all, the distribution of the error presents lower values of higher errors. The blue band is even here located where viscosity and yield stress are little. Increasing the solid content, both the parameters have to becomes bigger to minimize this error. The white point indicates the couple of rheological parameters which leads to a minimum value of the index considered.

Finally, the last column shows the overall errors. The yellow point identify the best combinations of parameters. For the first four cases, it is evident that this error is a compromise between the other two formulations of error. The blue areas are located in correspondence to the blue ones of the other graphs and the yellow point stays between the black and the white ones.

The red square is used to collocate the rheological parameters obtained by the viscometer tests on the graphs. On one hand, this is useful to evaluate the various combinations of viscosity and yield stress obtained. In this sense, the contours shows a good agreement between the best overall combination and the physical one. On the other hand, the presence of this red square help in the comprehension of the error committed if the rheological parameters are directly used in the model.

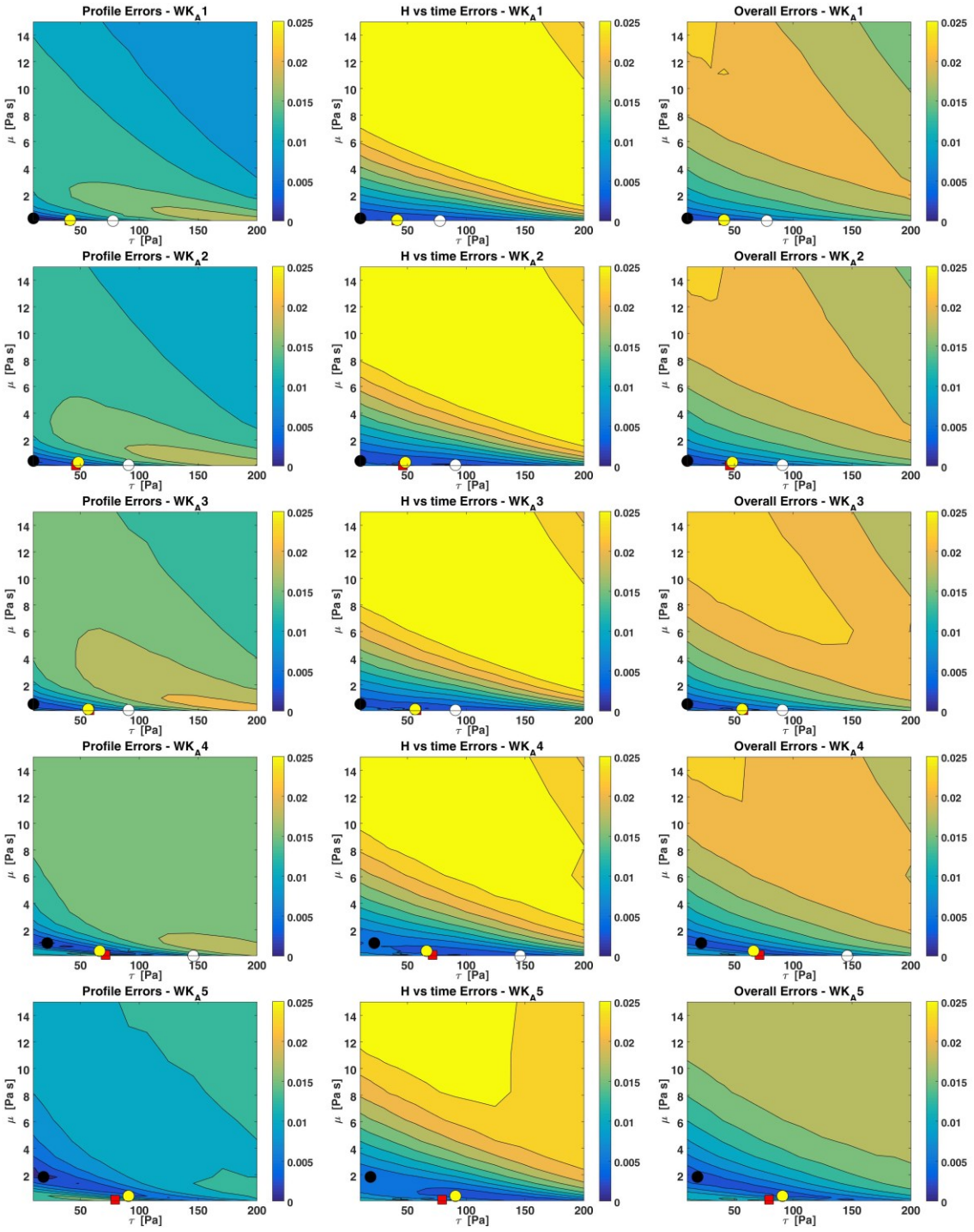

Figure 7.2.81 Contours of the errors depending on the combination of parameters chosen for the WKA cases: profile errors (1° column), heights vs time errors (second column) and overall errors (third column).

7.2.11.8 Simulations of the WK_A tests, using Voellmy rheology

The same procedure has been applied to the second rheological law chosen, the one of Voellmy. Again, the simulations able to minimize the three formulations of errors are identified among the 400 available.

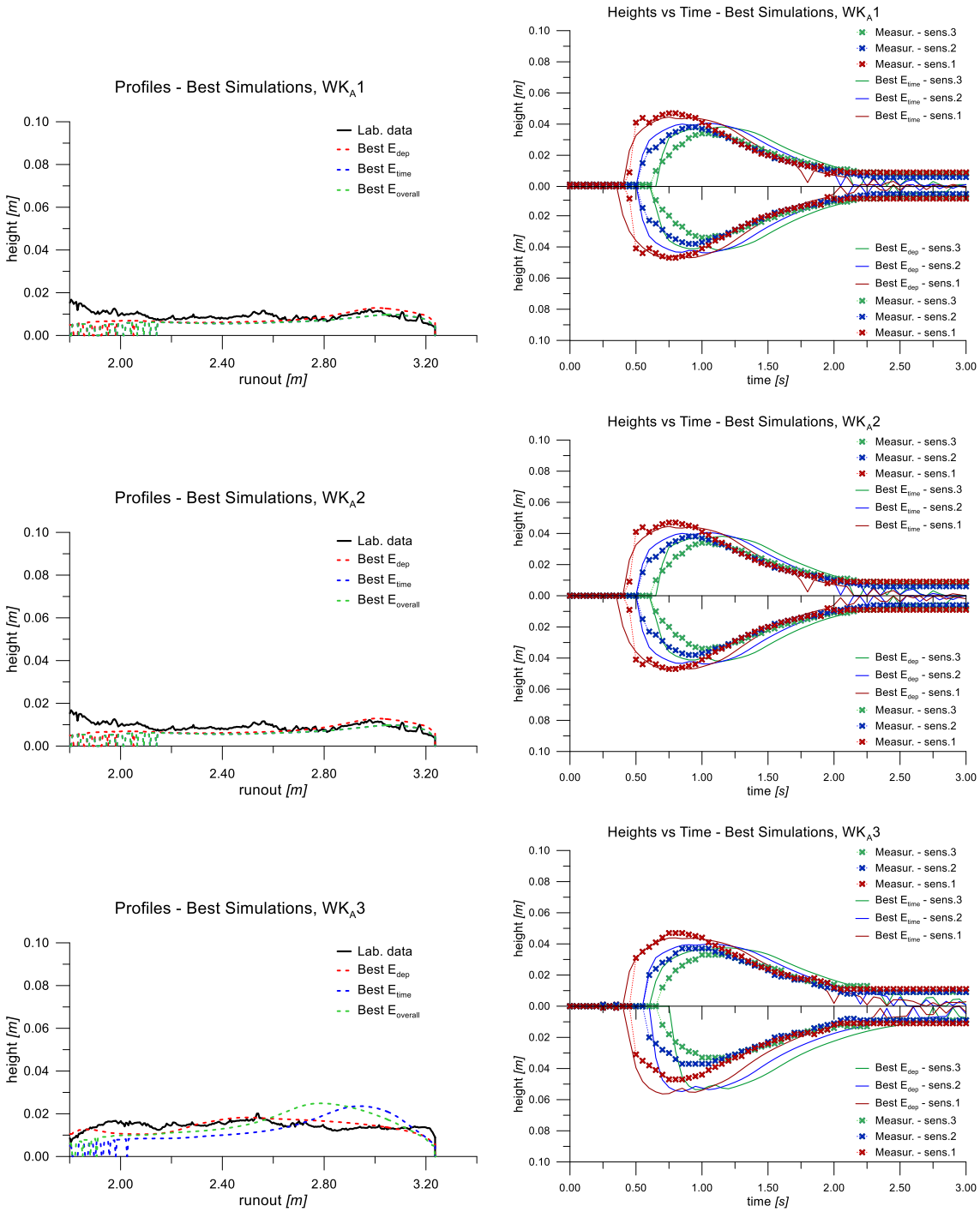

Figure 7.2.82 Profiles of the deposit of the best simulations for the WK_A tests, considering the likelihood of the profile and the laser measurements - Voellmy rheology (part 1).

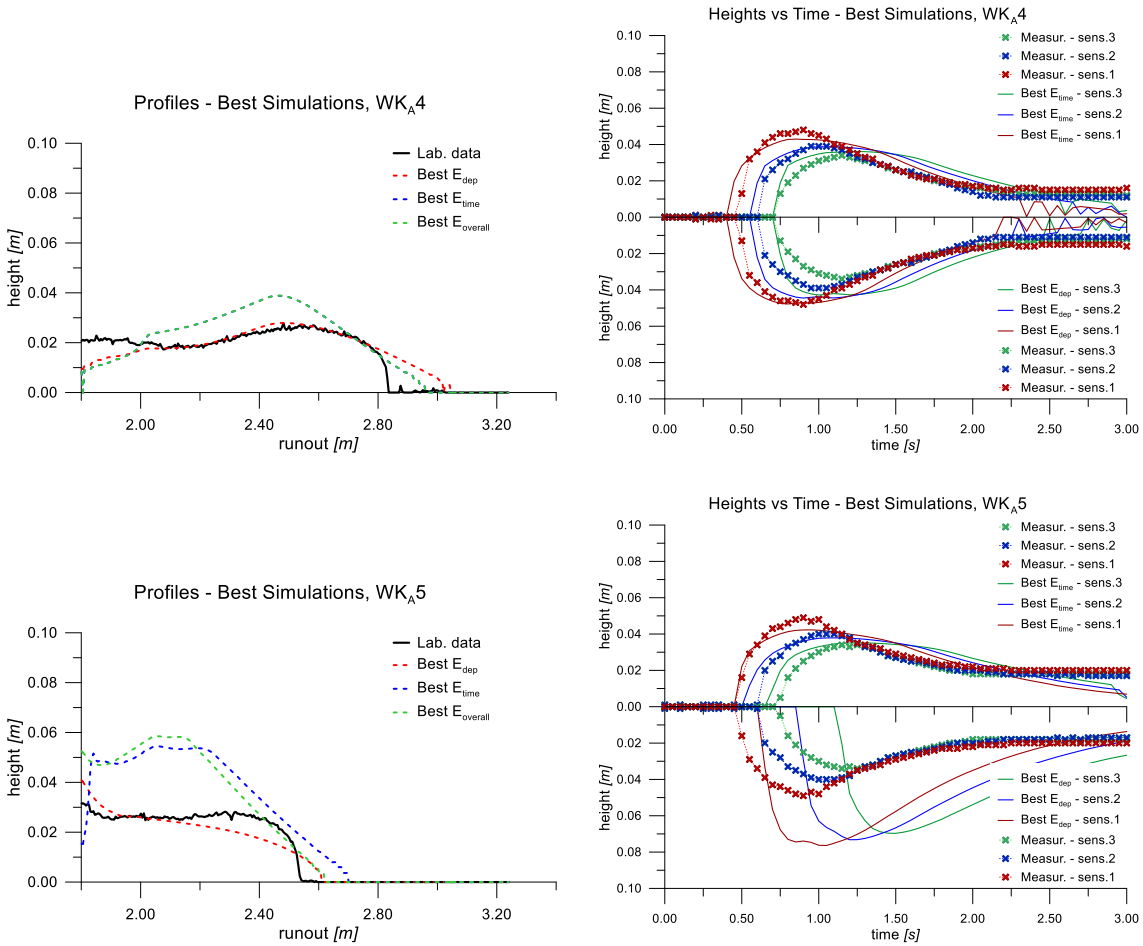

Figure 7.2.83 Profiles of the deposit of the best simulations for the WK$_A$ tests, considering the likelihood of the profile and the laser measurements - Voellmy rheology (part 2).

It is evident that sometime the simulation that minimize the value of E_{time}, minimize also $E_{overall}$. The blue and the green lines, in fact, in many figures coincide.

The results obtained using this frictional rheological regime are worst compared with the ones obtained implementing Bingham's law. This happens particularly with what concern the deposit shape, especially when the flow has a small runout. If we look at WK$_A$1 and WK$_A$2 profiles, the numerical model is able to be satisfactory with the heights of material stopped on the plane. It has to be noticed that it is not possible to evaluate the runouts, because both the experimental and numerical results reach the end of the deposit plane. In all the others WK$_A$ mixtures, the simulation that minimize E_{dep} overestimate the runout.

Anyway, it has to be said that the behavior along the channel is well reproduced, speaking both the velocities and the maximum heights.

7.2.11.9 Simulations of the WSK_A tests, using Voellmy rheology

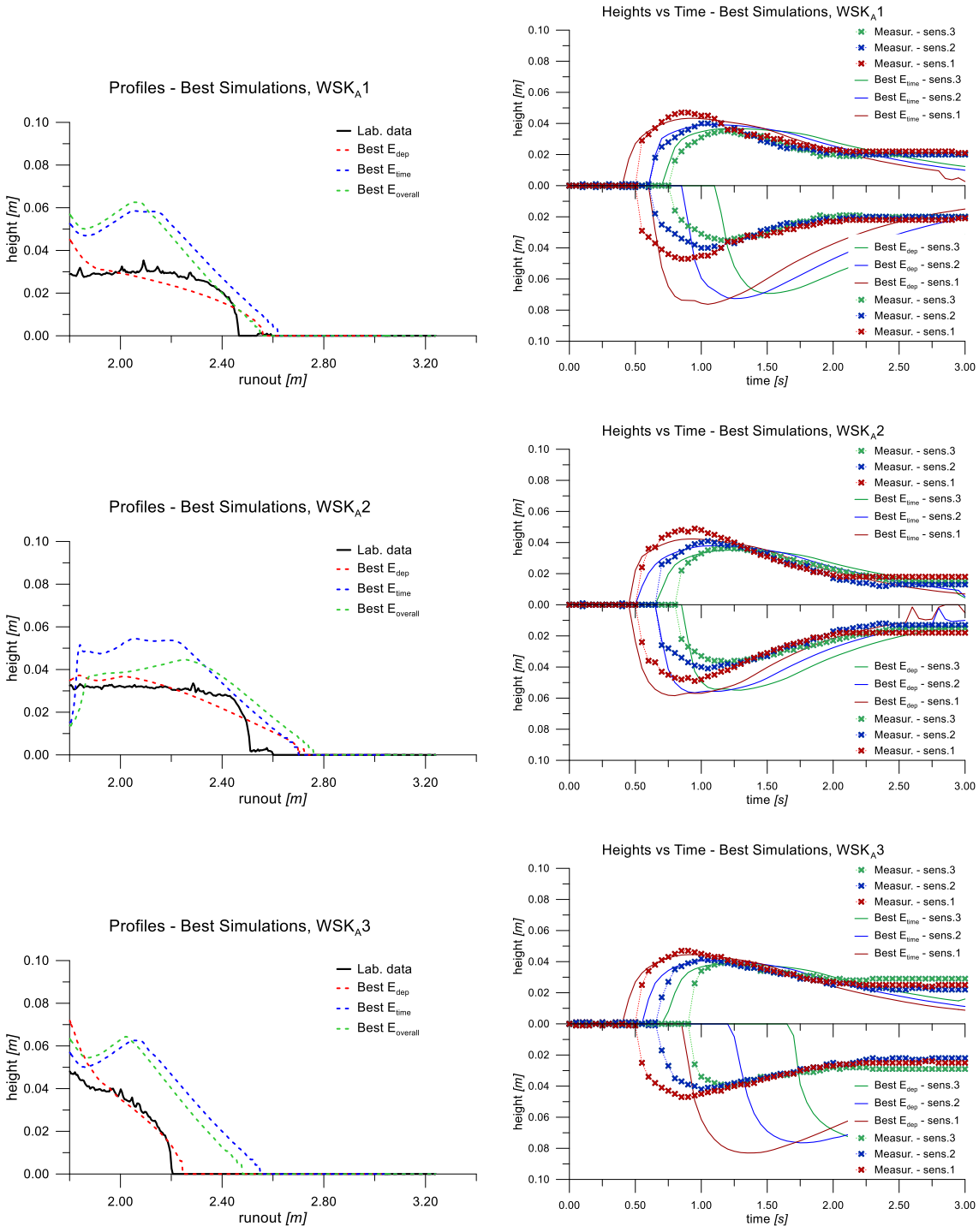

Figure 7.2.84 Profiles of the deposit of the best simulations for the WSK_A tests, considering the likelihood of the profile and the laser measurements - Voellmy rheology.

Again, the experiments that has short runouts are imprecisely reproduced. Looking at the first column of Figure 7.2.84, the runouts of the simulations that maximally reduces E_{dep} overestimate the real one and the deposit shapes always present some differences. Furthermore, these simulations lead to completely different behavior with what concerns the dynamical characteristics of the flow. Looking the right column, in fact, it is evident that the velocities field and the maximum heights of the "Best Profile" simulation are totally in disagreement with the physical results.

The model is, anyway, able to reproduce what happens along the channel. The simulations that minimize the E_{time} index, in fact, have in all the cases a good agreement with the real measurements. The velocities and the heights of material are well reproduced. Looking the deposit of these simulations, however, it is evident that what obtained by the model is not sufficiently similar with the experimental data. The runouts are quite different and both the shape and the heights distribution do not look like the measurements.

7.2.11.10 Simulations of the WSK_B tests, first group, using Voellmy rheology

The first group of the WSK_B tests deposits on the plane a fair amount of material. For this reason, the calibration is able to reach a higher quality of reproduction.

Considering the WSK_B1 case, it can be noticed that the "best overall" simulation gives a good approximation of the runout, while the others two underestimate the real value. Anyway, the red profile sufficiently resemble the measured one in terms of heights distribution. This simulation presents some inaccuracies with respect the behavior along the channel, during the motion. Contrarily, the simulation with the lowest E_{time} has a high agreement looking at the heights versus time, while gives a deposit shape evidently different from the real one. This numerical result underestimates the deposit of material where the horizontal plane begins and describes an excessive accumulation of material at the end.

Something similar happens with the WSK_B2 mixture. On one hand, the simulation that accurately reproduce the deposit has some inaccuracies along the channel. On the other hand, the numerical result that is satisfactory with what concerns the dynamical behavior of the flow, leads to big errors in the deposit profile. The "green" simulation effectively allows capturing the overall behavior of the phenomenon, by averaging the results of the other two simulations.

Exactly the same results are observable for the last mixture of this group.

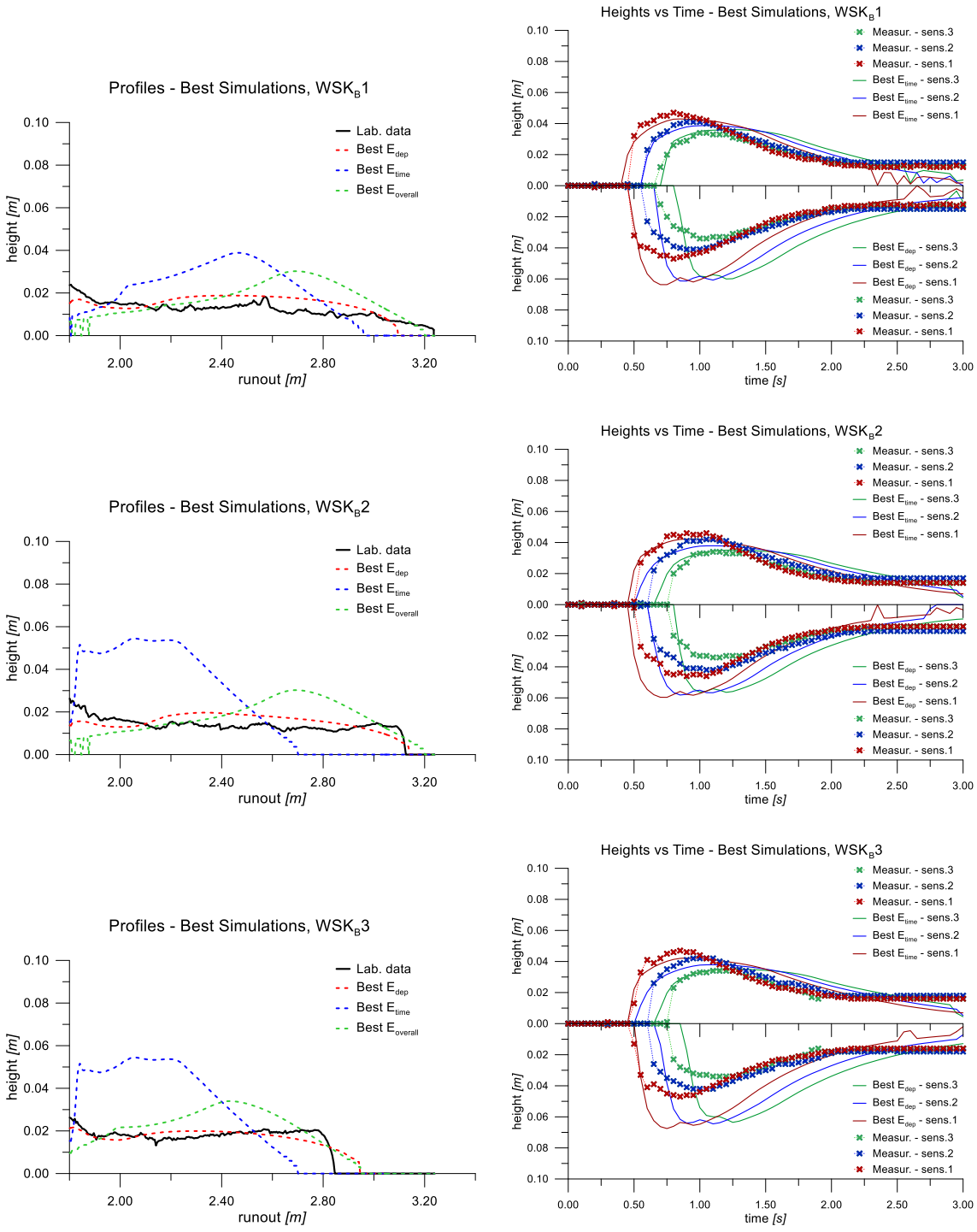

Figure 7.2.85 Profiles of the deposit of the best simulations for the WSK$_B$ tests (first group), considering the likelihood of the profile and the laser measurements - Voellmy rheology.

7.2.11.11 Simulations of the WSK$_B$ tests, second group, using Voellmy rheology

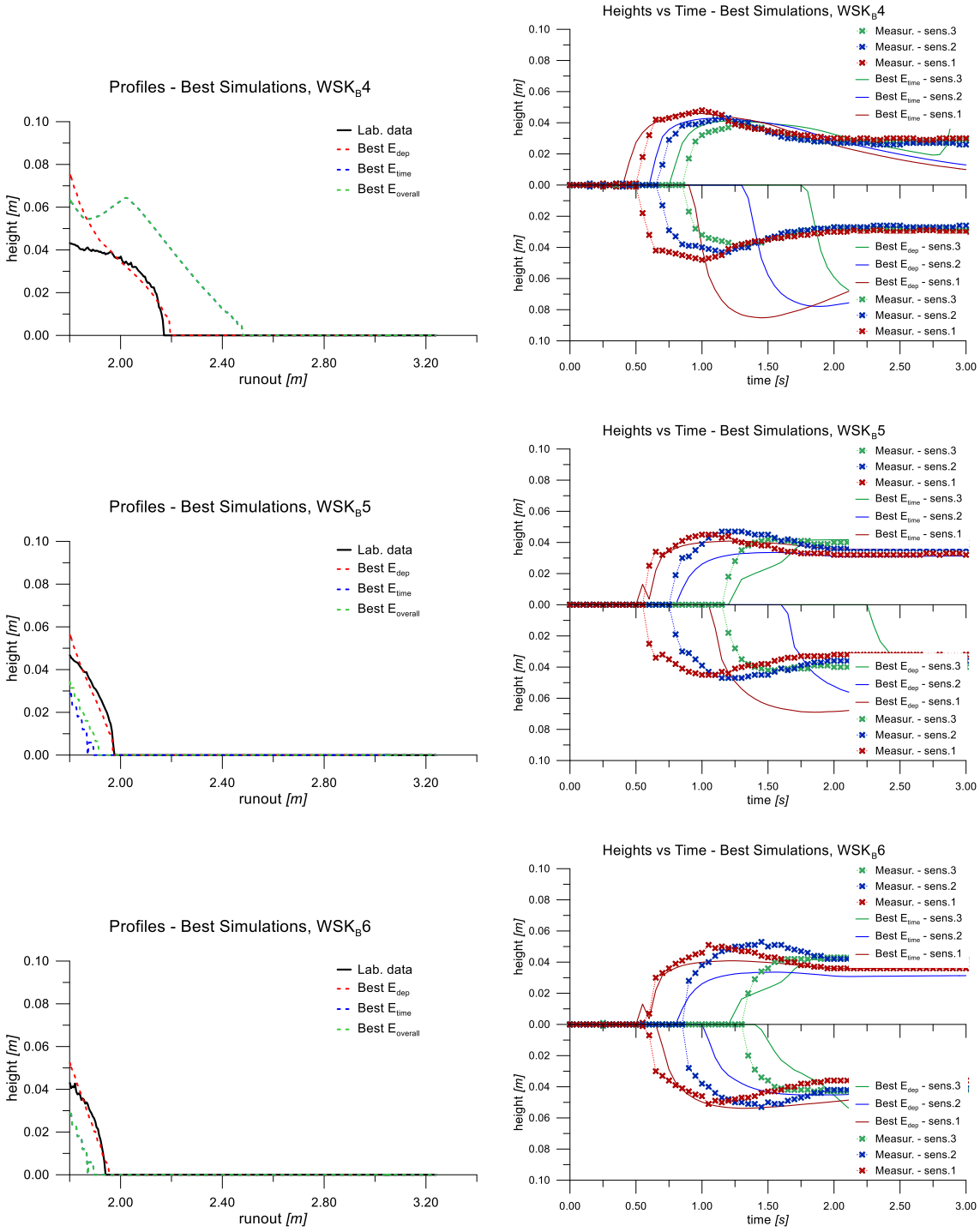

Figure 7.2.86 Profiles of the deposit of the best simulations for the WSK$_B$ tests (second group), considering the likelihood of the profile and the laser measurements - Voellmy rheology (part 1).

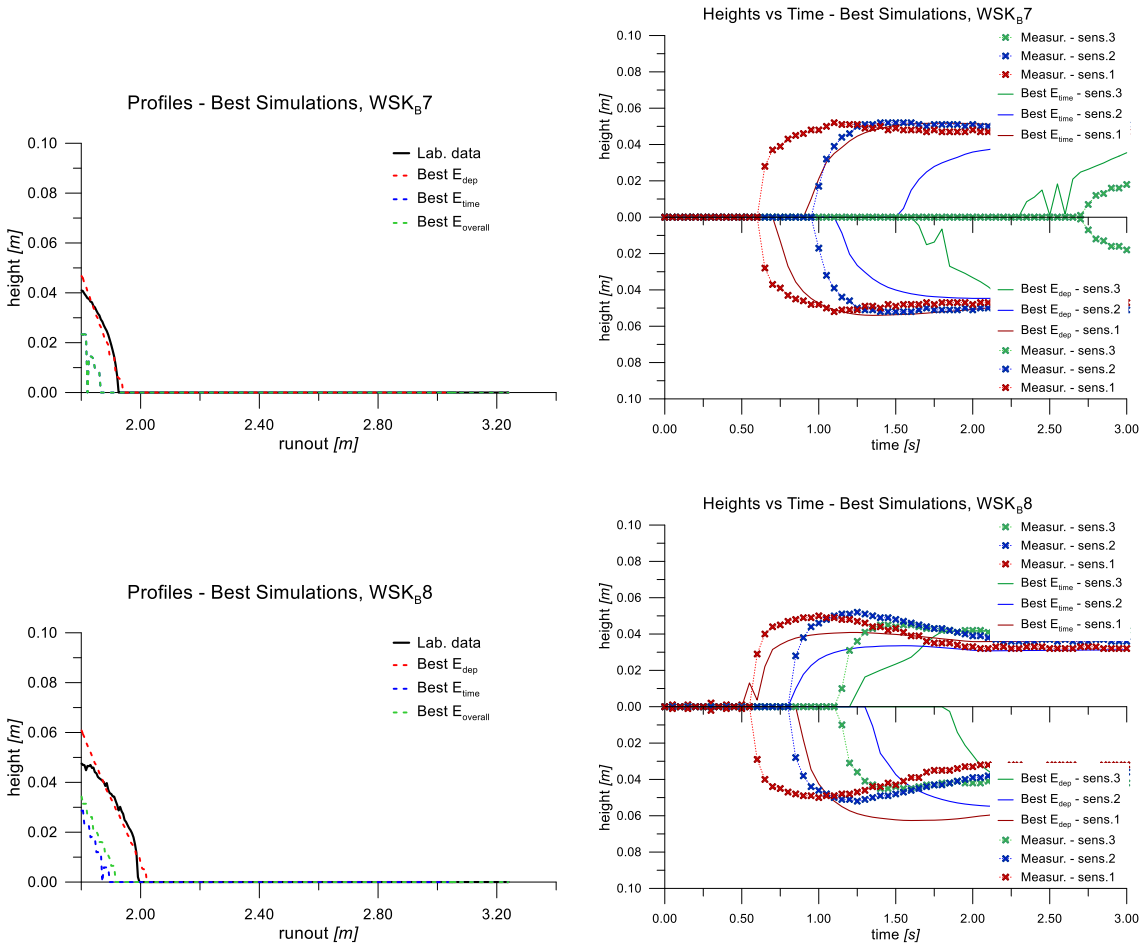

Figure 7.2.87 Profiles of the deposit of the best simulations for the WSK$_B$ tests (second group), considering the likelihood of the profile and the laser measurements - Voellmy rheology (part 2).

The second group of WSK$_B$ mixtures, as already affirmed, is characterized by short values of runout. As a consequence of this, it is difficult to identify the simulation that better looks like the laboratory result. The low quantity of material, in fact, limits the information of the flow with what concerns the deposit and leads consequently not to well describe the test with those information. It would be necessary to have measurements of the deposit of the material along the slope to better characterize each test behavior. This was not possible because the two acquisition technique used had some problems with the lateral walls of the channel, which were an obstacle to the correct data take-over.

Anyway, the procedure can be applied, considering that the results achieved would be inaccurate. The WSK$_B$4 case allows to sufficiently reproduce both the dynamical behavior and the deposit shape, with two different simulations. It has to be noticed that in this case is absolutely necessary to define which aspect of the flow you want to reproduce. This choice identify one simulation that evidently leads to not negligible errors in the other characteristics of the phenomenon.

7.2.11.12 Considerations about the calibrated Voellmy parameters

WK_A Mixtures									
Mixture	*Kaolin %*	c_v	$cos\phi_{prof}$	ξ_{prof} *[m s^{-2}]*	$cos\phi_{h\_time}$	ξ_{h_time} *[m s^{-2}]*	$cos\phi_{overall}$	$\xi_{overall}$ *[m s^{-2}]*
WK_A1	**44.4**	*0.235*	0.047	615.848	0.085	1000.000	0.085	1000.000
WK_A2	**45.9**	*0.246*	0.026	297.635	0.125	1000.000	0.125	1000.000
WK_A3	**47.4**	*0.257*	0.103	483.293	0.184	1000.000	0.152	1000.000
WK_A4	**48.7**	*0.268*	0.125	483.293	0.184	1000.000	0.184	1000.000
WK_A5	**50.0**	*0.278*	0.012	54.556	0.223	1000.000	0.223	784.760

Table 7.2.27 Parameters obtained from the calibration procedure for the WK_A mixtures, Voellmy rheology.

WSK_A Mixtures									
Mixture	*Kaolin %*	*Sand %*	c_v	$cos\phi_{prof}$	ξ_{prof} *[m s^{-2}]*	$cos\phi_{h\_time}$	ξ_{h_time} *[m s^{-2}]*	$cos\phi_{overall}$	$\xi_{overall}$ *[m s^{-2}]*
WSK_A1	**41.7**	**16.7**	*0.353*	0.026	54.556	0.223	784.760	0.223	615.848
WSK_A2	**38.5**	**23.1**	*0.385*	0.103	183.298	0.223	1000.000	0.184	615.848
WSK_A3	**35.7**	**28.6**	*0.415*	0.039	20.691	0.223	615.848	0.223	483.293

Table 7.2.28 Parameters obtained from the calibration procedure for the WSK_A mixtures, Voellmy rheology.

WSK_B Mixtures – first group									
Mixture	*Kaolin %*	*Sand %*	c_v	$cos\phi_{prof}$	ξ_{prof} *[m s^{-2}]*	$cos\phi_{h\_time}$	ξ_{h_time} *[m s^{-2}]*	$cos\phi_{overall}$	$\xi_{overall}$ *[m s^{-2}]*
WSK_B1	**40.0**	**10.0**	*0.280*	0.012	143.845	0.184	1000.000	0.152	1000.000
WSK_B2	**33.3**	**25.0**	*0.355*	0.026	183.298	0.223	1000.000	0.152	1000.000
WSK_B3	**28.6**	**35.7**	*0.416*	0.012	112.884	0.223	1000.000	0.152	615.848

Table 7.2.29 Parameters obtained from the calibration procedure for the WSK_B mixtures, Voellmy rheology.

WSK_B Mixtures – second group									
Mixture	*Kaolin %*	*Sand %*	c_v	$cos\phi_{prof}$	ξ_{prof} *[m s^{-2}]*	$cos\phi_{h\_time}$	ξ_{h_time} *[m s^{-2}]*	$cos\phi_{overall}$	$\xi_{overall}$ *[m s^{-2}]*
WSK_B4	**45.5**	**9.1**	*0.318*	0.400	615.848	0.223	483.293	0.223	483.293
WSK_B5	**41.7**	**16.7**	*0.353*	0.223	20.691	0.400	483.293	0.400	483.293
WSK_B6	**38.5**	**23.1**	*0.385*	0.329	112.884	0.400	379.269	0.400	379.269
WSK_B7	**35.7**	**28.6**	*0.415*	0.329	88.587	0.329	42.813	0.329	42.813
WSK_B8	**33.3**	**33.3**	*0.441*	0.271	42.813	0.400	379.269	0.400	483.293

Table 7.2.30 Parameters obtained from the calibration procedure for the WSK_B mixtures, Voellmy rheology.

It has to be noticed that, except for WSK_B second group cases, which are not so reliable, the value of the turbulent parameter is always very high. Most of the times, in fact, the calibration gives 1000ms^{-2} as the best value to use.As already performed in §7.2.11.7, the contours of the errors are reported, depending on the combination of parameters used. Again, the blue areas identify the zones where the performance indices are lowest.

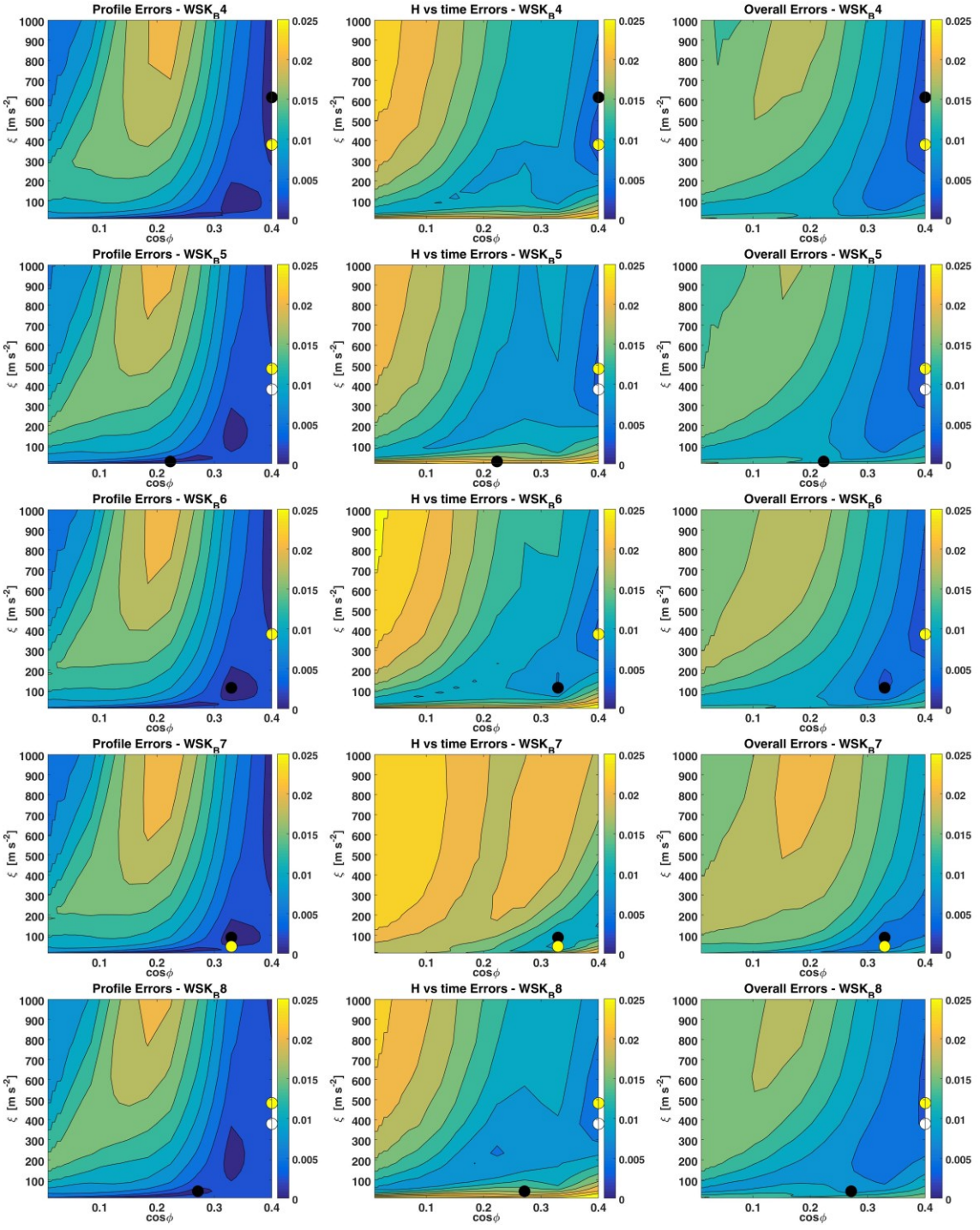

Figure 7.2.88 Contours of the errors depending on the combination of parameters chosen for the WSK_B cases, second group: profile errors (1° column), heights vs time errors (second column) and overall errors (third column).

The black point in Figure 7.2.88 identify the combination that minimizes E_{dep}. Looking at the position of this point in the others graphs, it is evident if this combination is acceptable for all the errors formulation or not. It is clear, for example, that the combination obtained looking for the

minimum of E_{dep} for the WSK_B6 mixture is adequate also for the remaining indices. The black point in fact stays in areas with low value of error.

Contrarily, the same reasoning applied to the WSK_B8 mixture underlines that not always looking just some aspects of the rapid landslides is sufficiently informative. The combination that minimizes the "profile error" leads to big values of error in in terms of E_{time}.

The white point identifies the combination that satisfy the request of minimum for the E_{time} index. Again, it can be noticed that sometimes this couple of parameters provides consistent results also for E_{dep} and $E_{overall}$, as it happens for WSK_B4, WSK_B6 and WSK_B7 mixtures. Other times, however, this does not occur and the simulation with the lowest E_{time} provides to not negligible errors looking at the deposit, as for WSK_B5 and WSK_B8 materials.

The yellow point indicates, finally, the overall best simulation. It is evident that sometimes this numerical result coincides with the one that minimizes E_{time}.

7.2.12 Conclusions

First of all, the contours in Figure 7.2.81 and Figure 7.2.88 underline the existence of more than one combination of parameters able to minimize the performance index chosen. In both the rheological laws included in the model, it is evident that the parameters involved in the calculation of the shear stress, even if they emphasize each a particular aspect of the phenomenon, however contribute to the total tension acting.

Consequently, an increment of the viscosity μ may be counterbalanced by a decrement of the yield stress τ. In the same way, various combinations of turbulence ξ and friction ϕ may lead to similar numerical results.

The more descriptive are the data you compare, the more precise will be the calibration, if the model is able to reproduce all the characteristics of the flow-like landslide.

Increasing the complexity of the system, anyway, increases also the difficulty of getting a numerical result very faithful to the experimental case. It was observed that not always the model was able to satisfactory reproduce both the dynamical behavior and the deposit shape of the test considered.

All considered it has to be said that the model simplifies the problem, giving average characteristics to the material, imposing boundary conditions, which do not perfectly capture the real ones, and assigning to the flow simplified velocities field.

To reproduce more precisely the case studies, probably it may be necessary to use a real 3D numerical model. Anyway, this choice would lead to a huge increment of the computational costs.

The depth-averaged model used is sufficiently able to reproduce the cases presented, especially the ones with a runout longer than 2.80m. The costs are quite limited, considering moreover the possibility of running parallel simulations at the same time.

The various performance indices, finally, help to underline the main aspect of the flow you want to reproduce and, consequently, the parameters that allow you in that sense.

7.3 THE ROTOLON DEBRIS FLOW

7.3.1 Introduction

The third case study presented considers a real debris flow, occurred in the Rotolon basin (Vicenza, Italy) in November 2010. As we previously described, the information collected about the pre and post-event morphology of the valley constituted a very useful database for obtaining a well calibration of GeoFlow-SPH model.

In general, considering the simulation of real flow-slide events, two approaches are possible:

1) To make a prediction of the phenomenon using values of the rheological models determined on the base of laboratory test results and eventually adapting the parameters in the second phases with a subsequent optimization (D'Agostino et al., 2010; Hürlimann et al., 2015). Even if the transition from small-scale to large-scale undoubtedly involves some problems, experimental measurements obtained in laboratory may be a good reference for an initial calibration activity.
2) To make a calibration of the model with a back-analysis that means to assign the rheological parameters in order to have a satisfied simulation of the real case. A reliability judgement of the simulation may be obtained on the base of one or more characteristics of debris flow events that have already occurred.

Even if various models have found wide approval within the scientific community and have been already applied to successfully describe artificial debris flows (Cola et al., 2011) as well as real events (Revellino et al., 2004; Quan Luna et al., 2011; Wu et al., 2013), an accurate simulation of real events is still problematic. This depends from the difficulty in obtaining accurate knowledge of the site's geometry and reliable information about suitable parameters to utilize depending on the rheological model or integration approach being adopted.

Until now, researchers have concentrated their efforts on using back analysis to calibrate their models for phenomena that have already taken place. Of course, values obtained from back analysis unequivocally depend on the correspondence of the simulated values with real in situ measurements. In the past, researchers often had at their disposal only a few measures of the valley's configuration before and after the events, but the availability of advanced, detailed technologies is presently reducing errors connected with reproduced geometry.

Another problem is the fact that usually the calibration procedure is performed manually. Since working on real debris flows the quantity of uncertainties about the material properties and the geometrical characteristics of the area increases exponentially, it is even more important to use a calibration procedure that is able to give an objective evaluation of the results achieved.

Parameter calibration is, of course, a problematic phase in developing numerical modelling and some strategies have already been utilized by other research fields to overcome this subjective process (e.g. Robinson & Wastald, 1987; Eckhardt & Arnold, 2001). Some attempts have likewise already been made to use automatic procedures for parameter calibrations for landslide analysis: Schädler et al. (2014), for example, proposed an inverse identification approach associated with a back analysis procedure to establish the constitutive parameters of a viscous-elastic-plastic finite element model used to reproduce displacement evolution over time with regard to the Corvara

landslide in Italy. To the authors' knowledge, similar attempts have not yet been made for debris flows phenomena.

The complexity of this third case study imposed the introduction of a statistical algorithm to improve the procedure and reach a higher level of precision. In this paragraph, the Rotolon catchment and the debris flow are described. The various steps of the calibration are therefore reported and the sensitivity of the model to the different parameters is taken into account. Finally, the Ensemble Smoother is applied and it is considered the dependency of the results on the errors that may characterize the measurements used for the back-analysis.

7.3.2 Study event

7.3.2.1 The Rotolon catchment

The Rotolon catchment is located in the Vicentine Prealps, on the South-eastern flank of the Little Dolomites group in the uppermost portion of the Agno river valley. It lies under the jurisdiction of the municipality of Recoaro Terme (NE of Italy) situated at the border with the Trento province (Figure 7.3.1).

The instability phenomena studied here concerns the mountain portion of the Rotolon stream that is about 5 km long and moves from an altitude of about 1350 m a.s.l. (the maximum altitude in its basin is 1942 m a.s.l. of Lovaraste Peak) to about 450 m a.s.l. where the 17 m-high Georgetti dam was constructed in the twenties to protect the small town of Recoaro Terme from flooding.

From a geomorphological point of view, the Rotolon Mountain can be ideally subdivided into two segments: an upper part between 1350 and 850 m of elevation (bed slope around 30%) and a lower one having a medium slope of less than 10%. At the junction of the two portions there is a 5 m high hydraulic weir and, immediately after, the injection of a small lateral stream, specifically the Agno of Campogrosso, which is generally dry and holds water only during exceptional rain events.

The path of the stream flows by a variety of formations (Barbieri et al., 1980; De Zanche & Mietto, 1981). The mountain peaks are constituted by sub-horizontally bedded, intensely fractured, mainly dolomitic limestones (Dolomia Principale, Mt. Spitz Limestone, Calcareous at Trinodosus, Recoaro Limestone) typical of the South Alpine Domain and appearing in succession moving from west to east. It is important to note that the passage from the Dolomia Principale to Mt. Spitz limestone is clearly indicated by the presence of a relatively thin layer of Raibl Formation, a sequence of conglomerates, sandstones, marls and dolomitic evaporates showing a discontinuous level of easily alterable and erodible rhyolitic-dacitic phorphyrities at the bottom.

The Werfen Formation can be found at the base of the dolomitic stratigraphic succession consisting of a varied sequence of sandstone and siltstone that outcrops near the confluence with the Campogrosso creek, just before the 5 m-high weir. Along the lower portion, the torrent moves through extremely thick talus and alluvial deposits up to the final area where the outcrops of fillade metamorphic rocks can be observed on the left-hand side.

As reported and confirmed by local popular, religious and administrative reports, instability processes, such as slope failures in the upper portion and consequent debris flows, have threatened the basin for centuries (Trivelli, 1991). Many mainly hydraulic-forest interventions were carried out between the two world wars and in the period between 1985 and 1990, just after the occurrence

of an important landslide followed by a large secondary debris flow. Those works mitigated the superficial erosion of the lateral slopes along the stream and prevented many flooding events but they were unable to stabilize the large landslides still active at the head of the Rotolon creek.

Many countermeasure structures exist In the 2nd segment: long stone-walls protect the lateral slope of the bed and several inclined flow deflectors or hydraulic weirs have been realized over the years to keep the water flow at the center of the bed; two bridges, i.e. the Parlati and Luna bridges, cross the stream and connect the small hamlets located in the valley. There is a lateral basin upstream of the villages that was created after the intense debris flow that took place in 1985 to contain the transported material.

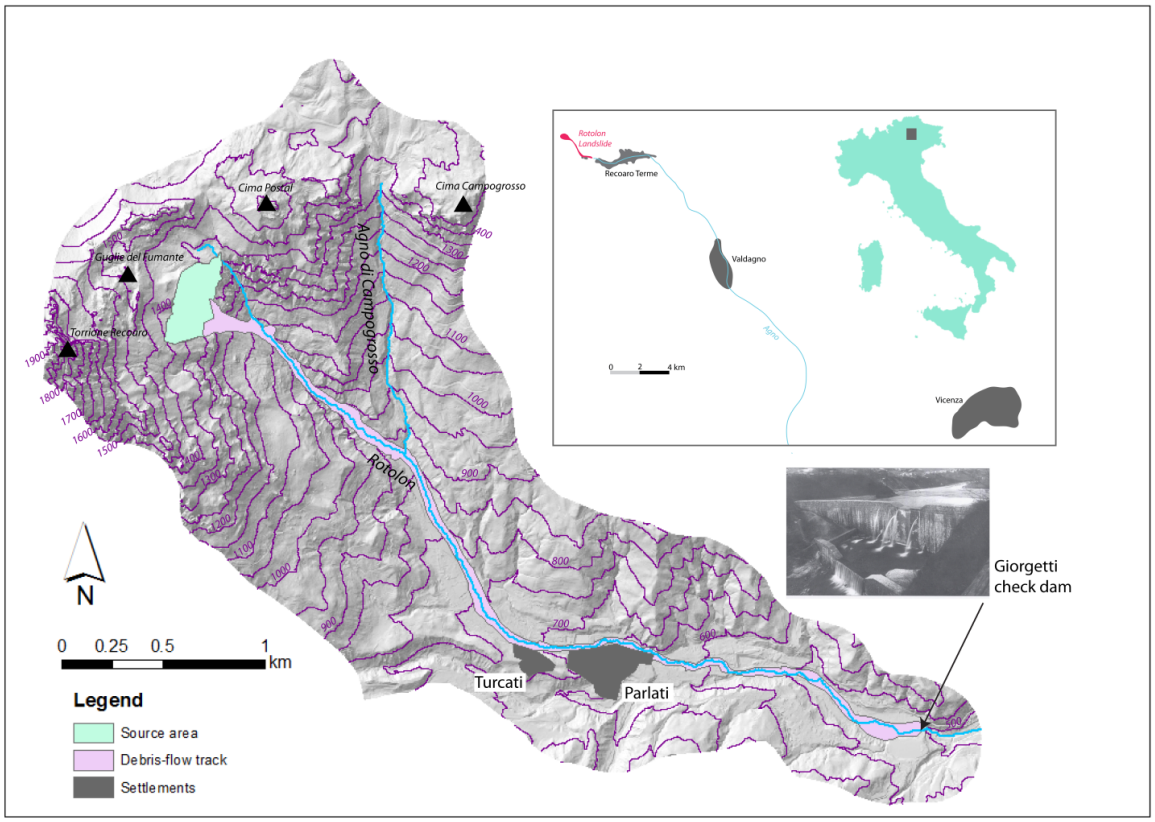

Figure 7.3.1 Location of the Rotolon landslide in the Upper Agno Valley.

7.3.2.2 The debris flows that took place in 2009 and 2010

Two important debris flows occurred in May 2009 and November 2010 after the detachment of about 50,000 m^3 and 330,000 m^3, respectively, at the head of the creek. In approximately 10 minutes the first debris flow reached the Parlati and Turcati villages, damaging some hydraulic weirs and forming a lateral watercourse weld deposits up to 5 m high. The second one flowed close to the Parlati village, obstructing a bridge and flooding a public road: at that time, the inclusion of fresh water from the Agno of Campogrosso creek facilitated the flow. Fortunately, there were no fatalities in either of these cases.

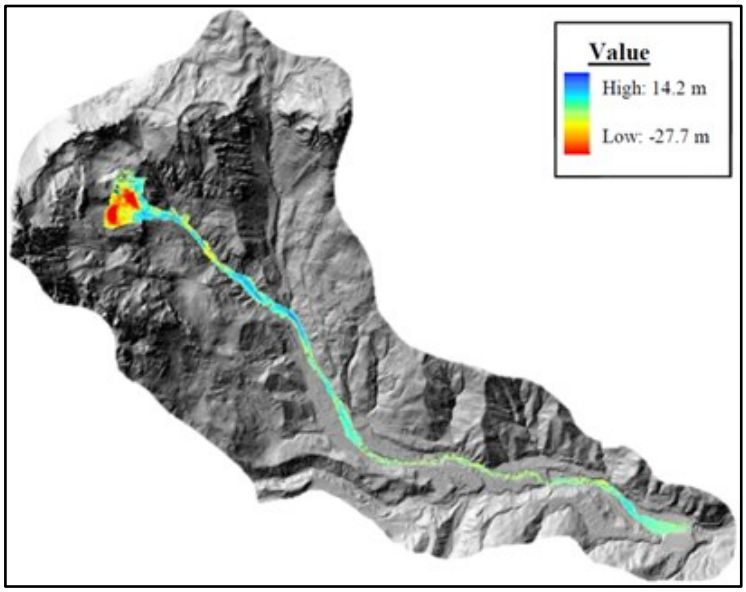

Figure 7.3.2 Map of deposited and eroded material obtained from the DoD analysis.

After the 2009 event and just before the second debris flow, the Regional Territorial Service performed a LiDAR survey of the area and repeated it immediately after the 2010 event. The comparison between the two derived Digital Terrain Models (DTMs) (Figure 7.3.2) provides a precise map of the flooded and erosion/deposition areas along the stream (Bossi et al., 2014) and makes it possible to calibrate a runout model.

Some erosive zones were highlighted by the sliding movement: the detachment area in the upper part with an erosion depth of up to 27 m and others along the path where the velocity of the flow or the geometry and the mechanical properties of the bed allowed excavations.

The basal topography and the initial volume of the sliding mass were defined and used in the GeoFlow-SPH code on the basis of these data.

7.3.3 Preliminary calibration attempts

The calibration of the model reproducing the Rotolon debris flow imposes some improving steps, to reach a satisfactory level of goodness.

Firstly, working on the data obtained by the surveys, it was possible to identify the shape of the source mass of material detached during the real event.

Secondly, due to the mainly frictional regime identified in the flow, it was decided to use the Voellmy rheological law, to study the stress and strain behaviors of the material during the motion. Once decided the topographical and geometrical characteristics of the case, the most difficult phases concerned the choice of the performance indices to use and therefore the identification of the most reliable parameters.

As explained in §6.4.2, many formulations of the error are available and it was necessary to identify the one able to give a more detailed feedback for this case. Moreover, it was opportune to identify the data to compare between the measurements collected with the surveys and the respective ones obtained from the simulations.

It was therefore important to decide the number of parameters to include in the model, eventually defining different areas of variation of the erosion rate and of the friction angle of the material.

A first attempt was performed subdividing the basin in two regions separated by the cross-section corresponding to the Agno of Campogrosso inlet. To preserve the simplicity of the model, the number of parameters was fixed to four: one turbulent parameter, one erosion rate and two friction angles (one for each regions). The identification of two frictional terms was consequence of the dilution of the material made by the inclusion of fresh water from the Agno of Campogrosso.

This first attempt allowed the comparison of the results achieved with two numerical models: the GEOFLOW-SPH (Pastor et al., 2008) and the DAN3D (Hungr & McDougall, 2009). The evaluation of the likelihood of the numerical results to the real data was essentially checked looking at the final map of erosion and deposition of the material and the results of these first simulations are reported in conference (Cola et al., 2015).

Then, to better reproduce the real disposition of material at the end of the flow, it was decided to increase the number of parameters. Two different erosion rates were considered, because it was observed the presence of areas with high loss of basal material, and others were this effect was less evident. Even the number of friction angles was increased, to reproduce the material breaking and changing its size during the motion. To this aim, it is necessary to remind that the complexity included in the flowing of a real mass has to be described by a model using a unique very simple rheological law. The solution adopted allowed to adapt the averaged characteristics of the single-phase material of the model to the heterogeneity of the real mass involved in the debris-flow, which could also change its composition and consistency along the path.

To evaluate the numerical results, initially, the comparison was made on the volumes of material deposited. Basically, ten areas were defined along the channel and for each of these areas, the volume of mass stopped was calculated both for the simulations and the real case. This approach gave a first evaluation of the best choice of parameters, but led to some inaccuracies. The calculation of the volumes was the results of an approximation and increased the entity of the error. On one hand, in fact, the measurements were affected by an instrumental error, and this approach expanded its distribution. On the other hand, the calculation of the volume of each simulation decreased the accuracy of the data directly obtained.

It was therefore decided to use the heights given by the model to perform the comparison. This choice reduced the approximation and the error propagation. The mean absolute error, the root mean square error and the percentage errors were calculated for each numerical result. The identification of these performance indices included all the measurements available, which were more than 15000. This step allowed to univocally identify the best parameters set, among the ones used.

Even if the results were sufficiently satisfactory, a further step was adopted. The possibility not to have considered some combination of parameters, which could have achieved a lower value of error, led to look for some statistical algorithm able to improve the calibration.

Working with the results already obtained, the Ensemble Smoother was finally implemented and applied and the calibration procedure was definitively completed.

7.3.4 Ensemble Smoothing

The calibration procedure developed by this project employs an Ensemble Smoother (ES) or data assimilation algorithm to provide improved estimations of geotechnical parameters. The ES is a Bayesian data assimilation method, which, by minimizing the variance of the estimation error, merges "prior" information from a theoretical system, i.e., the propagation model, with field data collected from the real phenomena in order to produce a corrected "posterior" estimate. In our case, the ES algorithm assimilates the prior information with the deposited soil heights determined by the comparison of pre- and post-event LiDAR surveys.

It follows a two-step forecast-update process: the forecast process is obtained using a Monte Carlo simulation of the system state, while the update, or correction, of the prior information takes place when available measurements are assimilated by applying a specific filter to the forecast model results.

7.3.4.1 Monte Carlo forecast and performance indices

In view of the proliferation over recent decades of the number and types of climatic and environmental models, interest in formulations that produce more accurate and precise estimates of variables of interest has increased. Using an advanced model in which the result is influenced by numerous parameters (being n_p the parameter number), the Monte Carlo analysis makes it possible to perform in an automatic way a large number of simulations, each carried out using an independent initial parameter set obtained by a random selection of values on the basis of a statistical distribution assigned to each parameter.

It is essential then to define statistical errors or performance indices, which can be used to compare model-produced estimates with reliable independent information or reference data.

The various types of errors are described in §6.4.2. It can be identified the mean absolute error (MAE), the root mean square error (RMSE) and the mean absolute percentage error (MAPE). Each formulation leads to underline different aspects of likelihood.

When a Monte Carlo forecast approach is used, evaluation of these indices makes it possible to identify which out of all the simulations carried out is the best one.

7.3.4.2 Update step or data assimilation phase

The estimated variables ($y_t\ (\vartheta)$ with t = 1, 2..., n) obtained with n_{sim} simulations according to the Monte Carlo analysis compose the forecast ensemble $U_{prior}\ [n_u \times n_{sim}]$, being $n_u = n_{hs} + n_p$: generally, the i^{th} column in the U_{prior} matrix lists the n_{hs} model variables $y_t\ (\vartheta)$ estimated with the i^{th} simulation and, below, the values of the n_p model parameters adopted to perform the same simulation. The forecast ensemble should be corrected or updated using n_{obs} field measurement data and the data assimilation algorithm. In general n_{obs} and n_{hs} can be different. In this case, we decided to extract the values to be compared $\widehat{y_t}$ corresponding to the same positions. Basically, it means that in the following, the symbol n will express the number of measured data as well as the number of data obtained from each simulation. We adopted the Kalman filter for the assimilation procedure (Baù et al., 2014; Evensen, 2003) having the follow formulation:

$$U_{post} = U_{prior} + K_t \cdot \left(D_t - H \cdot U_{prior}\right) \qquad \textit{Equation 7-7}$$

where:

- U_{post} [$n_u \times n_{sim}$] is the updated ensemble.
- H [$n \times n_{sim}$] is a matrix that maps measurement locations into the grid domain so that the product $H \cdot U_{prior}$ indicates model results at measurement locations. As explained above, the nodes chosen for the comparison between simulated and observed values are the same. Consequently, the matrix H simplifies by becoming identity one.
- D_t [$n \times n_{sim}$] is a matrix that holds the perturbed measurement data using an ensemble of Gaussian noises, stored in a matrix E [$n \times n_{sim}$] representing the measurement random error. If the measurements are error-free, all n_{sim} columns of D_t are equal to the data.

At the right-hand side of Equation 7-7, the residual $D_t - H \cdot U_{prior}$ defines the deviation between the forecasted state and the true state at the measurement locations. This residual forms the basis for correcting the forecast ensemble. The degree of this correction depends upon the uncertainty of both the forecast ensemble and the measurement data, which is contained in the Kalman Gain matrix K_t [$n_u \times n$]:

$$K_t = C\,H^T\,(H\,C\,H^T + R)^{-1} \qquad \textit{Equation 7-8}$$

where C [$n_u \times n_u$] is the forecast error covariance matrix, and R [$n \times n$] is the measurement error covariance matrix. These two matrices are defined as:

$$C = \frac{\left(U_{prior} - \overline{U}\right)\left(U_{prior} - \overline{U}\right)^T}{n_{sim} - 1} \qquad \textit{Equation 7-9}$$

$$R = \frac{E\,E^T}{n_{sim} - 1} \qquad \textit{Equation 7-10}$$

where each column of $\overline{U}$ [$n_u \times n_{sim}$] holds the average value of the ensemble for each node height distribution. Thus the matrices C and R contain the spread of the model values and the measurement values, respectively.

As explained by Baù et al. (2014), if the spread of the measurement values is small compared to the spread of the model values, the residual between the modelled and measured values is weighted more heavily in correcting the model value so that it is closer to the measurement one. In fact, the matrix K_t assumes the value of 1, so the prior matrix will be strongly updated. Conversely, if the spread of the measurements is large with respect to the spread of the model values, then the residual receives little weight in correcting the model value, which remains similar to the forecast estimate: the Kalman matrix approaches zero value, so the posterior results remain equal to the prior ones.

As an additional observation, it is interesting to note that the reversal operation contained in the calculation of K_t requires special conditions. In fact, if the matrix U_{prior} is excessively rectangular, the reversal of the residue in Equation 7-7 will lead to a nearly singular matrix, thus compromising the success of the algorithm. In particular, the more the forecast ensemble is square, the better the filter applied will converge into a reliable solution. It was for this reason that it was decided to perform 1000 simulations, equal to the number of data to compare.

A final explanation aims to clarify what exactly the updated matrix contains. The lower 8 lines of the U_{post} represent the corrected values of the parameters obtained by the filter. It is possible to plot their normal distributions and to compare them with the prior ones, as extracted by the Monte Carlo procedure. The upper part of the updated matrix contains the results of the application of the Kalman algorithm. The values there are not obtained from the propagation model, so their distribution only emphasizes how efficient the filter was in carrying out its work.

7.3.5 Application of data assimilation analysis

7.3.5.1 Selection of input data

Preliminary analyses carried out by Cola et al. (2015) have shown that the debris flow that occurred in the Rotolon catchment in 2010 could not be well simulated assuming a unique value for each parameter, and it was clear that the parameter values depending on the distance from the triggering zone needed to be varied.

As a result, in order to apply the data assimilation procedure, the basin was subdivided into 6 zones with limits identified according to specific elevations (Table 7.3.1 and Table 7.3.2). It should be noted that the zone extensions are very different because the limits were chosen subdividing the runout length in homogeneous parts with respect to the erosion/deposition behavior of the debris flow resulting from the preliminary analysis by Cola et al. (2015).

Zone	*1*		*2*		*3*	
(Limit elevation)	*(1576-1000)*		*(1000-978)*		*(978-834)*	
	mean	*std*	*mean*	*std*	*mean*	*std*
$tan\phi$	--	--	--	--	--	--
$tan\delta$	0.410	0.010	0.220	0.015	0.220	0.015
$E_s\,[m^{-1}]$	$3*10^{-04}$	$3*10^{-05}$	$3*10^{-04}$	$3*10^{-05}$	0	0
$\xi\,[m/s^2]$	--	--	--	--	--	--

Table 7.3.1 Limit elevations and rheological parameters assumed in the various zones (part 1).

Zone	*4*		*5*		*6*		*Common*	
(Limit elevation)	*(834-731)*		*(731-532)*		*(532-478)*		*(1576-478)*	
	mean	*std*	*mean*	*std*	*mean*	*std*	*mean*	*std*
$tan\phi$	--	--	--	--	--	--	0.6	0.05
$tan\delta$	0.130	0.015	0.020	0.005	0.020	0.005	--	--
$E_s\,[m^{-1}]$	0	0	$8*10^{-05}$	$3*10^{-06}$	0	0	--	--
$\xi\,[m/s^2]$	--	--	--	--	--	--	700	60

Table 7.3.2 Limit elevations and rheological parameters assumed in the various zones (part 2).

The mean value of rheological parameters was estimated using values indicated in the literature (Pirulli & Sorbino, 2008; Bertolo & Wieczorek, 2005) and the preliminary results obtained by Cola et al. (2015): the latter authors, for example, showed that the basal friction coefficient decreases along the path of the debris flow, probably due to an increase in the fluidity of the material or to an arrest due to large boulders blocking the path as the bed slope decreased.

The internal friction angle ϕ and the turbulence coefficient ξ were assumed constant for all the zones, because, as already explained, the current version of the GeoFlow-SPH does not allow different values for them: in particular, the internal friction angle ϕ is assumed equal to 30° ($\tan\phi$ = 0.6), the minus value for the critical angle of a granular soil, the value commonly adopted for describing debris and rock flow (Sosio et al., 2008); the turbulence coefficient ξ was chosen equal to 700 m/s^2, that is, a mean value within the range of 100 and 1000 m/s^2, as was suggested by Pirulli et al. (2008).

Other suggestions about the ξ value were also made by Sosio et al. (2008) who indicated a range of 450-1000 m/s^2 for rock avalanches and a range of 200-500 m/s^2 for debris flows: the use of a unique value for ξ might contrast with the nature of the phenomenon studied, which could be more similar to a rock avalanche in the detaching upper area when, after covering a part of its trip and receiving water from lateral tributaries, it assumes the characteristics of a debris flow. The use of a constant parameter equal to 700 m/s^2 seems in any case to be a compromise with values reported in the literature that would be compensated by assuming a normal distribution with a wide standard deviation.

The basal friction coefficient $\tan\delta$ could be defined differently for each zone and it is reasonable to think that, along the river, both the debris flow and the bed material reduce their grain-size composition and, consequently, the basal friction angle is reduced as the flow proceeds downstream. In particular, Cola et al. obtained a good reproduction of the event assuming $\tan\delta$ equal to 0.41 (δ=22.3°) and 0.02 (δ=1.1°), respectively, in the portions upstream and downstream the conjunction with the rio Campogrosso. Based on these observations, here we assumed 4 different mean values of δ: two different values for the 1st and the 6th zones and two other values for the 2nd and 3rd zones and for the 4th and 5th zones, respectively. The standard deviation was chosen proportionally to the mean value: for example, the basal friction coefficient in the first area, which has a mean value of 0.41, is associated with a relatively wide standard deviation of 0.03, while, on the contrary, the basal friction angle in the 4th zone has a smaller variation range because it it was important to be sure that negative values were not included in the parameter set.

Among all the erosional law available, it is decided to include in the model the one proposed by Hungr (1995).The mean value of the erosion parameter in the various zones was chosen on the basis of the DoD analysis: the E_s value was assigned equal to $3{\cdot}10^{-04}$, $8{\cdot}10^{-05}$ or zero if the comparison between pre and post DTMs in a zone prevalently showed erosion, both erosion and deposition or prevalently deposition, respectively.

Table 7.3.1 and Table 7.3.2 summarize the mean value and the standard deviation assigned to each zone for the forecast phase. There are 8 rheological parameters: 4 values of the basal friction angle, 2 values of the erosion coefficient, 1 of the internal friction angle and 1 of the turbulence coefficient.

In order to underline the role and the importance of each parameter, a sensitivity analysis was carried out before the data assimilation procedure was applied. This step is extremely useful to uncover to what extent an inaccurate choice of a parameter can affect model results.

7.3.5.2 Reference data and measurement error

In order to apply the calibration procedure, two other important issues needed to be solved: one regards the selection of the reference values to analyze the likelihood between simulated and measured values, the other the error associated to the reference data.

First of all, to make the calibration as complete as possible, it is appropriate to consider the highest number of values possible out of all those that are available. Each simulation with GeoFlow-SPH produces more or less 15000 data referring to the heights of deposited soil along the river at the end of the debris flow propagation (in the following briefly indicated as soil height or h_s); in the same way, the comparison between pre and post DTMs could supply a large amount of data, such as a million and half of values.

On the other hand, to be correctly applied, the Kalman procedure requires the number of simulations to be comparable to the number of measurements being compared.

In view of the fact that the computational cost of each simulation is approximately an hour, in order to procure a sufficiently representative sample we decided to limit the number of comparison data to 1000. The procedure would thus produce 1000 simulations (n_{sim}=1000) and from each of them it will take 1000 values of soil heights to compose the upper part of the forecast ensemble U_{prior}.

Once the number of data is fixed, another important issue is that of selecting the data which must describe the phenomenon as accurately as possible in all the source and deposition areas. For this reason the talweg and two parallel polylines 15m away from the talweg were identified on the DoD. The variables used for the comparison were the soil height in a selected number of nodes belonging to the polylines. In this way the talweg represents the longitudinal section of the landslide and the data along it take into account the total propagation of the debris flow, while information along the parallel polylines would take into account the mass spreading along the path. All together, there are about 4000 nodes on the three polylines, but, again, only 1000 nodes were selected in a random way out of the 4000 nodes that were available, obtaining the n reference data to compose the vector of the reference heights.

As previously described, the ES algorithm needs to assign the normal distribution of error associated to LiDAR data in order to produce matrix E [$n \times n_{sim}$] and the error distribution affects the final result in a significant manner: a large error would lead to information that is not sufficiently precise for parameter optimization, but, conversely, if the error assigned is too small, the expectation to provide sufficiently precise information could be excessive and the optimization algorithm may not provide reliable parameters.

In our case, no information about the Gaussian distribution of error of the LiDAR data was available: as a result, we set the error of each derived DTM to 0.2 m, a typical value of airborne LiDAR surfaces (Cavalli & Tarolli, 2011). The propagated error was consequently assumed constant in the DTM of Difference (DoD) analysis (G. Bossi et al., 2014) and equal to ±0.28 m. In the last part of the paper, a further analysis evaluating the influence of this parameter is presented together with some of our comments.

Finally, the procedure was performed extracting 1000 values from the normal distribution of each rheological parameter, defining 1000 combinations of parameters and performing the corresponding simulations. At the end of each simulation, the results were elaborated and 1000 data values were extracted from as many nodes. The final matrix has 1000 columns, one for each simulation, and 1000 rows, one for each node. The U_{prior} matrix is the result of concatenation of this matrix [1000x1000] with the random parameters used for the simulations.

7.3.5.3 Model sensitivity

As mentioned in §5.1, in order to underline the importance of each parameter, the results of a sensitivity analysis are presented. Once a variation range for each parameter was chosen, eight series of seven simulations were developed in which only one parameter at a time was modified: a total 56 simulations were carried out, as outlined in Table 7.3.3. The central column contains the values that remained the same during the variation of one parameter. It should be noted that the values assumed for friction and turbulence coefficients differ for a constant quantity depending on the value of the parameter, while the erosion coefficient values vary according to a geometrical series in one order of magnitude.

In the bar-plot of Figure 7.3.3 the range of variation of the MAE, RMSE and MAPE errors calculated for the seven simulations of each series is summarized. The horizontal line joins the error values obtained with the central combination of parameters. It is obvious that the larger the error variation is in function of a parameter variation, the larger is the influence of that parameter. Figure 7.3.3 shows, for example, that the internal friction coefficient $tan\phi$ has a secondary role because MAPE varies only between 25 and 30.6%. On the contrary, all the basal friction angles, in particular, the first three, are fundamental for the calibration process: in fact, small variations in their value cause significant fluctuations in the error. The influence of the erosion coefficient is likewise very strong.

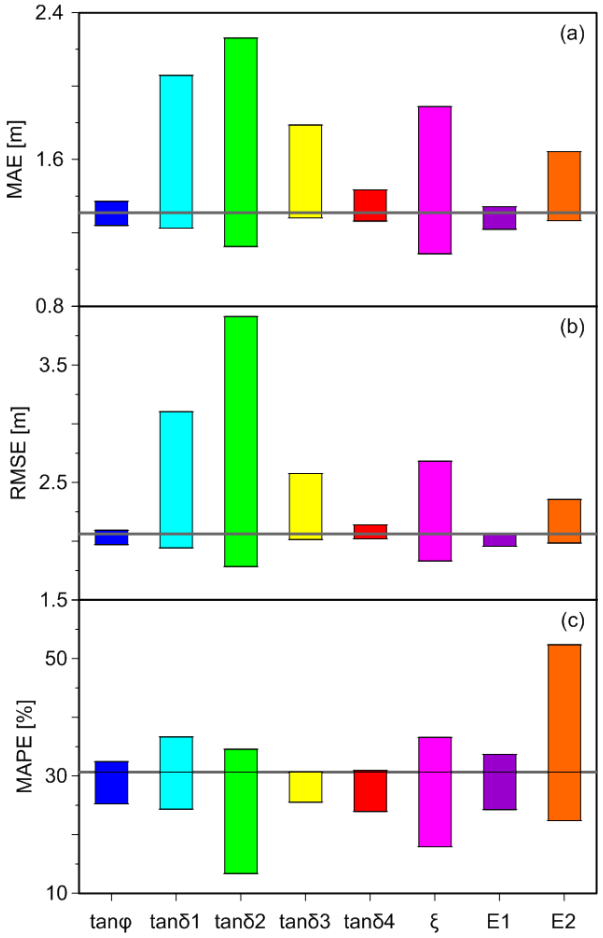

Figure 7.3.3 MAE (a), RMSE (b) and MAPE (c) of the analyses performed to evaluate the model's sensitivity.

It is also interesting to observe that the performance indices were calculated for all the nodes of the simulation, and not only the 1000 nodes chosen for the subsequent application of the Kalman filter. This was done in order to evaluate the totality of the phenomenon that was simulated compared to real values.

Parameter	Values						
$tan\phi$	0.450	0.500	0.550	0.600	0.650	0.700	0.750
$tan\delta_1$	0.320	0.340	0.360	0.380	0.400	0.420	0.440
$tan\delta_2$	0.160	0.180	0.200	0.220	0.240	0.260	0.280
$tan\delta_3$	0.090	0.100	0.110	0.120	0.130	0.140	0.150
$tan\delta_4$	0.006	0.009	0.012	0.015	0.018	0.24	0.036
$\xi\ [m/s^2]$	50.00	200.00	350.00	500.00	650.00	800.00	950.00
$E_1\ [m^{-1}]$	1.25E-06	2.50E-06	5.00E-06	1.00E-05	2.00E-05	4.00E-05	8.00E-05
$E_2\ [m^{-1}]$	3.75E-06	7.50E-06	1.50E-05	3.00E-05	6.00E-05	1.20E-04	2.40E-04

Table 7.3.3 Values of rheological parameters assumed in the sensitivity analysis.

A clarification must be made concerning calculation of the percentage error. The nodes that have a deposit or erosion in the simulation solutions are compared with the relative measurements. However, if an in-situ observed value proves null, division by zero in formulating MAPE introduces serious problems. To overcome this situation it was decided to exclude all nodes that have null measures or not null simulated values from the calculation of MAPE: of course, the mean value of error is calculated correcting the total number of compared data.

In our opinion, the best representative formula of error is the percentage one, because it weighs any difference in function of the respective measure. For this reason, in the following analysis we decided to refer only to this error formulation.

7.3.5.4 Data assimilation analysis

7.3.5.4.1 Prior results

To obtain the prior ensemble $U_{prior,}$ 1000 simulations were performed with the parameter sets extracted from the parameter Gaussian distribution using the Monte Carlo procedure, and then the soil height values in correspondence to 1000 points belonging to the three reference polylines were pulled out, as described in §5.2. The extracted soil heights are plotted in Figure 7.3.4 forming three longitudinal profiles, each of which composed of 333 node values.

The colored lines represent the results of all the simulations, while the thick black lines indicate the DoD measurements of the same nodes. Here we see that the prior solutions are quite spread out, which is an effect on the input parameter variances originally chosen. It is in any case important that all the measurement lines are included in the range of the simulation results: in this way, the statistical algorithm that is applied later can give good results.

A first assessment of these analyses can be obtained by means of the distribution obtained for the percentage error. The minimum MAPE of all the simulations is 16.2% while the mean and maximum values are 40.9% and 68.9%, respectively.

The soil heights in the reference nodes from each simulation form a vector 1000-long. By adding the combination of parameters used for the simulation to it, the vector becomes 1008-long. Assembling all of these vectors permits us to build the prior [1008x1000] matrix.

7.3.5.4.2 Posterior results

The most important part of the calibration process regards the stage during which the Kalman filter is applied. As has already been described, it takes the prior matrix U_{prior} and restitutes an updated matrix U_{post} containing the corrected values. The Kalman filter was first applied with a measurement error set at ±28 cm, which corresponds, as explained above, to the propagated error of the Dod analysis.

The upper part of this matrix expresses the performance of the algorithm applied: a reduction in the variety of the prior data underlines the fact that the posterior results are more similar to reality than the prior ones.

The lower part of the updated matrix can be compared with the lower part of the prior matrix. In particular, Figure 7.3.6 compares the frequency distribution of each parameter that was obtained from the prior and post matrices, a comparison which give us some information about the parameter values to be used and about the relevance of each parameter for the model. The more the algorithm reduces the variance of the normal distribution of a parameter, the more important and better defined it will be.

As the sensitivity analysis previously suggested, the most important parameters are the basal friction angles: for each of these the filter furnishes a better frequency distribution with respect to the input one. The internal friction angle carries out a secondary role since its frequency curve seems less restricted after the filter has been applied. The same can be said about the turbulence parameter even if the analysis indicates that the mean value is much smaller with respect to the input one.

A final consideration concerns the filter's indication about the erosion parameter: even if the mean value of E_1 introduced into the analysis was greater than E_2, its final value is one order of magnitude minor than the input one and minor than the E_2.

The mean values of the updated parameters are reported in Table 7.3.4. It is very interesting to compare the results of the simulation performed using these values as input with the measurements, as outlined in Figure 7.3.5. The correspondence between the total runout of debris-flow in-situ and in the model is very good, and the soil height distribution along the stream is

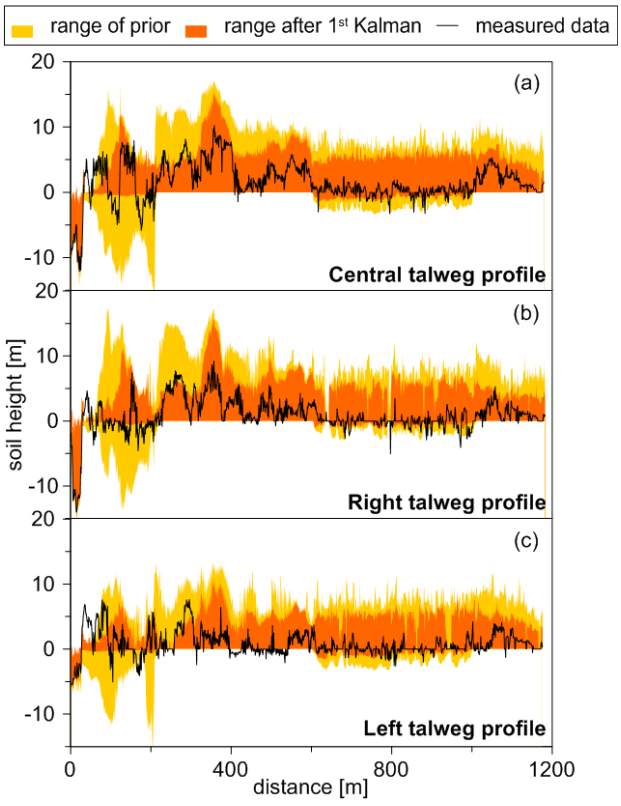

Figure 7.3.4 Soil height obtained with the 1000 GeoFlow-SPH forecast analyses of the nodes composing the talweg line (a) and the two parallel polylines (b,c).

also well described by the numerical model, even if the model seems to overestimate the deposition in the lower portion of the basin and, on the contrary, to underestimate the soil height in the upper part.

parameters	*tanϕ*	*tanδ1*	*tanδ2*	*tanδ3*	*tanδ4*	*ξ*	*E1*	*E2*
value	0.77	0.38	0.21	0.13	0.03	203.44	$2.93*10^{-05}$	$8.65*10^{-05}$

Table 7.3.4 Mean of the updated parameters after the first Kalman filter was implemented.

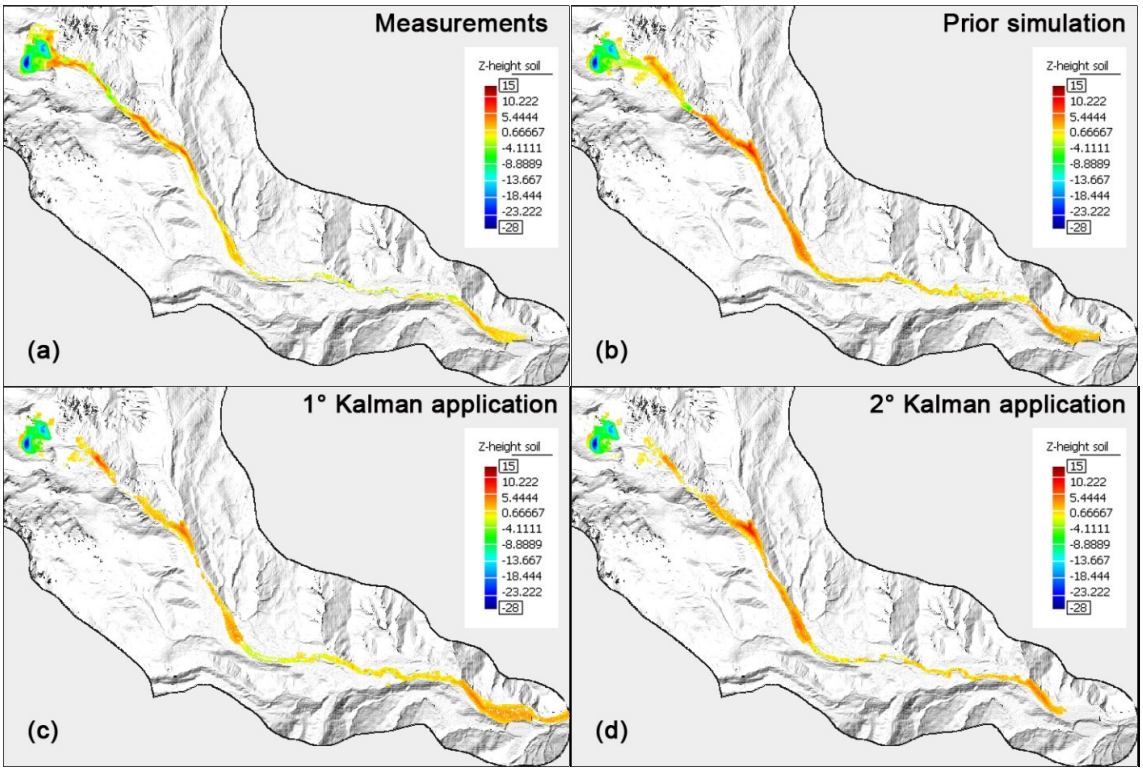

Figure 7.3.5 Comparison between the deposition and erosion maps of the data measured (a) and of the data before (b) and after the the Kalman filter was applied (c,d).

7.3.5.4.3 The second Kalman filter application

The last step of the procedure consists in carrying out 1000 new simulations with the parameters obtained using the Montecarlo procedure from the updated frequency distribution and then once again applying the Kaman filter. The same steps as those adopted previously should be used; even in this case it is possible to plot the soil height profiles along the reference polylines (Figure 7.3.4).

The spread of the soil height profiles is lower than the one in the first analyses (Figure 7.3.4). In fact, the orange lines remain closer to the line of the observed values (black line) than do the previous ones (yellow lines).

As before, the application of the Kalman algorithm provides a new updated matrix and new frequency distributions of parameters are obtained and compared with the input frequency distributions (Figure 7.3.6). With the second application of the Kaman algorithm, some distributions maintain the same mean value and further reduce the variance, as occurred for $\tan\delta_3$ (Figure 7.3.6d),

while, on the contrary, for other distributions, as in the case of the turbulence (Figure 7.3.6f), the algorithm gives new corrections even with regard to the mean value. It is necessary to clarify that the statistical filter applied considers each parameter as a number and does not take into account its physical meaning. This is the reason why the second application of the Kalman filter gives a negative value for the erosion coefficient E_1 (Figure 7.3.6g). We have interpreted this result as meaning that we need to set a null value of erosion in the areas where we entered E_1.

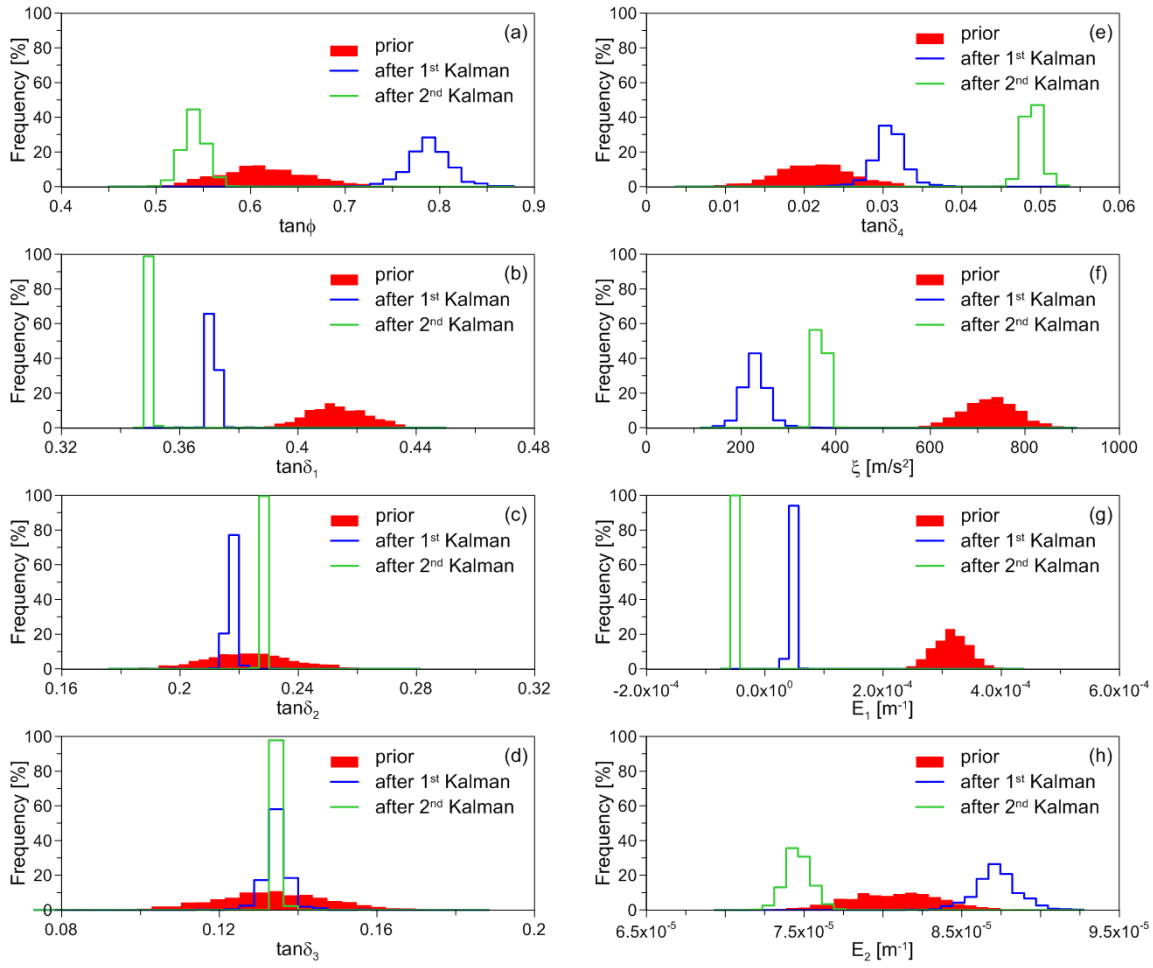

Figure 7.3.6 Frequency distribution of the rheological parameters in input and output from the data assimilation analysis of the three procedure steps.

Again, in Figure 7.3.5d the soil heights of the D.o.D. are compared with the heights obtained with a new simulation performed setting the average value of the updated normal distribution for each parameter. The MAPE of this last result reached the value of 26.9% (Table 7.3.5).

	user-defined parameter	*1° Kalman filter application*	*2° Kalman filter application*
MAPE %	36.9	33.9	26.9

Table 7.3.5 Percentage errors of the simulation obtained with the user-defined parameter set and the two obtained with the simulations using the parameter set suggested by the Kalman filter.

7.3.6 Discussion of results

7.3.6.1 Comparison among errors

Some initial comments can be made about the comparison of the distribution of the performance index defined in eq.(8), i.e. the MAPE. Figure 7.3.7 presents the comparison between the distribution of the percentage errors for the prior and post simulations, i.e. the simulations carried out with parameters extracted from the updated frequency distribution.

It is evident that the Kalman algorithm produces an important improvement in the distribution of the MAPE displayed here, but also of other performance indices. Even if the lowest values of the three errors for the updated group of simulations did not decrease, a significant reduction in the highest and mean values was observed. The improvement of the MAPE, which fell from 40.9% to 28.3%, is particularly evident (Table 7.3.6).

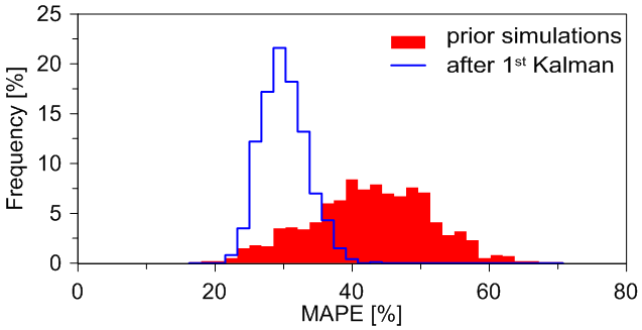

Figure 7.3.7 Normal distribution of the percentage errors of the first 1000 simulations compared with the normal distribution of the simulation after the Kalman filter was applied.

	user-defined parameter	*after 1° Kalman Filter application*
Min MAPE %	16.2	20.2
Mean MAPE %	40.9	28.3
Max MAPE %	68.9	41.5

Table 7.3.6 Percentage errors of the prior 1000 simulations compared with the 1000 ones obtained after the first Kalman filter was implemented.

After the 2nd application of the Kalman algorithm we could also compare the performance indices of the third group of simulations, i.e. those carried out with parameters extracted using the frequency distribution suggested by the 2nd Kalman filter.

As shown in the Table 7.3.5, the best MAPE obtained from the first simulation reached the value of 36.9%. After the first application of the filter, we obtained a MAPE of 33.9% from the simulation developed. At the end, after a new improvement procedure was implemented, we attained a MAPE of 26.9%.

7.3.6.2 *The effect of measurement error*

The algorithm makes it necessary to make some assumptions about the distribution of errors affecting the reference data. As has been explained before, the propagated error of the D.o.D. was set at a constant value but it may also be interesting to evaluate how the error value influences the optimization process results. In fact, if the assumed reference data are sufficiently descriptive of the debris flow and the model is really able to reproduce the phenomena, the posterior results should be stable regardless of error values.

To verify this condition, the Kalman algorithm was applied 10 times to the same prior matrix adopting error values varying from 10 cm to 1 m in a logarithmic way: the boxplot of Figure 7.3.8 summarizes distribution indicated by the filter for each parameter plotted versus the assumed error value and compares them with the forecast boxplot representing the normal distribution of the same parameter assumed at the beginning of the procedure. On each box, the central thick mark indicates the median value, the box edges the 25th and 75th percentiles respectively and the whiskers the 2.7$\sigma \div$ 99.3σ range, σ being the standard deviation of the normal distribution of each parameter. The model sensitivity to the error value is represented by the filter's ability to reduce the variance of the parameter distribution and to supply a unique mean value regardless of the assumed error.

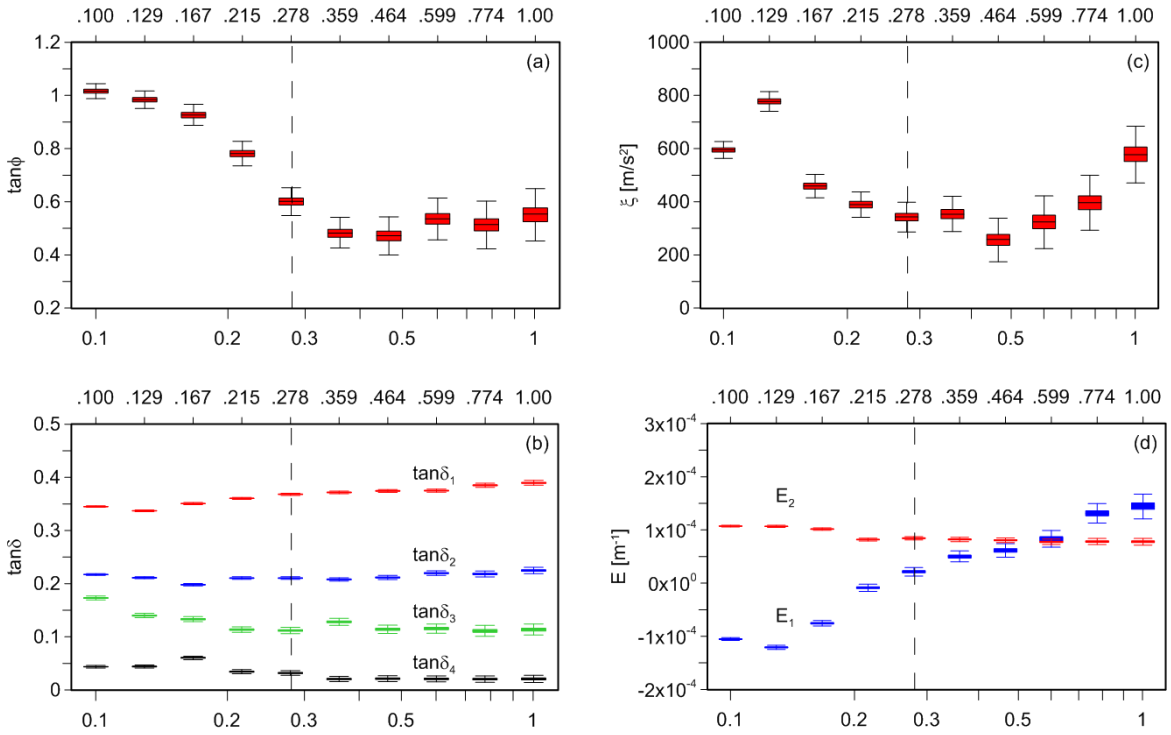

Figure 7.3.8 Boxplots of the results using different values for the measurements error for each parameter after the Kalman filter was applied.

All the posterior boxplots are more precise than the forecast distribution since in all cases the standard deviation is reduced, confirming that is algorithm is working well. Moreover, the results of Figure 7.3.8 are consistent with those already obtained by the sensitivity analysis outlined in section 5.3. In fact, the error value does not change the posterior values of the basal friction angles (*tanδ*)

and this confirms that these parameters have a strong influence on model calibration. Similar reasoning is appropriate for the erosion parameter in the lower part of basin E_2, but not for the erosion coefficient in the upper part of E_1 which has a mean value in output that is strongly dependent on the definition of the measurement error. Even this result confirms what was obtained in the previous sensitivity analysis.

Finally, modifications in the definition of error also produced different output values for the turbulence and internal friction parameters, but, after the filter was applied, their variance was reduced to a lesser extent with respect to the other parameters. This result can be justified by a variety of explanations. On the one hand, the internal friction angle seems to play a secondary role for the model because the model shows a greater tolerance in relating this parameter to the reference data. On the other, in view of the fact that the turbulence coefficient is extremely important for model calibration, it would probably be better to define different parameters for different zones. This consideration is made in the effort to explain the very different values for the turbulence coefficient that are found in the literature. In this way, it is probable that the values found in the literature in the future will be in better agreement with the real behavior of debris flows.

7.3.7 Conclusions

Models analyzing debris flow propagation are usually calibrated by comparing in a subjective way the predicted and measured lengths of the flow or heights of deposited soil in some particular sections. This procedure is, however, likely to be inaccurate if it is based on inappropriate performance indicators and may be further complicated by the fact that different combinations of values often lead to similar results.

The procedure proposed here, based on a data assimilation algorithm and the systematic use of performance indices, can be a useful tool because it presents some evident advantages, including the following ones:

- it is applied starting from a large number of possible parameter combinations obtained extracting values in a random manner from reliable statistical distributions;
- the comparison takes into account the totality of deposits along the debris flow path;
- the evaluation is carried out using indices that are not affected by subjective interpretation;
- it may be implemented in an automatic code in order to easily repeat its application numerous times and analyzing the effects of different initial assumptions;
- it can be improved by including other rheological parameters or the most probable distribution of error in measurements.

It is also important to indicate critical points that need to be checked for the correct application of a similar calibration procedure. The most important are the following:

- a large number of simulations have high computational costs depending on the time required to perform a single propagation analysis. At the same time, being able to simultaneously perform more than one simulation, depending on the number of processors that are available, may significantly reduce the computational time;

- the choice of the performance index is extremely important since not all error formulations are sufficiently representative and reliable;
- identifying the nodes to be considered for the Kalman filter application is an important step to converge to an optimal solution.

Some comments can also be made about the application of the data assimilation to the specific case history presented here. First of all, the subdivision of the basin into different portions with different parameters proved to be a good strategy that could be improved if it were possible to use different parameters and not just the basal friction angle.

In this case, the erosion evaluated using the Hungr formula resulted limited and the calibration of the representative parameters in the upper part of the basin did not furnish a reliable value, probably due to the minor relevance of the phenomena.

The basal friction angle, the turbulence coefficient, and the erosion rate in the lower basin are the most significant rheological parameters that must be carefully selected in order to reach a proper reproduction of the Rotolon debris-flow.

8 GENERAL CONCLUSIONS

The topic of this thesis is to underline how the calibration is a procedure directly dependent on some important and critical factors. A strategy that does not consider all the aspects and the problems that can be found would lead to unreliable or approximate results.

First of all, the choice of the numerical model to calibrate is fundamental. As already mentioned, some models consider the material as a mono-phase equivalent fluid, some others take into account all the components and the forces between them. The 2D models are useful to reproduce simple cases, where the system is axial-symmetric or the geometry allows considering a section sufficiently descriptive of the studied phenomenon.

The 3D depth-integrated models try to include a kind of three-dimensionality in the calculation. The hypothesis for the application of this type of code is that the horizontal length scale is much greater than the vertical length scale. Practically, this kind of model represents a compromise between the simplicity of a 2D model and the expensive complexity of a 3D one.

Obviously, it has some advantages, such as the limited computational costs, and some inaccuracies. The simplification that considers the mixture as a unique fluid with averaged physical and rheological characteristics is acceptable when the real material is not too much heterogeneous. The calibrated parameters lose any physical meanings when the try to average many different components of the flowing mass.

The boundary conditions are another critical point of the model construction. In §7.1, for example, it is shown how the real collapsing conditions are not considerable in the model. This approximation can cause differences in the model possibility of reproduction. The basic assumption is that the model has to be able to reproduce somehow the case study, if not the calibration lose completely sense.

In all the three case studies described, it is evident that the choice of the data to compare play a critical role in the good success of the identification of the best parameters. When a huge quantity of data is available, in fact, selecting what is necessary to consider and neglecting what is superfluous is important. In §7.3, for example, the variables to compare between measurements and simulated values conditioned the number of simulations to perform. In §7.2, instead, the choice of considering dynamical and deposit information or of neglecting one of those changed evidently the parameters obtained.

It is therefore important to decide the performance index to use. Different formulations of the error, in fact, underline various differences between the physical and the numerical model, as described in §6.4.2.

8.1 CRITICAL ISSUES

Some critical issues have been found during the calibration phases. In my opinion, even if the overall conclusions allow to consider satisfactory the procedure, it is opportune to underline the difficulties found and the remaining uncertainties still present.

The numerical model chosen is very useful to reproduce some aspects of a rapid landslide. Otherwise, it presents some limitations that can directly affects the calibration.

The first case study is considered taking into account its axial-symmetry. The model performs numerical results that have the same axial-symmetrical characteristics. The performance index used to calibrate the parameters simplifies the variables to consider and includes only information about the diametric section.

If this is satisfactory for the collapse of the cylinder, some deeper investigation is request working with the second case study. The data used for the calibration contains information both dynamical and about the deposit. Anyway, it has to be noticed that all the variables chosen refers to the central longitudinal section, neglecting the lateral spread distribution. The comprehension of the ability of the model to reproduce this aspect of the flow is absolutely interesting, in order to evaluate how the calibration can again depend on the data used for the comparison.

Figure 8.1.1 contains the contours of the deposit heights of the simulations that minimize the three formulation of the error, compared with the laboratory result for WK_A4 mixture.

It is immediately evident that the behavior of all the simulations is quite different from the one collected in laboratory. The calibration procedure has therefore to pay attention which aspect the numerical model is able to reproduce. If the goal is to understand the behavior of the central longitudinal section, the prediction may be extremely similar to the measurements. Contrarily, the model is not able to catch the three-dimensionality of the phenomenon.

Some considerations can be made to explain why the model gives so much different results, in terms of lateral spread.

First of all, the boundary conditions imposed in the simulations are different from the real ones. The experimental apparatus has two Plexiglas lateral walls that condition the direction of the flow. The material running along the channel may be in two different conditions: the central mass can flow undisturbed, while tangential frictional effects due to the contact with the sides affect the external volume. The lateral mass accumulates a delay, compared with the central one and causes a transversal velocity gradient of the flow along the channel.

The boundary conditions applied in the model impose zero velocity in a direction perpendicular to the segments located in correspondence of the lateral walls. This cause a homogeneous distribution of velocity along the slope, without any transversal difference.

A second point that can limit the similarity of the results concerns the mechanism regarding the outlet. As already mentioned in §7.2.6.2, the physical results achieved agree with Azimi et al. (2016). The behavior of the flow on the horizontal plane allows the identification of two regions, one that

shows the main flow along the longitudinal axis and one that shows the lateral spreading of the mixtures with an angle from the x axis.

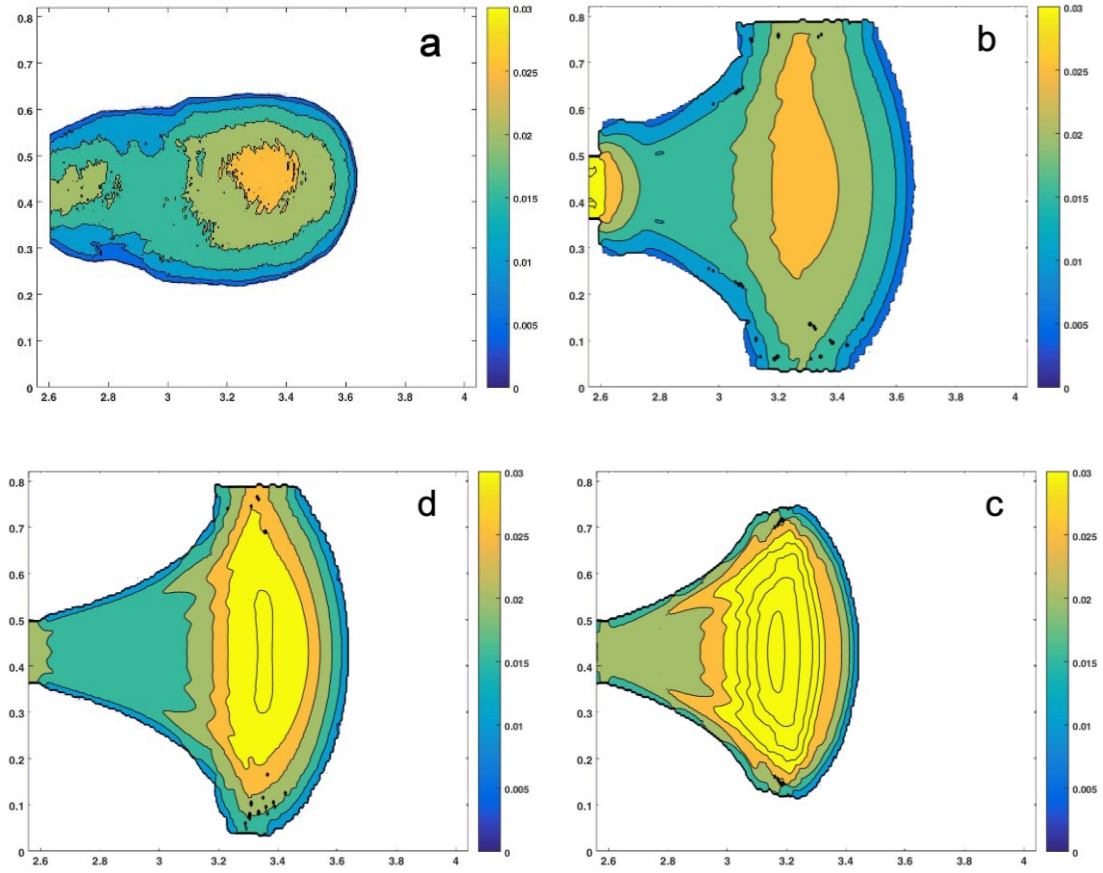

Figure 8.1.1 Comparison of the spread of the best simulations achieved: a) WK_A4 laboratory test; b) best profile simulation; c) best height vs time simulation; d) best overall simulation.

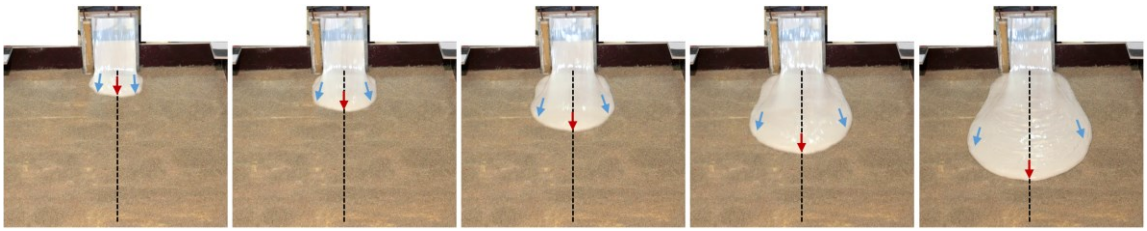

Figure 8.1.2 Behavior after the outlet of the laboratory tests.

Actually, the material flowing at the center of the transversal section continues its motion undisturbed on the plane (Figure 8.1.2). The external mass, contrarily, changes the direction of the velocity, goes out from the central flow and suddenly stop its run. In that way, the laboratory results are characterized by various runout and almost constant spread. Probably the transversal gradient of velocity mentioned above also contributes in that sense.

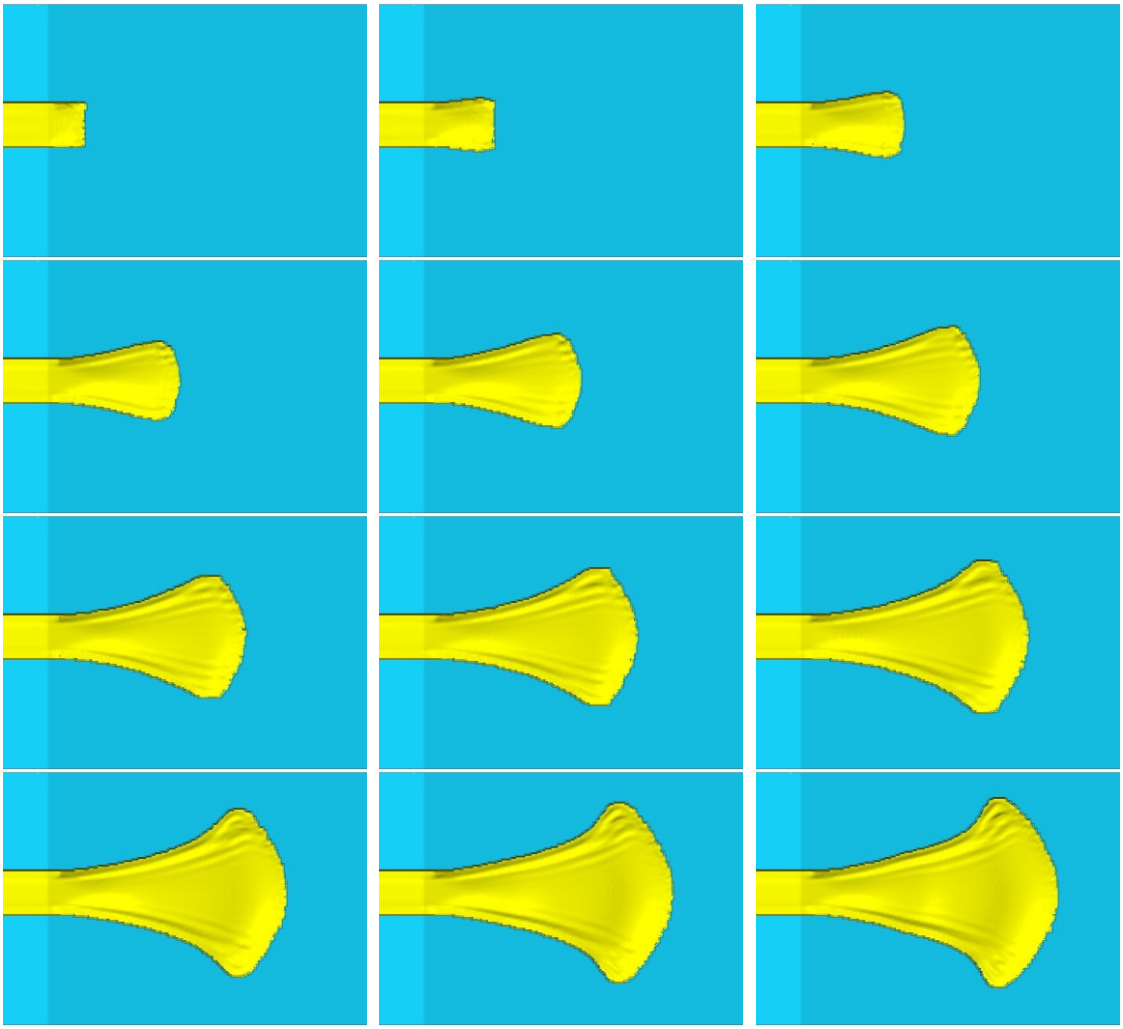

Figure 8.1.3 Behavior after the outlet of the simulations.

The behavior observed in all the simulations is quite different. Basically, the material comes out from the outlet maintaining a homogeneous transversal velocity. All the mass keeps the same direction of motion, parallel to the x axes. After a while, which depends on the rheological parameters chosen, the lateral spread start to increase (Figure 8.1.3). This increasing of the lateral spread does not stop and continues until the material has stopped.

The mechanism of deposit is therefore different and this leads important differences in the accumulation of the material on the plane.

It has to be underlined that the model is depth-averaged. All the properties are consequently averaged on the depth. This simplification may lead to some inaccuracies, especially speaking of the front of the material.

Chambon et al. (2014) developed some experimental tests on a viscoplastic material, in order to evaluate its behavior and its rheological characteristics. What is interesting concerns the trajectories of the front zone. Figure 8.1.4a underlines the complexity of the motion of the material, which is

not reachable by the used model. That is, probably, another important consideration about the possible causes that reduces the likelihood between the simulated and the measured values.

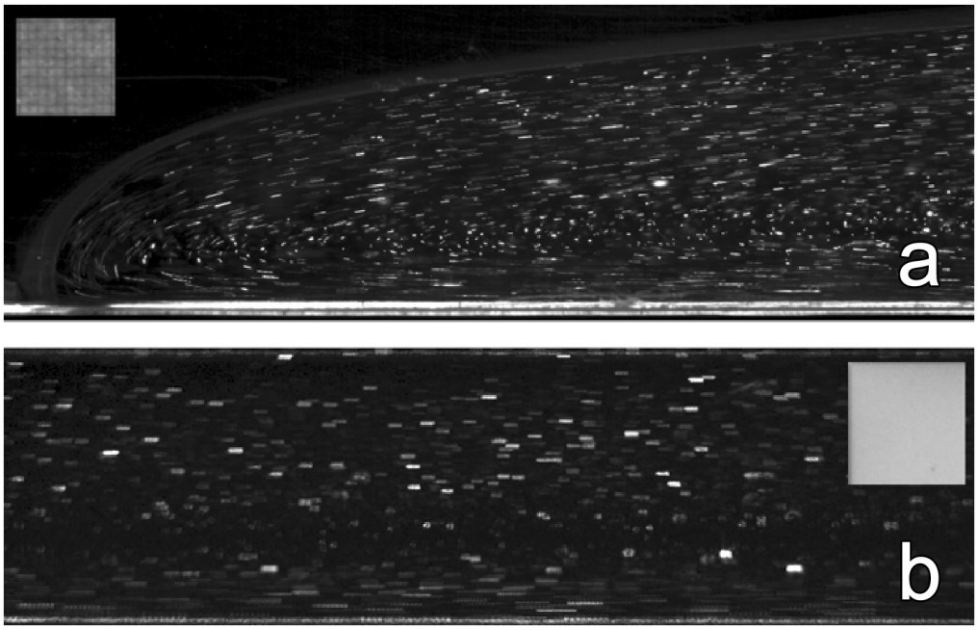

Figure 8.1.4 Observation of fluid trajectories within the flow using top lighting and long-exposure photography. The brightly illuminated objects correspond in this case to small air bubbles present in the material of the (a) Front zone; (b) Uniform zone.

The topic of the present thesis is to demonstrate how the calibration strategy adopted influences the parameter obtained. It is important to remember that, nowadays, every model try to reproduce a phenomenon, applying simplifications and approximations.

Many of the parameters included in the model are useful to adapt the results to what you are looking for. This possibility on one hand help the researcher to reach high quality of similarity. On the other hand, when these values move away from a physical meanings, become just number used to fix the inaccuracies.

To properly calibrate a numerical model is therefore opportune to consider all characteristics of the phenomenon and to interpret smartly the result achieved.

FIGURES INDEX

TABLES INDEX

REFERENCES

Ancey, C., 2007. Plasticity and geophysical flows: a review. *Journal of Non-Newtonian Fluid Mechanics*, 142(1), pp.4-35.

Armanini, A., Fraccarollo, L. & Rosatti, G., 2009. Two-dimensional simulation of debris flows in erodible channels. *Computers & Geosciences*, 35(5), pp.993-1006.

Artoni, R. et al., 2013. Collapse of quasi-two-dimensional wet granular columns. *Physical Review E*, 87(3).

Ayotte, D. & Hungr, O., 2000. Calibration of a runout prediction model for debris-flows and avalanches. In *Proceedings of the 2nd International Conference on Debris-Flow Hazards Mitigation: Mechanics, Prediction, and Assessment, Taipei, Taiwan*. AA Balkema, Rotterdam, 2000. Edited by GF Wieczorek and ND Naeser.

Azimi, A.H., 2016. Free surface flow characteristics of multi-phase viscoplastic fluids on inclined flumes and planes. *International Journal of Multiphase Flow*, 78, pp.59-69.

Bagnold, R.A., 1954. Experiments on a gravity-free dispersion of large solid spheres in a Newtonian fluid under shear. *Proceedings of the Royal Society of London A: Mathematical, Physical and Engineering Sciences*, 225(1160), pp.49-63.

Baltzer, A., 1875. *Über bergstürze in den Alpen. Verlag der Schabelitz'schen buchhandlung*. Zurich: C. Schmidt.

Barbieri, G. et al., 1980. Carta geologica dell'area di Recoaro. Padova, 1980. Mem. Sc. Geol. XXXIV. [in Italian].

Barbolini, M. et al., 2004. Laboratory study of erosion processes in snow avalanches. *Cold Regions Science and Technology*, 43(1), pp.1-9.

Bates, R.L. & Jackson, J.A., 1984. *Glossary of geology*. Falls Church, Virginia.

Baù, D., Ferronato, M., Teatini, P. & Gambolati, G., 2014. Ensemble Smoothing of Land Subsidence Measurements for Reservoir Geomechanical Characterization. *International Journal of Numerical and Analytical Methods in Geomechanics*, DOI: 10.1002/nag.2309.

Benz, W., 1990. Smooth particle hydrodynamics: a review. In *The numerical modelling of nonlinear stellar pulsations*. The Netherlands: Springer Netherlands. pp.269-88.

Bertolo, P. & Wieczorek, F., 2005. Calibration of numerical models for small debris flows in Yosemite Valley, California, USA. *Natural Hazard and Earth System Sciences*, 5, pp.993-1001. DOI: 10.5194/nhess-5-993-2005.

Bettella, F., Bisantino, T., D'Agostino, V. & Gentile, F., 2012. Debris-flow runout distance: laboratory experiments on the role of Bagnold, Savage and friction numbers. In *Monitoring, Simulation, Prevention and Remediation of Dense and Debris Flows IV. WIT Transactions on Engineering Science*., 2012. D. de Wrachien, C.A. Brebbia & S. Mambretti.

Bingham, E.C. & Green, H., 1919. Paint, a plastic material and not a viscous liquid; the measurement of its mobility and yield value. *Proc. Am. Soc. Test. Mater*, 19, pp.640-64.

Bossi, G. et al., 2014. Multi temporal LiDAR-DTMs as a tool for modelling a complex landslide: a case study in the Rotolon catchment (Eastern Italian Alps). *Natural Hazards and Earth System Sciences Discussions*, 2(10), pp.6453-74. DOI: 10.5194/nhessd-2-6453-2014.

Bossi, G. et al., 2015. The Rotolon Catchment Early-Warning System. *Engineering Geology for Society and Territory*, 3, DOI: 10.1007/978-3-319-09054-2.

Bull, W.B., 1964. *Alluvial fans and near-surface subsidence in Western Fresno County, California*. U.S. Geological Survey Professional Paper 437-A. Denver, CO: U.S. Geological Survey.

Canelli, L., Ferrero, A.M., Migliazza, M. & Segalini, A., 2012. Debris flow risk mitigation by the means of rigid and flexible barriers – experimental tests and impact analysis. *Natural Hazards and Earth System Sciences*, 12(5), pp.1693-99.

Capparelli, G. & Versace, P., 2011. FLaIR and SUSHI: two mathematical models for early warning of landslides induced by rainfal. *Landslides*, 8, pp.67-79. DOI: 10.1007/s10346-010-0228-6.

Cascini, L. et al., 2012. Modeling of propagation and entrainment phenomena for landslides of the flow type: the May 1998 case study. *Landslides and Engineered Slopes: Protecting Society through Improved Understanding. Proceedings of the 11th International & 2nd North American Symposium on Landslides*, 38.

Cavalli, M. & Tarolli, P., 2011. Application of lidar technology for rivers analysis. *Italian Journal of Engineering Geology and Environment*, Special Issue(1), pp.33-44. DOI: 10.4408/IJEGE.2011-01.S-03.

Chambon, G., Ghemmour, A. & Naaim, M., 2014. Experimental investigation of viscoplastic free-surface flows in a steady uniform regime. *Journal of Fluid Mechanics*, 754, pp.332-64.

Chen, C.-L., 1988. Generalized viscoplastic modeling of debris flow. *Journal of hydraulic engineering*, 114(3), pp.237-58.

Chen, C.L., 1988. Generalized viscoplastic modeling of debris flow. *Journal of hydraulic engineering*, 114(3), pp.237-58.

Chen, H.G., Crosta, G.B. & Lee, C.F., 2006. Erosional Effects on runout of fast landslides, debris flows and avalanches: a numerical investigation. *Geotechnique*, 56(5), pp.305-22.

Chen, H. & Lee, C.F., 2002. Runout analysis of slurry flows with Bingham model. *Journal of Geotechnical and Geoenvironmental Engineering*, 128(12), pp.1032-42.

Chen, H. & Lee, F., 2003. A dynamic model for rainfall-induced landslides on natural slopes. *Geomorphology* , 51(4), pp.269-88.

Chen, C.-l. & Ling, C.-H., 1996. Granular-flow rheology: role of shear-rate number in transition regime. *Journal of engineering mechanics*, 122(5), pp.469-80.

Christen, M., Kowalski, J. & Bartelt, P., 2010. RAMMS: numerical simulation of dense snow avalanches in three-dimensional terrain. *Cold Regions Science and Technology*, 63(1), pp.1-14.

Cleary, P.W. & Prakash, M., 2004. Discrete-element modelling and smoothed particle hydrodynamics: potential in the environmental sciences. *The Royal Society*, 362, pp.2003–30. DOI: 10.1098/rsta.2004.1428.

Cochard, S. & Ancey, C., 2009. Experimental investigation of the spreading of viscoplastic fluids on inclined planes. *Journal of Non-Newtonian Fluid Mechanics*, 158(1-3), pp.73-84.

Cola, S. et al., 2015. Applicability of two propagation models to simulate the Rotolon earth-flow occurred in November 2010. In *Engineering Geology for Society and Territory-Volume 2*., 2015. Springer International Publishing.

Cola, S., Calabrò, N., Simonini, P. & Pastor, M., 2011. Effects of Grain-Size Composition Examined in Laboratory and Numerical Tests on Artificial Mud-Flows. In *The Second World Landslide Forum*., 2011. Springer-Verlag Berlin Heidelberg 2013.

Costa, J., 1984. Physical geomorphology of debris flows. In *Developments and applications of geomorphology*. Springer Berlin Heidelberg. pp.268-317.

Coussot, P. et al., 1998. Direct determination of rheological characteristics of debris flow. *Journal of hydraulic engineering*, 124(8), pp.865-68.

Coussot, P. & Meunier, M., 1996. Recognition, classification and mechanical description of debris flows. *Earth-Science Reviews*, 40(3), pp.209-27.

Coussot, P. & Piau, J.M., 1994. On the behavior of fine mud suspensions. *Rheologica acta*, 33(3), pp.175-84.

Coussot, P. & Piau, J.M., 1995. A large-scale field coaxial cylinder rheometer for the study of the rheology of natural coarse suspensions. *Journal of Rheology*, 39(1), pp.105-24.

Coussot, P., Raynaud, J.S. & Ancey, C., 2003. Combined MRI-rheometry determination of the behavior of mud suspensions. *Debris Flow Mechanics and Mitigation Conference, Mills Press, Davos*, pp.291-301.

Crosta, G.B., Chen, H. & Frattini, P., 2006. Forecasting hazard scenarios and implications for the evaluation of countermeasure efficiency for large debris avalanches. *Engineering Geology*, 83(1), pp.236-53.

Cruden, D.M. & Vernes, D.J., 1996. Landslides: investigation and mitigation. Chapter 3-Landslide types and processes. *Transportation research board special report 247*, pp.36-75.

D'Agostino, V., Cesca, M. & Marchi, L., 2010. Field and laboratory investigations of runout distances of debris flows in the Dolomites (Eastern Italian Alps). *Geomorphology*, 115(3), pp.294-304.

Davidson, M.R., Hasan Khan, N. & Leong Yeow, Y., 2000. Collapse of a cylinder of Bingham fluid. *ANZIAM Journal*, 42, pp.499-517.

De Zanche, V. & Mietto, P., 1981. Review of the Triassic sequence of Recoaro (Italy) and related problems. Padova, 1981. Rend. Soc. Geol. It.

DeNatale, J.S. et al., 1999. Experimental testing of flexible barriers for containment of debris flows. *US Geolological Survey - Open File Report 99-205*, pp.1-38.

Dzuy, N.Q. & Boger, D.V., 1983. Yield stress measurement for concentrated suspensions. *Journal of Rheology*, 27(4), pp.321-49.

Egashira, S., Honda, N. & Itoh, T., 2001. Experimental Study on the Entrainment of Bed Material into Debris Flow. *Phys. Chem. Earth*, 26(9), pp.645-50.

Einstein, A., 1956. *Investigations on the Theory of the Brownian Movement*. Dover, New York: Courier Corporation.

Evensen, G., 2003. The Ensemble Kalman Filter: theoretical formulation and practical implementation. *Ocean Dynamics*, 53(4), pp.343-67. DOI: 10.1007/s10236-003-0036-9.

Frigerio, S. et al., 2014. A web-based platform for automatic and continuous landslide monitoring: The Rotolon (Eastern Italian Alps) case study. *Computers & Geosciences*, 63, pp.96-105. DOI: 10.1016/j.cageo.2013.10.015.

Gabrieli, F., 2009. *L'approccio particellare per la modellazione numerica dell'innesco di instabilità di versante in terreni granulari*. Università degli Studi di Padova.

Gabrieli, F., Artoni, R., Santomaso, A. & Cola, S., 2013. Discrete particle simulations and experiments on the collapse of wet granular columns. *Physics of fluids 25 103303*.

Gingold, R. & Monaghan, J.J., 1977. Smoothed particle hydrodynamics: theory and application to non-spherical stars. *Monthly notices of the royal astronomical society*, 181(3), pp.375-89.

Govier, G.W. & Aziz, K., 2008. The flow of complex mixtures in pipes. *New Orleans: Society of Petroleum Engineers*.

Guzzetti, F., Peruccacci, S., Rossi, M. & Stark , C.P., 2008. The rainfall intensity-duration control of shallow landslides and debris-flow: an update. *Landslides*, 5(1), pp.3-17. DOI: 10.1007/s10346-007-0112-1.

Haas, T. et al., 2015. Effects of debris flow composition on runout, depositional mechanisms, and deposit morphology in laboratory experiments. *Journal of Geophysical Research: Earth Surface*, 120(9), pp.1949-72.

Herschel, W.H. & Bulkley, R., 1926. Measurement of consistency as applied to rubber-benzene solutions. *Am. Soc. Test Proc.*, 26(2), pp.621-33.

Huang, X. & Garcia, M.H., 1998. A Herschel-Bulkley model for mud flow down a slope. *Journal of fluid mechanics*, 374, pp.305-33.

Hungr, O., 1995. A model for the runout analysis of rapid flow slides, debris flows, and avalanches. *Canadian Geotechnical Journal*, 32(4), pp.610-23. DOI: 10.1139/t95-063.

Hungr, O. & Evans, S.G., 1996. Rock avalanche runout prediction using a dynamic model. *Proceedings of the 7th International Symposium on Landslides, Trondheim, Norway*, 1.

Hungr, O., Evans, S.G., Bovis, M.J. & Hutchinson, J.N., 2001. Review of the classification of landslides of the flow type. *Environmental & Enineering Geoscience*, VII(3), pp.221-38.

Hungr, O., Leroueil, S. & Picarelli, L., 2014. The Varnes classification of landslide types, an update. *Landslides*, 11(2), pp.167-94.

Hungr, O. & McDougall, S., 2009. Two numerical models for landslide dynamic analysis. *Computers & Geosciences*, 35(5), pp.978-92.

Hungr, O., McDougall, S. & Bovis, M., 2005. Entrainment of material by debris flows. In *Debris-flow Hazards and Related Phenomena*. Springer Berlin Heidelberg. pp.135-58.

Hungr, O., Morgan, G.C. & Kellerhals, R., 1984. Quantitative analysis of debris torrent hazards for design of remedial measures. *Canadian Geotechnical Journal*, 21(4), pp.663-77.

Hungr, O. & Morgenstern, N.R., 1984. Experiments on the flow behaviour of granular materials at high velocity in an open channel. *Geotechnique*, 34(3), pp.405-13.

Hürlimann, M., McArdell, B.W. & Rickli, C., 2015. Field and laboratory analysis of the runout characteristics of hillslope debris flows in Switzerland. *Geomorphology*, 232, pp.20-32.

Hutchinson, J.N., 1988. General report: morphological and geotechnical parameters landslides in relation to geology and hydrogeology. In *Proceedings of the 5th International Symposium on Landslides*. Lausanne, 1988.

Imran, J., Parker, G., Locat, J. & Lee, H., 2001. 1D numerical model of muddy subaqueous and subaerial debris flows. *Journal of hydraulic engineering*, 127(11), pp.959-68.

Iverson, R.M., 1997. The physics of debris flows. *Reviews of Geophysics*, 35(3), p.245. DOI: 10.1029/97RG00426.

Iverson, R.M., 2012. Elementary theory of bed-sediment entrainment by debris flows and avalanches. *Journal of Geophysical Research: Earth Surface*, 117(F3).

Iverson, R.M., 2015. Scaling and design of landslide and debris-flow experiments. *Geomorphology*, 244, pp.9-20.

Iverson, R. & Denlinger, R., 2001. Flow of variably fluidized granular masses across three-dimensional terrain: 1. Coulomb mixture theory. *Journal of Geophysical Research: Solid Earth*, 106(B1), pp.537-52.

Iverson, R.M., Logan, M. & Denlinger, R.P., 2004. Granular avalanches across irregular three-dimensional terrain: 2. Experimental tests. *Journal of Geophysical Research: Earth Surface*, 109(F1), pp.1-16.

Iverson, R.M., Logan, M., LaHusen, R.G. & Berti, M., 2010. The perfect debris flow? Aggregated results from 28 large-scale experiments. *Journal of Geophysical Research*, 115.

Jan, C.-D. & Shen, H.W., 1997. Review dynamic modeling of debris flows. In *Recent Developments on Debris Flows*. Springer Berlin Heidelberg. pp.93-116.

Johnson, A.M., 1965. A model for debris flow. *Ph.D Thesys at the Pennsylvania State University*.

Johnson, A.M., 1970. *Physical processes in geology;: A method for interpretation of natural phenomena; intrusions in igneous rocks, fractures, and folds, flow of debris and ice*. University of Minnesota: Freeman, Cooper.

Johnson, C.G. et al., 2012. Grain-size segregation and levee formation in geophysical mass flows. *Journal of Geophysical Research: Earth Surface*, 117(F1).

Julien, P.Y. & Lan, Y., 1991. Rheology of hyperconcentrations. *Journal of Hydraulic Engineering*, 117(3), pp.346-53.

Julien, P.Y. & Leòn, C.A., 2000. Mud floods, mudflows and debris flows classification, rheology and structural design. In *Proc., Int Workshop on the Debris Flow Disaster of December 1999 in Venezuela*. Universidad Central de Venezuela, Caracas, Venezuela, 2000.

Kaitna, R., Rickenmann, D. & Schatzmann, M., 2007. Experimental study on rheologic behaviour of debris flow material. *Acta Geotechnica*, 2(2), pp.71-85.

Kang, Z. & Zhang, S., 1980. A preliminary analysis of the characteristics of debris flow. *Proc. int. symp. river sed., Beijing, China*, 1, pp.213-26.

Keefer, D.K. & Johnson, A.M., 1983. *Earthflows: morphology, mobilization and movement*. USGS Professional Paper 1264.

Körner, H.J., 1976. Reichweite und Geschwindigkeit von Bergstürzen und Fließschneelawinen. *Rock mechanics*, 8(4), pp.225-56.

Krieger, I.M. & Dougherty, T.J., 1959. A mechanism for non-Newtonian flow in suspensions of rigid spheres. *Transactions of the Society of Rheology*, 3, pp.111-36.

Krone, R.B., 1986. The significance of aggregate properties to transport processes. In *Estuarine cohesive sediment dynamics*. New York: Springer. pp.66-84.

Lacasse, S. & Nadim, F., 2009. Landslide risk assessment and mitigation strategy. *Landslides - Disaster Risk Reduction*, pp.31-62. DOI: 10.1007/978-3-540-69970-5_3.

Laigle, D. & Coussot, P., 1997. Numerical modeling of mudflows. *Journal of Hydraulic Engineering*, 123(7), pp.617-23.

Lajeunesse, E., Mangeney-Castelnau, A. & Vilotte, J.P., 2004. Spreading of a granular mass on a horizontal plane. *Physics of Fluids*, 16(7), pp.2371-81.

Larcher, M., Fraccarollo, L., Armanini, A. & Capart, H., 2007. Set of measurement data from flume experiments on steady uniform debris flows. *Journal of Hydraulic Research*, 45.sup1, pp.59-71.

Larsen, I.J., Montgomery, D.R. & Korup, O., 2010. Landslide erosion controlled by hillslope material. *Nature Geoscience*, 3(4), pp.247-51.

Liu, G.R. & Liu, M.B., 2003. *Smoothed Particle Hydrodynamics: a meshfree particle method*. World Scientific.

Liu, M.B. & Liu, G.R., 2010. Smoothed Particle Hydrodynamics (SPH): an Overview and Recent Developments. *Archives of Computational Methods in Engineering*, 17(1), pp.25–76. DOI: 10.1007/s11831-010-9040-7.

Mainali, A. & Rajaratnam, N., 1994. Experimental study of debris flows. *J. Hydraul. Eng.*, 230(2), pp.104-23.

Major, J.J., 1997. Depositional Processes in Large-Scale Debris-Flow Experiments. *Journal of Geology*, 105(3), pp.345-66.

Major, J.J. & Pierson, T.C., 1992. Debris Flow Rheology' Experimental Analysis of Fine-Grained Slurries. *Water resources research*, 28(3), pp.841-53.

Mangeney-Castelnau, A. et al., 2003. Numerical modeling of avalanches based on Saint Venant equations using a kinetic scheme. *Journal of Geophysical Research: Solid Earth*, 108(B1).

Manzanal, D. et al., 2016. Application of a New Rheological Model to Rock Avalanches: An SPH Approach. *Rock Mechanics and Rock Engineering*, 49(6), pp.2353-72.

Marchetti, M., 2000. *Geomorfologia fluviale*. Pitagora ed.

McDougall, S. & Hungr, O., 2004. A model for the analysis of rapid landslide motion across three-dimensional terrain. *Canadian Geotechnical Journal*, 41(6), pp.1084-97. DOI: 10.1139/t04-052.

McDougall, S. & Hungr, O., 2005. Dynamic modelling of entrainment in rapid landslides. *Canadian Geotechnical Journal*, 42(5), pp.1437-48. DOI: 10.1139/t05-064.

McTigue, D.F., 1982. A nonlinear constitutive model for granular materials: application to gravity flow. *Journal of Applied Mechanics*, 49(2), pp.291-96.

Medina, V., Hürlimann, & Bateman, A., 2008. Application of FLATModel, a 2D finite volume code, to debris flows in the northeastern part of the Iberian Peninsula. *Landslides*, 5(1), pp.127-42.

Monaghan, J.J., 1992. Smoothed particle hydrodynamics. *Annual Review of Astronomy and Astrophysics*, 30, pp.543-74. DOI: 10.1146/annurev.aa.30.090192.002551.

Monaghan, J.J. & Gingold, R.A., 1983. Shock simulation by the particle method SPH. *Journal of computational physics*, 52(2), pp.374-89.

Monaghan, J.J. & Lattanzio, J.J., 1985. A refined particle method for astrophysical problems. *Astronomy and astrophysics*, 149, pp.135-43.

Morgenstern, N.R., 1992. The evaluation of slope stability: a 25 year perspective. *Stability and performance of slopes and embankments, ASCE Geotechnical Special Publication 31*, 1, pp.1-26.

O'Brien, J.S. & Julien, P.Y., 1985. Physical properties and mechanics of hyperconcentrated sediment flows. *Proc. ASCE HD Delineation of landslides, flash flood and debris flow Hazards*.

O'Brien, J.S. & Julien, P.Y., 1988. Laboratory analysis of mudflow properties. *Journal of hydraulic engineering*, 114(8), pp.877-87.

O'brien, J.S., Julien, P.Y. & Fullerton, W.T., 1993. Two-dimensional water flood and mudflow simulation. *Journal of hydraulic engineering*, 119(2), pp.244-61.

Parsons, J.D., Whipple, K.X. & Simoni, A., 2001. Experimental study of the grain-flow, fluid-mud transition in debris flows. *The Journal of Geology*, 109(4), pp.427-47.

Pastor, M. et al., 2014. Application of a SPH depth-integrated model to landslide run-out analysis. *Landslides*, 11, pp.793-812. DOI: 10.1007/s10346-014-0484-y.

Pastor, M. et al., 2008. A depth-integrated, coupled SPH model for flow-like landslides and related phenomena. *International Journal for Numerical and Analytical Methods in Geomechanics*, 33(2), pp.143-72. DOI: 10.1002/nag.705.

Pastor, M. et al., 2004. Modelling of landslides (II) propagation. In V.I. Darve F, ed. *Degradation and Instabilities in Geomaterials*. New York: Springer Wien. pp.319-67.

Pirulli, M., 2005. *Numerical modelling of landslide runout, a continuum mechanics approach*. Ph.D. Degree in Geotechnical Engineering, Politecnico di Torino (Italy).

Pirulli, M. & Mangeney, A., 2008. Results of back-analysis of the propagation of rock avalanches as a function of the assumed rheology. *Rock Mechanics and Rock Engineering*, 41(1), pp.59-84.

Pirulli, M. & Pastor, M., 2012. Numerical study on the entrainment of bed material into rapid landslides. *Geotechnique*, 62(11), pp.959-72. DOI: 10.1680/geot.10.P.074.

Pirulli, M. & Sorbino, G., 2008. Assessing potential debris flow runout: a comparison of two simulation models. *Natural Hazard and Earth System Sciences*, 8(4), pp.961-71. DOI: 10.5194/nhess-8-961-2008.

Pitman, B.E. & Le, L., 2005. A two-fluid model for avalanche and debris flows. *Philosophical Transactions of the Royal Society of London A: Mathematical, Physical and Engineering Sciences*, 363(1832), pp.1573-601.

Pudasaini, S.P., 2012. A general two-phase debris flow model. *Journal of Geophysical Research: Earth Surface*, 117(F3).

Pudasaini, S., Wang, Y. & Hutter, K., 2005. Modelling debris flows down general channels. *Natural Hazards and Earth System Science*, 5(6), pp.799-819.

Pudasaini, S.P., Wang, Y. & Hutter, K., 2005. Modelling debris flows down general channels. *Natural Hazards and Earth System Science*, 5(6), pp.799-819. DOI: 10.5194/nhess-5-799-2005.

Quan Luna, B. et al., 2011. The application of numerical debris flow modelling for the generation of physical vulnerability curves. *Natural Hazard and Earth System Sciences*, 11, pp.2047-60. DOI: 10.5194/nhess-11-2047-2011.

Revellino, P., Hungr, O., Guadagno, F.M. & Evans, S.G., 2004. Velocity and runout simulation of destructive debris flows and debris avalanches in pyroclastic deposits, Campania region, Italy. *Environmental Geology*, 45, pp.295-311. DOI: 10.1007/s00254-003-0885-z.

Rosatti, G. & Begnudelli, L., 2013. Two-dimensional simulation of debris flows over mobile bed: Enhancing the TRENT2D model by using a well-balanced Generalized Roe-type solver. *Computers & Fluids*, 71, pp.179-95.

Salm, B., 1966. Contribution to avalanche dynamics. In *Proceedings of International Symposium on Scientific Aspects of Snow and Ice Avalanches*. IAHS, Christchurch (New Zeland), 1966.

Savage, S.B. & Hutter, K., 1989. The motion of a finite mass of granular material down a rough incline. *Journal of fluid mechanics*, 199, pp.177-215.

Savage, S.B. & Hutter, K., 1991. The dynamics of avalanches of granular materials from initiation to runout. Part I: Analysis. *Acta Mechanica*, 86(1-4), pp.201-23.

Schädler, W. et al., 2014. Geomechanical assessment of the Corvara earthflow through numerical modelling and inverse analysis. *Landslides*, DOI: 10.1007/s10346-014-0498-5.

Schatzmann, M. et al., 2009. Schatzmann, M., Bezzola, G. R., Minor, H. E., Windhab, E. J., & Fischer, P. (2009). Rheometry for large-particulated fluids: analysis of the ball measuring system and comparison to debris flow rheometry. *Rheologica Acta*, 48(7), pp.715-33.

Schatzmann, M., Fischer, P. & Bezzola, G.R., 2003. Rheological behavior of fine and large particle suspensions. *Journal of Hydraulic Engineering*, 129(10), pp.796-803.

Sharpe, C.F.S., 1938. *Landslides and related phenomena*. NY: Columbia University Press.

Simonett, D., 1967. Landform Studies from Australia and New Guinea. In *Australian National Univ. Press*. Jennings, J. N. & Mabbutt, J. A. pp.64-84.

Skempton, A.W. & Hutchinson, J., 1969. Stability of natural slopes and embankment foundations. *Proceedings, 7th. International conference of soil mechanics and foundation engineering, Mexico, State of the Art volume*, pp.291-340.

Sosio, R., Crosta, G. & Hungr, O., 2008. Complete dynamic modeling calibration for the Thurwieser rock avalanche (Italian Central Alps). *Engineering Geology*, 100(1-2), pp.11-26. DOI: 10.1016/j.enggeo.2008.02.012.

Swanston, D.N., 1974. *Slope stability problems associated with timber harvesting in mountainous regions of the Southwestern United States*. Forest Service General Technical Report PNW-021. Washington, DC: U. S. Department of U. S. Department of Agriculture.

Takahashi, T., 1978. Mechanical characteristics of debris flow. *Journal of the Hydraulics Division*, 104(8), pp.1153-69.

Takahashi, T., 1980. Debris flow on prismatic open channel. *Journal of the Hydraulics Division*, 106(3), pp.381-96.

Takahashi, T., 1991. Debris flow. *International Association for Hydraulic Research, Balkema, Rotterdam*.

Takahashi, T., 2014. *Debris Flow: Mechanics, Prediction and Countermeasures*. 2nd ed.

Takahashi, T. & Kuang, S.F., 1986. Formation of debris flow on varied slope bed. *Annuals, Disas. Prev. Res. Inst., Kyoto University*, 29B(2), pp.343-59.

Tang, C. et al., 2012. Catastrophic debris flows on 13 August 2010 in the Qingping area, southwestern China: the combined effects of a strong earthquake and subsequent rainstorms. *Geomorphology*, 139, pp.559-76.

Trivelli, G., 1991. *Storia del territorio e delle genti di Recoaro*. Novara: Istituto Geografico De Agostini [in Italian].

Varnes, D.J., 1954. Landslide types and processes. *Highway research board special report 29*, pp.20-47.

Varnes, D.J., 1978. Slope movement types and processes. *Transportation Research Board Special Report 176*, pp.11-33.

Voellmy, A., 1955. Über die Zerstörungskraft von Lawinen. *Schweiz Bauzeitung*, 73, pp.159-165, 212–217, 246–249, 280–285.

Wieczorek, G., 1987. Effect of rainfall intensity and duration on debris flows in central Santa Cruz Mountains, California. *Reviews in Engineering Geology*, 7, pp.93-104.

Willmott, C.J. & Matsuura, K., 2005. Advantages of the mean absolute error (MAE) over the root mean square error (RMSE) in assessing average model performance. *Climate research*, 30(1), pp.79-82.

Wu, Y.-H., Liu, K.-F. & Chen, Y.-C., 2013. Comparison between FLO-2D and Debris-2D on the application of assessment of granular debris flow hazards with case study. *Journal of Mountain Science*, 10(2), pp.293-304. DOI: 10.1007/s11629-013-2511-1.

Yano, K. & Daido, A., 1965. Fundamental study on mud-flow. *Bulletin od the Disaster Prevention Research Institute*, 14(2), pp.69-83.

Zhou, G.G.D. et al., 2015. Experimental study on the triggering mechanisms and kinematic properties of large debris flows in Wenjia Gully. *Engineering Geology*, 194, pp.52-61.

Zienkiewicz, O.C., 1982. Basic formulation of static and dynamic behaviour of soil and other porous media. *Numerical methods in geomechanics*, Springer Netherlands, pp.39-55.

Zienkiewicz, O.C. & Shiomi, T., 1984. Dynamic behaviour of saturated porous media; the generalized Biot formulation and its numerical solution. *International journal for numerical and analytical methods in geomechanics*, 8(1), pp.71-96.

APPENDIX

The Matlab codes written to automatically run the simulations are in this section reported.

1. FIRST MATLAB SCRIPT: IT PREPARES AND LAUNCHES THE SIMULATIONS.

```
%*********************************************************%
%*********************************************************%
% IT CREATES THE INPUT FILES WITH THE UPDATED PARAMETERS %
%        parameter generation, input file creation       %
%              launch of the simulations                 %
%*********************************************************%

clc
clear all
close all

prefix = 'can_';
root = 'D:/Documents/NumericalModel/Simulations';
root_py = 'D:\Documents\NumericalModel\Simulations';
disco = 'D';

start = 1;                  %  first simulation to run

% time parameters %
%-----------------------------%
DT = 0.001;                   % time step
T_tot = 3.1;                  % total time
ITER=(T_tot/DT)*200;          % max. num. of iterations
%-----------------------------%

% input files %
%-------------------------------------------------------------------%
filepts = [root,'/','StartingFiles','/',pref_old,'.pts'];         %
filetop = [root,'/','StartingFiles','/',pref_old,'.top'];         %
pastor = 'SPH_2014.exe';                                          %
fileexe = [root,'/','StartingFiles','/',pastor];                  %
%-------------------------------------------------------------------%

% output files, folder and variables %
%-------------------------------------------------------------------------%
output = 'Output';                                                  % Output
folder
FileOutput = 'FileOutput';                                        %
parameter_txt=[root,'/',output,'/','parameter.txt'];                % parameters
file
resul=[root,'/',output,'/','results','.txt'];                       % results
matrix
```

```
resul_all_er=[root,'/',output,'/','resultsALL_er','.txt'];          % erosion -
results matrix
resul_all_hs=[root,'/',output,'/','resultsALL_Hs','.txt'];          % heights -
results matrix
matrix=[root,'/',output,'/','matrix','.txt'];                       % results
matrix + param. matrix
valut_all=[root,'/',output,'/performance_all.txt'];                 %
performance indices matrix
valut=[root,'/',output,'/performance.txt'];                         %
performance indices matrix
%--------------------------------------------------------------------%


%----------------------------%
%%% parameters generation   %%%
%----------------------------%

dens=1400;      % mixture density

% Bingham rheology ------
Tau_min=10;     % [Pa]
Tau_max=200;    % [Pa]
Mu_min=0.05;    % [Pa*s]
Mu_max=15;      % [Pa*s]
Nn=20;          % number of parameters (in total N*N simulations)

% Voellmy rheology ------
X_min= 10;     % [m*s^-2]
X_max= 1000;   % [m*s^-2]
fi_min= 0.01;
fi_max= 0.5;

% PARAM=GeneraParamEGU(Tau_min,Tau_max,Mu_min,Mu_max,Nn); % if Bingham
PARAM=GeneraParamEGU(X_min,X_max,fi_min,fi_max,Nn);     % if Voellmy
num_sim =Nn*Nn;                %  number of simulations

mkdir([root,'/Figures']);

h=figure('visible','off');
for i=1:2
    subplot(2,1,i)
    hist(PARAM(i,:),num_sim);
    xlabel('value')
    ylabel('frequency')
    if i==1
        title(['\tau','_0'])
    else if i==2
            title('\mu')
        end
    end
```

```
end
saveas(h,[root,'/Figures/','GaussParam_prior'])
saveas(h,[root,'/Figures/','GaussParam_prior.jpg'])
pause(5);

mkdir([root,'/',output]);       % output folder creation
dlmwrite(parameter_txt, PARAM, 'delimiter', '\t','precision', '%.8f','newline',
'pc');
mkdir([root,'/',FileOutput]);   % txt output folder creation
% mkdir([root,'/KalmanElab']);  % folder for data assimilation, if included


%-----------------------------------------%
%%%         input files creation          %%%
%-----------------------------------------%

%---% file dat for 2014 SPH-code
tic
for j = start:num_sim

    mkdir([root_py,'/Simulations/',prefix,num2str(j,'%03d'),'/','Pastor']);
% folders rot001-rot002.../Pastor creation

    filedatnew =
[root,'/Simulations/',prefix,num2str(j,'%03d'),'/','Pastor','/',prefix,num2str(j,
'%03d'),'.dat'];
    out = fopen(filedatnew,'w');

    %     A=[9.81,dens,0,0,4,PARAM(1,j),PARAM(2,j),0,0.3,0.001,0,0.03,0,0,0.001];
% if Bingham
    B=[9.81,dens,PARAM(1,j),0,7,0,0,0,PARAM(2,j),0.001,0,PARAM(2,j),0,0,0.001];
% if Voellmy

    fprintf(out,'%i\r\n',1);
    fprintf(out,'%s\r\n',[prefix,num2str(j,'%03d')]);
    fprintf(out,'%s\r\n','ic_SW_Alg  0 landslides');
    fprintf(out,'      %i\r\n',0);
    fprintf(out,'%s\r\n','nhist');
    fprintf(out,'      %i\r\n',0);
    fprintf(out,'%s\r\n','ndim');
    fprintf(out,'      %i\r\n',2);
    fprintf(out,'%s\r\n',' ic_soil  ic_water  ic_vps  ic_abs');
    fprintf(out,'   %i         %i       %i       %i\r\n',[1,0,0,3]);
    fprintf(out,'%s\r\n','Soil unkno  h_inf_SW');
    fprintf(out,'   %i        %f\r\n',[6,0.001]);
    fprintf(out,'%s\r\n','pts file name');
    fprintf(out,'%s\r\n',[prefix,num2str(j,'%03d')]);

    fprintf(out,'%s\r\n','narcs   nsegs info for Vn0');
    fprintf(out,'   %i        %i\r\n',[0,4]);
```

```
    fprintf(out,'%s\r\n','  seg 1  x0  y0  xf  yf  //+ ds  Zext(useless)');
    fprintf(out,'%s\r\n','          0.   0.345   2.56   0.345  ');
    fprintf(out,'%s\r\n','          0.002  10 ');
    fprintf(out,'%s\r\n','  seg 2  x0  y0  xf  yf  //+ ds  Zext(useless)');
    fprintf(out,'%s\r\n','          0.   0.515  2.56   0.515');
    fprintf(out,'%s\r\n','          0.002  10 ');
    %     fprintf(out,'%s\r\n','  seg 3  x0  y0  xf  yf  //+ ds  Zext(useless)');
    %     fprintf(out,'%s\r\n','          2.55   0.0  2.56   0.36');
    %     fprintf(out,'%s\r\n','          0.002  10 ');
    %     fprintf(out,'%s\r\n','  seg 4  x0  y0  xf  yf  //+ ds  Zext(useless)');
    %     fprintf(out,'%s\r\n','          2.55   0.5  2.56   0.82');
    %     fprintf(out,'%s\r\n','          0.002  10 ');
    fprintf(out,'%s\r\n','  seg 5  x0  y0  xf  yf  //+ ds  Zext(useless)');
    fprintf(out,'%s\r\n','          0.   0.0   4.04   0.0  ');
    fprintf(out,'%s\r\n','          0.002  10 ');
    fprintf(out,'%s\r\n','  seg 6  x0  y0  xf  yf  //+ ds  Zext(useless)');
    fprintf(out,'%s\r\n','          0.   0.82  4.04   0.82');
    fprintf(out,'%s\r\n','          0.002  10 ');

    fprintf(out,'%s\r\n','pa_sph,  nnps, sle, skf');
    fprintf(out,'   %i         %i       %i       %i\r\n',[2,2,2,1]);
    fprintf(out,'%s\r\n',' sum_den,  av_vel, virt_part , nor_dens  ');
    fprintf(out,'%s\r\n','    T         T      F            F       ');

    fprintf(out,'%s\r\n',' grav   dens   turb    eros    reologia     Tauy0   mu
visco   tanfi8  hfrict0    c11   tanfi0   .Bfact     14..   15..Comp  end  ');
    %     fprintf(out,'%4.2f   %6.1f %6.1f    %g      %g        %4.4f %4.4f
%2.1f   %4.2f   %g   %2.1f   %4.2f   %2.1f   %2.1f   %g\r\n',A);    % con Bingham
    fprintf(out,'%4.2f   %6.1f %6.1f    %g      %g        %4.4f %4.4f   %2.1f
%4.2f   %g   %2.1f   %4.2f   %2.1f   %2.1f   %g\r\n',B);    % con Voellmy
    fprintf(out,'%s\r\n','K0 activated?');                  % if Voellmy
    fprintf(out,'  %i\r\n',0);                              % if Voellmy
    fprintf(out,'%s\r\n',' icpwp ');
    fprintf(out,'  %i\r\n',0);
    fprintf(out,'%s\r\n','coarse mesh saving utility?');
    fprintf(out,'  %i\r\n',0);
    fprintf(out,'%s\r\n','control points?');
    fprintf(out,'  %i\r\n',0);
    fprintf(out,'%s\r\n','GID filter   1.hs  2.disp 3.v  4.Pw  5 eros   6.Z
7.hrel  8.hw  9.eta  10.hs+hw  11.dumm   12.dumm');
    fprintf(out,'%s\r\n','               1      1     1    0      0       0     0
0      0      0      0          0         0');
    fprintf(out,'%s\r\n','T_change_to_W');
    fprintf(out,'%s\r\n','  1.e+12 ');

    fclose(out);
end

%---% file MASTER.dat  for 2014 SPH-code
tic
```

```
for j = start:num_sim

    filemasterdatnew =
[root,'/Simulations/',prefix,num2str(j,'%03d'),'/','Pastor','/',prefix,num2str(j,
'%03d'),'.MASTER.dat'];
    out = fopen(filemasterdatnew,'w');

    fprintf(out,'%i\r\n',1);
    fprintf(out,'%s\r\n',[prefix,num2str(j,'%03d')]);
    fprintf(out,'%s\r\n','if_sph if_gfl if_tgf');
    fprintf(out,'   %i       %i       %i\r\n',[1,0,0]);
    fprintf(out,'%s\r\n','SPH_problem_type   SPH_t_integ_Alg');
    fprintf(out,'   %i        %i\r\n',[1,4]);
    fprintf(out,'%s\r\n','sph problem name');
    fprintf(out,'%s\r\n',[prefix,num2str(j,'%03d')]);
    fprintf(out,'%s\r\n','dt      time_end   maxtimesteps');
    fprintf(out,'%g     %g    %g\r\n',[DT,T_tot,ITER]);
    fprintf(out,'%s\r\n','print_step   save_step  plot_step');
    fprintf(out,'  %i    %i    %i\r\n',[50,50,50]);
    fprintf(out,'%s\r\n','dt_sph  ic_adapt   ');
    fprintf(out,'   %f        %i\r\n',[0.001,1]);
    fprintf(out,'%s\r\n','Ntime curves     max pts in them');
    fprintf(out,'   %i        %i\r\n',[0,6]);
    fprintf(out,'%s\r\n','dt      time_end   maxtimesteps');
    fprintf(out,'%i     %g    %g\r\n',[-1,T_tot,ITER]);
end

dat=toc;
disp(['time for file .dat is ',num2str(dat)])
tic

%---% file top for 2014 SPH-code

for j = start:num_sim
    filetopnew =
[root,'/Simulations/',prefix,num2str(j,'%03d'),'/','Pastor','/',prefix,num2str(j,
'%03d'),'.top'];
    copyfile(filetop,filetopnew);
end
fclose ('all');


top=toc;
disp(['time for file .top is ',num2str(top)])
tic

%---% file pts , file exe  for 2014 SPH-code

for j = start:num_sim
```

```
    fileptsnew =
[root,'/Simulations/',prefix,num2str(j,'%03d'),'/','Pastor','/',prefix,num2str(j,
'%03d'),'.pts'];
    copyfile(filepts,fileptsnew)

    fileexenew =
[root,'/Simulations/',prefix,num2str(j,'%03d'),'/','Pastor','/',pastor];
    copyfile(fileexe,fileexenew)
end
fclose ('all');

ptsexe=toc;
disp(['time for file .pts & .exe is ',num2str(ptsexe)])
tic

fclose ('all');


%-------------------------------------------------------%
%%%        script for running the simulations       %%%
%-------------------------------------------------------%

for z = start:num_sim
    fileau3new =
[root,'/Simulations/',prefix,num2str(z,'%03d'),'/','esegui',num2str(z,'%03d'),'_f
ortran.au3'];
    out = fopen(fileau3new,'w');

    fprintf(out,'%s\r\n','run ("cmd")');
    fprintf(out,'%s\r\n','Sleep(500)');
    fprintf(out,'%s\r\n','send ("{ENTER}")');
    fprintf(out,'%s\r\n','Sleep(500)');
    fprintf(out,'%s\r\n',['send ("',disco,':")']);
    fprintf(out,'%s\r\n','Sleep(500)');
    fprintf(out,'%s\r\n','send ("{ENTER}")');
    fprintf(out,'%s\r\n','Sleep(1000)');
    fprintf(out,'%s\r\n',['send ("cd
',root_py,'\Simulations\',prefix,num2str(z,'%03d'),'\','Pastor','")']);
    fprintf(out,'%s\r\n','Sleep(500)');
    fprintf(out,'%s\r\n','send ("{ENTER}")');
    fprintf(out,'%s\r\n','Sleep(1000)');
    fprintf(out,'%s\r\n',['send
("',root_py,'\Simulations\',prefix,num2str(z,'%03d'),'\','Pastor','\',pastor,'")'
]);
    fprintf(out,'%s\r\n','Sleep(500)');
    fprintf(out,'%s\r\n','send ("{ENTER}")');
    fprintf(out,'%s\r\n','Sleep(1000)');

    fprintf(out,'%s\r\n',['send ("',prefix,num2str(z,'%03d'),'")']);
    fprintf(out,'%s\r\n','Sleep(1000)');
```

```
    fprintf(out,'%s\r\n','send ("{ENTER}")');
    fprintf(out,'%s\r\n','Sleep(2000)');

    fprintf(out,'%s\r\n',['send ("',prefix,num2str(z,'%03d'),'")']);
    fprintf(out,'%s\r\n','Sleep(1000)');
    fprintf(out,'%s\r\n','send ("{ENTER}")');
    fprintf(out,'%s\r\n','Sleep(1000)');
    fclose(out);
end

fclose ('all');


script=toc;
disp(['time for file .au is ',num2str(script)])

clear h
save([root,'/variabili_1_parte','.mat']);



%-----------------------------------------%
%%%        simulations launcher          %%%
%-----------------------------------------%

% laser sensors position with GeneraMesh_canal_5.m for 2014 SPH-code
sensor1=69949;
sensor2=70014;
sensor3=70079;

% laboratory results for WKA mixtures
Coord_lab01=dlmread([root,'/StartingFiles','/lab_data_test_01.txt']); % test 01
[m]
Coord_lab02=dlmread([root,'/StartingFiles','/lab_data_test_02.txt']); % test 04
[m]
Coord_lab03=dlmread([root,'/StartingFiles','/lab_data_test_03.txt']); % test 03
[m]
Coord_lab04=dlmread([root,'/StartingFiles','/lab_data_test_04.txt']); % test 05
[m]
Coord_lab05=dlmread([root,'/StartingFiles','/lab_data_test_05.txt']); % test 06
[m]

SizePostRes = 190000000; % used for the pause between two groups of simulations

% variables to check the already performed simulations
for i=1:num_sim
    fileres=
[root,'/Simulations/',prefix,num2str(i,'%03d'),'/','Pastor','/',prefix,num2str(i,
'%03d'),'.post.res'];
    check(i,1)=i;
```

```
    if exist(fileres,'file')
        fileInfo=dir(fileres);
        fileSize = fileInfo.bytes;

        if fileSize>=SizePostRes
            check(i,2)=1;
            disp(i)
        else
            check(i,2)=0;
        end
    else
        check(i,2)=-1;
    end
end

control=zeros(num_sim,3);
mkdir([root,'/','Grafici']);         % graphs folder
mkdir([root,'/','FileOutput2']);     % txt folder

N=50; % number of simulations to run at the same time
k=0;  % counter

save([root,'/variabili_2_parte','.mat']);

% simulations launcher
pause(5);
for p = start:num_sim
    control(p,1)=p;
    if check(p,2)<=0.9

lanciaexe=[root_py,'\Simulations\',prefix,num2str(p,'%03d'),'\esegui',num2str(p,'
%03d'),'_fortran.au3'];

        system(lanciaexe);
        pause(5);

        if rem(p,N)==0
            k=k+1;
            if k>=2
                for i=p-2*N+1:p-N

postres=[root,'/Simulations/',prefix,num2str(i,'%03d'),'/','Pastor','/',prefix,nu
m2str(i,'%03d'),'.post.res'];
                    if exist(postres,'file')
                        try
                            disp(['extracting simulation num. ',num2str(i)])
                            Height_extract_gen16
(prefix,i,root,sensore1,sensore2,sensore3) % results extraction
                            control(i,2)=0;
```

```
                            disp(['OK!! completed the simulation n.
',num2str(i)])

                        catch
                            disp(['*** non è andato Height_extract_gen16 n.
',num2str(i)])
                            control(i,2)=1;
                        end
                    else
                        disp(['-->> non esiste post.res n. ',num2str(i)])
                        control(i,3)=1;
                    end
                end
                CL=clock;
                disp(['inizio pausa alle ore ',num2str(CL(4:5),'%2i:%2i')])
                pause(2*60);
            else
                CL=clock;
                disp(['inizio pausa alle ore ',num2str(CL(4:5),'%2i:%2i')])
                pause(10*60)
            end


fileres=[root,'/Simulations/',prefix,num2str(p,'%03d'),'/','Pastor','/',prefix,nu
m2str(p,'%03d'),'.post.res'];
            if exist(fileres,'file')
                for q=1:100
                    fileInfo=dir(fileres);
                    fileSize = fileInfo.bytes;
                    if fileSize<=SizePostRes
                        disp([num2str(q),' pausa prolungata di 5 minuti'])
                        pause(5*60)
                    else
                    end
                end

            end
            CL=clock;
            disp(['fine pausa alle ore ',num2str(CL(4:5),'%2i:%2i')])
        else

        end
    end
end

for i=num_sim-N+1:num_sim
    try
        disp(['extracting simulation num. ',num2str(i)])
        Height_extract_gen16 (prefix,i,root,sensore1,sensore2,sensore3)
        control(i,2)=0;
```

```
        disp(['OK!! completed the simulation n. ',num2str(i)])
    catch
        disp(['*** non è andato Height_extract n. ',num2str(i)])
        control(i,2)=1;
    end
end

% check of the performed simulations
for i=1:num_sim
    fileres=
[root,'/Simulations/',prefix,num2str(i,'%03d'),'/','Pastor','/',prefix,num2str(i,
'%03d'),'.post.res'];
    check(i,1)=i;
    if exist(fileres,'file')
        fileInfo=dir(fileres);
        fileSize = fileInfo.bytes;

        if fileSize>=SizePostRes
            check(i,2)=1;
            disp(i)
        else
            check(i,2)=0;
        end
    else
        check(i,2)=-1;
    end
end
```

2. SECOND MATLAB SCRIPT: IT ANALYZES THE SIMULATIONS RESULTS.

```
%*********************************************************%
%    IT ELABORATES THE OUTUT FILES OF THE SIMULATIONS    %
%       matrices construction, performance indices       %
%            best simulations identifications            %
%*********************************************************%

% Data in TIME
%-----------------------------------------------------------------

% to interpolate the simulated data on a given time grid
time=transpose(0:0.05:3); % time grid

p=1;
for j = start:num_sim
    disp(j)
    clear values_simul_time
    file_txt=[root,'/FileOutput/Sens_all_',num2str(j,'%03d'),'.txt'];
    file_txt_out=[root,'/FileOutput2/Sens_all_mod_',num2str(j,'%03d'),'.txt'];

    dati=dlmread(file_txt);
```

```
    f=dati(:,1);

    values_simul_time(:,1)=time;
    values_simul_time(:,2)=interp1(dati(:,1),dati(:,2),time);
    values_simul_time(:,3)=interp1(dati(:,1),dati(:,3),time);
    values_simul_time(:,4)=interp1(dati(:,1),dati(:,4),time);
    p=find(values_simul_time(:,2),1);

    dlmwrite(file_txt_out,values_simul_time, 'delimiter', '\t','precision',
'%.8f','newline', 'pc');
    matrix_all(:,:,j)=values_simul_time(:,:);

Alt_time{:,j}=[matrix_all(p:size(time),2,j);matrix_all(p:size(time),3,j);matrix_a
ll(p:size(time),4,j)];
    Alt_time_all(:,p+1:p+3)=values_simul_time(:,2:4);
    p=p+3;
end

Alt_time_all(:,1)=time';
Alt_time_all_txt=[root,'/Output/Time_all_sensors.txt'];
p=1;
for i=1:num_sim
    clear A

    file_txt_out=[root,'/FileOutput2/Sens_all_mod_',num2str(i,'%03d'),'.txt'];
    A=dlmread(file_txt_out);
    Alt_time_all(:,p+1:p+3)=A(:,2:4);
    p=p+3;
end

dlmwrite(Alt_time_all_txt,Alt_time_all,'delimiter', '\t','precision',
'%.9f','newline', 'pc');


% Data at the END of the flow
%--------------------------------------------------

% to assign the xyz coordinates to the SPH nodes
XYZ_dati=dlmread([root,'/StartingFiles/XYZ.txt']);

for i =0:164  % horizontal plane nodes
    nodes_Gid(i+1,:)=(513+i*809:809+i*809);
end

for i=1:size(nodes_Gid,1)*size(nodes_Gid,2) % xyz coordinates of the deposit
plane nodes
    disp(['completed ',num2str(i/(size(nodes_Gid,1)*size(nodes_Gid,2))*100),'
%'])
    coord_nodes(i,1)=(nodes_Gid(i));
    coord_nodes(i,2)=XYZ_dati(find((nodes_Gid(i)==XYZ_dati(:,1))),2);
```

```
    coord_nodes(i,3)=XYZ_dati(find((nodes_Gid(i)==XYZ_dati(:,1))),3);
    coord_nodes(i,4)=XYZ_dati(find((nodes_Gid(i)==XYZ_dati(:,1))),4);
end


% to extract the simulation data on the deposit plane nodes at the last time step
[m]
for i=1:num_sim
    disp(['extracting values of simulation num. ',num2str(i)])
    dati_txt =
[root,'/Simulations/',prefix,num2str(i,'%03d'),'/Hs_',num2str(i,'%03d'),'.txt'];
% contiene nodo X Y Z h h+Z tutto in cm dell'ultimo istante temporale
    Hs_Gid=dlmread(dati_txt);

    for j=1:size(nodes_Gid,1)*size(nodes_Gid,2)  % all the values are located in
one matrix, one column for each simulation

        if isempty(find((nodes_Gid(j)==Hs_Gid(:,1))))
            Alt(j,i)=0;
        else
            Alt(j,i)=Hs_Gid(find((nodes_Gid(j)==Hs_Gid(:,1))),5);

        end
    end

    for k=1:size(nodes_Gid,1)                    % this 3D-matrix contains the
data of all simulations, where the third dimension is the simulation number
        for c=1:size(nodes_Gid,2)
            if isempty(find((nodes_Gid(k,c)==Hs_Gid(:,1))))
                Matr_sim(k,c,i)=0;
            else
                Matr_sim(k,c,i)= Hs_Gid(find((nodes_Gid(k,c)==Hs_Gid(:,1))),5);
            end
        end
    end

end

% to extract the dat aof the central longitudinal section of deposit
Psim_all(:,1)=(2.56:0.005:4.04);

for i=1:num_sim
    clear Hs_Gid Section_out Section

    dati_txt =
[root,'/Simulations/',prefix,num2str(i,'%03d'),'/Hs_',num2str(i,'%03d'),'.txt'];
% contiene nodo X Y Z h h+Z tutto in cm dell'ultimo istante temporale
    Hs_Gid=dlmread(dati_txt);

    Section_out(:,1)=(70087:1:70383);
```

```
    Section_out(:,2)=(2.56:0.005:4.04);
    Section_out(:,3)=zeros;
    Section_out(:,4)=zeros;

    Section(:,1)=Hs_Gid(find(Hs_Gid(:,3)==0.43),1);
    Section(:,2)=Hs_Gid(find(Hs_Gid(:,3)==0.43),2);
    Section(:,3)=Hs_Gid(find(Hs_Gid(:,3)==0.43),3);
    Section(:,4)=Hs_Gid(find(Hs_Gid(:,3)==0.43),6);

    c=0;
    for p=1:size(Section,1)
        if isempty(find(Section_out(:,1)==Section(p,1)))
        else
            c=c+1;
            Section_out(c,3)=Section(p,3);
            Section_out(c,4)=Section(p,4);
        end
    end

    Psim_all(:,i+1)=Section_out(:,4);

end
Psim_all(:,1)=Psim_all(:,1)-0.804;
Psim_all_txt = [root,'/Output/Profile_all.txt'];
dlmwrite(Psim_all_txt,Psim_all,'delimiter', '\t','precision', '%.5f','newline',
'pc');

% variables saving
save([root,'/variabili_3B_parte','.mat']);


% ERROR CALCULATION [m]
% --------------------------------------------------------------------

% files containing the laboratory measurements and the simulated data
Lab_profiles=dlmread([root,'/Comparison/Lab_profiles.txt']); % laboratory data
Lab_laser=dlmread([root,'/Comparison/Lab_laser.txt']);       % laboratory data
Lab_vel=dlmread([root,'/Comparison/Lab_vel.txt']);           % laboratory
velocities
Voellmy_profiles=dlmread([root,'/Comparison/Profile_all_Voellmy.txt']);  %
simulated data with Voellmy law
Voellmy_laser=dlmread([root,'/Comparison/Voellmy_laser.txt']);           %
simulated data with Voellmy law
Bingham_profiles=dlmread([root,'/Comparison/Profile_all_Bingham.txt']);  %
simulated data with Bingham law
Bingham_laser=dlmread([root,'/Comparison/Bingham_laser.txt']);           %
simulated data with Bingham law

% to assign zero value to all the data lower than 0m
for i=1:289
```

```
    for j=2:25
        if Lab_profiles(i,j)>=0
            Lab_profiles(i,j)= Lab_profiles(i,j);
        else
            Lab_profiles(i,j)=0;
        end
    end
end

% laboratory tests runouts
runout_Lab(1,:)=[3.236,3.236,3.236,2.990,3.236,2.835,2.290,2.505,2.535,...
    3.236,2.465,2.515,2.205,...
    2.236,3.130,2.845,...
    1.940,2.171,1.975,1.981,1.940,1.925,1.925,1.995];


% simulations runouts
for j=1:num_sim % Bingham
    try

runout_B(1,j)=Bingham_profiles(find(Bingham_profiles(:,j+1)>0.0001,1,'last'),1);
    catch
        runout_B(1,j)=NaN;
    end
end

for j=1:num_sim % Voellmy
    try

runout_V(1,j)=Voellmy_profiles(find(Voellmy_profiles(:,j+1)>0.0001,1,'last'),1);
    catch
        runout_V(1,j)=NaN;
    end
end

% calculation of the time for the arrival to each sensor
for j=1:num_sim*3 % Bingham
    try
        T_B(1,j)=Bingham_laser(find(Bingham_laser(:,j+1)>0,1,'first'),1);
    catch
        T_B(1,j)=NaN;
    end
end
time_B=reshape(T_B,3,400);
for i=1:num_sim  %in prima riga è scritta la prima velocità, in seconda riga la
seconda
    vel_B(1,i)=0.34/(time_B(2,i)-time_B(1,i)); % 0.34m è la distanza tra i
sensori
    vel_B(2,i)=0.34/(time_B(3,i)-time_B(2,i));
end
```

```
for j=1:num_sim*3 % Voellmy
    try
        T_V(1,j)=Voellmy_laser(find(Voellmy_laser(:,j+1)>0,1,'first'),1);
    catch
        T_V(1,j)=NaN;
    end
end
time_V=reshape(T_V,3,400);
for i=1:num_sim  %in prima riga è scritta la prima velocità, in seconda riga la
seconda
    vel_V(1,i)=0.34/(time_V(2,i)-time_V(1,i)); % 0.34m è la distanza tra i
sensori
    vel_V(2,i)=0.34/(time_V(3,i)-time_V(2,i));
end


% errors of the longitudinal central section (PROFILE)
for i=2:size(Lab_profiles,2)
    for j=1:num_sim
        for z=1:size(Lab_profiles,1)
            Error_profile_Bingham(i-1,j)=sum(abs(Lab_profiles(:,i)-
Bingham_profiles(:,j+1)))/size(Lab_profiles,1);
            Error_profile_Voellmy(i-1,j)=sum(abs(Lab_profiles(:,i)-
Voellmy_profiles(:,j+1)))/size(Lab_profiles,1);

        end
    end
end

% errors of the heights of material in time (LASER SENSORS)
p=0;
q=0;
for i=2:3:size(Lab_laser,2)
    p=p+1;
    q=0;
    for j=2:3:num_sim*3+1
        q=q+1;
        Error_laser1_Bingham(p,q)=sum(abs(Lab_laser(1:20:1201,i)-
Bingham_laser(:,j)))/size(Bingham_laser,1);
        Error_laser2_Bingham(p,q)=sum(abs(Lab_laser(1:20:1201,i+1)-
Bingham_laser(:,j+1)))/size(Bingham_laser,1);
        Error_laser3_Bingham(p,q)=sum(abs(Lab_laser(1:20:1201,i+2)-
Bingham_laser(:,j+2)))/size(Bingham_laser,1);

        Error_laser1_Voellmy(p,q)=sum(abs(Lab_laser(1:20:1201,i)-
Voellmy_laser(:,j)))/size(Voellmy_laser,1);
        Error_laser2_Voellmy(p,q)=sum(abs(Lab_laser(1:20:1201,i+1)-
Voellmy_laser(:,j+1)))/size(Voellmy_laser,1);
```

```
        Error_laser3_Voellmy(p,q)=sum(abs(Lab_laser(1:20:1201,i+2)-
Voellmy_laser(:,j+2)))/size(Voellmy_laser,1);


Error_laser_Bingham(p,q)=(Error_laser1_Bingham(p,q)+Error_laser2_Bingham(p,q)+Err
or_laser3_Bingham(p,q))/3;

Error_laser_Voellmy(p,q)=(Error_laser1_Voellmy(p,q)+Error_laser2_Voellmy(p,q)+Err
or_laser3_Voellmy(p,q))/3;
    end
end

Error_Bingham=(Error_profile_Bingham+Error_laser_Bingham)/2;
Error_Voellmy=(Error_profile_Voellmy+Error_laser_Voellmy)/2;


% best simulations identification
% ------------------------------------------------------------------------
% WKA:   test1/test9  test4  test3/test8  test5  test2/test6/test7
% WSKA:  (test11)  test12  test13  test14
% WSKB1: test20  test18  test19
% WSKB2: test16/test17  test23/test24  test21  test22/test25  test15
% ------------------------------------------------------------------------

% Bingham
for i=1:size(Lab_profiles,2)-1
    Best_all_B{i,1}=find(min(Error_Bingham(i,:))==(Error_Bingham(i,:)));

Best_laser_B{i,1}=find(min(Error_laser_Bingham(i,:))==(Error_laser_Bingham(i,:)))
;

Best_profile_B{i,1}=find(min(Error_profile_Bingham(i,:))==(Error_profile_Bingham(
i,:)));
end

%Voellmy
for i=1:size(Lab_profiles,2)-1
    Best_all_V{i,1}=find(min(Error_Voellmy(i,:))==(Error_Voellmy(i,:)));

Best_laser_V{i,1}=find(min(Error_laser_Voellmy(i,:))==(Error_laser_Voellmy(i,:)))
;

Best_profile_V{i,1}=find(min(Error_profile_Voellmy(i,:))==(Error_profile_Voellmy(
i,:)));
end

% summary
Best_simulation_B={Best_laser_B,Best_profile_B,Best_all_B};
Best_simulation_V={Best_laser_V,Best_profile_V,Best_all_V};
```

```
% CREATION OF THE OUTPUTS
% ------------------------------------------------------------------------

% to print the contours of alla the simulations deposit
X_nodes=reshape(coord_nodes(:,2),[165 297]);
Y_nodes=reshape(coord_nodes(:,3),[165 297]);

for i=start:num_sim
    figur_out = [root_B,'/Contours/','contour_',num2str(i,'%03d'),'.jpg'];

    h=figure('visible','off');
    contourf(X_nodes,Y_nodes,Matr_sim(:,:,i))
    caxis([0,0.03])
    colorbar
    saveas(h,figur_out)
end

% to print the spread graphs depending on the parameters
h1=figure;
figur_out = [root,'/Figures/TauVSspread.jpg'];
for i=1:20
    plot(PARAM(1,20*(i-1)+1:20*i),Spread(1,20*(i-1)+1:20*i))
    hold on
end
xlabel('\tau')
ylabel('Spread')
title(['\tau',' vs Spread'])
plot(40.578,Spread_cl(1,1),'X')
plot(46.23,Spread_cl(1,2),'X')
plot(57.69,Spread_cl(1,3),'X')
plot(71.543,Spread_cl(1,4),'X')
plot(79.623,Spread_cl(1,5),'X')
hold off
saveas(h1,figur_out)

% to print the runout graphs depending on the parameters
h2=figure;
figur_out = [root,'/Figures/TauVSrunout.jpg'];
for i=1:20
    plot(PARAM(1,20*(i-1)+1:20*i),Runout(1,20*(i-1)+1:20*i))
    hold on
end
xlabel('\tau')
ylabel('Runout')
title(['\tau',' vs Runout'])
plot(40.578,Runout_cl(1,1),'X')
plot(46.23,Runout_cl(1,2),'X')
plot(57.69,Runout_cl(1,3),'X')
plot(71.543,Runout_cl(1,4),'X')
```

```
plot(79.623,Runout_cl(1,5),'X')
hold off
saveas(h2,figur_out)

% to print the area graphs depending on the parameters
h3=figure;
figur_out = [root,'/Figures/TauVSarea.jpg'];
for i=1:20
    plot(PARAM(1,20*(i-1)+1:20*i),Area(1,20*(i-1)+1:20*i))
    hold on
end
xlabel('\tau')
ylabel('Area')
title(['\tau',' vs Area'])
plot(40.578,Area_cl(1,1),'X')
plot(46.23,Area_cl(1,2),'X')
plot(57.69,Area_cl(1,3),'X')
plot(71.543,Area_cl(1,4),'X')
plot(79.623,Area_cl(1,5),'X')
hold off
saveas(h3,figur_out)

% to print the perimeter graphs depending on the parameters
h4=figure;
figur_out = [root,'/Figures/TauVSperim.jpg'];
for i=1:20
    plot(PARAM(1,20*(i-1)+1:20*i),Perimeter(1,20*(i-1)+1:20*i))
    hold on
end
xlabel('\tau')
ylabel('Perimeter')
title(['\tau',' vs Perimeter'])
plot(40.578,Perimeter_cl(1,1),'X')
plot(46.23,Perimeter_cl(1,2),'X')
plot(57.69,Perimeter_cl(1,3),'X')
plot(71.543,Perimeter_cl(1,4),'X')
plot(79.623,Perimeter_cl(1,5),'X')
hold off
saveas(h4,figur_out)

% to print the eccentricity of the deposit behavior depending on the parameters
for i=1:400
    Eccentricity(1,i)=Runout(1,i)/Spread(1,i);
end
h5=figure;
figur_out = [root,'/Figures/TauVSeccentricity.jpg'];
for i=1:20
    plot(PARAM(1,20*(i-1)+1:20*i),Eccentricity(1,20*(i-1)+1:20*i))
    hold on
end
```

```
xlabel('\tau')
ylabel('Eccentricity')
title(['\tau',' vs Eccentricity'])
plot(40.578,Runout_cl(1,1)/Spread_cl(1,1),'X')
plot(46.23,Runout_cl(1,2)/Spread_cl(1,2),'X')
plot(57.69,Runout_cl(1,3)/Spread_cl(1,3),'X')
plot(71.543,Runout_cl(1,4)/Spread_cl(1,4),'X')
plot(79.623,Runout_cl(1,5)/Spread_cl(1,5),'X')
hold off
saveas(h1,figur_out)

% to extract the longitudinal central profiles of the simulations
--------------------------------------------------------------------------
root_cloud = 'D:/Documents/Laboratory';
XYZ_dati=dlmread([root_cloud,'/clouds','/XYZ.txt']);
for i =0:164  % horizontal plane nodes
    nodes_Gid(i+1,:)=(513+i*809:809+i*809);
end

for i=1:size(nodes_Gid,1)*size(nodes_Gid,2) % xyz coordinates of the deposit
plane nodes
    disp(['completed ',num2str(i/(size(nodes_Gid,1)*size(nodes_Gid,2))*100),'
%'])
    coord_nodes(i,1)=(nodes_Gid(i));
    coord_nodes(i,2)=XYZ_dati(find((nodes_Gid(i)==XYZ_dati(:,1))),2);
    coord_nodes(i,3)=XYZ_dati(find((nodes_Gid(i)==XYZ_dati(:,1))),3);
    coord_nodes(i,4)=XYZ_dati(find((nodes_Gid(i)==XYZ_dati(:,1))),4);
end
num_cloud=25;
X_nodes=reshape(coord_nodes(:,2),[165 297]);
Y_nodes=reshape(coord_nodes(:,3),[165 297]);

for i=1:num_cloud
    clear F1 P1_XYZ cloud cloud_mod Z_cloud C1_XY C1_max C1 h1

    cloud_txt =
[root_cloud,'/clouds/photometry/test',num2str(i,'%02d'),'_crop.txt'];

    if exist (cloud_txt,'file')
        cloud = dlmread(cloud_txt);
        cloud(:,4:9)=[];

        dlmwrite(cloud_txt,cloud,'delimiter', '\t','precision', '%.9f','newline',
'pc');
        P1_XYZ_txt =
[root_cloud,'/clouds/photometry/txt/test',num2str(i,'%02d'),'_prof2.txt'];
C1_XY_txt =
[root_cloud,'/clouds/photometry/txt/test',num2str(i,'%02d'),'_cont.txt'];

        vector=(2.6:0.005:4.1);
```

```
        vector(2,:)=0.43;
        F1=TriScatteredInterp(cloud(:,1),cloud(:,2),cloud(:,3));
        P1_XYZ(:,3)=F1(vector(1,:),vector(2,:));
        P1_XYZ(:,1:2)=vector(1:2,:)';
        P1_XYZ(isnan(P1_XYZ(:,3)),3)=0;
        P1_XYZ(1,3)=0;
        plot(P1_XYZ(:,1),P1_XYZ(:,3))
        dlmwrite(P1_XYZ_txt,P1_XYZ,'delimiter', '\t','precision',
'%.4f','newline', 'pc');

        P2_XYZ=[vector(1,:)'-0.804,P1_XYZ(:,3)];
        P2_XYZ_txt =
[root_cloud,'/clouds/photometry/txt/test',num2str(i,'%02d'),'_prof_final.txt'];
        dlmwrite(P2_XYZ_txt,P2_XYZ,'delimiter', '\t','precision',
'%.5f','newline', 'pc');

        % to exctract the contours
        cloud_mod(:,1:2)=coord_nodes(:,2:3);
        cloud_mod(:,3)=F1(coord_nodes(:,2),coord_nodes(:,3));
        cloud_mod(isnan(cloud_mod(:,3)),3)=0;

        for k=1:size(cloud_mod,1)
            if cloud_mod(k,3)<0.003
                cloud_mod(k,3)=0;
            else
                cloud_mod(k,3)=cloud_mod(k,3);
            end
        end
        Z_cloud=reshape(cloud_mod(:,3),[165 297]);

        [C1,h1]=contourf(X_nodes,Y_nodes,Z_cloud,[0.001 0.001]);
        C1_max=find(max(C1(2,:))==C1(2,:));

C1_XY=[C1(1,C1_max+1:C1_max+C1(2,C1_max))',C1(2,C1_max+1:C1_max+C1(2,C1_max))'];
        C1_XY=[C1_XY(:,1),C1_XY(:,2)-0.4349];
        C1_XY(find(C1_XY(:,1)==2.6),2)=0;
        dlmwrite(C1_XY_txt,C1_XY,'delimiter', '\t','precision', '%.4f','newline',
'pc');
    else
    end
end

% to create the best simulations graphs
% it contains [Best_Profile Best_Laser Best_All Best_Ruonout1 Best_Ruonout2
Best_Velocity]
num_best_B=dlmread([root,'/Comparison/num_best_B.txt']);  % Bingham
num_best_V=dlmread([root,'/Comparison/num_best_V.txt']);  % Voellmy

%
Lab_laser_mod(:,:)=Lab_laser(1:20:1201,:);
```

```
name_test={'WKa1_test1';'WKa1_test9';'WKa2_test4';'WKa3_test3';
    'WKa3_test8';'WKa4_test5';'WKa5_test2';'WKa5_test6';'WKa5_test7';
    'WSKa0_test11';'WSKa1_test12';'WSKa2_test13';'WSKa3_test14';
    'WSKb1_test20';'WSKb2_test18';'WSKb3_test19';
    'WSKb4_test16';'WSKb4_test17';'WSKb5_test23';'WSKb5_test24';
    'WSKb6_test21';'WSkb7_test22';'WSkb7_test25';'WSkb8_test15'};

% to create the files containing the best simulations data for each laboratory
test
% Bingham
for i=1:24
    clear M_B_out L_B_out
    M_B_out(:,1)=Lab_profiles(:,1);
    L_B_out(:,1)=Lab_laser_mod(:,1);
    M_B_out(:,2)=Lab_profiles(:,i+1);
    L_B_out(:,2)=Lab_laser_mod(:,(i-1)*3+2);
    L_B_out(:,3)=Lab_laser_mod(:,(i-1)*3+3);
    L_B_out(:,4)=Lab_laser_mod(:,(i-1)*3+4);
    if num_best_B(i,1)==0
        M_B_out(:,3)=0;
        L_B_out(:,5)=0;
        L_B_out(:,6)=0;
        L_B_out(:,7)=0;
    else
        M_B_out(:,3)=Bingham_profiles(:,num_best_B(i,1)+1);
        L_B_out(:,5)=Bingham_laser(:,(num_best_B(i,1)-1)*3+2);
        L_B_out(:,6)=Bingham_laser(:,(num_best_B(i,1)-1)*3+3);
        L_B_out(:,7)=Bingham_laser(:,(num_best_B(i,1)-1)*3+4);
    end
    if num_best_B(i,2)==0
        M_B_out(:,4)=0;
        L_B_out(:,8)=0;
        L_B_out(:,9)=0;
        L_B_out(:,10)=0;
    else
        M_B_out(:,4)=Bingham_profiles(:,num_best_B(i,2)+1);
        L_B_out(:,8)=Bingham_laser(:,(num_best_B(i,2)-1)*3+2);
        L_B_out(:,9)=Bingham_laser(:,(num_best_B(i,2)-1)*3+3);
        L_B_out(:,10)=Bingham_laser(:,(num_best_B(i,2)-1)*3+4);
    end
    if num_best_B(i,3)==0
        M_B_out(:,5)=0;
        L_B_out(:,11)=0;
        L_B_out(:,12)=0;
        L_B_out(:,13)=0;
    else
        M_B_out(:,5)=Bingham_profiles(:,num_best_B(i,3)+1);
        L_B_out(:,11)=Bingham_laser(:,(num_best_B(i,3)-1)*3+2);
        L_B_out(:,12)=Bingham_laser(:,(num_best_B(i,3)-1)*3+2);
        L_B_out(:,13)=Bingham_laser(:,(num_best_B(i,3)-1)*3+2);
```

```
    end
    if num_best_B(i,4)==0
        M_B_out(:,6)=0;
        L_B_out(:,14)=0;
        L_B_out(:,15)=0;
        L_B_out(:,16)=0;
    else
        M_B_out(:,6)=Bingham_profiles(:,num_best_B(i,4)+1);
        L_B_out(:,14)=Bingham_laser(:,(num_best_B(i,4)-1)*3+2);
        L_B_out(:,15)=Bingham_laser(:,(num_best_B(i,4)-1)*3+2);
        L_B_out(:,16)=Bingham_laser(:,(num_best_B(i,4)-1)*3+2);
    end
    if num_best_B(i,5)==0
        M_B_out(:,7)=0;
        L_B_out(:,17)=0;
        L_B_out(:,18)=0;
        L_B_out(:,19)=0;
    else
        M_B_out(:,7)=Bingham_profiles(:,num_best_B(i,5)+1);
        L_B_out(:,17)=Bingham_laser(:,(num_best_B(i,5)-1)*3+2);
        L_B_out(:,18)=Bingham_laser(:,(num_best_B(i,5)-1)*3+2);
        L_B_out(:,19)=Bingham_laser(:,(num_best_B(i,5)-1)*3+2);
    end
    if num_best_B(i,6)==0
        M_B_out(:,8)=0;
        L_B_out(:,20)=0;
        L_B_out(:,21)=0;
        L_B_out(:,22)=0;
    else
        M_B_out(:,8)=Bingham_profiles(:,num_best_B(i,6)+1);
        L_B_out(:,20)=Bingham_laser(:,(num_best_B(i,6)-1)*3+2);
        L_B_out(:,21)=Bingham_laser(:,(num_best_B(i,6)-1)*3+2);
        L_B_out(:,22)=Bingham_laser(:,(num_best_B(i,6)-1)*3+2);
    end
    M_B_out_txt=[root,'/Comparison/file_best/',name_test{i},'_P.txt'];
    L_B_out_txt=[root,'/Comparison/file_best/',name_test{i},'_L.txt'];
    dlmwrite(M_B_out_txt, M_B_out, 'delimiter', '\t','precision',
'%.8f','newline', 'pc');
    dlmwrite(L_B_out_txt, L_B_out, 'delimiter', '\t','precision',
'%.8f','newline', 'pc');
end

% Voellmy
for i=1:24
    clear M_V_out L_V_out
    M_V_out(:,1)=Lab_profiles(:,1);
    L_V_out(:,1)=Lab_laser_mod(:,1);
    M_V_out(:,2)=Lab_profiles(:,i+1);
    L_V_out(:,2)=Lab_laser_mod(:,(i-1)*3+2);
    L_V_out(:,3)=Lab_laser_mod(:,(i-1)*3+3);
```

```
L_V_out(:,4)=Lab_laser_mod(:,(i-1)*3+4);
if num_best_V(i,1)==0
    M_V_out(:,3)=0;
    L_V_out(:,5)=0;
    L_V_out(:,6)=0;
    L_V_out(:,7)=0;
else
    M_V_out(:,3)=Voellmy_profiles(:,num_best_V(i,1)+1);
    L_V_out(:,5)=Voellmy_laser(:,(num_best_V(i,1)-1)*3+2);
    L_V_out(:,6)=Voellmy_laser(:,(num_best_V(i,1)-1)*3+3);
    L_V_out(:,7)=Voellmy_laser(:,(num_best_V(i,1)-1)*3+4);
end
if num_best_V(i,2)==0
    M_V_out(:,4)=0;
    L_V_out(:,8)=0;
    L_V_out(:,9)=0;
    L_V_out(:,10)=0;
else
    M_V_out(:,4)=Voellmy_profiles(:,num_best_V(i,2)+1);
    L_V_out(:,8)=Voellmy_laser(:,(num_best_V(i,2)-1)*3+2);
    L_V_out(:,9)=Voellmy_laser(:,(num_best_V(i,2)-1)*3+3);
    L_V_out(:,10)=Voellmy_laser(:,(num_best_V(i,2)-1)*3+4);
end
if num_best_V(i,3)==0
    M_V_out(:,5)=0;
    L_V_out(:,11)=0;
    L_V_out(:,12)=0;
    L_V_out(:,13)=0;
else
    M_V_out(:,5)=Voellmy_profiles(:,num_best_V(i,3)+1);
    L_V_out(:,11)=Voellmy_laser(:,(num_best_V(i,3)-1)*3+2);
    L_V_out(:,12)=Voellmy_laser(:,(num_best_V(i,3)-1)*3+2);
    L_V_out(:,13)=Voellmy_laser(:,(num_best_V(i,3)-1)*3+2);
end
if num_best_V(i,4)==0
    M_V_out(:,6)=0;
    L_V_out(:,14)=0;
    L_V_out(:,15)=0;
    L_V_out(:,16)=0;
else
    M_V_out(:,6)=Voellmy_profiles(:,num_best_V(i,4)+1);
    L_V_out(:,14)=Voellmy_laser(:,(num_best_V(i,4)-1)*3+2);
    L_V_out(:,15)=Voellmy_laser(:,(num_best_V(i,4)-1)*3+2);
    L_V_out(:,16)=Voellmy_laser(:,(num_best_V(i,4)-1)*3+2);
end
if num_best_V(i,5)==0
    M_V_out(:,7)=0;
    L_V_out(:,17)=0;
    L_V_out(:,18)=0;
    L_V_out(:,19)=0;
```

```
    else
        M_V_out(:,7)=Voellmy_profiles(:,num_best_V(i,5)+1);
        L_V_out(:,17)=Voellmy_laser(:,(num_best_V(i,5)-1)*3+2);
        L_V_out(:,18)=Voellmy_laser(:,(num_best_V(i,5)-1)*3+2);
        L_V_out(:,19)=Voellmy_laser(:,(num_best_V(i,5)-1)*3+2);
    end
    M_V_out(size(M_V_out,1)+1,1)=3.236;
    M_V_out(size(M_V_out,1),2:7)=0;
    M_V_out_txt=[root,'/Comparison/file_best/Voellmy1/',name_test{i},'_P_V.txt'];
    L_V_out_txt=[root,'/Comparison/file_best/Voellmy1/',name_test{i},'_L_V.txt'];
    dlmwrite(M_V_out_txt, M_V_out, 'delimiter', '\t','precision',
'%.8f','newline', 'pc');
    dlmwrite(L_V_out_txt, L_V_out, 'delimiter', '\t','precision',
'%.8f','newline', 'pc');
end

% errors calculation
for j=1:24
    Err_out_B(j,1)=num_best_B(j,1);
    Err_out_B(j,2)=Error_runout_Bingham(j,num_best_B(j,1));
    Err_out_B(j,3)=Error_vel_Bingham(j,num_best_B(j,1));

    Err_out_B(j,4)=num_best_B(j,2);
    Err_out_B(j,5)=Error_runout_Bingham(j,num_best_B(j,2));
    Err_out_B(j,6)=Error_vel_Bingham(j,num_best_B(j,2));

    Err_out_V(j,1)=num_best_V(j,1);
    Err_out_V(j,2)=Error_runout_Voellmy(j,num_best_V(j,1));
    Err_out_V(j,3)=Error_vel_Voellmy(j,num_best_V(j,1));

    Err_out_V(j,4)=num_best_V(j,2);
    Err_out_V(j,5)=Error_runout_Voellmy(j,num_best_V(j,2));
    Err_out_V(j,6)=Error_vel_Voellmy(j,num_best_V(j,2));
end


% to create the contours of the error behavior depending on the parameters
combination
root = 'D:/Documents/NumericalModel';
root_B = 'D:/Documents/NumericalModel/Bingham';
root_V = 'D:/Documents/NumericalModel/Voellmy';

parameterB_txt=[root_B,'/','Output','/','parameter.txt'];
parameterV_txt=[root_V,'/','Output','/','parameter.txt'];
parameterVisco_txt=[root,'/Comparison/Param_visco.txt'];

PARAM_B=dlmread(parameterB_txt);         % Bingham parameters
PARAM_V=dlmread(parameterV_txt);         % Voellmy parameters
Param_visco=dlmread(parameterVisco_txt); % Viscometer parameters
```

```
x_tau=reshape(PARAM_B(1,:),20,20);
y_mu=reshape(PARAM_B(2,:),20,20);
x_fi=reshape(PARAM_V(2,:),20,20);
y_turb=reshape(PARAM_V(1,:),20,20);
font_size=20;
MarkerSize=20;
name_test1={'WK_A1';'WK_A1';'WK_A2';'WK_A3';
    'WK_A3';'WK_A4';'WK_A5';'WK_A5';'WK_A5';
    'WSK_A0';'WSK_A1';'WSK_A2';'WSK_A3';
    'WSK_B1';'WSK_B2';'WSK_B3';
    'WSK_B4';'WSK_B4';'WSK_B5';'WSK_B5';
    'WSK_B6';'WSK_B7';'WSK_B7';'WSK_B8'};

int_vett=(0:0.0025:0.025);

% Bingham
for i=1:24
    clear z_profile_B z_laserB  z_all_B
    z_profile_B=reshape(Error_profile_Bingham(i,:),20,20);
    z_laserB=reshape(Error_laser_Bingham(i,:),20,20);
    z_all_B=reshape(Error_Bingham(i,:),20,20);
    if i>=1&&i<=9
        h1=figure('visible','off');
        contourf(x_tau,y_mu,z_profile_B,int_vett),set(gca,'FontSize',font_size),
hold
        plot(Param_visco(i,2),Param_visco(i,1),'--gs',...
            'MarkerSize',MarkerSize,...
            'MarkerEdgeColor','k',...
            'MarkerFaceColor','r')

plot(PARAM_B(1,num_best_B(i,1)),PARAM_B(2,num_best_B(i,1)),'ok','MarkerSize',Mark
erSize,...
            'MarkerEdgeColor','k',...
            'MarkerFaceColor','k');

plot(PARAM_B(1,num_best_B(i,2)),PARAM_B(2,num_best_B(i,2)),'ok','MarkerSize',Mark
erSize,...
            'MarkerEdgeColor','k',...
            'MarkerFaceColor','w');

plot(PARAM_B(1,num_best_B(i,3)),PARAM_B(2,num_best_B(i,3)),'ok','MarkerSize',Mark
erSize,...
            'MarkerEdgeColor','k',...
            'MarkerFaceColor','y');
        hold off
        xlabel(['\tau','  [Pa]'],'FontSize',font_size,'FontWeight','bold')
        ylabel(['\mu','  [Pa s]'],'FontSize',font_size,'FontWeight','bold')
        title(['Profile Errors - ',name_test1{i}])
        colorbar
        caxis([0, 0.025])
```

```
        h2=figure('visible','off');
        contourf(x_tau,y_mu,z_laserB,int_vett),set(gca,'FontSize',font_size),
hold
        plot(Param_visco(i,2),Param_visco(i,1),'--gs',...
            'MarkerSize',MarkerSize,...
            'MarkerEdgeColor','k',...
            'MarkerFaceColor','r')

plot(PARAM_B(1,num_best_B(i,1)),PARAM_B(2,num_best_B(i,1)),'ok','MarkerSize',Mark
erSize,...
            'MarkerEdgeColor','k',...
            'MarkerFaceColor','k');

plot(PARAM_B(1,num_best_B(i,2)),PARAM_B(2,num_best_B(i,2)),'ok','MarkerSize',Mark
erSize,...
            'MarkerEdgeColor','k',...
            'MarkerFaceColor','w');

plot(PARAM_B(1,num_best_B(i,3)),PARAM_B(2,num_best_B(i,3)),'ok','MarkerSize',Mark
erSize,...
            'MarkerEdgeColor','k',...
            'MarkerFaceColor','y');
        hold off
        xlabel(['\tau','  [Pa]'],'FontSize',font_size,'FontWeight','bold')
        ylabel(['\mu','  [Pa s]'],'FontSize',font_size,'FontWeight','bold')
        title(['H vs time Errors - ',name_test1{i}])
        colorbar
        caxis([0,0.025])

        h3=figure('visible','off');
        contourf(x_tau,y_mu,z_all_B,int_vett),set(gca,'FontSize',font_size), hold
        plot(Param_visco(i,2),Param_visco(i,1),'--gs',...
            'MarkerSize',MarkerSize,...
            'MarkerEdgeColor','k',...
            'MarkerFaceColor','r')

plot(PARAM_B(1,num_best_B(i,1)),PARAM_B(2,num_best_B(i,1)),'ok','MarkerSize',Mark
erSize,...
            'MarkerEdgeColor','k',...
            'MarkerFaceColor','k');

plot(PARAM_B(1,num_best_B(i,2)),PARAM_B(2,num_best_B(i,2)),'ok','MarkerSize',Mark
erSize,...
            'MarkerEdgeColor','k',...
            'MarkerFaceColor','w');

plot(PARAM_B(1,num_best_B(i,3)),PARAM_B(2,num_best_B(i,3)),'ok','MarkerSize',Mark
erSize,...
            'MarkerEdgeColor','k',...
```

```
            'MarkerFaceColor','y');
        hold off
        xlabel(['\tau','  [Pa]'],'FontSize',font_size,'FontWeight','bold')
        ylabel(['\mu','  [Pa s]'],'FontSize',font_size,'FontWeight','bold')
        title(['Overall Errors - ',name_test1{i}])
        colorbar
        caxis([0, 0.025])
    else

        h1=figure('visible','off');
        contourf(x_tau,y_mu,z_profile_B,int_vett),set(gca,'FontSize',font_size),
hold

plot(PARAM_B(1,num_best_B(i,1)),PARAM_B(2,num_best_B(i,1)),'ok','MarkerSize',Mark
erSize,...
            'MarkerEdgeColor','k',...
            'MarkerFaceColor','k');

plot(PARAM_B(1,num_best_B(i,2)),PARAM_B(2,num_best_B(i,2)),'ok','MarkerSize',Mark
erSize,...
            'MarkerEdgeColor','k',...
            'MarkerFaceColor','w');

plot(PARAM_B(1,num_best_B(i,3)),PARAM_B(2,num_best_B(i,3)),'ok','MarkerSize',Mark
erSize,...
            'MarkerEdgeColor','k',...
            'MarkerFaceColor','y');
        hold off
        xlabel(['\tau','  [Pa]'],'FontSize',font_size,'FontWeight','bold')
        ylabel(['\mu','  [Pa s]'],'FontSize',font_size,'FontWeight','bold')
        title(['Profile Errors - ',name_test1{i}])
        colorbar
        caxis([0, 0.025])

        h2=figure('visible','off');
        contourf(x_tau,y_mu,z_laserB,int_vett),set(gca,'FontSize',font_size),
hold

plot(PARAM_B(1,num_best_B(i,1)),PARAM_B(2,num_best_B(i,1)),'ok','MarkerSize',Mark
erSize,...
            'MarkerEdgeColor','k',...
            'MarkerFaceColor','k');

plot(PARAM_B(1,num_best_B(i,2)),PARAM_B(2,num_best_B(i,2)),'ok','MarkerSize',Mark
erSize,...
            'MarkerEdgeColor','k',...
            'MarkerFaceColor','w');

plot(PARAM_B(1,num_best_B(i,3)),PARAM_B(2,num_best_B(i,3)),'ok','MarkerSize',Mark
erSize,...
```

```
            'MarkerEdgeColor','k',...
            'MarkerFaceColor','y');
        hold off
        xlabel(['\tau','  [Pa]'],'FontSize',font_size,'FontWeight','bold')
        ylabel(['\mu','  [Pa s]'],'FontSize',font_size,'FontWeight','bold')
        title(['H vs time Errors - ',name_test1{i}])
        colorbar
        caxis([0, 0.025])

        h3=figure('visible','off');
        contourf(x_tau,y_mu,z_all_B,int_vett),set(gca,'FontSize',font_size), hold

plot(PARAM_B(1,num_best_B(i,1)),PARAM_B(2,num_best_B(i,1)),'ok','MarkerSize',Mark
erSize,...
            'MarkerEdgeColor','k',...
            'MarkerFaceColor','k');

plot(PARAM_B(1,num_best_B(i,2)),PARAM_B(2,num_best_B(i,2)),'ok','MarkerSize',Mark
erSize,...
            'MarkerEdgeColor','k',...
            'MarkerFaceColor','w');

plot(PARAM_B(1,num_best_B(i,3)),PARAM_B(2,num_best_B(i,3)),'ok','MarkerSize',Mark
erSize,...
            'MarkerEdgeColor','k',...
            'MarkerFaceColor','y');
        hold off
        xlabel(['\tau','  [Pa]'],'FontSize',font_size,'FontWeight','bold')
        ylabel(['\mu','  [Pa s]'],'FontSize',font_size,'FontWeight','bold')
        title(['Overall Errors - ',name_test1{i}])
        colorbar
        caxis([0, 0.025])
    end

saveas(h1,[root_B,'/Figures/Contour1/Profile/','contour_test_B',num2str(i,'%2d'),
'.jpeg'])

saveas(h2,[root_B,'/Figures/Contour1/Time/','contour_test_B',num2str(i,'%2d'),'.j
peg'])

saveas(h3,[root_B,'/Figures/Contour1/All/','contour_test_B',num2str(i,'%2d'),'.jp
eg'])
    close all
end

% Voellmy
for i=1:24
    clear z_profile_V z_laser_V  z_all_V
    z_profile_V=reshape(Error_profile_Voellmy(i,:),20,20);
    z_laser_V=reshape(Error_laser_Voellmy(i,:),20,20);
```

```
    z_all_V=reshape(Error_Voellmy(i,:),20,20);

    h1=figure('visible','off');
    contourf(x_fi,y_turb,z_profile_V,int_vett),set(gca,'FontSize',font_size),
hold

plot(PARAM_V(2,num_best_V(i,1)),PARAM_V(1,num_best_V(i,1)),'ok','MarkerSize',Mark
erSize,...
        'MarkerEdgeColor','k',...
        'MarkerFaceColor','k');

plot(PARAM_V(2,num_best_V(i,2)),PARAM_V(1,num_best_V(i,2)),'ok','MarkerSize',Mark
erSize,...
        'MarkerEdgeColor','k',...
        'MarkerFaceColor','w');

plot(PARAM_V(2,num_best_V(i,3)),PARAM_V(1,num_best_V(i,3)),'ok','MarkerSize',Mark
erSize,...
        'MarkerEdgeColor','k',...
        'MarkerFaceColor','y');
    hold off
    xlabel('cos\phi','FontSize',font_size,'FontWeight','bold')
    ylabel(['\xi','  [m s^-^2]'],'FontSize',font_size,'FontWeight','bold')
    title(['Profile Errors - ',name_test1{i}])
    colorbar
    caxis([0, 0.025])

    h2=figure('visible','off');
    contourf(x_fi,y_turb,z_laser_V,int_vett),set(gca,'FontSize',font_size), hold

plot(PARAM_V(2,num_best_V(i,1)),PARAM_V(1,num_best_V(i,1)),'ok','MarkerSize',Mark
erSize,...
        'MarkerEdgeColor','k',...
        'MarkerFaceColor','k');

plot(PARAM_V(2,num_best_V(i,2)),PARAM_V(1,num_best_V(i,2)),'ok','MarkerSize',Mark
erSize,...
        'MarkerEdgeColor','k',...
        'MarkerFaceColor','w');

plot(PARAM_V(2,num_best_V(i,3)),PARAM_V(1,num_best_V(i,3)),'ok','MarkerSize',Mark
erSize,...
        'MarkerEdgeColor','k',...
        'MarkerFaceColor','y');
    hold off
    xlabel('cos\phi','FontSize',font_size,'FontWeight','bold')
    ylabel(['\xi','  [m s^-^2]'],'FontSize',font_size,'FontWeight','bold')
    title(['H vs time Errors - ',name_test1{i}])
    colorbar
    caxis([0, 0.025])
```

```
    h3=figure('visible','off');
    contourf(x_fi,y_turb,z_all_V,int_vett),set(gca,'FontSize',font_size), hold

plot(PARAM_V(2,num_best_V(i,1)),PARAM_V(1,num_best_V(i,1)),'ok','MarkerSize',Mark
erSize,...
        'MarkerEdgeColor','k',...
        'MarkerFaceColor','k');

plot(PARAM_V(2,num_best_V(i,2)),PARAM_V(1,num_best_V(i,2)),'ok','MarkerSize',Mark
erSize,...
        'MarkerEdgeColor','k',...
        'MarkerFaceColor','w');

plot(PARAM_V(2,num_best_V(i,3)),PARAM_V(1,num_best_V(i,3)),'ok','MarkerSize',Mark
erSize,...
        'MarkerEdgeColor','k',...
        'MarkerFaceColor','y');
    hold off
    xlabel('cos\phi','FontSize',font_size,'FontWeight','bold')
    ylabel(['\xi','  [m s^-^2]'],'FontSize',font_size,'FontWeight','bold')
    title(['Overall Errors - ',name_test1{i}])
    colorbar
    caxis([0, 0.025])

saveas(h1,[root_V,'/Figures/Contour2/Profile/','contour_test_V',num2str(i,'%2d'),
'.jpeg'])

saveas(h2,[root_V,'/Figures/Contour2/Time/','contour_test_V',num2str(i,'%2d'),'.j
peg'])

saveas(h3,[root_V,'/Figures/Contour2/All/','contour_test_V',num2str(i,'%2d'),'.jp
eg'])
    close all
end
```

3. FIRST MATLAB FUNCTION: IT EXTRACTS THE DATA OF THE PROFILES FROM THE POST.RES FILE FOR EACH TIME STEP, AND WRITES THEM IN A TXT FILE.

```
function Pastor2TxtvsTime (prefix,ind,root)

% function to export in txt files the height values of each simulations, step by
step (to use in CloudCompare)
% ----------------------------------------------------------------------------
-----------------------------------

fileres =
[root,'/Simulations/',prefix,num2str(ind,'%03d'),'/','Pastor','/',prefix,num2str(
ind,'%03d'),'.post.res'];
```

```
if exist([root,'/Simulations/',prefix,num2str(ind,'%03d'),'/File_Txt'],'dir')
else
    mkdir([root,'/Simulations/',prefix,num2str(ind,'%03d'),'/File_Txt']);
end

XY_dati=dlmread([root,'/XY.txt']);
Z_dati=dlmread([root,'/Z.txt']);

XYZ_dati(:,1:3)=XY_dati(:,1:3);
XYZ_dati(:,4)=Z_dati(:,4);

Bound=fopen(fileres);  % to find the starting and ending indices in the post.res
file, for each time step
lengthfileres = CountLines(fileres);
k=0;
for i=1:lengthfileres;

    linea=fgetl(Bound);

    if size(linea,2)>16

        if linea(9:21)=='"height soil"'
            k=k+1;
            I(k,1)=i;
            firstline=textscan(linea,'%s %s %s %s %s %f %s %s %s');
            time(k,1)=firstline{1,6};
        elseif linea(2:13)=='Result "dis"'
            I(k,2)=i-1;
        end
    end
end
fclose(Bound);
fclose('all');

k=1;
p=1;

Bound=fopen(fileres);
for i=1:lengthfileres;
    linea=fgetl(Bound);

    if k<=size(I,1)

        if i>I(k,1)+1&&i<I(k,2)
            Linea=textscan(linea,'%f %f %f %f'); % to extract the results and to
print them in the txt files
```

```
            Dati(p,1)=Linea{1,1};
            Dati(p,2)=XYZ_dati(Dati(p,1),2);
            Dati(p,3)=XYZ_dati(Dati(p,1),3);
            Dati(p,4)=XYZ_dati(Dati(p,1),4);
            Dati(p,5)=Linea{1,4};
            Dati(p,6)=Dati(p,4)+Dati(p,5);
            p=p+1;

        end

        if i==I(k,2)-1

dati_txt=[root,'/Simulations/',prefix,num2str(ind,'%03d'),'/File_Txt/',prefix,num
2str(ind,'%03d'),'_',num2str(k,'%02d'),'.txt'];
            dlmwrite(dati_txt, Dati*100, 'delimiter', '\t','precision',
'%.8f','newline', 'pc');
            clear Dati
            p=1;
            k=k+1;
        end

    end
end
fclose(Bound);
fclose('all');
```

4. SECOND MATLAB FUNCTION: IT EXTRACTS THE DATA OF THE FINAL PROFILES FROM THE POST.RES FILE AND WRITES THEM IN A TXT FILE.

```
function Pastor2Txt (filebon,fileflaviares,fileres,filetxt,fileOUT2)

% filebon =
[root,'/Simulations/',prefix,num2str(ind,'%03d'),'/','Pastor','/',prefix,num2str(
ind,'%03d'),'3d.flavia.bon'];
% fileflaviares =
[root,'/Simulations/',prefix,num2str(ind,'%03d'),'/','Pastor','/',prefix,num2str(
ind,'%03d'),'3d.flavia.res'];
%
fileOUT2=[root,'/Simulations/',prefix,num2str(ind,'%03d'),'/','Pastor','/',prefix
,num2str(ind,'%03d'),'3d_2.flavia.res'];
% fileres =
[root,'/Simulations/',prefix,num2str(ind,'%03d'),'/','Pastor','/',prefix,num2str(
ind,'%03d'),'.post.res'];

bound=fopen(filebon); % results file to read

a=7;
```

```
% cycle to read the i upper values

for i=1:a

    linea=fgetl(bound); % to read the row and move to the new line

    if i==7;
        ELE=textscan(linea,'%d %d %d'); % to read the 7th line
        ELEM=cell2mat(ELE); % to transform the cell array in matrix
        nelem=ELEM(1);
        npoing=ELEM(2);
        COnodi=zeros(npoing,3); % to initialize a zero matrix
        a=nelem+npoing+9; % last row index

    else
    end
end


% cycle to read the npoig values, i.e. the coordinates
for i=1:a

    linea=fgetl(bound);

    if i>=2 && i<(npoing+2)
        CO=textscan(linea,'%f %f %f %f');
        COn=cell2mat(CO);
        COnodi(i-1,1)=COn(1,1);
        COnodi(i-1,2)=COn(1,2);
        COnodi(i-1,3)=COn(1,3);
    else
    end


end
```

5. THIRD MATLAB FUNCTION: IT APPLIES THE ENSEMBLE SMOOTHER ALGORITHM.

```
function [U]=KalmanFun2 (root,U_f,E,num_sim,D_vect,output)

n_mc = num_sim;                    % num. of columns of the simulations matrix
n_f = size(U_f,1);                 % num. of rows of data+parameters
m_mc = size(D_vect,1);             % num. of measurements
H = eye(m_mc,n_f);                 % matrix to relate the simulations and the
measurements matrices (in this case identity)
```

```
HU = H * U_f;

D=zeros(m_mc,n_mc);
for i = 1:m_mc
    for j = 1:n_mc
        D(i,j) = D_vect(i)+E(i,j); % to create the D matrix [m_mc x n_mc],
summing to vector D_vect the random value of error E
    end
end

R = (1/(n_mc-1)) * E * transpose(E);

Sum = zeros(n_f,1);
for i = 1:n_f
    for j = 1:n_mc
        Sum(i) = Sum(i) + U_f(i,j);
    end
end

DeltaU=zeros(n_f,n_mc);
for i = 1:n_f
    for j = 1 : n_mc
        DeltaU(i,j) = U_f(i,j) - (Sum(i)/n_mc);
    end
end

C_f = (1/(n_mc-1)) * (DeltaU) * transpose(DeltaU);
HC = H * C_f;
HCH = HC * transpose(H);
HCH_R = HCH + R;
INVERSE = inv(HCH_R);
K_t = C_f * transpose(H) * INVERSE;

U = U_f + K_t * (D - HU);           % to update the simulations matrix

kalman_txt=[root,'/',output,'/','kalman','.txt'];
dlmwrite(kalman_txt, U, 'delimiter', '\t','precision', '%.8f','newline', 'pc');
% to print the results
```

Acknowledgements

During my Ph.D. I could luckily meet many special persons, who helped me in different ways. Therefore, I would like to thank those who have helped and supported the writing of this thesis.

First of all, I want to thank my supervisor Simonetta Cola, who has always been available and helpful. With a friendly behavior, she took me in a field that was new for me, with ambition and patience.

I want to say thank to Fabio Gabrieli, for the time he shared with me, looking for solutions to the problems that I have had during these years. I want to thank Fabio also for his genuine friendship.

My period in Vienna was really amazing to me. The experience I made in Austria has been possible thanks to Simonetta Cola and Roland Kaitna. I really appreciated the opportunity they gave me, which allowed to create a great collaboration and to obtain meaningful results. I really want to thank Roland for his special behavior, personable and professional at the same time. Thank also to Martin for being always nice and available, even when he had no time.

I want to thank my mother and my father for always supporting me, especially when their opinions are different from mine. Thank also to Simone, Celia and to the sweet Noah for their love.

Finally, some friends played important roles during these years. Thank to Riccardo and Mattia for our conversations, for our laughs and for the help they gave me. Thank to Jacopo and Carlo for the free time spent together, for their moral support and for their friendship. I can't forget Stefano for his help at the beginning of my period in Vienna, and for the special friendship that was born. Thank also to Cecilia for her important support, particularly with the Spanish language.

Thanks to Giulia, important friend of mine, always ambitious and comforting. Thank for her changeless help, for her time and for being here.

Thank to Gigi, one of my best friends, for supporting me in every situation.